Addressing and tailoring the electronic properties of semiconductor nanostructures: nanowires and transition metal dichalcogenides

Università di Roma "La Sapienza"

Dottorato di Ricerca in Materials science – XXX Ciclo

Candidate

Davide Tedeschi
ID number 1343024

Thesis Advisor

Prof. Antonio Polimeni

A thesis submitted in partial fulfillment of the requirements
for the degree of Doctor of Philosophy in Mathematical Models for Engineering, Electromagnetics and Nanosciences

November 3, 2017

Thesis defended on 20 December 2017
in front of a Board of Examiners composed by:

Prof. Massimiliano Aschi (chairman)
Prof. Alessandro Ruocco
Prof. Giovanni Sotgiu

Addressing and tailoring the electronic properties of semiconductor nanostructures: nanowires and transition metal dichalcogenides
Ph.D. thesis. Sapienza – University of Rome

© 2017 Davide Tedeschi. All rights reserved

This thesis has been typeset by LaTeX and the Sapthesis class.

Version: 20 December 2017

Author's email: davide.tedeschi@uniroma1.it

To Sara and my Family

Preface

During the three years of my Ph.D. course, I had the opportunity to conceive and run experiments on two different topics of great impact in materials science. Indeed, my supervisor gave me the chance to investigate semiconductor nanowires (NWs)- grown by the group of Prof. C. Jagadish at the Australian National University- and mechanically exfoliated flakes of transition-metal dichalcogenides (TMD). The former topic has collected a steadily growing interest from a widespread community of scientists ranging from theoretical physicists to biologists; see the ISI web of science (`https://apps.webofknowledge.com/`). The interest in this topic started in the nineties, when the group of professor C. M. Lieber at the Harvard University became a worldwide leader in the vapor-liquid-solid growth technique. The number of publications in the field and of their citations has been increasing year by year since then, reaching a maximum in 2015; see Figs. 1a and 1b.

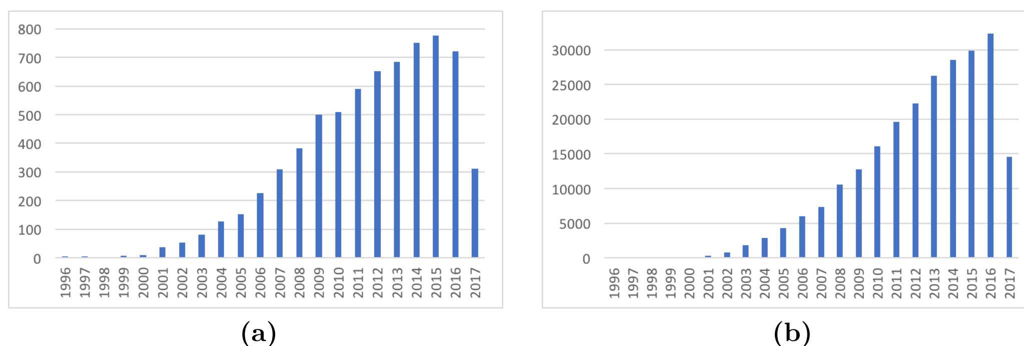

(a) **(b)**

Figure 1. a) Number of articles concerning semiconductor NWs and published each year from 1996 to 2017. b) Number of citations of NW papers from 1998 to 2017. (From `https://apps.webofknowledge.com/`)

The interest in TMDs arose and rapidly blew up, instead, at the end of 2010 when the pioneering article of K. Mak *et al.* (*Phys. Rev. Lett.* **105**, 136805) showed the enormous potential of TMDs layered at an atomic scale. As a matter of fact, the indirect band-gap typical of bulk TMDs turns into a direct band-gap in mono-layer TMDs, thus giving rise to an exponential increase in the number of articles focused on TMD layered materials and published in 2015 and 2016; see Figs. 2a and 2b. The new possibilities offered by this fascinating topic compelled my supervisor and me to begin an investigation of the effects that post-growth treatments with protons -a process usually followed to improve the optical quality of III-V bulk semiconductors- have on TMD flakes.

In the first part of this Ph.D. thesis, I will present the results obtained on semiconductor InP NWs with zincblende and/or wurtzite crystal-structure, in particular with the wurtzite structure whose physical properties are not well assessed since this structure is characteristic only of NWs. In the second part, I will discuss the results achieved on both mono- and multi-layer flakes of MoSe2, MoS2, WSe2, and WS2.

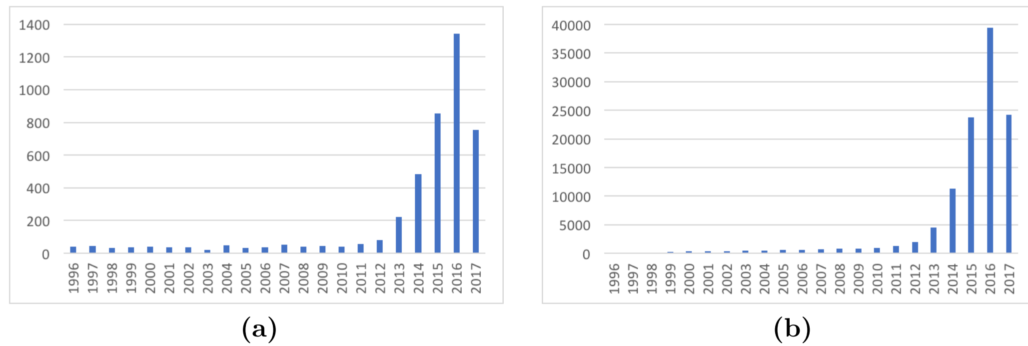

Figure 2. a) Number of articles concerning TMDs and published each year from 1996 to 2017 . b) Number of citations of TMD papers from 1998 to 2017. (From `https://apps.webofknowledge.com/`)

Introduction

Semiconductor materials played and still play a pivotal role in the technological development of modern life. From personal computer to data storage (*e.g.* solid-state disk-drives), from solar cells and cell phones to LEDs and biological sensors, there has always been a new system to study, a novel application to develop, and a solution to an otherwise unsolvable problem in which semiconductors play an essential role. All those technological goals have been achieved thanks to the synergic works carried out by basic researches in materials science, in particular in the semiconductor field. In the last decades, tremendous efforts have been made to miniaturize semiconductor devices at a nanometer scale, aiming at obtaining more compact devices with optimized speed and reduced power consumption. Unfortunately, or *fortunately*, the physical properties of any material dramatically change when the material dimensions are reduced to nanometer-lengths. Therefore, many efforts are required to understand the properties of any desired nanostructure, if they have to play a central role in technological applications.

In recent years, a great interest has grown in the investigation and applications of nanowires (NWs). NWs are several micron-long filamentary-crystals whose diameters range from few to hundreds of nanometers. Their dimensions make NWs suitable to bridge the gap between the microscopic and the nanoscopic world in both research and technology fields. Although several types of materials can be grown in a NW form, *e.g.* metals, insulators, and semiconductors, the latter are the most interesting and promising materials. As a matter of fact, owing to their peculiar shape and dimensions, semiconductor NWs are valuable candidates for novel nanoscale devices, in which they act as both functionalized components and interconnects. Moreover, semiconductor NWs represent nanostructured systems for which some key parameters in device engineering, *e.g.* chemical composition, size, and crystal phase, are well controlled nowadays. This is mainly due to the technique used to grow NWs. NWs are usually fabricated via the *vapor-liquid-solid* (VLS) technique, in which metal nanoparticles are used as catalyst seeds to induce a one-dimensional crystal growth. This well-controlled process allows for the synthesis of a wide range of semiconductor systems in the NW form, ranging from IV-IV to II-VI, with a high degree of manageability of both the chemical composition and morphology. In addition, under suitable VLS conditions, non-nitride III-V NWs can crystallize in the hexagonal wurtzite (WZ) structure in materials that, instead, are notoriously stable in the cubic zinc-blende (ZB) structure. The opportunity to controllably grow NWs in different crystal phases, namely, the *polytypism*, adds a new degree of freedom in device engineering. The presence of a WZ crystal phase in many III-V NWs offers also the opportunity to address the electronic band structure of this poorly known structure,

whose presence itself is a subject of fundamental interest in materials science and chemistry. As an example, there is no experimental information concerning the variation of the spin and transport properties, *i.e.* gyromagnetic factors and carrier effective-masses, respectively, when the phase transition from ZB to WZ occurs. Even the fundamental band-gap value of some WZ semiconductor materials have not been determined, yet. Therefore, a comprehensive study aimed at the investigation of the correlation between the NW electronic properties and NW crystal structure is mandatory nowadays.

A great interest has grown also in the field of layered materials. Since the discovery of graphene in 2004, it has been understood the great potential of layered systems for advanced-technological applications. As a matter of fact, layered materials thinned to their physical limits -and usually referred to as two-dimensional (2D) materials- exhibit properties quite different from those of their bulk counterparts. A very wide spectrum of 2D materials has been then investigated. The most studied material is graphene because of its exceptional electronic and mechanical properties. Group VI transition metal dichalcogenides (TMDs) have also attracted the attention of researchers involved in the semiconductor field. TMDs have a crystal structure similar to that of graphite. Their layered structure, X-M-X, where M is the transition metal and X is the chalcogen atom, is characterized by weak interlayer van der Waals bonds and strong intralayer covalent bonds. That structure allows for an easy mechanical exfoliation, as in the graphene case, which is a major advantage of 2D materials, together with their synthesis techniques, cheap and easy as compared to the *molecular-beam-epitaxy* or *metal-organic chemical-vapor-deposition* techniques used for the fabrication of other nanostructured systems. The most surprising feature observed in 2D TMDs is the transition from an indirect band-gap in the infrared region to a direct band-gap in the visible region when they are thinned to the monolayer limit. That feature, coupled with the TMD extremely high flexibility, elasticity, and resistance, makes TMDs suitable in the field of low-dimensional optoelectronic devices. In addition, the TMD high surface-to-volume ratio is valuable in biological fields, as they can be used as highly reactive sensors. Besides, the TMD unique properties in the single-layer limit of valley-valley coupling and valley-spin coupling render TMDs the suitable candidates for novel technologies based on valleytronic and spintronic. However, almost all these aforementioned properties are at the early stage of investigation and systematic studies are necessary before TMDs could be exploited in future applications.

In this thesis, the electronic properties of InP NWs and MX_2 TMDs, with M=Mo or W and X=S or Se, are thoroughly investigated mainly by means of optical spectroscopy, in particular photoluminescence (PL) in combination with external perturbations, *e.g.* high magnetic fields. The response of semiconductor TMDs to hydrogen irradiation is studied, too. The thesis is therefore structured in two parts, the first one, from chap. 1 to chap. 3, is devoted to InP NWs, the second one, from chap. 4 to chap. 6, is devoted to 2D TMDs.

- In the *first chapter*, the high degree of freedom achieved in NW fabrication is presented and accounted for by the VLS technique, which is also discussed in details together with its recent development: the *selective-area-epitaxy* technique. Then, the differences between the structural, electronic, and optical

properties of WZ and ZB crystal phases are discussed. The striking variation induced in the band structure by the crystal phase-transition is highlighted, too. Moreover, the different optical anisotropies of the two crystal phases are summarized. The chapter is concluded by a review of the technological applications of semiconductor NWs in the fields of optoelectronic, energy conversion, biosensoring, and as probes of elusive quantum effects.

- The *second chapter* comprehends a systematic investigation of InP NWs in both the ZB and WZ crystal-phases. The morphological characteristics of the investigated samples as accessed through scanning-electron-microscopy, transmission-electron-microscopy, and selective-area-diffraction patterning are also presented. The basic optical properties of InP in both crystal phases are assessed by either PL or μ-PL experiments as a function of lattice temperature and power excitation. Polarization-resolved measurements are shown, too. The three lowest-energy critical points of the WZ band-structure are investigated by PL excitation (PLE) as a function of lattice temperature. A quantitative reproduction of those spectra allows for establishing the temperature dependence of the A, B, and C inter-band transitions. A comparison with ZB results is made, too. Finally, the hot-carrier effect in NWs is found and its dependence on NW morphology is investigated.

- In the *third chapter*, the transport and spin properties of WZ InP are assessed by PL spectroscopy under high magnetic fields (up to $28\,T$). A brief review of the effects that a magnetic field has on the energy and symmetry of exciton recombinations and of free-electron-to-acceptor and donor-to-acceptor transitions in WZ crystal is presented. Both diamagnetic shift and Zeeman splitting depend on the magnetic-field direction with respect to the NW symmetry-axis, namely the WZ $\hat{c}$-axis. That dependence has been investigated by applying the magnetic field either parallel or orthogonal to the NW axis. The obtained results are compared with the literature of both theoretical models of WZ InP and experimental results in other WZ compounds, such as GaN, InN, and ZnO. Finally, the non-linearity observed in the Zeeman splitting for magnetic fields above $10\,T$ and parallel to the NW axis is compared to a theoretical prediction.

- In the *fourth chapter*, the lattice, electronic, and vibrational properties of 2D TMDs are described. In particular, the lattice structures of several polytypes are shown, with special emphasis on the 2H polytype, whose electronic and vibrational properties are investigated and its different properties in the bulk and single-layer regimes highlighted. Then, several methods aimed at reaching the mono-layer limit are presented and top-down exfoliations from bulk materials are singled out from bottom-up syntheses. The chapter ends with a brief review of the technological applications of semiconductor 2D TMDs in the fields of optoelectronic, energy conversion and storage, and molecular sensing.

- The *fifth chapter* comprehends a systematic investigation of the effects of hydrogen irradiation on the emission properties of *single- and bi-layer* TMDs, such as $MoSe_2$ and WSe_2. Firstly, a wide variety of experimental results con-

cerning MX_2 optical band-gaps and vibrational mode-energies are summarized. A brief description of the investigated samples is presented, too. The optical properties of pristine samples are assessed by means of either μ-Raman or μ-PL experiments whose room- and low-temperature results agree well with the existing literature. Then, the pristine flakes are irradiated with progressively increasing doses of hydrogen and the results thus obtained are reported. In the single-layer regime, a worsening of the material optical quality is observed together with the appearances of very sharp peaks below the band-gap energy. Conversely, a small improvement in the PL efficiency is obtained in the bi-layer regime. Finally, a solution to the worsening of the optical quality observed in hydrogenated single-layer flakes is provided.

- In the *sixth chapter*, the effects of hydrogen irradiation on the morphological and optical properties of *multi-layer* TMDs are discussed. Surprisingly, hydrogenation favors unique conditions for the production and accumulation of molecular hydrogen just one or few layers beneath the crystal surface of all the multi-layer MX_2 compounds investigated. That turns into the creation of atomically-thin domes filled with hydrogen molecules. The results of an atomic-force-microscopy and optical investigation of these new fascinating nanostructures are discussed. Finally, the possibility to tailor the dome position, size, and density is demonstrated, which provides a tool to manage the mechanical and electronic structure of 2D materials.

- The main results obtained in this work are summarized in the conclusive remarks.

- In the *appendix*, the theoretical basis of the optical-spectroscopy techniques here used, such as PL, PLE, magneto-PL, and Raman spectroscopy, are provided. PL and PLE are complementary techniques that enable a complete characterization of the electronic states of any optically-efficient material. Indeed, PL is an extremely sensitive probe of low-density electronic states, such as impurities or defects, while PLE can address the full density of states, *i.e*, it mimics absorption measurements, at least under certain approximations. On the other hand, PL spectroscopy under magnetic field allows for the determination of carrier effective-masses and g-factors, while Raman allows for getting information about the lattice properties of solids. A description of all the used experimental setups is also given. Finally, a description of the experimental apparatus used for hydrogen irradiation and atomic-force-microscopy measurements is provided.

- Finally, a list of the publications to which the author of this thesis has contributed is provided, along with a list of poster/oral contributions to international conferences given by the author of this thesis during his PhD studies.

Contents

I Optical properties of InP Nanowires **1**

1 Semiconductor nanowires **3**
1.1 Why do we deal with nanowires? 4
1.2 Growth of nanowires 5
1.3 Polytypism in nanowires 9
1.3.1 Zincblende and wurtzite band structure 12
1.3.2 Zincblende and wurtzite NW optical properties 14
1.4 Technological development of NW based devices 17
1.4.1 Nanowires for opto-electronics applications 17
1.4.2 Nanowires for energy applications 20
1.4.3 Nanowires to probe elusive fundamental quantum physics effects 22
1.4.4 Nanowires as biosensor 24

2 Optical properties of InP nanowires **27**
2.1 State of art of wurtzite-InP band-structure 27
2.2 Investigated samples 28
2.3 Addressing the band-structure's properties of WZ and ZB InP-NWs 34
2.3.1 PL characterization 34
2.3.2 μ-PL polarization experiments on mixed-phase single-NWs . 37
2.3.3 Temperature dependence of WZ critical points addressed by PLE 40
2.4 Hot carrier in NWs 47
2.4.1 Dependence of carrier temperatures on NW diameter and lattice temperature 49
2.4.2 Homostructures based on single NW as promising photothermoelectric device 54

3 Magneto-photoluminescence studies on wurtzite InP nanowires **57**
3.1 Magnetic-field effects on optical transitions 58
3.1.1 Free-exciton recombination in WZ crystals 58
3.1.2 Free-electron to neutral-acceptor transition 60
3.1.3 Neutral-donor to neutral-acceptor transition 61
3.2 Values of the electron and hole effective-masses 62
3.2.1 Theoretical predictions 62
3.2.2 Experimental results 63
3.3 Carrier g-factors 71

II Tailoring the properties of transition metal dichalcogenide flakes **77**

4 Two-dimensional transition-metal dichalcogenides **79**
4.1 Crystalline structure 80
4.1.1 Band structure 82
4.1.2 Vibrational properties 85
4.2 Growth techniques 89
4.2.1 Top-down approach 89
4.2.2 Bottom up approach 92
4.3 Technological development of TMD based devices 92
4.3.1 Opto-electronic devices 93
4.3.2 Electrocatalysis 95
4.3.3 Molecular sensing applications 96
4.3.4 Energy storage applications 97

5 Effects of hydrogen irradiation on single- and bi-layer TMDs **99**
5.1 State of the art of MX_2 physical properties 99
5.1.1 Why hydrogen? 101
5.1.2 Investigated samples 103
5.2 Optical properties of pristine $MoSe_2$ and WSe_2 103
5.2.1 μ-Raman investigation 104
5.2.2 μ-PL investigation 105
5.3 Optical properties of hydrogenated $MoSe_2$ and WSe_2 110

6 Hydrogen filling of bulk TMD domes induced by proton irradiation **115**
6.1 Domes formation in bulk TMDs 115
6.1.1 AFM investigation 116
6.1.2 Is there something inside the domes? 118
6.2 Light emission from domes 121
6.2.1 Temperature investigation 129
6.3 Tailoring the size, density, and position of domes 132

Conclusion **135**

A Experimental details **139**
A.1 Optical spectroscopy 139
A.2 Optical experimental setup 151
A.3 Post-growth hydrogen-implantation and electron-beam lithography . 158
A.4 Atomic force microscopy 160

Publications and conferences **163**

Bibliography **167**

Part I

Optical properties of InP Nanowires

Chapter 1

Semiconductor nanowires

Semiconductor nanowires (NWs) are several-micron-long filamentary-crystals whose diameters range from few to hundreds of nanometers and whose cross-sections perpendicular to the NW symmetry-axis are typically characterized by symmetric shapes, e.g., hexagons, circles, or squares. NWs are considered the smallest structures able to conduct current and light in the nanoscale regime [1]. Nowadays, these fascinating nanostructures are grown in several forms, morphologies, and chemical compositions. That high degree of freedom in NW fabrication will be discussed in the first section of this chapter.

Semiconductor NWs have been observed for the first time in 1963 by Wagner and Ellis [2], who obtained what they called whiskers[1], namely, silicon NWs grown *via* the *vapor-liquid-solid* (VLS) technique. The authors proposed that the catalyst activity of gold nanoparticles could favor the vertical and one-dimensional growth of NWs [2] in a scalable and controllable way. Details of the VLS growth and of its recent development, the *selective-area-epitaxy* (SAE) growth that allows a NW growth on ordered patterns, will be given in the second section of this chapter.

The particular VLS growth-conditions account for several astonishing properties of semiconductor NWs. One of the most remarkable of those property is the presence of different crystal phases in a same NW, *i.e.*, polytipism. In particular, the occurrence of a wurtzite (WZ) crystal structure in NWs made of non-nitride III-V materials, which are in a zincblende structure in a bulk form, has provided a number of opportunities, especially in band-structure engineering. The difference between zincblende (ZB) -the stable configuration of bulk non-nitride III-V semiconductor at ambient conditions- and WZ phase will be discussed in the third section of this chapter, where the different optical anisotropies of the two crystal phases in the NW form will be highlighted, too.

In the fourth and last section, the opportunity given by the peculiar NW shapes and dimensions will be discussed and the main NW technological achievements will be reviewed. Indeed, NWs exhibit physical features different from those of their bulk counterpart, which allows the development of new nanodevices.

[1]The whisker lateral dimensions were of the order of μm, thus much greater than those of NWs.

1.1 Why do we deal with nanowires?

Whiskers and NWs have not attracted much interest till InAs NWs were accidentally grown on a GaAs substrate [3] and it was discovered that gold nanoparticles act as catalyst of the VLS growth [4]. These discoveries triggered a worldwide research on NWs and a lot of efforts were done to improve and understand the VLS growth. At the beginning, most researches were focused on the understanding of the mechanism by which NWs nucleate and grow. Gold-catalyzed randomly-oriented GaAs NWs with homogeneous diameter [5] (and, shortly after, precisely oriented NWs) were grown. Meanwhile, theoretical efforts provided an understanding of the nucleation theory and of the phase diagram of the *semiconductor-metal alloy* during the nucleation process [6]. All those experimental and theoretical efforts allowed the fabrication of NWs made from different materials and highly controlled in diameter, length, areal density, and orientation. As an example, ordered InP NWs with a very high WZ crystalline quality (demonstrated by the observation of room temperature lasing from a single NW) and uniform diameters and lengths are grown nowadays; see ref. [7]. It should be remarked that NWs are a bridge between the nano and micro-scale, due to their large aspect ratio (typically a factor of 100) between length and radius. Furthermore, the radial dimensions of these nanostructures are close to the characteristic length scales of several solid-state phenomena: the exciton Bohr-radius ($\sim 10\,nm$), the wavelength of VIS-NIR light ($400 \div 2000\,nm$), the phonon mean-free-path ($\sim 100\,nm$), the carrier diffusion-length ($\sim \mu m$), etc. [8]. Therefore, some physical properties of bulk semiconductors are significantly affected by NW size. As an example, the NW large *surface-to-volume ratio* allows NWs to accommodate lattice strain, thus enabling the growth of NWs on lattice mismatched substrates [9]. Finally, NWs are optimum chemical reagents because of their great *surface-to-volume ratio*.

To date, almost every bulk semiconductors have been grown in the NW form: III-V binary compounds (*e.g.*, GaAs, InP, InAs, GaP, GaN, *etc.*), ternary alloys (*e.g.*, InGaAs, InGaP, InGaN, *etc.*), and even single-element NWs (*e.g.*, Si, Ge) and II-VI compounds (*e.g.*, ZnO). Owing to the lattice strain relaxation, different materials have been grown together in a single NW [10], thus pushing further the development of nano-scale devices, such as NW radial *hetero-structures* (tunable emitting-diodes [11]) and NW axial *hetero-structures* (single tunnel-diodes [12]). The *bottom-up* approach, hence the VLS technique and the catalytic action of nanoparticles, are crucial features to obtain both radial and axial *hetero-structured* NWs, as explained in ref. [13]. The occurrence of a WZ-NW crystal-phase in semiconductor materials that crystallize in a ZB phase in the bulk form enables also the growth of *homo-structures* because it is possible to switch from one crystal phase to the other one during the NW growth. The different physical properties of the two crystal phases, to be discussed in section 1.3, give the opportunity to tailor electron and hole wave-functions and therefore to control the dynamic and energy of carriers [14]. Another NW degree of freedom is the growth of NWs with any kind of *shapes*, which adds new functionality to NW devices. As a matter of fact, several studies have succeeded in determining the growth conditions required to change the NW growth orientation on demand [15], thus yielding any NW shape, as exemplified in figure 1.1. It has been demonstrated that the variation of the reactant pressure during the silicon NW

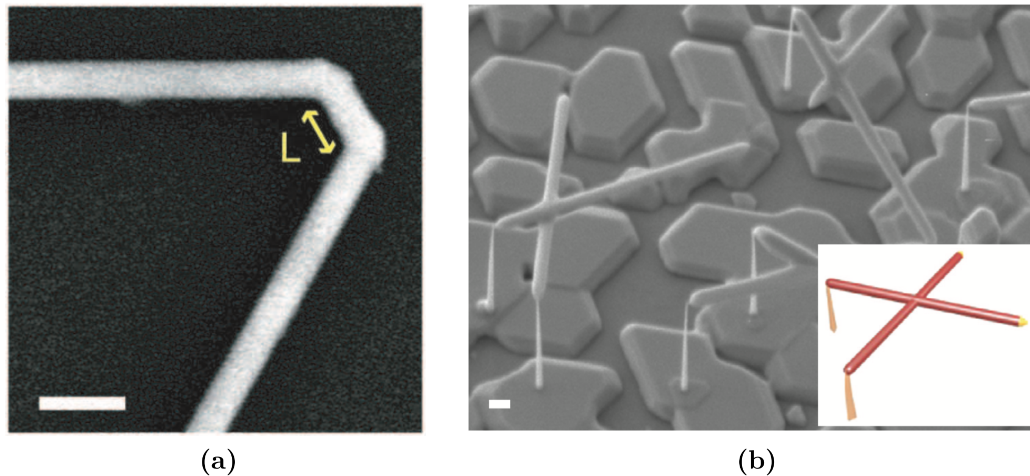

(a) (b)

Figure 1.1. a) Scanning-electron-microscopy (SEM) image of a doubly kinked NW used as a bioprobe. L indicates the length of the segment between two adjacent kinks. Scale bar is 200 nm [16]. b) Scanning-electron-microscopy image showing two InSb NWs merging together to form a crossed single-crystal-device. The inset is a sketch of the SEM image. Scale bar is 200 nm. After ref. [17].

growth introduces reproducible 120° kinks, thus creating NWs characterized by a V shape (see figure 1.1a). Furthermore, p-n diodes and field-effect transistors have been fabricated and used as bioprobes for intracellular PH sensitivity [16]. Finally, the switch from a vertical growth of InAs-InP stems to that of horizontal InSb NWs allows the meeting and merging together of two nearby NWs, as shown in figure 1.1b. The peculiar planar-crossed single-crystal device is a promising system for the observation of Majorana fermions [17]. All the features and potentials of NWs shortly discussed here have a common origin: the *vapor-liquid-solid* growth. Indeed, the chance of having all these degrees of freedom in the design of NW nanostructures must be attributed to the nucleation processes on catalytic regions occurring during the NW growth itself. In the next section, we will catch better the NW methodology and growth process.

1.2 Growth of nanowires

Two main approaches to the growth of semiconductor nanostructures are usually followed: the *top-down* and *bottom-up* approach. In the *top-down* growth, the nanostructures are obtained by lithographically removing selected regions from a previously grown epilayer. In a *bottom-up* growth, the elementary constituents which will form the desired nanostructure gather during the growth in a process that implies a self-organization between the atoms and mimics the spontaneous mechanism of crystal growth. Albeit self-organization can lead to undesired effects, such as random orientations and positions of the planned structures, the *bottom-up* approach is often preferred to the *top-down* one [18] because of a better nanostructure crystal- and optical-quality. It is impossible, indeed, to avoid a surface damage in the etching process involved in the *top-down* approach and almost all good quality NWs are

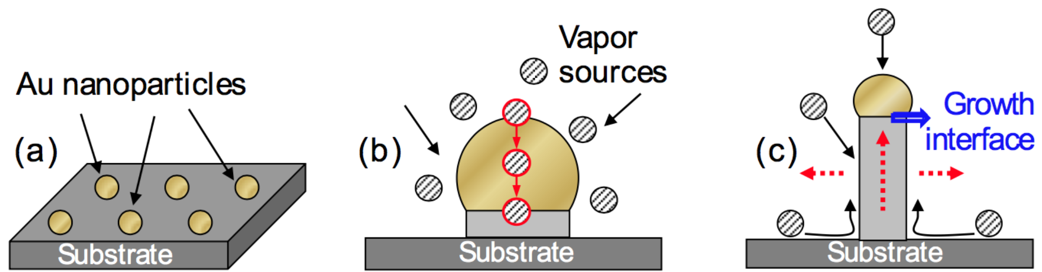

Figure 1.2. Steps of the VLS technique for the NW growth. a) Metal nanoparticles, usually gold, are dispersed on the substrate by various methods. b) Au nanoparticles, heated just above the melting point, act as a sink for the surrounding vapor reactants thus forming an eutectic alloy with one of the NW elements, usually the group III element in III-V NWs. The red path describes the processes of adsorption at the vapor-liquid interfaces, diffusion through the liquid droplet, and precipitation of adatoms at the liquid-solid interfaces. (c) The black lines indicate other possible diffusion paths of adatoms, which may cause further NW axial- and radial-growth.

grown nowadays via the *bottom-up* approach. Therefore, this chapter section will be devoted to describe the latter approach. *Vapor-phase-epitaxy* (VPE) is probably the most widely used NW-growth technique. A vapor-phase synthesis is a process where the initial reactants in the NWs growth are in a gas phase of pure elemental materials or, more often, of chemical precursors. The gases are individually fed into a chamber designed to achieve a laminar gas flow across the substrate surface. The growth parameters determine the gradient in the material concentration resulting on the substrate because of the gas flow [8, 18]. *Metal-organic* VPE (MOVPE) is a VPE subcategory where metallorganic species (typically the group III in a III-V system, *e.g.*, trimethylindium) are used as precursor materials. Another technique similar to VPE is the *molecular-beam-epitaxy* (MBE), where a beam of elementary materials are used as reactants and directed towards the substrate. MBE requires a high vacuum environment to prevent oxidation and contamination from foreign elements. MBE is potentially much more controllable than MOVPE and allows a better understanding and control of the fundamental processes ruling the crystal growth. Nevertheless, MBE is more expensive, far less versatile, and less suited to mass production than MOVPE. Finally, the *chemical beam epitaxy* (CBE) is an hybrid technique where one or more beams contain precursor molecules, rather than elemental material. CBE is more versatile than MBE and generally more expensive and time-consuming than MOVPE.

The above mentioned growth techniques cannot result in a one dimensional growth of NWs unless the growth rate in one dimension is enhanced (and that along the other two dimensions is possibly suppressed, as it can be achieved by a template that confines the forming crystal to a pre-defined shape [19]). In this thesis, we will focus on NWs grown by enhancing the growth rate along one dimension. That enhancement is usually obtained in catalytic regions where the reactants preferentially sediment. As observed in ref. [2], gold nanoparticles catalyze the formation of Si NWs in a VLS growth where the vapour-phase precursor is ($SiCl_4$) and liquid AuSi nanoparticles are the catalytic spots. The majority of *free-standing*

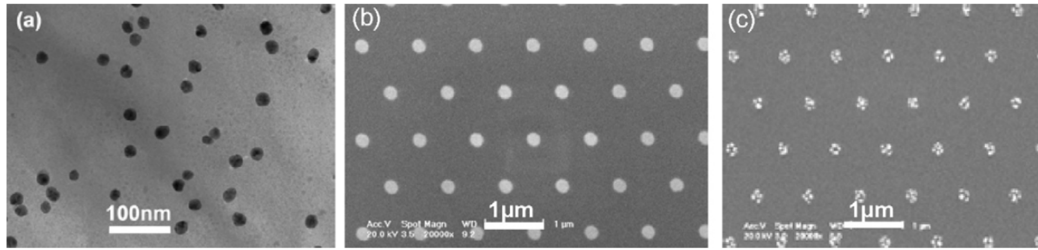

Figure 1.3. Deposition of gold nanoparticles on a substrate. a) Randomly dispersed gold nanoparticles after a thermal annealing of a gold thin film. b) Ordered gold nanoparticles as obtained by electron-beam-lithography. (c) Splitting of the gold nanoparticles in the case of too thin gold films. After. ref. [20].

NWs, including those investigated in this thesis, are grown by improvements of this growth, which has been extended to several different compounds as well as to the case of self-catalysis. In the following, the three steps of a VLS growth schematically shown in fig. 1.2 will be described in some details [8, 18, 20].

- The first step consists in depositing and melting metal nanoparticles (usually gold) whose diameters range from tens to hundreds of nm. To this purpose, first a thin film of gold is deposited on the substrate. Then, a thermal annealing leads to the formation of droplets made from randomly dispersed gold nanoparticles (see figure 1.3.a)): the thinner the film, the smaller the droplet radius. However, too thin gold films result in a splitting of the gold nanoparticles, as shown in figure 1.3.c), and in lower quality gold nanoparticles. Lithography techniques are an approach to a droplet ordering on a substrate, as shown in figure 1.3.b), and droplet size greater uniformity. When the gold nanoparticles are heated above their melting point, an eutectic between gold and the semiconductor material of the substrate may form[2]. A temperature in a range from 300 and 1100 ° C is kept fixed in order to maintain the nanoparticles in a liquid state (see figure 1.2.a)).
- In the second step, the atoms of which NWs are formed diffuse in a vapor phase and impinge onto the substrate. Gas adsorption at the gas/liquid interface is energetically more favored than that at the gas/solid interface and, therefore, group-III atoms with which Au forms the eutectic itself are preferentially adsorbed by the eutectic (the solubility in gold of the group-V elements is very low). The continuous adsorption of group III and group V atoms leads to a super-saturation. Since precipitation of adatoms is favored at a liquid/solid interface (namely, the growth interface) and the melting temperature of the NW material is higher than that of the eutectic, III-V NWs nucleate and grow below the eutectic (see figure 1.2.b)).
- Finally, adatoms can reach the forming NW by three different paths: direct impingement on the eutectic, diffusion through the already formed NW side-walls, direct collection from the substrate (see figure 1.2.c)). The relative

[2]An eutectic is a mixture of substances that melts at a temperature lower than the melting points of the separate constituents.

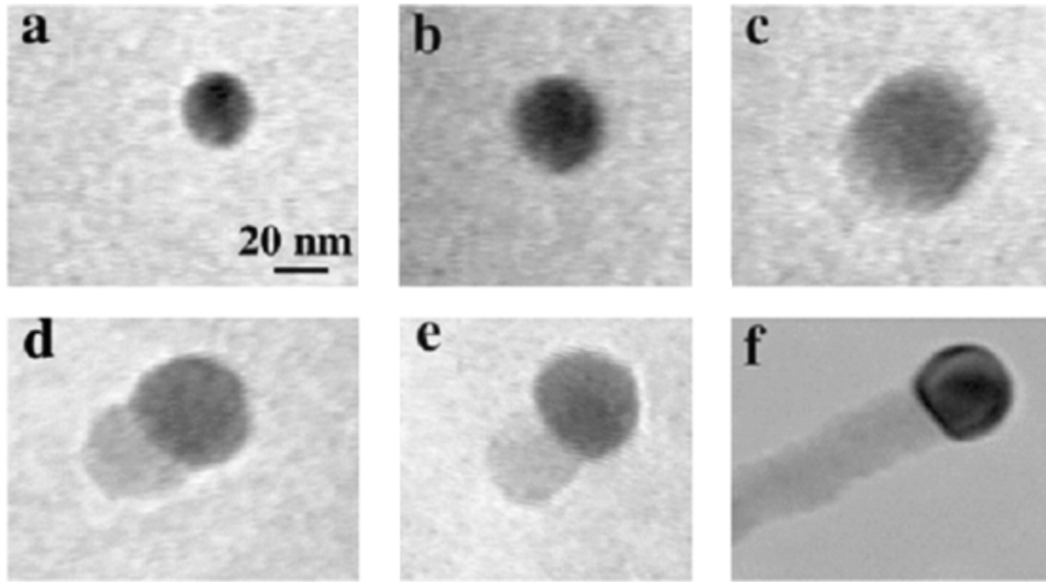

Figure 1.4. In situ transmission-electron-microscopy images taken during a NW growth. (a) Gold nanoparticles in the solid state (at 500 °C). (b) Beginning of the eutectic formation (at 800 °C). (c) Liquid Au/Ge eutectic. (d) Nucleation of Ge nanocrystals below the eutectic. (e) Further Ge condensation and elongation. (f) Formation of a nanowire. After ref. [21].

contribution of those different paths to the NW growth is tuned by the growth parameters (temperature, III-V ratio, and pressure) and, therefore, the NW morphology can be changed on demand: *e.g.*, NW tapering can be avoided by decreasing the second and third path contribution with respect to diffusion through the eutectic.

The above model has been confirmed by *in-situ* transmission-electron-microscopy (TEM) images taken during a NW growth. Figure 1.4 shows the several different steps occurring during the growth of a Ge NW [21]. At the beginning, the gold nanoparticles are in the solid state (Fig. 1.4.a)), then, for increasing temperature and amount of Ge vapor, an eutectic forms (Fig. 1.4.b)-c)). The nucleation begins when Ge supersaturates in the eutectic (Fig. 1.4.d)-e)). Once the Ge nanocrystals nucleate, further condensation/dissolution of Ge vapor into the system maintains the NW growth (Fig. 1.4.f)). Albeit the model seems very simple and intuitive, a full nucleation theory has not been developed, yet, and thermodynamics and chemical-reaction kinetics are still highly debated. In particular, the effect of the geometry of the gold/solid interface, the state of the metal catalyst, and the role played by the three interface energies are still not completely understood [18]. Nevertheless, the lack of theoretical comprehension has not prevented to achieve an excellent control of the NW growth, which has further enabled a large-scale fabrication of complicated NW-based devices, otherwise impossible to get by a *top-down* approach.

Finally, NWs can grow also in the absence of gold nanoparticles (*self-catalysed growth*), which in some cases is a great advantage. Indeed, gold atoms could diffuse in the NWs and be a highly undesirable contaminant, *e.g.* in silicon where

they act as trap centers. Moreover, ordered patterns of non-tapered NWs with almost the same diameter and length can be obtained by patterning by electron-beam-lithography arrays of hexagonal openings in a 30-nm-thick silicon dioxide layer previously deposited on the substrate (*selective-area-epitaxy*, the most recent development of the VLS technique)[7, 22]. This short section is only a short overview on the state of art of NW growth. The reader is referred to thorough reviews for a more comprehensive description of that topic [8, 18, 20]. In the next section, new charming physical properties of NWs will be highlighted.

1.3 Polytypism in nanowires

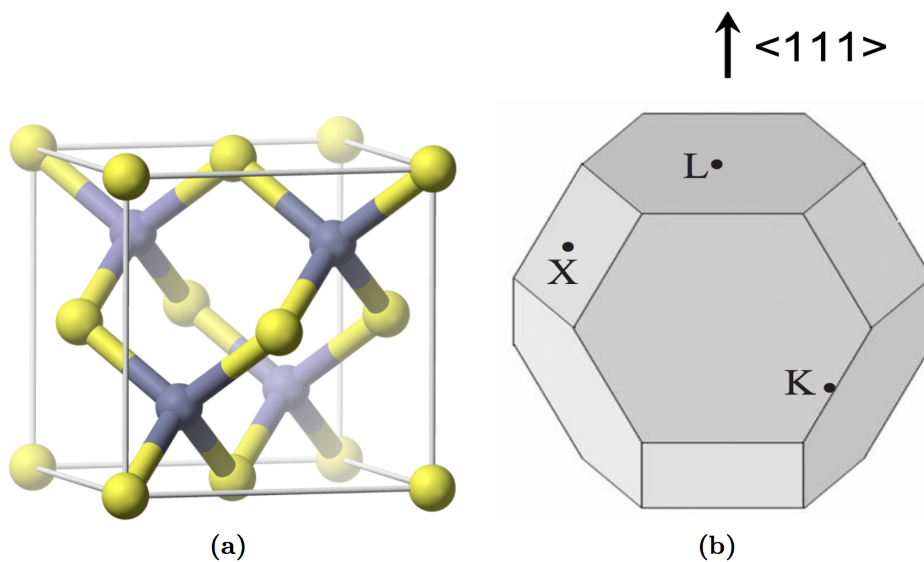

Figure 1.5. (a) Unit cell of a ZB lattice in a stick-and-ball model. Different colors correspond to different atoms. (b) Brillouin zone of the ZB reciprocal lattice. High symmetry points are labeled with Greek capital letters.

Bulk III-V semiconductors, except nitrides, crystallize in the *zincblende* (ZB) structure. Conversely, NWs made of non-nitride III-V semiconductors crystallize also in the hexagonal WZ structure (III-V ZB NWs are actually the exception rather than the rule)[23, 24, 25]. The WZ structure has been reported in NWs made of GaAs [26], InP [27], GaP [28], Si [29], and almost all III-V semiconductors [25], which is one of most surprising NW findings and a topic of significant importance in materials science. The lattice of a ZB structure is a face-centered-cube (FCC) with a bi-atomic base: one atom is located at the origin, the other at $a_{ZB}/4$ from the origin along the (111) direction, where a_{ZB} is the ZB lattice constant. Figure 1.5 shows the unit cell of the ZB lattice (a) and its Brillouin zone (BZ) in the reciprocal space (b). In the ZB structure, each atom is surrounded by four tetrahedrally coordinated atoms of the other species. The atomic orbitals involved in the chemical bonds are not fully covalent sp_3 hybrids because the electro-negativities of the two species are usually quite different. The lattice of a WZ crystal structure is a hexagonal-compact-packed (HCP) structure with two different atoms per lattice

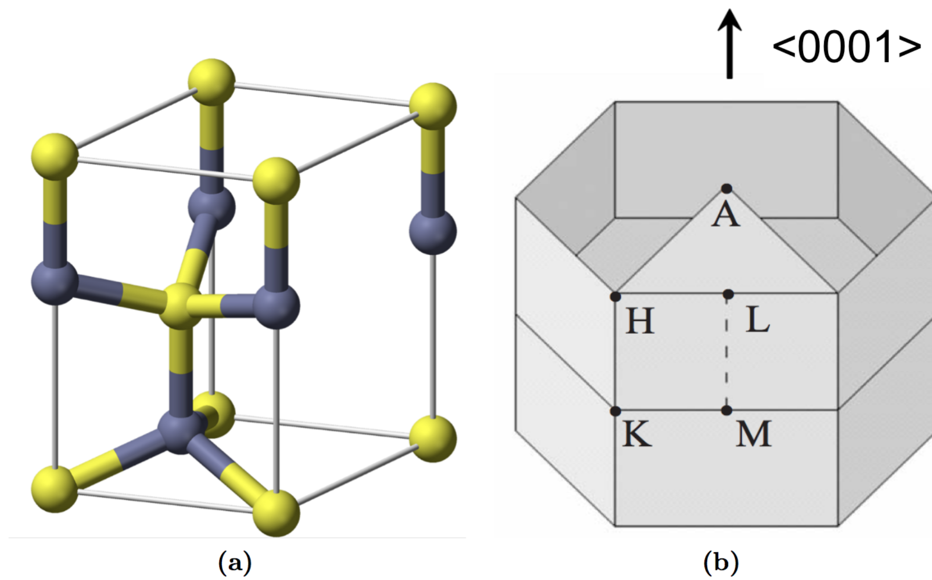

Figure 1.6. (a) Unit cell of WZ lattice in a stick-and-ball model. Different colors correspond to different atoms. (b) Brillouin zone of the WZ reciprocal lattice. High symmetry points are labeled with Greek capital letters.

site. Figure 1.6 shows the unit cell of the WZ lattice (a) and its Brillouin zone in the reciprocal space (b). In the WZ configuration, as in the ZB one, each atom is surrounded by four tetrahedrally coordinated atoms of the other species. Moreover, 9 of the 12 second nearest neighbors are in the same positions they occupy in the ZB structure. The difference between the two phases is given by the remaining three second nearest-neighbors and the third nearest-neighbors. That difference is related to the strength of the III-V bond, where the lower average interatomic distance in the WZ crystal structure would suggest bond-strengths higher than those in the ZB structure. As a matter of fact, bulk materials with high electro-negativity and thus high bond-strength, such as nitrides, crystallize in the WZ structure whereas a low electro-negativity leads non-nitride III-Vs to crystallize in a ZB structure. For the same reason the diamond structure -namely, a ZB structure with two identical atoms per lattice site- is routinely found in materials as C, Si, and Ge with full covalent bonds. The reason why NWs grow preferentially in the WZ structure is a topic still under debate. The very similar structure of the ZB and WZ phases results in a very low difference in the cohesive energy ΔE_{WZ-ZB} (about 24 meV per III–V pair in GaAs [30]). It has been debated if the contributions to the total energy of either the lateral facets [31] or the vertical edges between facets[3] might slightly favor the WZ structure in the case of small-diameter NWs (with large surface-to-volume ratio). Unfortunately, the critical diameters observed for the formation of III–V WZ NWs (> 50 nm) are much greater than those theoretically predicted. It has been demonstrated that WZ nucleation occurs *if and only if* nucleation begins at the NW edge (triple line or three-phase boundary) [30]. However, this model fails to explain the growth of self-catalysed NWs. It has been also stated that the crystal

[3]Provided the energy of these facets in WZ is smaller than that of ZB [32].

structure is controlled mainly by the growth kinetics [33] as well as demonstrated (via probabilistic approaches and explicitly including interlayer interactions beyond nearest neighbors) that high super-saturation in the seed nanoparticles is required to obtain a WZ crystal structure [34].

Polytipism, namely, the presence along a same NW of both ZB and WZ phases, is likely due to the fact that NWs most often grow layer-by-layer in the <111> direction (ZB) and in the <0001> (WZ). Along these very close directions the ZB and WZ structures are hexagonal stacked-layers that differ only in the stacking sequence, as shown in Figure 1.7. Therein, the stacking sequences of the WZ (a)

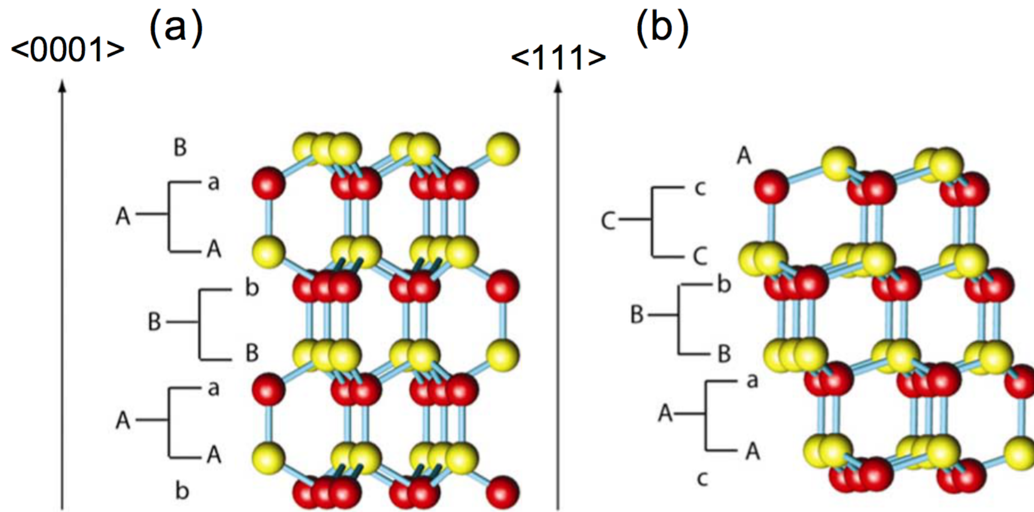

Figure 1.7. Sketch of the atomic structure of a WZ (a) and ZB (b) crystal in the $< -110 >$ viewing direction. Group-III and -V atoms are marked by different colors, upper- and lower-case letters indicate different layers of atoms. After ref. [25].

and ZB (b) crystal structures are shown. The ZB stacking sequence is $ABCABC$, where capital letters refer to hexagonal layers stacked along the <111> direction and different letters label the sites that pairs of group-III and group-V atoms may occupy in a hexagonal plane. By labeling group-III and group-V atoms in each layer with upper and lower cases, the ZB stacking sequence can be written as $AaBbCcAaBbCc$, as shown in figure 1.7.b). The WZ stacking sequence is, instead, $ABABAB$ in the former notation, or $AaBbAaBbAaBb$ in the latter notation, as shown in figure 1.7.a). Therefore, a small variation in the layer sequence during the *layer-by-layer* <111> growth may easily lead to a change from the WZ to the ZB structure. The layer-by-layer growth can also give rise to crystal defects, as often found in NWs. Those defects can be classified in two families: *stacking faults* and *twin planes*. Stacking faults are local breaks in the stacking sequence, *e.g.*, $ABAB\bar{C}AB$ in a WZ structure. A twin plan, instead, is a 60° rotation of a hexagonal layer along the growth direction, as can be found mainly in a ZB structure, e.g., a stacking $ABC\bar{A}CBA$ where a mirror image of the crystal across the twin plane occurs. Crystal defects and phase mixing are harmful, in particular in electronic applications, because they increase carrier scattering along the NWs axis [35]. Moreover, a mixture of ZB and WZ crystal phases with different energy gaps is a challenge for optical applications [36],

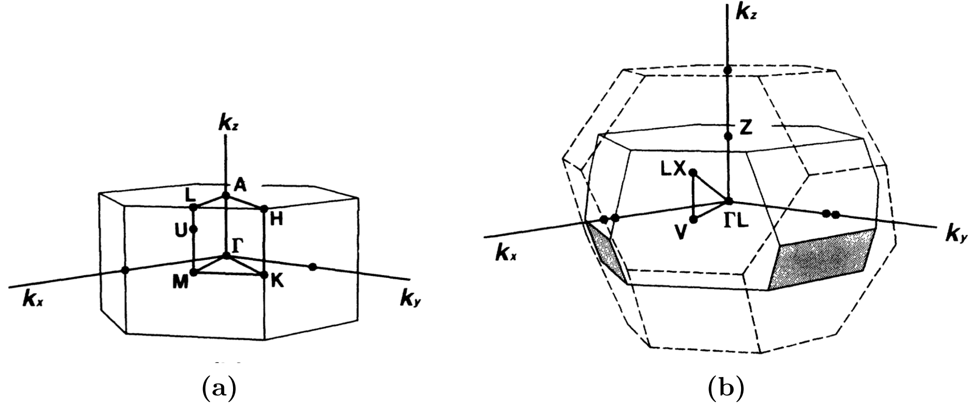

Figure 1.8. a) Brillouin zone of the WZ reciprocal lattice, as already shown in fig. 1.6.b). BZ of the ZB reciprocal lattice (dashed lines), as already shown in fig. 1.5.b), drawn in the same scale and viewed from the same point as in fig. 1.5.a). Solid lines indicate the half-size BZ that corresponds to a doubled unit cell in real space. V is located at the center of the front surface of the half-size BZ, LX is at the center of the hexagon of the FCC BZ, just above V along the [111] direction and inside the half-size BZ. Surfaces common to both BZs are indicated as shaded planes. After ref. [40]

as it will be detailed in subsection 1.3.1. However, an engineering of crystal defects and phase mixing has a potential for novel devices. *E.g.*, the decrease in NW thermal conductivity due to the phonon backscattering [37] induced by the surface roughness produced by periodical twin planes [38] opens the way to thermoelectric applications of NWs. Finally, controlled crystal-phase mixing in chemically homogeneous NWs led to the formation of quantum dots, with a potential for single photon emitters [39].

1.3.1 Zincblende and wurtzite band structure

All similarities in stacking sequences and unit cells between the two crystal phases result in similar band structures. An understanding of the differences among the ZB and WZ structures is more easily achieved by looking at the similarities between the Brillouin zones of the two structures, shown in fig. 1.5.b) and 1.6.b), respectively. A correspondence between states with the same wave-vector can be established for BZs with different shapes provided they have a same volume [40]. In the present case, this is easily realized by doubling the ZB unit cell in the [111] direction in the real space. The resulting Brillouin zone in the reciprocal space is halved, as shown in Figure 1.8.b) by solid lines. The main new feature of the halved ZB Brillouin zone is a folding on Γ of one of the four non-equivalent L points of the full ZB Brillouin zone (1.5.b)), labeled ΓL^{ZB} in the figure. The other L and X points are folded together and labeled LX^{ZB}. Those ΓL^{ZB} and LX^{ZB} have, respectively, the same wave vector as Γ^{WZ} and U^{WZ}, where the latter point divides the WZ $L-M$ line at a $1:2$ ratio. Figure 1.9 shows the relationships between states with the same wave-vector in the WZ (right) and ZB (left) structure. Due to the folding of L points in Γ in the WZ structure, as discussed above, and neglecting spin-orbit coupling, the Γ_1, L_1, and L_3 states in ZB correspond to Γ_1, Γ_3, and Γ_5, in the order, in WZ. Therefore, ZB

bulk-semiconductors with an indirect band gap due to a minimum in the conduction band at or near the L point are expected to become direct gap materials in the WZ structure, as is the case in WZ GaP NWs [28]. In the quasi-cubic approximation, a deformation of the ZB lattice along the <111> direction induces a uniaxial strain, usually called *crystal field* (Δ_{CR}), which may lead to a WZ structure [41]. In the absence of spin-orbit coupling, the *crystal field* splits the p-like Γ_{15} state of ZB into a fourfold degenerate Γ_6 state, corresponding to p_x, p_y, and a doubly degenerate Γ_1 state, corresponding to p_z. The inclusion of the spin-orbit coupling lifts also other degeneracies, as in the case of the Γ_{6V} state that splits into a heavy hole (Γ_{9V}) and a light hole (Γ_{7Vu}) state[4]. Three optical direct-transitions, commonly defined as A ($\Gamma_{7C} \leftrightarrow \Gamma_{9V}$), B ($\Gamma_{7C} \leftrightarrow \Gamma_{7Vu}$), and C ($\Gamma_{7C} \leftrightarrow \Gamma_{7Vl}$) transitions are allowed in a relatively narrow energy-range. In the quasi-cubic approximation, the extent of the

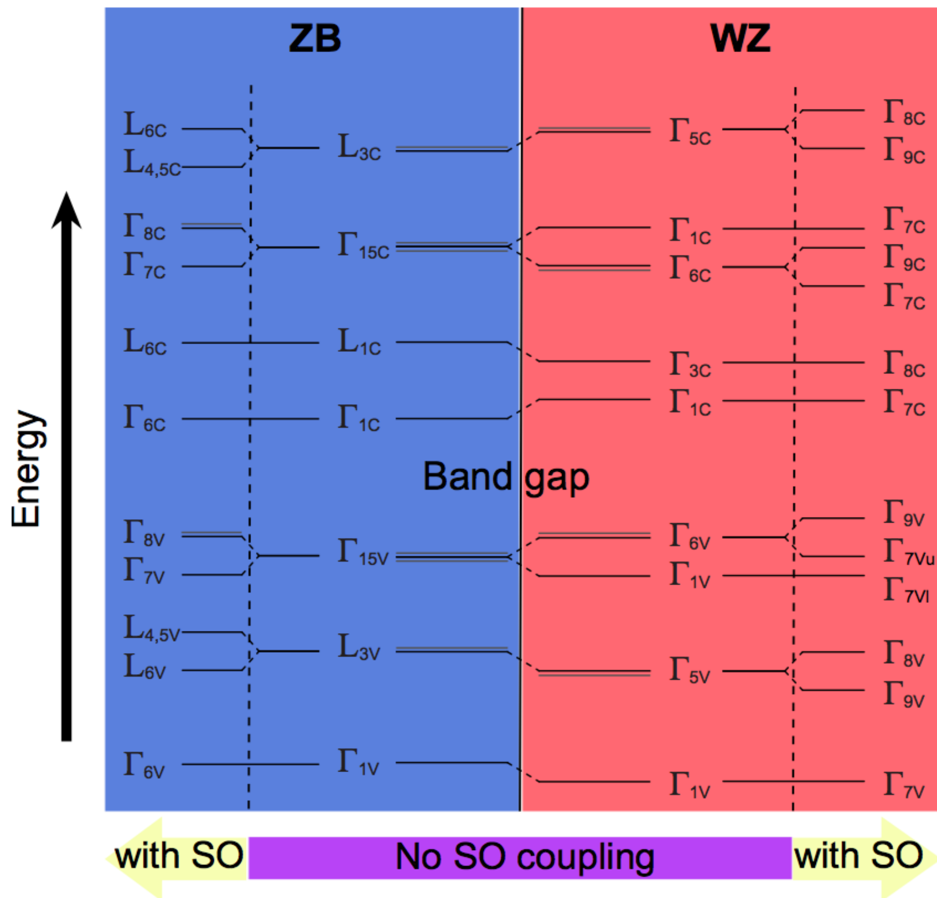

Figure 1.9. Sketch of the correspondence between energy levels at the Γ and L points for the WZ (right) and ZB (left) crystal phases, with and without spin-orbit coupling. Degenerate states are highlighted as thin gray lines, dashed oblique lines mark connected energy levels. After ref. [42].

crystal-field term and the spin-orbit-coupling term (Δ_{SO}) can be derived from the

[4]Subscripts u and l distinguish upper from lower energy levels.

following equation once the difference in energy between hole levels is known:

$$E(\Gamma_{7Vu,l}) - E(\Gamma_{9V}) = -\frac{\Delta_{SO} + \Delta_{CR}}{2} \pm \sqrt{\left(\frac{\Delta_{SO} + \Delta_{CR}}{2}\right)^2 - \frac{2}{3}\Delta_{SO} \cdot \Delta_{CR}} \quad (1.1)$$

and a perfect WZ structure is assumed, namely, $\hat{a}/\hat{c} = 3/8$, where $\hat{a}$ and $\hat{c}$ are the in-plane and out-of-plane hexagonal WZ lattice-parameters, respectively. Valence-band ordering is thus determined by the intensity of the spin-orbit coupling with respect to the crystal-field term. It should be noticed that negative values of the spin-orbit coupling could lead to a very different valence-band ordering with respect to the diagram depicted in figure 1.9, as in the case of WZ ZnO where an ordering (Γ_{7Vu}, Γ_{9V}, Γ_{7Vl}) was found [43]. The band structure of WZ III-V compounds has been calculated by several groups that obtained quite scattered results, mainly because different values of the lattice parameter and different theoretical approaches were used: density functional theory (DFT) within the local density approximation (LDA) [40, 44], $\mathrm{k} \bullet \mathrm{p}$ approach within DFT [45], GW approximation using plane waves and pseudopotentials [46], tight binding [47], and empirical pseudo-potentials [42]. Almost all possible III-V compounds have been calculated in refs. [44] and [42]. De and Pryor have calculated the full electronic band-structure of non-nitride III-V semiconductors in the WZ phase by means of transferable empirical pseudo-potentials including the spin-orbit coupling [42]. All the In-based materials result to be direct-gap semiconductors with a Γ_{7C} conduction-band minimum and an energy gap greater than that of the corresponding ZB materials. Aluminum- and gallium-based materials are direct-gap semiconductors with a Γ_{8C} conduction-band minimum whose WZ band-gap values are either greater (AlAs) or smaller (GaAs) than those of the corresponding well-known ZB values. Bechstedt and Belabbes have calculated the full electronic band structures of non-nitride III-V semiconductors for both the WZ and ZB crystal-structures as well as for the 4H and 6H polytypes [44]. In particular those authors found a Γ_{7C} conduction-band minimum and a band-gap energy of WZ GaAs greater than that of ZB GaAs, at variance with De and Pryor's results.

1.3.2 Zincblende and wurtzite NW optical properties

From an experimental point of view, the ZB and WZ phases differ in crystal structure, band structure, and optical selection rules. The cubic ZB crystal-structure is symmetric: no preferential direction and no anisotropy hold in the optical and transport properties, *e.g.*, carrier effective masses. Instead, the hexagonal WZ crystal-structure is not symmetric, with a preferential direction along the $\hat{c}$ axis, hence some anisotropy characterizes many physical properties. Optical selection rules in hexagonal crystals with space group C_{6V}^4 have been determined by group-theory arguments [48]. Here, we will focus on transitions at $k = 0$ involving only Γ_{7C}, Γ_{9V}, Γ_{7Vu}, and Γ_{7Vl} energy levels. We will neglect the transitions involving Γ_{8C} since we will focus on InP NWs, whose conduction band minimum is at Γ_{7C}. As reported in ref. [49], the dipole-allowed optical transitions at $\vec{k} = 0$ for light polarization $\vec{\epsilon}$ parallel or perpendicular to the WZ $\hat{c}$ axis are:

- without spin-orbit coupling

$$\begin{aligned} \vec{\epsilon} \perp \hat{c}: &\quad \Gamma_{1C} \leftrightarrow \Gamma_{6V} \\ \vec{\epsilon} \parallel \hat{c}: &\quad \Gamma_{1C} \leftrightarrow \Gamma_{1V} \end{aligned} \tag{1.2}$$

- with spin-orbit coupling

$$\begin{aligned} \vec{\epsilon} \perp \hat{c}: &\quad \Gamma_{7C} \leftrightarrow \Gamma_{9V} \\ &\quad \Gamma_{7C} \leftrightarrow \Gamma_{7Vu} \\ &\quad \Gamma_{7C} \leftrightarrow \Gamma_{7Vl} \\ \vec{\epsilon} \parallel \hat{c}: &\quad \Gamma_{7C} \leftrightarrow \Gamma_{7Vu} \\ &\quad \Gamma_{7C} \leftrightarrow \Gamma_{7Vl} \end{aligned} \tag{1.3}$$

The spin-orbit perturbation, which mixes p_x and p_y orbitals with p_z and s orbitals, severely affects selection rules: *e.g.*, the $\Gamma_{1C} \leftrightarrow \Gamma_{1V}$ transition, which is always forbidden in absence of the spin-orbit interaction, turns into the $\Gamma_{7C} \leftrightarrow \Gamma_{7Vl}$ transition, which is allowed by the spin-orbit interaction for $\vec{\epsilon} \perp \hat{c}$. Similarly, the mixing of the atomic orbitals p and s turns the Γ_{8V} state into the Γ_{7Vu} state, which allows the $\Gamma_{7C} \leftrightarrow \Gamma_{7Vu}$ transition -otherwise forbidden- for $\vec{\epsilon} \parallel \hat{c}$. The strength of those transitions strongly depends on the solution of the appropriate secular equation that gives the weights of the orbital atomic functions in each high-symmetry energy-level. That analytical solution, therefore, determines the nature of what is naively expected to be predominantly p_x- and p_y-like, because originating from a Γ_{6V} state, or $(s + p_z)$-like, because deriving from a $Gamma_{1V}$ state [41]. In summary, the $\Gamma_{7C} \leftrightarrow \Gamma_{9V}$ transition is allowed only for light polarization perpendicular to the $\hat{c}$ axis, whereas no strict selection rules hold for the $\Gamma_{7C} \leftrightarrow \Gamma_{7Vu}$ and $\Gamma_{7C} \leftrightarrow \Gamma_{7Vl}$ transitions. It should be noted that the weaker is the spin-orbit coupling, the stronger the original character and strength of those transitions will be: in the limit of weak spin-orbit coupling, the $\Gamma_{7C} \leftrightarrow \Gamma_{7Vu}$ transition will be stronger for $\vec{\epsilon} \perp \hat{c}$ than for $\vec{\epsilon} \parallel \hat{c}$ because of the strong Γ_{6V} character retained by Γ_{7Vu}. Optical anisotropies that do not originate from optical selection-rules have been observed in semiconductor WZ NWs as well in pure ZB NWs [50]. Those anisotropies are due to carrier quantization and/or electromagnetic-field confinement, which takes place when the NW dielectric constant differs from that of the environment. Quantum confinement occurs for NW diameters *smaller or comparable to* the exciton[5] Bohr radius and gives rise to a quantization of the full band structure, thus modifying the NW optical-matrix and polarization-properties [51]. However, all the NWs studied in this work are well above the quantization limit, namely, their diameter exceeds 50 nm and, thus, quantum effects are negligible. The second mechanism is a purely classical phenomenon, independent of crystal phase, and is due to the

[5]Excitons are quasi-particles which are due to the Coulomb interaction between photoexcited holes and electrons and whose characteristic size is given by the Bohr radius, of the order of 10 nm in almost all III-V semiconductors. In appendix A.1 the theory of excitons in semiconductors is given in some detail.

peculiar shape and aspect ratio of NWs, ideally approximated to dielectric cylinders of infinite length [52, 53]. All NWs are subjected to this effect, independently of their crystal phase. Therefore, the main features of that effect will be discussed in the following. The components of a static electric field E_0 are affected by the presence of a dielectric cylinder, in particular they may change on going from the outside to the inside of a semiconductor NW: the component perpendicular to the NW axis, $E_0^{\perp}$, changes inside the NW, whereas the parallel component, $E_0^{\parallel}$, does not change. Inside the NW, the perpendicular component, $(E_i^{\perp})$, is obtained by solving the Dirichlet problem of electrostatic in cylindrical coordinates with the appropriate boundary-conditions. The dependence of $E_i^{\perp}$ on the dielectric constants of the NW, ϵ, and of the environment (vacuum), ϵ_0 is given by eq. 1.4:

$$E_{\perp}^{i} = \frac{2\epsilon_0}{\epsilon_0 + \epsilon} \cdot E_{\perp}^{e}, \tag{1.4}$$

where $E_e^{\perp}$ is the perpendicular component outside the NW [54]. Though Eq. 1.4 was initially derived for static electric-fields, it remains valid as long as the NW diameter is smaller than the electromagnetic wave-length. This approximation is called the *sub-wave-length* regime and is valid in the microwave, infrared, and visible spectrum provided that the NW diameters are smaller than 100 nm. Since the dielectric constant of semiconductor NWs is higher than that of vacuum, the component of the emitted or absorbed light perpendicularly polarized with respect to the NW axis decreases inside the NWs ($E_i^{\perp} < E_e^{\perp}$). In the case of absorbed light, the degree of linear polarization can be defined as:

$$\rho_{abs} = \frac{I_{\parallel} - I_{\perp}}{I_{\parallel} + I_{\perp}} = \frac{1 - \alpha_{abs}}{1 + \alpha_{abs}}, \tag{1.5}$$

where α is the attenuation ratio between the light components polarized perpendicularly and parallel to the NWs axis and can be derived by eq. 1.4:

$$\alpha_{abs} = \frac{I_{\perp}}{I_{\parallel}} = \frac{|E_{\perp}^{i}|^2}{|E_{\parallel}^{i}|^2} = \left[\frac{2\epsilon_0}{\epsilon + \epsilon_0}\right]^2. \tag{1.6}$$

The value of the experimental degree of linear polarization of absorbed light, as measured on a single InP ZB-NW[50], is $\rho_{exp} = 0.96$, namely, equal to the value $\rho_{theo} = 0.96$ estimated for $\epsilon = 12.4$. This agreement validate the *sub-wave-length* approximation. In that same work, the authors found that ρ_{exp} was independent of the NW diameter (provided that it is greater than 10 nm), thus excluding that quantum effects were affecting the polarization anisotropy. In the case of emitted light, the emission from all possible dipole directions has to be taken into account. An integration over Poynting vectors rather than over electric fields should be performed because the radiation from different dipoles is not coherent. As discussed in depth in ref. [52], the attenuation ratio for the emitted light (α_{em}) is then equal to:

$$\alpha_{em} = \frac{I_{\perp}}{I_{\parallel}} = \frac{6\epsilon_0^2}{(\epsilon + \epsilon_0)^2 + 2\epsilon_0^2}. \tag{1.7}$$

The agreement between the value of the linear polarization degree estimated for the light emitted by a single InP ZB-NW ($\rho_{theo} = 0.94$) and that experimentally found ($\rho_{exp} = 0.92$) is very good, too[50].

Several polarization measurements, especially of emitted light, have been reported in the NW literature [55, 56, 57, 58, 59, 60]. In some works, the optical properties of ZB NWs were addressed by taking into account only the contribution to the anisotropy caused by the electromagnetic-field confinement[59, 60]. However, in the case of ZB NWs the polarization of the emitted light is preferentially parallel to the NW symmetry-axis mainly as a consequence of the dielectric mismatch. In WZ NWs, where the polarization of the light absorbed or emitted at the band-gap energy is, instead, substantially perpendicular to the WZ $\hat{c}$-axis, selection rules play the main role [55, 56, 57, 58] whilst the dielectric mismatch can be considered just as a *renormalization factor*[61]. It should be pointed out that selection rules and dielectric mismatch oppositely contribute to the polarization properties of the emitted or absorbed light in WZ NWs whose $\hat{c}$-axis coincides with the symmetry-axis, as usually is the case. Since the linear polarization degree is negative (ideally equal to -1) in WZ NWs, positive (and small) in ZB NWs, polarization resolved optical experiments are a valuable tool, easier than electronic microscopy and x-ray diffraction, to distinguish between crystal phases in semiconductor NWs.

1.4 Technological development of NW based devices

Semiconductor NWs have attracted a great attention from the scientific community for both their novel physical properties and enormous potential for applications in almost all technological fields. As in other emerging research frontiers, people working in the NW field are indeed constantly pushing to develop new fundamental science as well as potential applications. However, no production-scale NW-based device has reached the market place to date. An overview of possible applications of NW-based devices will be given in the present section of the thesis, whereas thorough reviews of this topic can be found in ref. [62, 63]. The section is organized in four subsections that cover the field of opto-electronics, energy conversion, biosensors, and platforms to probe elusive quantum physical effects.

1.4.1 Nanowires for opto-electronics applications

The requirement for more powerful, integrable, and low-consuming electronic systems pushes for devices where semiconductor NWs should play a prominent role. Indeed, the **field effect transistor** (FET), the most basic component of integrated circuits, has been developed using NWs made of various materials, thus taking advantage of the benefits of single crystals in the nanometer-size regime. It should be noted also that NWs can be controllably doped, as for their bulk counterpart, which is a critical aspect in device engineering. Finally, the great aspect-ratio makes NWs suitable as interfaces with top-down fabrication techniques, the most-used in the microelectronics industry. Early silicon NW-based FETs have been fabricated via back- [67] or top-gated [65] geometries. In these geometries, the end facets of the NW act as source or drain of a current that flows along the axis of a NW lying on a substrate. In the former case, the dielectric gate is placed beneath the NW and above the highly doped substrate (the quasi-metallic gate; see figure 1.10.a)), whereas in the latter case a dielectric gate, followed by a metallic gate, has to be grown or deposited on the NW surface (see figure 1.10.b)). In the latter case, the

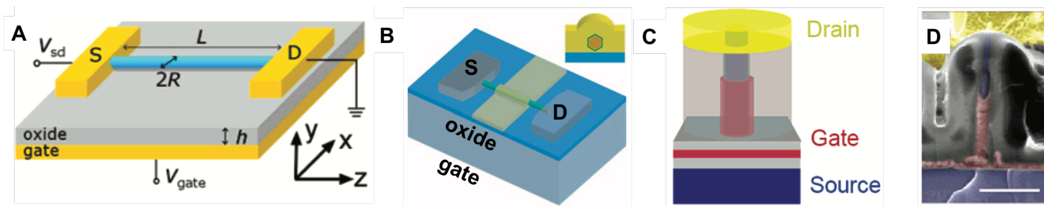

Figure 1.10. Scheme of various geometries of FET-based NW-devices: a) back-gated; b) top-gated (the inset is a cross section of the device geometry); c) vertical NWFET and d) SEM image of vertically integrated surround-gate silicon-NWFET. Scale bar is 500 nm. False colors in the SEM image are added to link this image to the schematic shown in figure 1.10.c). After ref. [64, 65, 66].

NW is completely embedded between the dielectric structure, allowing for a more accurate calculation of the gate coupling and avoiding an underestimation of carrier mobility [68]. However, defects formed on the oxide interface play a prominent role in the device performance due to the NW large surface-to-volume ratio. Indeed, these interface defects may affect the applied gate voltage and increase the carrier scattering [69]. Therefore, passivation techniques, such as hydrogen termination [70] or atomic layer deposition [71], are mandatory to improve the device performances. Both back- and top-gated geometries involve NWs lying on a substrate. However, most of the growth techniques lead to NWs oriented perpendicularly to or almost away from the substrate. Therefore, a single *vertical* In_2O_3 NW FET, where the gate is placed above the drain at the end of the channels, has been realized [72]. Alternatively, the dielectric and metallic gates can completely surround the NW, as displayed in figure 1.10.c), that shows a schematic of such geometry, and in figure 1.10.d), that shows a SEM image of such a kind of surrounding gate NW FET [64]. This configuration allows for a superior electrostatic control of the conductivity in the channel and offers the possibility to drive a current per device area higher than that in a planar architecture. Also III-V materials and metal-oxides have been incorporated into several FET geometries aimed at improving both device performance and material characterization. InAs NWs characterized by light carrier-masses were employed in top-gated FETs without surface passivation. The room temperature mobility of those devices reached 6580 $cm^2V^{-1}s^{-1}$ [73]. ZnO NWs were as good as InAs NWs when their surfaces were passivated with metal-oxide procedures compatible with semiconductors [74]. In those devices, a mobility equal to 4120 $cm^2V^{-1}s^{-1}$ was achieved, which makes ZnO NW-based devices suitable for applications in high frequency integrated electronics. NWs have an enormous potential also in the field of optoelectronic and optical devices, where NWs act as nano-scale photonic-components such as **wave-guides**, **light emitting diodes** (LEDs), and **photonic circuits**. In a photonic circuit, light generated from a miniaturized source, *e.g.*, a quantum dot, is captured and sent precisely to the next component according to the logical sequence of the circuit, as in an electrical circuit. NWs have exhibited advantages in photonic-circuit building-blocks such as photonic diodes. As a matter of fact, asymmetric light propagation can be achieved by wave-guiding the light in composition graded CdS_xSe_{1-x} NWs, as shown in figure 1.11.a) [76]. Indeed, the chemical composition of NWs can be purposely tuned owing

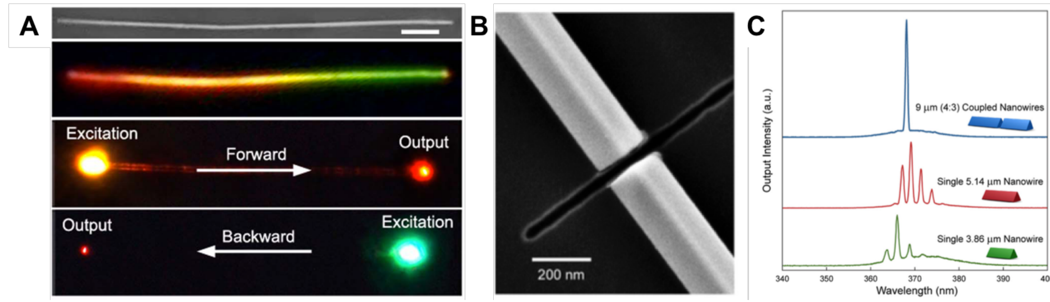

Figure 1.11. a) Asymmetric light propagation in CdS_xSe_{1-x} NWs with a composition gradient along the NW. The top panel reports a SEM image of a composition-graded NW; scale bar is 7 mm. In the second panel from the top, a real-color PL photograph of the NW under diffusive illumination is shown. The two bottom panels show real-color PL photographs with local excitation at each of NWs end facets. b) A SEM image shows the axially coupled GaN NWs. c) Single-wave-length lasing from a coupled cavity (top curve, blue). Multiple wavelength lasing from separated cavity components (bottom curves). After ref. [75, 76].

to the NW ability to relax the lattice strain, as discussed in section 1.1. Therefore, a uniform composition-gradient can tune the CdS_xSe_{1-x} NW band-gap from 2.4 eV to 1.7 eV, leading to different light propagations along the two opposite ways of a same axial direction. The NW peculiar shapes together with their high optical gain permit to get lasing from single NWs. In 2001, ultraviolet (UV) lasing emission was observed in ZnO NWs [77] and since then optically pumped coherent laser emission from NWs was achieved in various materials. Indeed, NWs act simultaneously as optical cavities and gain media. Moreover, thanks to the small volume of the gain medium, lasing threshold was reached with just hundred μA in electrically driven NWs laser [78]. Nowadays, almost all the visible, UV, and near-infrared spectral regions have been covered by NW lasers. Furthermore, multicolor NW lasers have been developed by means of multi quantum-well (MQW) NW hetero-structures consisting of a GaN core surrounded by an epitaxial InGaN/GaN core-shell MQW, which serves as a gain medium tunable in composition[79]. Albeit a lot of effort has been devoted to control the NW shape, size, and composition, most of the NW lasers suffer from a simultaneous emission at multiple frequencies due to the longitudinal modes of the optical cavity (made by the NW itself). Single-energy laser-emission is, indeed, an important figure of merit because it avoids temporal pulse-broadening and allows for a lower threshold-gain. Until now, two schemes have been proposed to get single frequency lasers. Lasing at 738 nm was demonstrated in a single CdS NW forming a small loop at one end thanks to the Vernier effect [80]. Another opportunity to increase the free spectral-range is the coupling of two optical cavities through an air gap, known as cleaved-coupled cavity and shown in figure 1.11.b). Lasing at a single UV wavelength at room temperature was observed in cleaved-coupled GaN NWs (see fig. 1.11.c) and it was even shown that cleaved-coupled NWs operate with a threshold-gain lower than that of the individual components [75]. Lastly, it has been possible to go beyond the diffraction limit by integrating plasmonic effects in NWs. In **hybrid plasmonic-wave-guides** consisting of CdS NWs and silver films separated by a 5-nm-thick insulating MgF_2 gap, a surface-plasmon amplification

by stimulated emission of radiation (SPASER) was achieved, thus leading to the generation of light concentrated into an area well below the diffraction limit (with a resolution hundred times smaller than the operating wavelength) [81].

1.4.2 Nanowires for energy applications

Semiconductor NWs have shown advantages in the development of **thermoelectric** devices, which are aimed at converting thermal energy into electrical energy and viceversa. In presence of a temperature gradient between two sides of a semiconductor rod, majority charge carriers diffuse from the hot to the cold rod side until an opposing electric-field forms and stops this charge flow. Alternatively, a voltage applied across the two rod sides leads to a current flow of majority carriers moving from one rod side to the other side with an ensuing temperature gradient. A material dependent property, namely, the Seebeck coefficient (S), rules the linear proportionality between the temperature gradient and the voltage difference between the two rod sides ($\Delta T = S\Delta V$). Therefore, thermoelectric devices can be implemented as solid-state coolers or energy converters. So far, the main efforts were aimed at using thermoelectric devices as energy converters. Indeed, those devices can be used to *re-utilize* part of the heat wasted to the environment thus enhancing the overall energy-conversion efficiency [82]. A dimensionless figure of merit, ZT, characterizes the performance of thermoelectric devices:

$$ZT = \frac{S^2\sigma}{k_e + k_{ph}}T, \tag{1.8}$$

where σ is the electrical conductivity and k_e and k_{ph} are, respectively, the electronic and lattice contributions to the thermal conductivity. Thus, a high Seebeck coefficient, high electrical conductivity, and low thermal conductivity are required to maximize the performance of thermoelectric devices. Unfortunately, that goal is very challenging because the Seebeck coefficient is *inversely* proportional to carrier concentration, whereas the electrical conductivity is *directly* proportional to this same parameter [83].

In this complicated trade-off between various physical parameters, NW geometry offers two main potential advantages in order to maximize ZT. First, the change in the NW band-structure should lead to an increase in the *power factor* ($S^2\sigma T$): theoretical estimates of ZT values as large as ~ 14 have been made in Bi_2Te_3 quantum wires [85]. Nevertheless, to date the enhancement in the NW power-factor is small [86] although values greater than those obtained in bulk Bi_2Te_3 have been achieved [87]. The breakthrough in the optimization of thermoelectric devices is given by a reduction of the lattice thermal-conductivity without affecting the bulk electrical-conductivity. This is made possible by the great difference (by orders of magnitude) between the phonon and electron wavelengths. The phonon mean-free-path in NWs ranges roughly from $10\,nm$ to $10\,\mu m$ and can be decreased by increasing the phonon scattering from the NW boundaries. This would not change the electrical conductivity, contrarily to what takes place in the bulk case, because of the lower range of the electron mean-free-path in NWs with respect to that in the bulk. In Si NWs synthesized by VLS (see fig. 1.12.b)), values of the thermal conductivity lower than those in the bulk have been reported, thus highlighting their

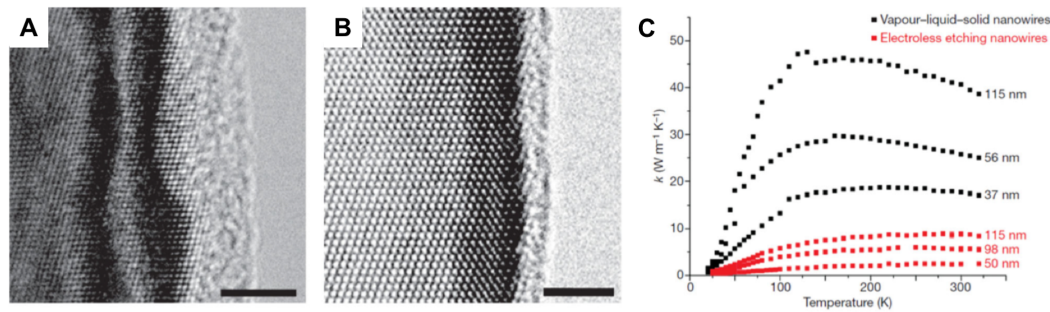

Figure 1.12. a) High-resolution TEM image of a Si NW synthesized by electroless aqueous etching (EE). Scale bar is 4 nm. b) High-resolution TEM of a Si NW synthesized by VLS. Scale bar is 3 nm. A difference in the surface roughness is clearly visible. c) Temperature dependent thermal conductivity of EE and VLS NWs. EE NWs exhibit a suppressed thermal conductivity with respect to that of VLS NWs with the same diameter. After ref. [84].

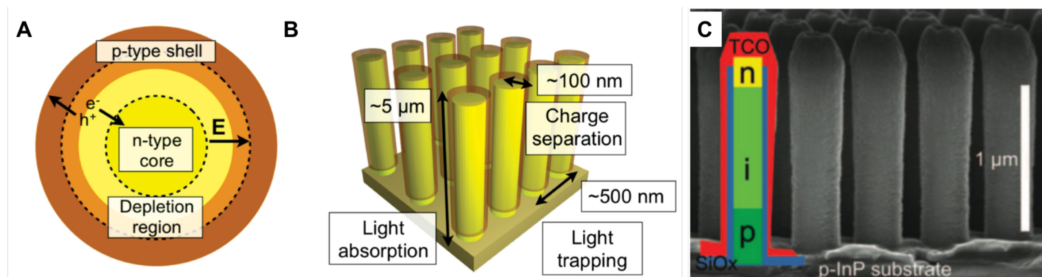

Figure 1.13. a) Top-view sketch of a core-shell NW solar-cell showing the built-in electric-field which separates charge carriers between *n*- and *p*-type regions. b) Sketch of an array of NW solar-cells showing length scales that improve light absorption and charge separation. c) Diagram and SEM image of an array of InP NW solar-cells. After ref. [63, 93]

clear dependence on NW size [88]. Later on, $ZT = 0.6$ has been measured at room temperature in silicon rough NWs synthesized by electroless etching (see fig. 1.12.a) and 1.12.c)), a value two orders of magnitude higher than that in bulk silicon [84]. Although phonon scattering mechanisms in NWs are not clearly understood yet [89], the enhancement in ZT is a potential advantage for the design of thermoelectric NW-based devices [87, 90]. Large diameter NWs, well beyond the quantum limit, are also suitable for efficient and inexpensive **solar cells**. Their main advantage is a tunable geometry: the great NW surface-to-volume ratio as well as dimensions on the same length scale of light wavelength and carrier diffusion-length offer, indeed, unprecedented opportunities to improve charge collection and light absorption. The fundamental properties of materials are investigated in single NW solar-cells, while amounts of power comparable to those produced by thin-film photovoltaic-devices are pursued in arrays of NW solar-cells. Finally, NW solar-cells can be potentially integrated into flexible devices [91, 92] and, moreover, are characterized by cheaper low-temperature fabrication-techniques. Therefore, arrays of NW solar-cells should most likely lead to a second-generation of thin-film photovoltaic-devices with low processing costs and high efficiency. Among all the advantages of NW geometry

in solar-cell applications, the opportunity to improve separation and collection of photogenerated charges, as shown in Figures 1.13.a) and 1.13.b), was one of the earliest recognized advantages. In radial *p-n* junctions, length scales for adsorption and separation of charges are decoupled: light absorption occurs along the NW axis whereas photo-generated minority-carries are collected along the NW radius. This geometry allows the making of NW solar-cells with materials whose optical absorption-length is longer than the minority-carrier diffusion-length, which cannot happen in planar thin-film solar-cells [94]. Therefore, less expensive and less pure materials can be employed in arrays of NW solar-cells, thus reducing the fabrication cost of photovoltaic devices. Another relevant advantage is a greater light-trapping in NWs array, which enables a greater light-absorption with respect to the case of thin-film devices. Two main effects rule light trapping: the sub-wavelength diameter of a single NW, which enables wave-guiding effects, and a *collective* scattering from several neighbors NW-air interfaces, which enhances the overall absorption [95]. In 2013, an array of solar cells based on InP NWs first reached an efficiency comparable to that of their planar counterpart [93]. Figure 1.13.c) shows a SEM image and the scheme of this device, namely, a *p-i-n* doped axial-junction of InP WZ NWs epitaxially grown on a patterned array. The efficiency of this array was 13.8%, smaller than that of a planar solar cell (22.1%) but for an active area 8 times smaller than that of the planar device. To date, the world-record efficiency for arrays of NW solar-cells (17.8%) is held by an array of InP NW solar-cells where hemispherical nanoparticles enhance light absorption [96].

1.4.3 Nanowires to probe elusive fundamental quantum physics effects

Semiconductor NWs provide an ideal platform for various low-dimensional devices aimed at studying elusive fundamental quantum-physics effects. **Majorana fermions** [97] and **Aharonov-Bohm** [98] effects are probably the most interesting ones among those effects. Majorana fermions are particles identical to their own antiparticles[6]. They are characterized by zero charge and zero energy at rest and their experimental observation is very challenging and not trivial. In the Aharonov-Bohm effect, whose experimental observation is also very challenging, the wave-function of a charged particle confined in a region with no magnetic field acquires a phase shift that depends on the enclosed flux. Thus, the Aharonov-Bohm effect plays an eminent role in the study of the interaction between a charged particle and an electromagnetic potential. Majorana fermions are predicted to appear once a superconducting electrode in an external magnetic field is coupled to a semiconductor NW with a strong spin-orbit interaction [99, 100]. The magnetic field should be directed parallel to the NW axis to open a gap in the split spin-orbit bands (*Zeeman term*). The proximity of the superconducting electrodes to the semiconductor NWs gives rise to an ordinary superconducting *s*-wave. This induces a pairing in the NWs between electron states of opposite momentum and opposite spins and opens a gap (Δ) between the two states. To obtain topological superconductors and observe Majorana fermions, $E_z > (\Delta^2 + \mu^2)^{1/2}$, where $E_z = 1/2\mu_B g B$ is the Zeeman energy

[6] More precisely, in second quantization the creation and annihilation operators coincide.

(with μ_B Bohr magneton and g carrier gyromagnetic-factor) and μ is the Fermi level. Majorana fermions should arise as zero-energy bound states where $E_z = (\Delta^2 + \mu^2)^{1/2}$, *i.e.*, mainly at the end of the NW where the electron density is reduced to zero and Majorana fermions could be revealed by tunnelling spectroscopy from a normal conductor [101]. Signatures of Majorana fermions have been detected in hybrid

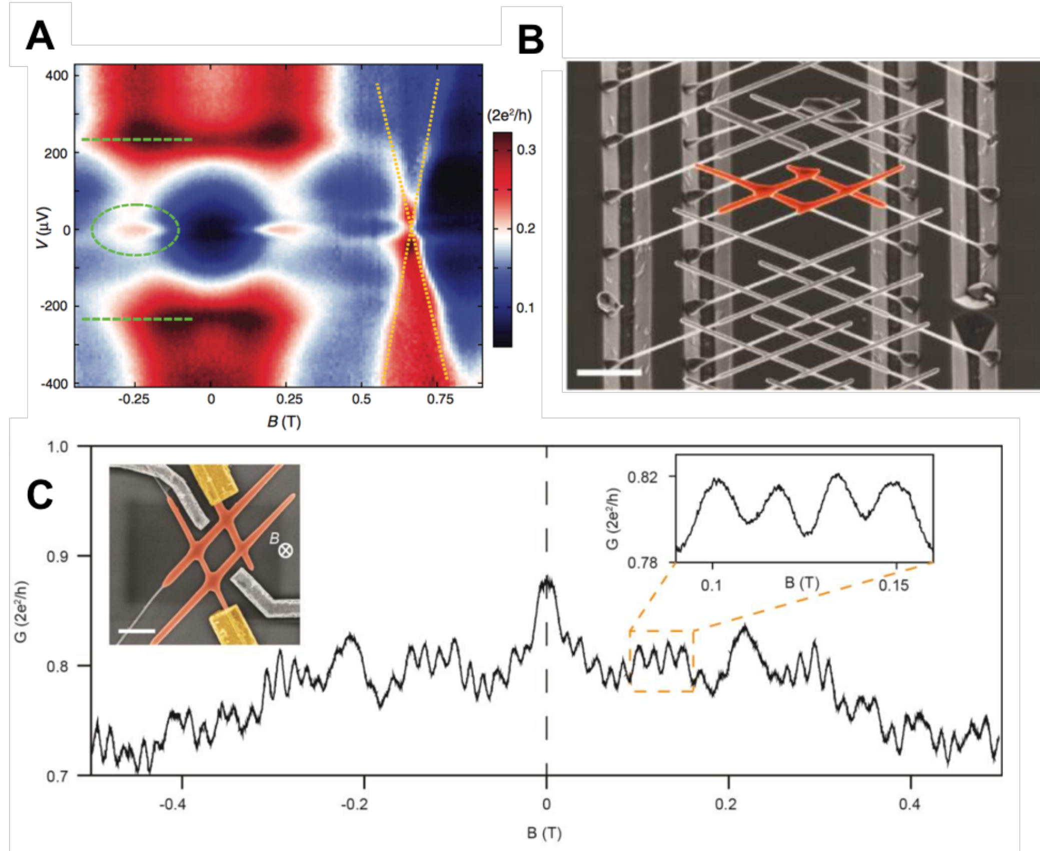

Figure 1.14. a) Colour-scale plot of differential conductance versus voltage and magnetic field in a hybrid superconductor-semiconductor InAs structure. The zero-energy bound state is highlighted by a dashed oval; green dashed lines indicate the gap edges. At 0.6 T, a non-Majorana state is crossing the zero state with a slope indicated by yellow dotted lines. b) SEM image of an InSb NW-junction quantum-network. Scale bar is 1 μm. c) Magneto-conductance measurements of a *hashtag*-shaped NW-network showing periodic Aharonov-Bohm oscillations. False-coloured SEM image of an InSb *hashtag* (red) contacted with normal metal-electrodes (yellow). Scale bar corresponds to 500 nm. After ref. [102, 103]

superconductor-semiconductor InSb [102] and InAs [104, 105] NW systems, both possessing high gyromagnetic factors, which is a promising feature for the observation of Majorana fermions. Figure 1.14.a) shows a plot of differential conductance versus voltage and magnetic field in a hybrid superconductor-semiconductor InSb-NW-system highlighting the existence of Majorana fermions. Therein, zero-energy bound states are visible for magnetic fields of the order of $100\,mT$. These states disappear for magnetic fields equal to zero or perpendicular to the NWs axis as well as by replacing the superconductor with a normal metal, in agreement with theoretical

predictions [102]. Finally, the definitive proof of Majorana fermions should be given by their non-Abelian statistics, which can be observed when two Majorana fermions move around one another, as in the case of *hashtag*-shaped NW-networks like those reported in fig. 1.14.b) [103]. The Aharonov-Bohm effect should be observed if the wave-function of a quantum particle moving in a magnetic field has a phase shift proportional to the magnetic flux with all physical observables periodic with a period equal to the flux quantum, $\Phi_0 = h/e$. Modulated-phase interferences can then affect magneto-transport measurements at low temperatures whenever the phase coherence-length is long enough, or magneto-photoluminescence experiment whenever the optical recombination involves charged carriers. Core-shell NWs, owing to their high aspect ratio, are predicted to be ideal systems to perform that type of measurements [106, 107]. To date, Aharonov-Bohm oscillations have not been detected in photoluminescence experiments in *NWs*, while they have been reported in several magneto-optical measurements on type II *quantum dots* [108, 109] or *quantum rings* [110].

As regards transport measurements, magneto-conductance oscillations have been observed in several NW structures. Quantum interference effects in the magneto-resistance measurements of core/shell (In_2O_3/InO_x) hetero-structure NWs have been observed [111]. The relationship between the oscillation period and the core width indicated that the current flows dominantly through the core/shell interface. Magneto-transport experiments were also performed on epitaxial GaAs/InAs core/shell NWs, where periodic oscillations of the NW conductance were highlighted [112]. Finally, such a kind of oscillations have been observed in *hashtag*-shaped junction InSb NWs, as reported in figure 1.14.c), owing to the quantum interference of electron waves emanating from the two transport channels of which the *hashtag* is made [103].

1.4.4 Nanowires as biosensor

Nanowire shapes and sizes have allowed also their interfacing with living cells. Nanowire cross-section is smaller than the dimensions of typical cells but still greater than those of the lipid bilayer. Therefore, it can easily penetrate cell membranes while leaving cell structures and functions intact [113]. Moreover, the NW large surface-to-volume ratio boosts cell-NW interaction for chemical, biological, and electrical sensing and allows an optical and electrical communication across cellular membranes [114, 115] with high-resolution and addressable intracellular-monitoring. Integration of NW-based field-effect-transistors (FET) with **live cells** was achieved first in 2006 by means of silicon NWs [116]. Figure 1.15 shows an optical image of a five NW–axon structure in which the rate, amplitude, and shape of signals propagating along individual axons of live mammalian neurons have been measured simultaneously at the NW-neuron junctions. This task could be hardly fulfilled with traditional micropipettes, due to the difficulty in signal multiplexing, or with micro-fabricated electrode arrays, due to their poor spatial resolution for detection and stimulation of neural activities. Nowadays, a neuron-physiology technique based on NW FET is able to record extracellular and intracellular action potentials with high signal-to-noise ratios [117, 118] leading to applications as label-free sensing of bio-molecules and cellular electrophysiological recording. [119]. Bio-probes based on

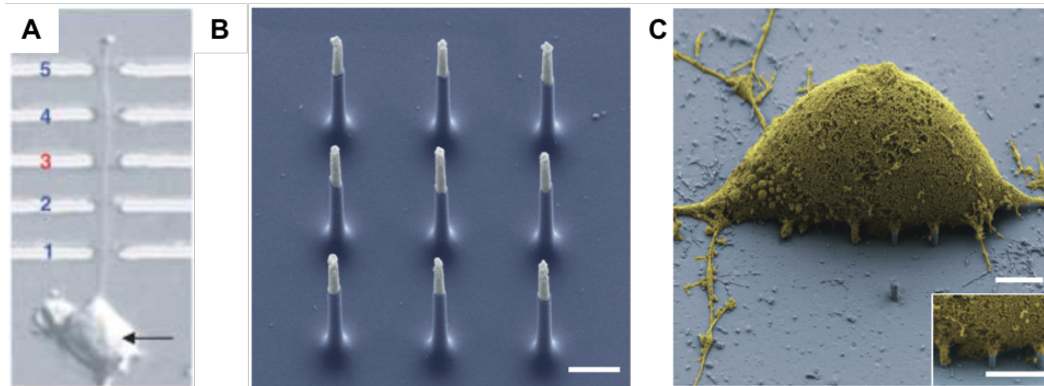

Figure 1.15. a) Optical image showing the structure of a five NW–axon structure, where NW_3 serves as input and other NWs as receivers. b) SEM false-color image of a vertical-nanowire electrode-array pad made up of nine Si NWs (blue) with metal coated tips (white). Scale bar is 1 μm. c) SEM false-color image of a rat cortical cell (yellow) on a vertical-nanowire electrode-array pad (blue), showing NWs interfaced with the cellular membrane (inset is a magnification). Scale bars are 2.5 μm. After ref. [114, 116]

vertical-NW arrays should be an even better platform for a high-throughput live-cell manipulation and assays. In 2007, the direct interconnection of an array of silicon NWs with a mouse embryonic-stem-cell directly cultured on the NW array has been first demonstrated [120]. Therein, penetration of silicon NWs into the cell did not require an external force, thus extending the stem-cell survival to several days without affecting the cell vitality, structure, and functions [120]. This ground-breaking work has shown, therefore, the potential of NWs to introduce programmable electrical and chemical stimuli to guide a stem-cell differentiation. Furthermore, intracellular mapping of neuron activity is made easier by using vertical NWs, owing to the NW capability of penetrating inside live cells without affecting their vitality, structures, and functions. Indeed, electrical currents in a given cell were traditionally measured using micropipette electrodes, which are extremely invasive and/or can harm the cell membrane or interfere with its activity. Finally, vertical-NW electrode-arrays (see Figs. 1.15.b and.c) can record and stimulate intracellular neuronal activity in rat cortical neurons and can also be used to map multiple individual synaptic-connections [114]. Although the signal amplitude for vertical NW-arrays is one order of magnitude smaller than that usually reported for NW-based FET bio-probes [121], the possibility to pack hundreds of thousands of these NW electrodes into flexible sheets, thus leading to minimal tissue damage, makes still them interesting for studying bioelectricity in nerves and heart muscles, and for mapping the brain activity.

Chapter 2

Optical properties of InP nanowires

In this chapter, the electronic properties of InP NWs are investigated in details by PL, μ-PL, and PLE measurements. The first section is devoted to a review of the state of the art regarding the InP band-structure in the WZ crystal-phase. As anticipated in section 1.3.1, little is known about the electronic band structure of non-nitride III-V semiconductors in the WZ crystal-phase. Theoretical calculations and experimental results on the energy-band diagram of WZ InP will be reported and compared with the well known ZB-InP results.

In the second section, a complete listing of all types of investigated NWs will be made. Indeed, several classes of NWs characterized by different crystal structures (WZ vs ZB), shapes (tapered vs columnar NWs), and growth methods (vapor-liquid-solid vs selective-area-epitaxy growth) were studied.

In the third section, an optical characterization of each class will be presented and the PL dependence on power, temperature, and/or polarization both on single NWs or ensembles of NWs will be shown. A quantitative simulation of high resolution PLE and PL spectra at different temperatures will allow us to establish the temperature dependence of the interband (A,B,C) transitions in WZ InP-NWs. A comparison with ZB results will also be reported.

In the last section, the hot-carrier effect in NWs will be demonstrated by a full quantitative analysis of the PL line-shape. We will show that carriers can thermalize at temperatures much higher than those of the lattice even in the quasi-equilibrium conditions typical of continuous-wave PL. The dependence of the mismatch between carrier and lattice temperature on NW size and class will be addressed. Finally, a promising development of photothermoelectric-device performance will be reported.

2.1 State of art of wurtzite-InP band-structure

Several experimental works have been carried out to characterize by optical techniques the WZ-InP electronic properties [7, 57, 58, 59, 60, 122, 123, 124, 125, 126, 127, 128, 129, 130, 131]. The low-temperature ($T = 4 \div 10\,K$) experimental values of the fundamental energy band-gap of WZ InP, namely, the A transition, fall in the $1.486 \div 1.508\,eV$ energy range. All these values display a blue-shift of $65 \div 87\,meV$

Reference (year)	$E_{g,WZ}(eV)$	$\Delta E_{g,WZ/ZB}(meV)$	$\Delta_{AB}(meV)$	$\Delta_{AC}(meV)$
[40] (1994)	1.20	84		
[42] (2010)	1.474	65	63	348
[47] (2010)	1.490	70		
[132] (2011) [1]	1.494	98	45	243
[44] (2013)	1.576	101	13	127
[45] (2016)	1.494		35	145

Table 2.1. Theoretical predictions of WZ-energy band-gap ($E_{g,WZ}$) and its energy difference ($\Delta E_{g,WZ/ZB}$) with respect to the ZB band-gap, as calculated within a same approach. Δ_{AB} and Δ_{AC} report the energy splitting between heavy- and light-hole energy-levels and heavy- and split-off energy-levels, respectively.

with respect to the InP-ZB energy band-gap ($1.421\,eV$ at $T = 4\,K$). The energy values of the B and C transitions have been well established, especially by means of PLE, in a smaller number of works. The low-temperature experimental energy values of the B transition fall in a relatively sharp energy range, $1.530 \div 1.538\,eV$ [122, 123, 124, 125, 127, 129, 131].

As regards the C transition, instead, the reported energy values fall in a wide range ($1.665 \div 1.690\,eV$) [122, 123, 124, 127, 129, 131]. [122, 123, 124, 127, 129, 131].

Although the experimental results quite well agree with each other, the same statement does not apply to theoretical predictions. This discrepancy is most likely due to the different theoretical approaches used to calculate the energy values of the different transitions. In table 2.1, quite scattered theoretical estimates of the energy levels of WZ-InP band-structure are reported (a similar scattered picture applies to theoretical predictions of the hole and electron effective masses, as it will discussed in section 3.2). Band-gap values in the $1.2 \div 1.576\,eV$ energy range were estimated, with theoretical differences between the ZB- and WZ-crystal phase-energies ($\Delta E_{g,WZ/ZB}$) in the $70 \div 101\,meV$ range. In a few cases, also the energy differences between heavy- and light-hole (Δ_{AB}) and heavy and split-off (Δ_{AC}) energy-levels were estimated and largely scattered values were found. As regards the order of the two lowest energy levels of the conduction band, all theoretical works agree on the sequence $\Gamma_{7c} < \Gamma_{8c}$ [40, 42, 44, 45]. Moreover, magneto-PL measurements on WZ InP-NWs support the Γ_{7c} character of the lowest conduction-band state [58].

2.2 Investigated samples

In this section, the structural properties of all investigated samples are described and the growth conditions are summarized. This description is necessary to fully understand the differences in the optical properties to be highlighted in the following. All the samples were grown by Prof. C. Jagadish's group at the Department of Electronic Materials Engineering in the Australian National University (ANU) of Canberra. The samples can be divided in four main classes distinguished by their

[1] A full potential linearised Augmented Plane Wave method (APW) is employed in these calculations.

crystal structure, morphology, and growth technique. In particular, the investigated samples were:

- WZ-phase NWs grown by *selective-area-epitaxy* with a perfectly prismatic shape and very high crystal quality;
- WZ-phase NWs grown by *vapor-liquid-solid* epitaxy with a high tapered structure, like a staggered *pyramid*;
- ZB/WZ mixed-phase *kinked* NWs grown by VLS, characterized by two different segments whose crystal phases and diameters differ;
- ZB-phase NWs grown by VLS and almost untapered.

NWs were grown in a horizontal flow MOVPE reactor in which chemical precursors were phosphine (PH_3) and trimethylindium (TMIn). In the SAE growth, a $30\,nm$ thick SiO_2 layer was deposited on an InP substrate and patterned by electron-beam lithography to create an array of holes. The pattern was then transferred onto the InP substrate by etching the SiO_2 mask with a buffered hydrogen-fluoride solution. Then, the samples were immediately transferred into the reactor and annealed for 10 minutes under a PH_3 flow before initiating the NW growth. The V/III ratio was 80.

In the VLS growth, colloidal gold nanoparticles (diameter $\sim 30\,nm$) were directly dispersed on the ZB-InP substrate and then annealed for few minutes under a PH_3 flow to enhance the alloying between the substrate and the Au particles before the NW growth. The V/III ratio was 350 for all the NWs grown by the VLS technique. Scanning-electron-microscopy images were taken at the CNIS Laboratory (Rome) and in the ANU Laboratory, while the crystal structure was investigated in the ANU Laboratory by a JEOL 2100 F transmission-electron-microscope operated at 200 kV.

WZ phase, SAE growth

Figure 2.1.a) shows a representative top-view SEM-image of an array of NWs grown by SAE. In order to grow ordered arrays of NWs with different diameters, four different patterned masks have been fabricated on the top of InP substrates. Hole diameters were 45, 120, 310, and $650\,nm$, the corresponding pitches -namely, the distance between one hole and its nearest one- were 500, 200, 600, and $1000\,nm$, in the order. For the sake of clarity, in figure 2.1.a) only the sample with hole diameters of $310\,nm$ is shown. The NWs were grown along the $< 111 >$ direction for 20 minutes at $T_g = 730°C$. Figure 2.1.b) shows a 45° tilted-view SEM-image of an array of NWs with diameter equal to $310\,nm$. All the four samples feature the same morphological characteristics, namely, the NWs are untapered, $\sim 5\,\mu m$ long, perfectly perpendicular to the substrate, equally spaced, and with hexagonal cross-section. They have a defect-free WZ crystal-structure, as supported by the high-resolution transmission-electron-microscopy (HR-TEM) shown in fig. 2.1.c). The very high crystal-quality is confirmed by the selective-area electron-diffraction (SAED) pattern shown in the inset. The reader is referred to ref. [7] for a more comprehensive morphological and structural characterization of this class of samples.

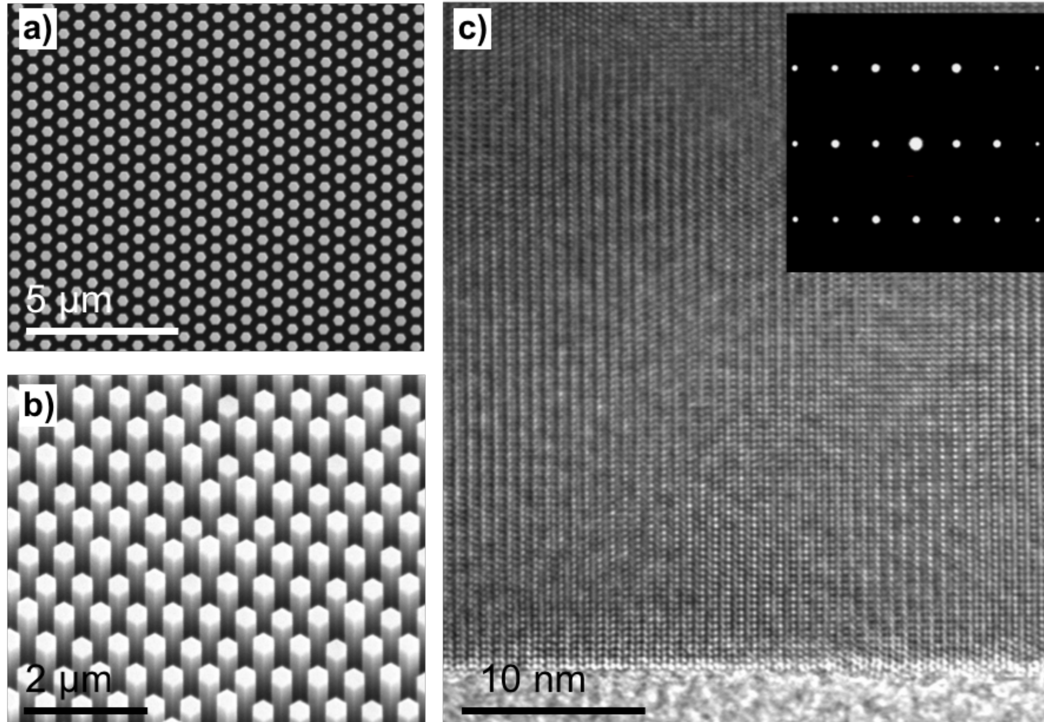

Figure 2.1. a) Top-view SEM image of an ordered array of NWs grown via SAE technique. Hole diameters are equal to 310 nm. b) 45° tilted-view SEM-image of a region equivalent to that displayed in (a). NWs are parallel to each other, perpendicular to the substrate, and all with the same length. c) HR-TEM image of a NW belonging to the array shown in (a,b). A high crystalline quality of the WZ structure is manifest, as confirmed by the SAED pattern shown in the inset. After ref. [133, 134].

WZ phase, VLS growth

Figure 2.2.a) displays a 45° tilted view of an ensemble of WZ NWs grown along the $< 111 >$ direction for 20 minutes at $T_g = 480°C$ on a semi-insulated InP (111)B-oriented substrate. The NWs stand perpendicular to the substrate and parallel to each other. They are approximately 1 μm long and show a highly tapered, staggered *ziggurat*-like structure which can be described as made by three different parts: a basal part, 400 nm long with a triangular cross section defined by 180 nm sides; a middle part, 400 nm long with an hexagonal cross section defined by 60 nm sides; a top part, 200 nm long with an hexagonal cross section defined by 15 nm sides (see the top-right inset) and topped with a gold nanoparticle. We point out that straight, non-tapered WZ NWs grown by VLS in the same laboratory under slightly different conditions tend to show a poor crystal and optical quality [27, 135, 136]. A very high WZ crystalline quality is shown, instead, by all highly tapered NWs, whose $\hat{c}$ axis is parallel to the NWs symmetry axis, as shown in the HR-TEM image and in the SAED pattern of fig. 2.2.b). No ZB insertions are present along the NW axis, with the exception of few staking faults on the NW tip (not shown here), which form during the cooling process. Further morphological and structural characterizations of this sample can be found in ref. [27, 58, 57, 135, 136] together with the dependence

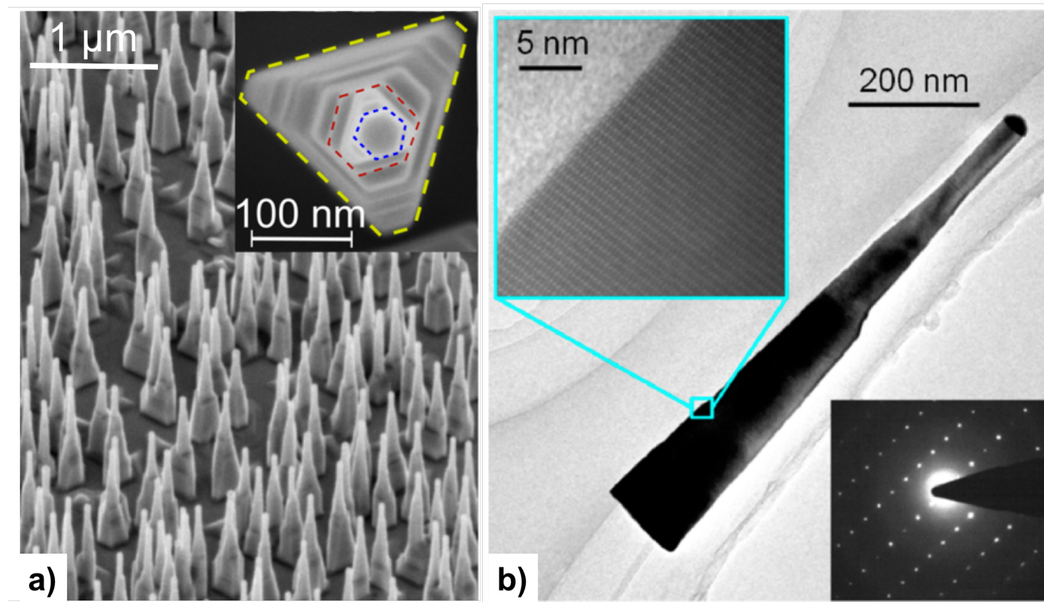

Figure 2.2. a) 45° tilted-view SEM-image of an InP-NW ensemble grown by VLS. Inset: Top-view SEM-image of a single NW. The NW shape can be approximated to a staggered structure consisting of the three parts highlighted by differently colored lines. b) TEM image of a WZ NW belonging to the ensemble shown in (a). The top-left inset is a HR-TEM image taken close to the wire base, as indicated by the square. This image and the SAED pattern (bottom-right inset) confirm the WZ crystal-structure of the NW. After ref. [57, 131].

of the structural proprieties on different growth parameters.

ZB-WZ phase, VLS growth

The kinked NWs were grown by VLS on InP (100) substrates at $T_g = 475°C$. The growth was initiated with TMIn and PH_3 flows corresponding to a V/III ratio of 350 to ensure a high yield of vertical [100] segments [137]. After 15 minutes of growth the V/III ratio was reduced to 220 in order to minimize the lateral growth. Growth was continued for further 165 min before switching off TMIn and cooling down under PH_3. After a 90 minute growth, all [100] NWs kink to a [111] B orientation by forming inclined twins [137]. It should be noticed that this spontaneous change of growth direction takes place without any change in growth parameters. It most likely takes place when the NW length is greater than the diffusion length of In in the NW, with an ensuing decrease below a critical value of the In supply to the Au particle [137, 138].

Figure 2.3.a) displays a 45° tilted-view SEM-image of an ensemble of kinked NWs with both WZ and ZB structures. The bottom region, highlighted in blue, is characterized by a ZB crystal-phase. All NWs are parallel to each other, with a diameter of $\sim 120\,nm$ and <100> growth-direction. The top region, highlighted in red, is characterized, instead, by WZ NWs with a diameter of $\sim 70\,nm$ and <111> growth direction. Both NW crystal-phases are almost not tapered and $\sim 1.4\,\mu m$

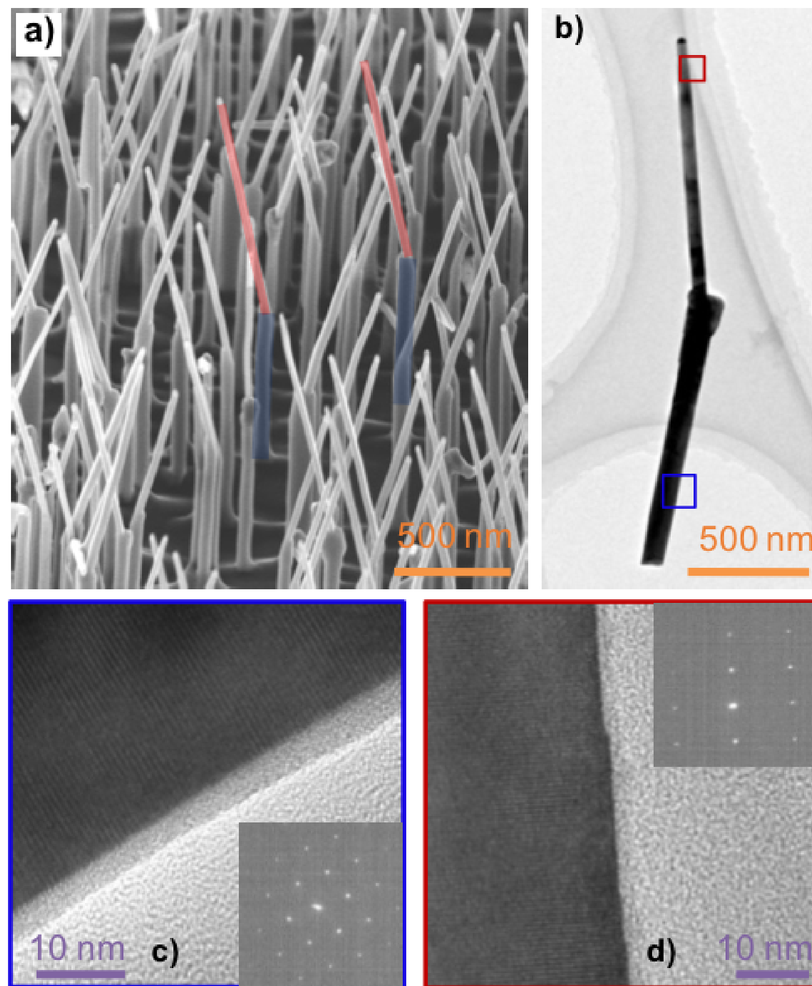

Figure 2.3. a) 45° tilted-view SEM-image of a kinked NW ensemble. The regions highlighted in red and blue denote the WZ and ZB parts of the NW, respectively. b) TEM image taken on a single wire. It shows the good quality of the sample and the interface where the kink occurs. The blue and red boxes mark the regions reported in panels c) and d), respectively, where the high-resolution TEM-images were obtained. The very high quality of the crystal structures is also confirmed by the selected-area diffraction-patterns shown in the insets in panels c) and d).

long. Figure 2.3.b) reports a TEM image of a single NW. Therein, the kinking angle, equal to $\sim 17°$, and the good quality of the sample is manifest: there is a very low density of stacking faults and twin planes, except for the region where the kink occurs. The NW very high quality is supported by the HR-TEM images of the ZB and WZ parts shown in fig. 2.3.c) and 2.3.d), respectively, which were obtained in the regions marked by blue and red boxes in fig. 2.3.b). The attribution of the ZB and WZ crystal phases is confirmed, finally, by the SAED patterns reported in the insets in figs. 2.3.c) and 2.3.d). It should be noticed that these NWs cannot be considered as *polytypic* NWs as they do not include WZ and ZB sections *alternating* along the NW axis.

ZB phase, VLS growth

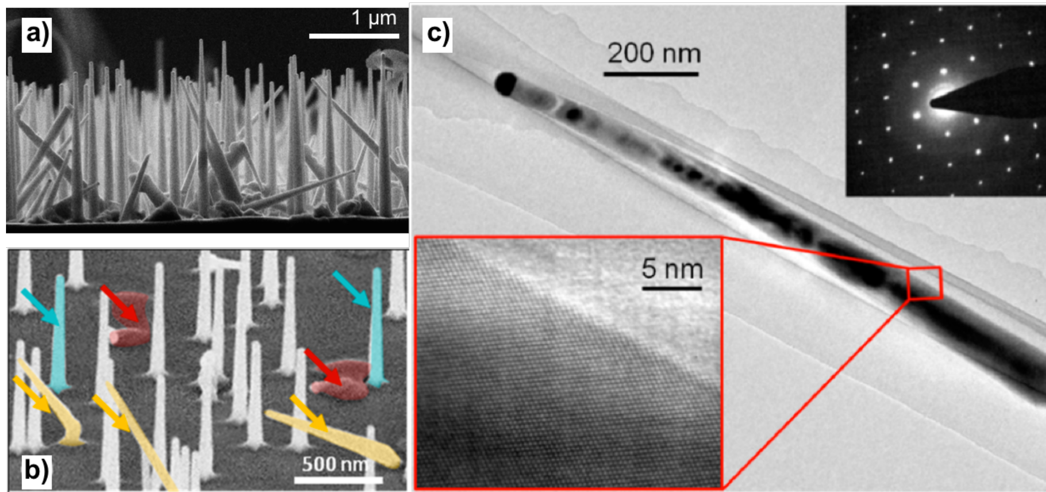

Figure 2.4. a) Side-view SEM-image of a ZB NW-ensemble. Vertical and non-vertical NWs are manifest. b) 45° tilted-view SEM-image of the three main types of NWs grown on an InP (100) substrate: vertical NWs in blue, tilted NWs in yellow, and planar NWs in red. c) TEM image of a vertical ZB InP-NW, whose HR-TEM image is shown in the bottom-left inset. The atomic pattern indicates a ZB phase, as confirmed by the SAED pattern in the top-right inset. After ref. [131, 137].

Figure 2.4.a) displays a side-view SEM-image of an ensemble of NWs grown on a (100) substrate for 20 minutes at $T_g = 450°C$. Although this sample was grown to achieve perfect vertically-oriented ZB-NWs to be compared to WZ NWs, not all the NWs are actually vertically oriented. Three main different classes can be identified, as shown in fig. 2.4.b) by different colors: vertical NWs (blue), tilted NWs, at an angle with respect to the substrate surface (yellow), and wires lying on the substrate (red). Further details on this intriguing ensemble of NWs can be found in ref. [137], where an in-depth analysis of growth directions, facets, side facets, and crystal structure has been made for each NW class. Most NWs are vertical, with a pure ZB structure, as shown in fig. 2.4.c). Those NWs have a square cross-section, stand vertically along the <100> direction, are $1\,\mu m$ long and slightly tapered, with facets $70\,nm$ wide at the base and $45\,nm$ at the top. The other classes of NWs feature different crystal structures depending on the crystal-growth orientation. Although there are both WZ and ZB NWs, as extensively explained in ref. [137], the very-low density and crystalline quality of WZ NWs (not shown here) make this sample suitable only for the study of the physical properties of defect-free ZB NWs. On the contrary, the physical properties of WZ NWs have been investigated in all the three samples previously described.

We have also compared results in ZB InP-NWs with those we obtained in bulk (ZB) InP to highlight any possible difference between these two forms of ZB InP. A $3\,mm$-thick (100) epilayer grown at $650°C$ by MOCVD in the reactor of Prof. C. Jagadish's group in the ANU of Canberra has been chosen as a bulk reference sample. The last $300\,nm$ were grown at a lower rate to ensure a high crystal-quality

to the topmost layers.

2.3 Addressing the band-structure's properties of WZ and ZB InP-NWs

2.3.1 PL characterization

Figure 2.5 shows macro-PL spectra from all the samples described in section 2.2. Those spectra were taken at $T = 10\,K$ with $P_{exc} = 3\,W/cm^2$ in the back-scattering configuration described in section A.2. In fig. 2.5.a), the PL spectrum from an array of ordered NWs grown by SAE with hole diameter equal to $650\,nm$ and whose morphological features are shown in fig. 2.1 is given by a thick red-line. The doublet structure at highest energy ($\sim 1.493\,eV$) is due to a free-exciton recombination in the WZ crystal-structure [123, 129]. The nature and physical origin of that doublet will be addressed below in the discussion of figure 2.7. An intense emission observed at $1.452\,eV$ has been previously attributed [7, 57] to a free-electron to acceptor (carbon, (e, C^0)) transition. Indeed, the $41\,meV$ energy difference between the latter recombination and that of the FE is similar to the well known ionization energy of a C acceptor in InP [139] and in ZB InP-NWs [140], provided that one can reasonably assume that the binding energy of C -the most common shallow acceptor in MOVPE grown NWs- is roughly the same in ZB and WZ NWs. However, our measurements highlight the presence of two almost degenerate impurity-related transitions, as shown in figure 2.6: a donor-to-acceptor transition[2], (D^0, C^0), on the low-energy side of the $1.452\,eV$ recombination, and a free-electron-to-acceptor transition, (e, C^0), on the high-energy side of the same band. Finally, a much less intense emission at $1.409\,eV$ is attributed to a phonon replica of the (D^0, C^0) and (e, C^0) emissions. The energy difference between the main band and its replica is equal, indeed, to $42\,meV$, namely, the longitudinal-phonon energy[141].

In fig. 2.5.b), the PL spectrum from an ensemble of NWs grown by VLS, whose morphological features are shown in fig. 2.2, is given by a thick green-line. Its analysis is less straightforward than that of the PL spectrum in fig. 2.5. a). A FE recombination appears at $\sim 1.492\,eV$, a value very close to that previously reported for the SAE NWs, but with no evidence of a doublet structure. The sharp peak observed at $1.486\,eV$ has been previously ascribed to the recombination of an exciton bound to a neutral acceptor (BE, A^0) [126] or to the recombination of an unknown impurity [125]. The broad emission band at $1.42 \div 1.48$ eV is attributed to different acceptors and line defects, as staking faults along the NWs axis [39, 59]. Finally, PL emission from the ZB-InP substrate shows up at the lowest energy. Therein, a weak emission at $1.378\,eV$ is due to the recombination of a free electron to neutral carbon ($(e, C^0)_{ZB}$), as supported by the spectra reported in fig. 2.5.c), where the PL emission of ZB InP is shown.

In C, the PL emission from an InP epilayer is given by a thin black line, that from an ensemble of ZB InP-NWs grown by VLS is shown, instead, by a thick magenta line. The morphological features of those NWs were shown in figure 2.4. The FE emission-band of ZB InP is at $1.418\,eV$ in both NW and bulk PL-spectra. Because of

[2] We will assume that acceptors are due to the presence of carbon impurities.

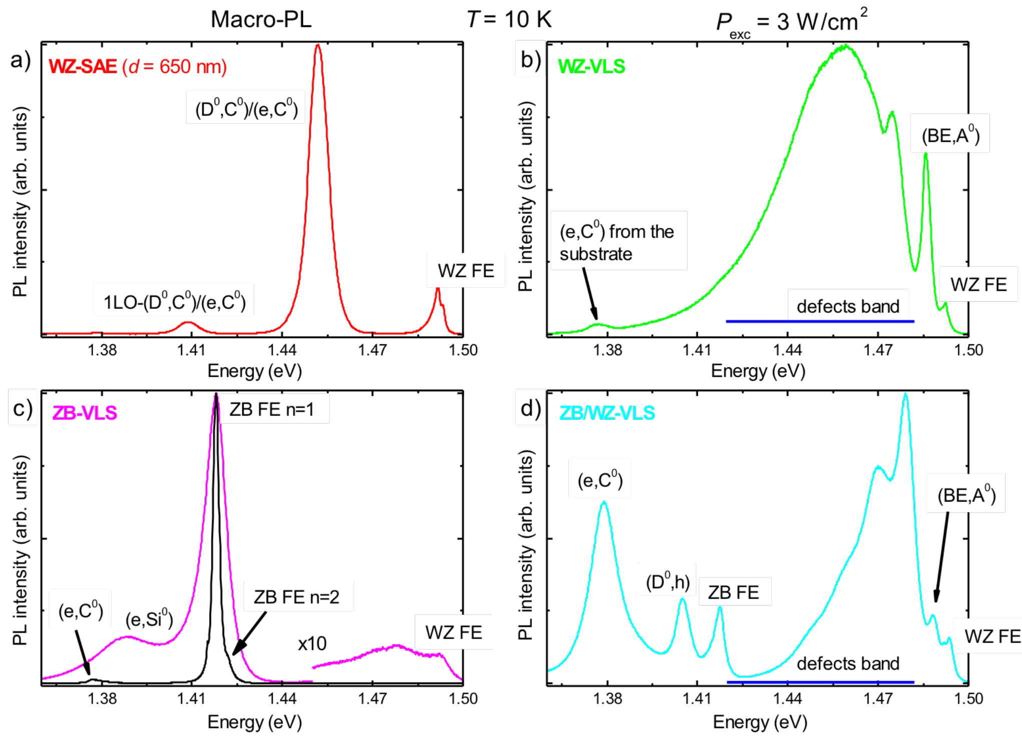

Figure 2.5. PL spectra at $T = 10\,K$ at intermediate excitation power density ($P_{exc} = 3\,W/cm^2$) of all classes of NWs described in section 2.2. The back-scattering configuration was used to collect PL from an ensemble of NWs in the macro-PL setup (see appendix A.2). a) PL spectrum of SAE-grown WZ-NWs. b) PL spectrum of VLS-grown WZ-NWs *pyramidal*. c) PL spectrum of VLS-grown ZB-NWs (thick magenta line). PL spectrum of a bulk InP reference epilayer (thin black-line). d) PL spectrum of ZB/WZ *kinked* NWs grown by VLS epitaxy.

the high crystal-quality and -purity of the InP bulk-epilayer, the recombination from $n = 2$ exciton state is visible as a shoulder at $1.422\,eV$. From those two measurements and via eq. A.2, we get a value of $R_{eff} = 5.3\,meV$ for the exciton Rydberg in InP ZB. That value is very close to those previously reported in the literature [142]. The recombination of a free electron to a neutral acceptor is observed at low energy, in both bulk and NW spectra. The recombination at $1.378\,eV$ coincides with the lowest recombination shown in fig. 2.5.b). It is ascribed to a (e, C^0) transition: its ionization energy ($40\,meV$) well matches that of a C acceptor in ZB InP [139]. The recombination at $1.388\,eV$ in the NW PL-spectrum is attributed, instead, to silicon acceptors ($E_b = 30\,meV$) [139]. We point out that this class of NWs shows some structures that crystallize in the WZ structure, see discussion of fig. 2.4, with an ensuing broad, weak emission at $1.45 \div 1.50$ eV.

Figure 2.5.d) shows the PL emission of the last class of investigated NWs, namely, the kinked mixed phase NWs whose morphological features are shown in fig. 2.3. In that NW class, emissions from both ZB and WZ InP-NWs are visible. The WZ part of the PL spectrum is almost identical to that reported in fig. 2.5.b) and emission bands from WZ FE, (BE, A^0), acceptors and/or line defects are observed. The ZB part of the PL spectrum shows the FE recombination at $1.418\,eV$, followed by a

transition at around 1.404 eV, which is ascribed to a recombination of a free hole to a neutral donor. The recombination of a free electron to a carbon impurity located at 1.388 eV is observed also here and originates from both the substrate and/or the NWs.

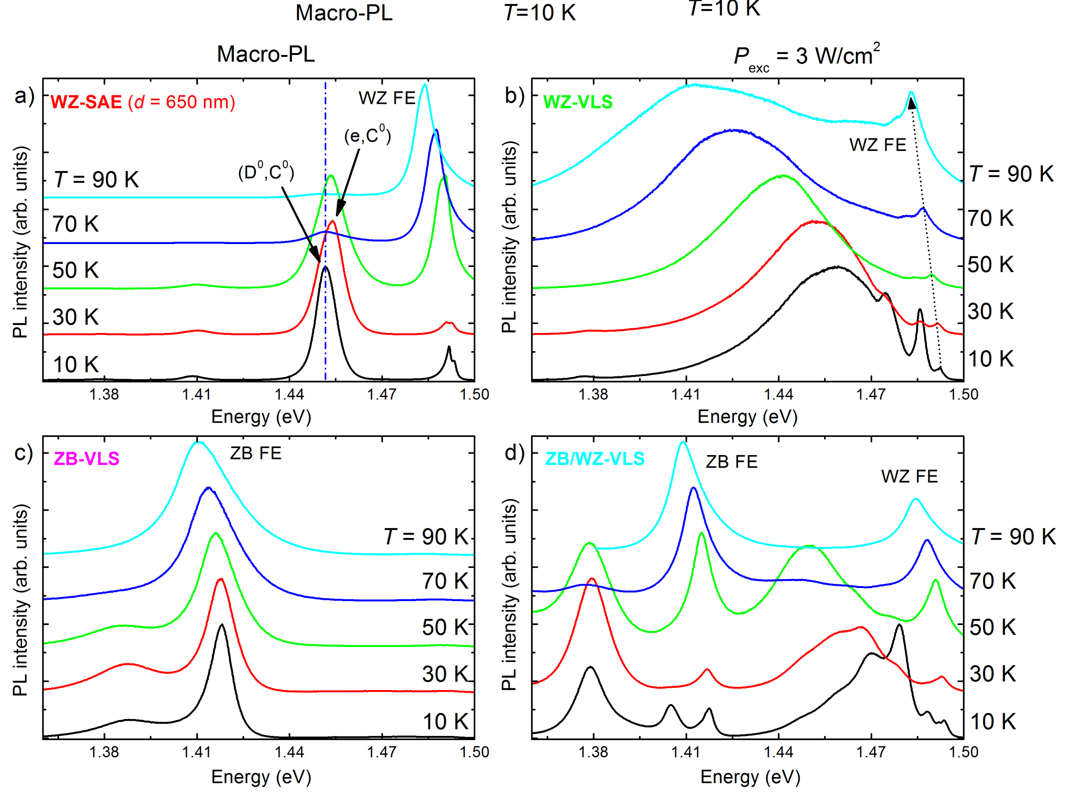

Figure 2.6. Normalized PL spectra taken from 10 K to 90 K with $P_{exc} = 3\,W/cm^2$ in all classes of NWs described in section 2.2. Those PL spectra have been taken in a back-scattering configuration in the macro-PL setup (see appendix A.2) from an ensemble of: a) WZ NWs grown by SAE; b) WZ *pyramidal* NWs grown by VLS; c) ZB NWs grown by VLS; d) ZB/WZ *kinked* NWs grown by VLS.

All those assignments to extrinsic or intrinsic recombination bands stem from the temperature studies shown in figure 2.6 where the evolution of the PL spectra from $T = 10\,K$ to $T = 90\,K$ is shown for all classes of NWs described in section 2.2. The relative weight of all recombination bands previously ascribed to extrinsic transitions decreases for increasing temperature, except that of the broad defect in the WZ NWs grown by VLS (see cyan line in fig. 2.6.b)). However, for increasing temperature the relative weight of the FE recombination increases with respect to that of the broad defect band. The intrinsic character of the FE recombination is confirmed by its asymmetric broadening for increasing temperature, which is due to the conversion of the FE emission in a band-to-band recombination characterized by a Maxwell Boltzmann high energy tail, as described in appendix A.1. The intense emission in fig. 2.6.a), which has been previously ascribed to (D^0, C^0) and (e, C^0) recombinations, first blue-shifts and gains intensity for increasing temperature, then red-shifts and loses intensity, as expected and already reported in bulk ZB InP [143, 144]. This

attribution is confirmed by magneto-PL measurements, to be discussed in chapter 3.

Let now discuss the nature of the doublet FE-structure $1.493\,eV$ in fig. 2.5.a). Figures 2.7.a) and 2.7.b) show the PL spectra of a NW ensemble grown by SAE ($d = 650\,nm$) as a function of P_{exc} and T, respectively. A doublet structure has already been observed in the FE band of high-purity ZB bulk-InP [145] and GaAs [146]. The energy difference between the lower- and upper-energy components (labeled L and U in fig. 2.7, respectively) is sample dependent and equal to $\sim 1.6 - 1.8\,meV$. The dependence on temperature and laser power excludes the attribution of the lower-energy component to a bound-exciton state, for which a much more rapid ionization, for increasing T, and intensity saturation, for increasing P_{exc}, should be expected. The intrinsic nature of that doublet is confirmed by the PLE spectra shown in fig. 2.7.c) and taken in the experimental configuration described in appendix A.2. Indeed PLE, as described in appendix A.1, is sensitive to states with large volume density ($10^{19}cm^{-3} \div 10^{22}cm^{-3}$, in contrast to PL that is dominated by low-energy states (usually related to defect levels) even when their volume density is relatively small ($\sim 10^{16}cm^{-3}$). Those L and U spectral features eventually merge at temperatures above $30\,K$. In PLE, the L and U peaks are Stokes-shifted with respect to their PL counterparts by only $0.6\,meV$, an indication of the excellent optical quality of the NW samples. The FE doublet has been attributed to the elastic scattering between neutral donors and excitons [146, 147]. At specific exciton energies, the elastic scattering cross-section of neutral donors has a maximum, with an ensuing depletion of the exciton contribution to the PL signal and the insurgence of a dip in PL spectra like those shown here and in fig. 2.5.a).

The simplest and cleanest WZ PL-spectrum is that of NWs grown by SAE, where all physical origins of the different recombination bands that contribute to the PL spectra have been identified. Therefore, magneto-PL studies have been performed on those NWs in order to determine both the electron and hole reduced masses in WZ InP, as it will be discussed in chapter 3.

2.3.2 μ-PL polarization experiments on mixed-phase single-NWs

We studied the polarization properties of WZ- and ZB-InP PL in a single *kinked* NW grown by VLS. Our aim was to highlight the different selection rules between ZB and WZ crystal-phases in a same NW. To that end, single *kinked* NWs were transferred on a silicon substrate via the drop-cast method, which prevents the breaking of the NW into several parts -a common result of the dry-transfer method. The top (bottom) panel of figure 2.8.a) shows the μ-PL spectrum obtained by collecting the μ-PL (see A.2) emission from the WZ (ZB) section of a *kinked* NW ($P_{exc} = 0.3\,kW/cm^2$ and $T = 5\,K$). The FE bands of the two crystal phases show up at their respective energies, as discussed in the previous section. Both bands are accompanied by a defect-related broadband-emission with a sizeably lower intensity, due to the saturation of the defect-related emission at the high power density of μ-PL. In the top panel, a signal at the energy of the ZB FE is observed even if the μ-PL signal is collected from the WZ NW-section. There are several reasons for this anomalous signal: *i)* the size of the WZ section is of the order of the μ-PL resolution, thus the Gaussian profile of the laser beam overlaps also the ZB section; *ii)* the volume of the ZB section is greater than that of the WZ section; *iii)* the

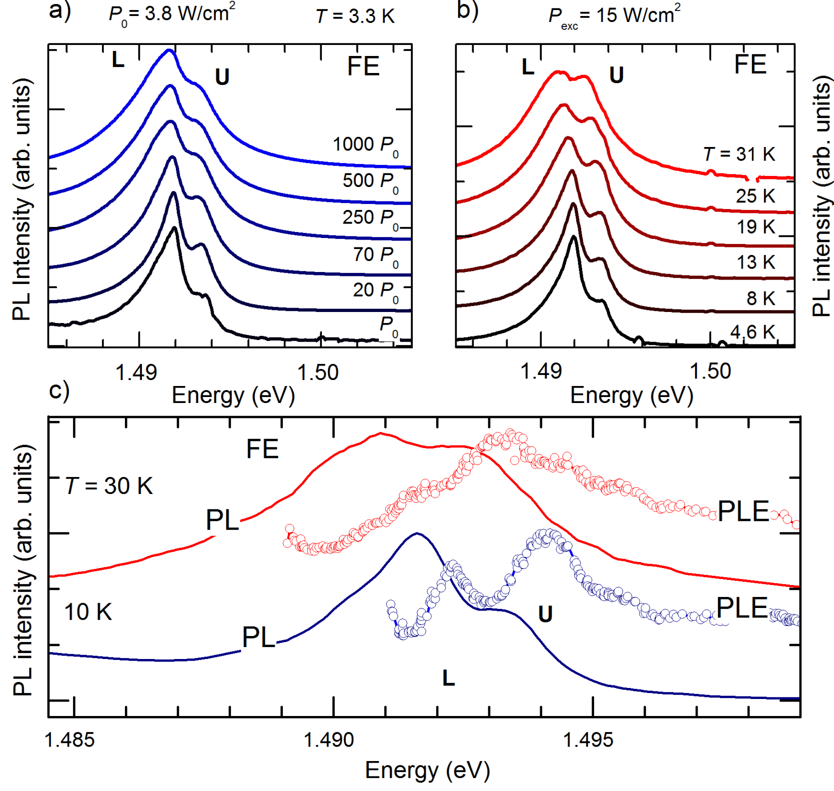

Figure 2.7. a) PL spectra taken on NWs grown by SAE ($650\,nm$ diameter) at fixed temperature and various laser power-densities. The free-exciton band has a clear splitting into a lower- (L) and an upper- (U) energy component. b) Same as a) at various temperatures and fixed laser power-density. c) PL (solid lines) and PLE (open symbols) spectra taken in the FE energy-region at two different temperatures on NWs similar to those of panels a) and b). After ref. [134].

ZB PL-efficiency is higher than that of WZ because the ZB phase has a smaller surface-to-volume ratio and thus the detrimental contribution of surface defects is lower than that in the WZ phase.

For each NW section, PL emission is collected filtering the polarization of light parallel and perpendicular to the NW axis, namely, the $\hat{c}$ axis in the WZ case. The degree of linear polarization (ρ) is defined as:

$$\rho = \frac{I_{\perp} - I_{\parallel}}{I_{\perp} + I_{\parallel}}, \tag{2.1}$$

where $I_{\perp}$ ($I_{\parallel}$) is the PL intensity for light perpendicular (parallel) to the NWs axis. The degrees of linear polarization are reported as black solid-lines in the two panels of fig. 2.8.a). In the top panel, the PL emission in the WZ energy-region ($1.44 \div 1.5\,eV$) is mainly polarized perpendicular to the $\hat{c}$ axis, with a maximum, positive value of $\rho = 0.5$, in agreement with the WZ selection rules for the band-gap transition discussed in 1.3. In the bottom panel, the PL degree of linear polarization of the ZB energy-region ($1.38 \div 1.42\,eV$) is shown. It is small and negative ($\rho = 0.25$), as

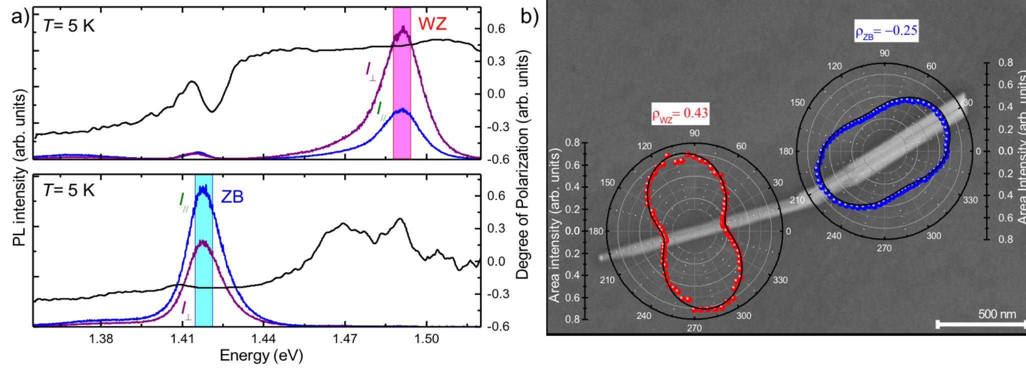

Figure 2.8. a) PL spectra taken at $T = 5\,K$ on single *kinked* InP-NW. PL emission collected from the WZ section, top panel, and ZB section, bottom panel. In each panel, PL emissions polarized parallel and perpendicular to the NW axis are given by a blue and purple line, respectively. Black solid-lines give the degree of linear polarization as obtained by eq. 2.1. The magenta and cyan boxes denote the energy regions considered to evaluate the PL total intensities reported in b). b) SEM image of the NW studied. Polar plots corresponding to WZ (red) and ZB (blue) PL emissions are superimposed to the image.

it should be expected on the ground of the dielectric-mismatch effect discussed in 1.3. The low values of those polarization degrees can be ascribed to a quite difficult optical alignment, and/or to the contribution of the highly defected region where the ZB and WZ sections join and the crystal symmetry is messed up. It is worth to notice that a positive linear polarization is measured also in the WZ energy-region of the bottom panel, in spite of a very weak signal -too small to be visible in the figure- and of an optical alignment optimized for measuring the polarization of the ZB NW-section.

The dependence $I(\Theta)$ of the emitted light on the angle Θ between the polarizer and the NW axis can be derived via the Malus' law:

$$I(\Theta) = \frac{1+\rho}{2}\cos^2(\Theta - \Theta_0) + \frac{1-\rho}{2}\sin^2(\Theta - \Theta_0), \tag{2.2}$$

where Θ_0 is an offset angle. In order to make all measurements insensitive to the polarization response of the optical setup, this dependence has been measured by rotating -in 5° steps with respect to the NW axis- an half-wave plate placed before a polarizer whose axis was, instead, fixed. In each PL spectrum, both in the ZB and WZ case, the PL intensity was integrated over an energy-region $10\,meV$ wide and centered at the FE peak, as schematically indicated by the magenta and cyan boxes in fig. 2.8.a). The two resulting red and blue polar plots are reported in fig. 2.8.b) where they are superimposed, respectively, to the WZ and ZB NW-sections of the investigated NW SEM-image. In the WZ case, light is clearly polarized perpendicular to the NW axis, whereas in the ZB case light is polarized parallel to the NW axis. Moreover, the polar plots can be exploited to calculate the angle between the ZB and the WZ segments by reproducing the data via eq. 2.2 and considering that the WZ intensity should be maximum at an angle of 90° with respect to the WZ $\hat{c}$ axis. A value of 16° is thus found, in good agreement with the angle directly obtained by

the SEM image ($\sim 17°$).

2.3.3 Temperature dependence of WZ critical points addressed by PLE

The PL studies discussed so far allowed us to investigate the energy levels in WZ and ZB InP close to and/or below the fundamental band-gap energy. To probe and study high energy levels in the WZ band structure, namely, the B and C transitions, PLE is is the most suitable experimental technique. Figure 2.9.a) shows the PLE spectrum (green line, $E_{det} = 1.486\,eV$) taken at $T = 10\,K$ in the back scattering configuration described in A.2 from an ensemble of NWs grown by VLS. Three step-like absorption-edges characterize the WZ PLE-spectrum. They correspond to three transitions involving the bottommost conduction-band energy-level (Γ_7^c) and the three topmost valence-band energy-levels (Γ_9^v, Γ_{7u}^v, and Γ_{7l}^v), which are labelled A, B, and C, in the order, as shown in the inset. At low temperature, the energies of these three transitions are $E_a = 1.493\,eV$, $E_B = 1.537\,eV$, and $E_C \sim 1.675, eV$, in good agreement with previous experimental results [122, 123, 125, 127]. The A and B transitions display extremely sharp excitonic features (line width $\sim 2\,meV$), whose lack in the case of the C transition impedes an accurate determination of its resonance energy. A tiny feature marked as a is observed at $\sim 1.725\,eV$, just above the C step-edge. It is ascribed to a recombination of a hole in the topmost valence-band, Γ_9^v, with an electron in the second conduction-band, Γ_8^c. Therefore, the $\sim 232\,meV$ energy separation between the A and a transitions should match the CB ($\Gamma_C^8 - \Gamma_C^7$) energy separation, in good agreement with other experimental [129] and theoretical studies [42].

The red line is a PLE spectrum taken on an array of NWs grown by SAE in the energy region of the A and B transitions. Although the SAE and VLS PLE-spectra have been taken in the same experimental conditions and PL spectra are better in NWs grown by SAE, the SAE PLE-spectrum displays a lower spectral quality than the VLS spectrum: the excitonic resonances and step-like absorption edges in the former spectrum are less defined (and the whole spectrum noisier) than those in the latter spectrum. Therefore, all the following PLE measurements aimed at addressing the temperature dependence of WZ critical points have been performed on ensembles of VLS grown NWs.

The dependence of E_{gap} on T provides valuable information on the lattice thermal-expansion and electron-phonon-interaction strength [148, 149]. In addition, T-dependent optical studies hold a great importance with regard to the potential of NWs for room-temperature devices as photodetectors and solar cells. Moreover, the temperature dependence of the band-gap energy in WZ InP-NWs has been addressed so far only by PL studies with conflicting results. The temperature dependence of the PL peak-energies in WZ and ZB InP-NWs, and ZB bulk-InP was reported in ref. [60]. All those dependences were fitted via a modified Varshni's formula [150]:

$$E(T) = E(T = 0) - \frac{\alpha T^4}{T^3 + \beta}, \tag{2.3}$$

where $E(0)$ is the band-gap energy at $T = 0\,K$, and α and β are material-dependent fitting parameters. The T^4 and T^3 terms replace the T^2 and T terms, respectively,

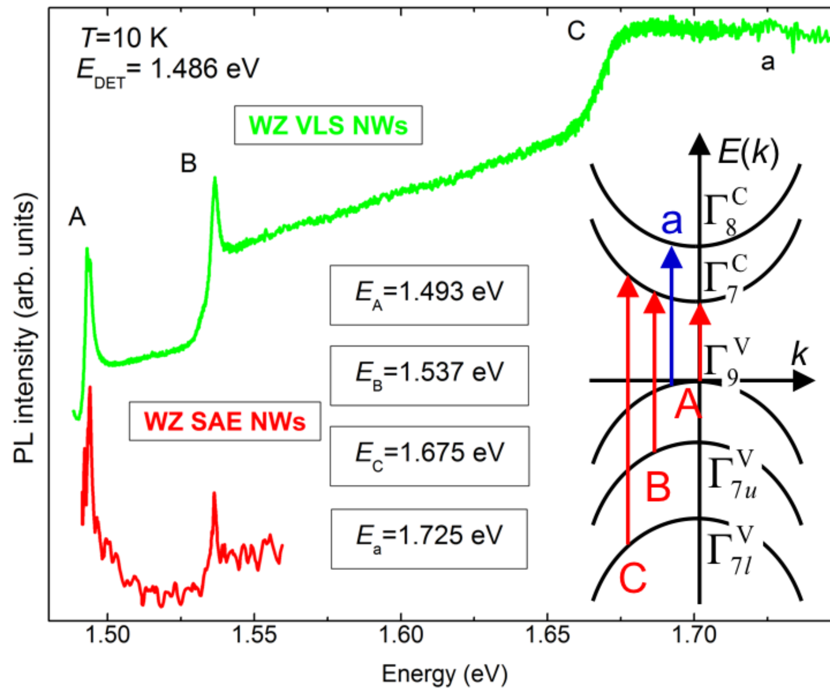

Figure 2.9. a) PLE spectra ($E_{det} = 1.486\,eV$) taken at $T = 10\,K$ on an array of ordered WZ InP-NWs grown by SAE (red line) and on an ensemble of WZ InP-NWs grown by VLS (green line). The schematic inset depicts the WZ A, B, C, and a transitions, whose corresponding absorption edges appear in the PLE spectrum. The values of the transition energies are also reported. After ref. [131].

of the standard Varshni's equation[149]. The temperature dependence of the PL peak-energies in WZ NWs and ZB bulk were similar. Quite surprisingly, instead, the high-temperature dependence of the PL peak-energy in ZB NWs was quite smaller than that found at high temperatures in WZ NWs *and* ZB bulk. No explanation for this puzzling difference was given. In refs. [58, 59], instead, where the temperature dependence of the PL peak-energies in ZB and WZ InP-NWs has been fitted by a standard Varshni formula, no major difference in the fitting parameters was found, with the exception of band-gap energies. Finally, the data in ref. [127], that could not be fitted by the modified Varshni's formula, were fitted by the Viña's relation [151]:

$$E(T) = E_b - a\left[1 + \frac{2}{e^{\Theta/T} - 1}\right], \tag{2.4}$$

where $(E_B - a) = E(0)$ is the band-gap energy at $T = 0\,K$, a is a rough estimate of the strength of the electron-phonon interaction, and $k_b\Theta$ is an average phonon-energy.

All the above mentioned studies, which rely on PL measurements, are invaluable in most instances but not suitable to address the temperature-dependence of critical points. Firstly, they do not give information about the highest energy transitions, such as B and C. Secondly, defect-related localized states are the primary component of PL spectra at low-T; see fig. 2.5. Localized states may blur the band-gap free-exciton peak, whose temperature dependence is also severely distorted by the progressive ionization of these states [152, 153]. Thirdly, the evolution from an

exciton to a band-to-band recombination-regime with increasing T can hamper the determination of the thermal variation of the band-gap. Fourthly, all the emission peaks are affected by a temperature-dependent Stokes-shift that, in turn, depends on the interplay between disorder effects and thermal occupation of energy levels by carriers[154]. Finally, an extremely precise band-gap energy determination is hindered at high temperature by the thermal broadening [127, 155]. The last three factors prevent an accurate estimate of the energy gap from PL measurements alone and could be the cause of some of the aforementioned discrepancies reported in the literature.

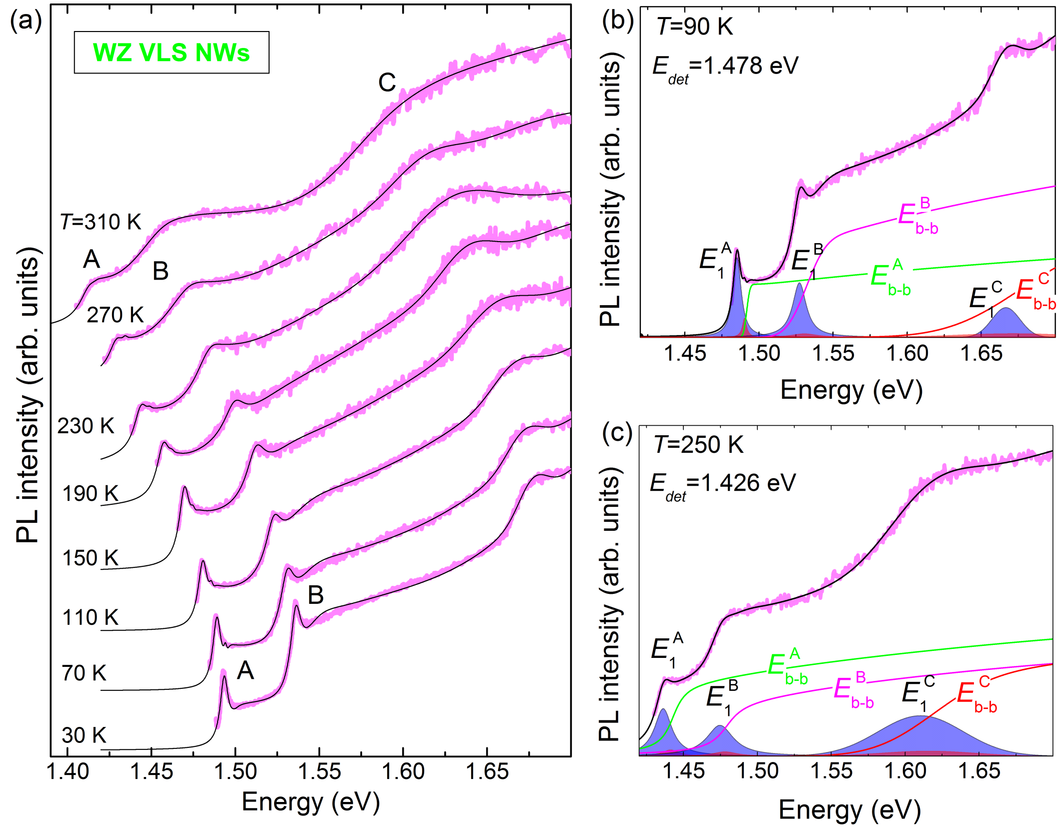

Figure 2.10. a) PLE (thick magenta-lines) spectra taken at different temperatures on an ensemble of WZ InP-NWs grown by VLS. Detection energies were set on the low-energy side of the fundamental band-gap free-exciton. Thin black solid-lines are fits of eq. A.6 to the data. A, B, and C label the three lowest-energy transitions pertinent to the WZ band-structure. b) Fit (thin black-line) of eq. A.6 to the $T = 90\,K$ PLE-spectrum (thick magenta-line) shown in panel a). The various exciton contributions E_n^i (with $i = A$, B, and C and $n = 1, 2$) are indicated by filled, red-colored areas (for clarity purposes, labels E_2^a, E_2^b, and E_2^c are not shown). Contributions of continuum states E_{b-b}^i (with $i = A$, B, and C) are given by thin colored-lines. c) Fit as in b) of the $T = 250\,K$ PLE-spectrum (thick magenta-line) shown in panel a). After ref. [131].

Figure 2.10.a) shows PLE spectra taken at different temperatures from $T = 30\,K$ to $T = 310\,K$ in $40\,K$ steps on an ensemble of WZ InP-NWs grown by VLS. At each temperature, the detection energy was set on the low-energy side of the A peak. The three A, B, and C transitions appear as three distinct absorption-edges with

a well-defined step-like shape at all temperatures. The A and B absorption edges display very intense and sharp excitonic features, up to almost room-temperature. However, the spectral resonances are affected by thermal broadening, especially for temperatures exceeding $190\,K$.

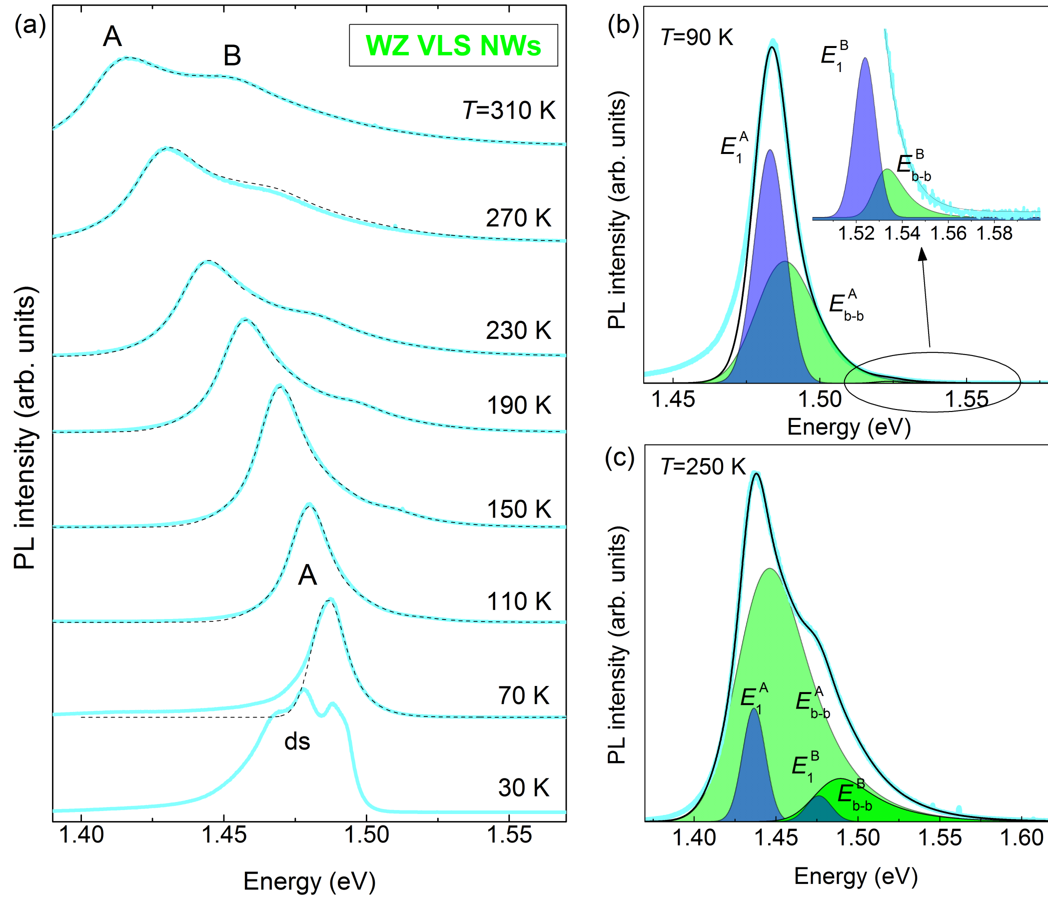

Figure 2.11. a) PL spectra (thick cyan-lines) taken at different temperatures on an ensemble of WZ InP-NWs grown by VLS. "ds" in the bottommost spectrum labels carrier recombination at point and line defects in the lattice. The B transition appears above $T = 150\,K$. Thin black dashed-lines are best fits of eq. A.4 to the data. b) Best fit (black line) of eq. A.4 to the PL spectrum (thick cyan-line) taken at $T = 90\,K$ on an ensemble of WZ InP-NWs. The various contributions to the PL spectra are indicated. The misfit on the low-energy side of the spectrum is due to the contribution of defect states. The inset highlights the contributions of B transition to the spectrum. c) Fit as in b) of the $T = 250\,K$ PL-spectrum (thick cyan-line) shown in panel a). After ref. [131].

The fits (thin black-lines) of eq. A.6 to the PLE spectra allow an accurate determination of the dependence on temperature of the critical-point energies. Fit parameters are the relative amplitudes of the different contributions, the A, B, and C band-gap energies $E_{g,i}$, and the full-width at half-maximum of the broadening functions $A_{b,i}$ [3]. The exciton binding energy $R_{eff,i}$ is calculated in the hydrogenic

[3] We used Lorentzian functions for the A and B transitions, and a Gaussian function for the C

effective-mass approximation for WZ crystals. By defining a dimensionless parameter $\gamma = (\epsilon_\perp/\epsilon_\parallel)(\mu^\perp_{exc}/\mu^\parallel_{exc})$ the effective-mass equation for excitons in WZ crystals can be solved by using a linear variational method for fixed γ. Then, the exciton binding energy is obtained in units of an effective Rydberg, $R^* = (e^4/(2\hbar^2))(\mu^\perp_{exc}/(\epsilon_\perp\epsilon_\parallel))$, provided $\gamma \leq 1$ [156]. The values of the dielectric constants estimated in WZ InP are $\epsilon_\parallel = 10.44$ and $\epsilon_\perp = 12.81$ [157]. Although the exciton reduced-mass of the A transition is experimentally determined in this thesis, for consistency reasons theoretical values from ref. [42] were used for all exciton reduced-masses. The obtained values for the A and B transitions were $R_{eff,A} = 6.4\,meV$ and $R_{eff,B} = 3.8\,meV$. We were not able to determine $R_{eff,C}$ because $\gamma > 1$. Since the PLE spectra do not show any clear excitonic resonance for the C transition, good fits of the PLE spectra were obtained for $R_{eff,C}$ values ranging from 3 to $10\,meV$. Therefore, we used a binding-energy value equal to that of the A exciton, namely, $R_{eff,C} = 6.4\,meV$

For the sake of clarity, the details of the fitting procedure of the PLE spectra taken at $T = 90$ and $250\,K$ are displayed in figs. 2.10.b) and .c), respectively, where all the contributions to the spectra are highlighted. In particular, the exciton contributions are represented by filled areas, the continuum contributions by solid lines. The thin black-lines shown in the figures are the sum of all those contributions. A very-good agreement between fits and experimental data is achieved at the two temperatures as well as at all other temperatures, as shown in fig. 2.10.a).

The excellent quality of our model is confirmed by the results shown in figure 2.11. Fig. 2.11.a) shows PL spectra taken at different temperatures from $T = 30\,K$ to $T = 310\,K$ in $40\,K$ steps on an ensemble of WZ InP-NWs grown by VLS. Each spectrum is very well reproduced by fitting eq. A.4 to data. Only the spectrum taken at $T = 30\,K$ could not be fitted because of the low-energy broad defect-band ("ds"). Notice that the quality of the fit of the low-energy region increases with increasing temperature due to the ionization of those defect states. For increasing temperature, the PL spectra broaden asymmetrically and exhibit a pronounced Boltzmann-like tail, according to eq. A.4. Moreover, for $T \geq 150\,K$ a shoulder rises about $40\,meV$ above the energy of the fundamental band-gap as a result of thermal population of high-energy states. That shoulder corresponds to the B transition.

As an example, the details of fitting procedure on PL spectra taken at $T = 90$ and $250\,K$, respectively, are displayed in figs. 2.11.b) and .c). The inset in figure 2.11.b) highlights the B-transition contributions to the $T = 90\,K$ PL-spectrum. Therein, all the contributions to the PL spectrum are highlighted and shown as in figs. 2.10.b) and .c). In the fits of PL spectra, only the $n = 1$ exciton states have been considered because the high energy states should not contribute much and, in any case, their inclusion did not lead to major improvements in the PL fitting-accuracy. The sum of all contributions to the spectra is shown by a thin black-line in each figure. In the fitting procedure, the relative amplitudes of the different contributions, the fundamental band gap energy $E_{g,A}$[4], the carrier effective-temperature in $f(\hbar\omega, T)$, and the full-width at half-maximum of the broadening functions[5] were used as free

transition. These choices gave us the best agreement between data and model.

[4]The energy differences of the contributions associated with the B transition with respect to $E_{g,A}$ were fixed to those derived from the PLE analysis.

[5]We arbitrarily used Lorentzian or Gaussian functions depending on the quality of the resulting

parameters. The exciton binding energy $R_{eff,i}$ was calculated in the same way as discussed in the PLE-spectra analysis.

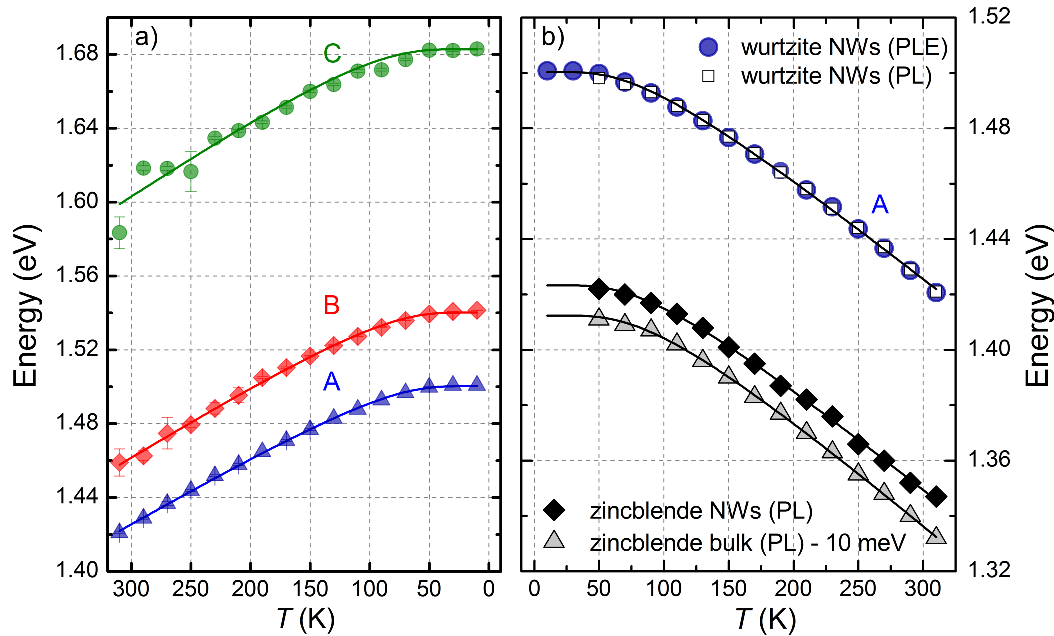

Figure 2.12. a) Temperature dependence of the band-gap energies associated with transitions A, B, and C in WZ InP-NWs. The solid lines are fits of eq. 2.4 to the data with the parameter values reported in Table 2.2. b) Temperature dependence of $E_{g,A}$ of WZ InP-NWs derived by PL (small open-squares) and PLE [large full-dots; same data as in panel a)] measurements. Diamonds and triangles show the band-gap energies for ZB InP-NWs and InP bulk, respectively. The triangles are downward shifted by $10\,meV$ for sake of clarity. The solid lines are a fit of eq. 2.4 to the data with parameter values reported in Table 2.2. After ref. [131].

Figure 2.12.a) shows the energy shift with temperature of the three transitions $E_{g,i}$, with $i = A, B, C$, as obtained by the fitting procedure of the PLE spectra. Triangles, diamonds, and circles denote the band-gap energy values for the A, B, and C transitions, respectively. The fits (solid lines) of eq. 2.4 to the data very well reproduce the PLE spectra. A similar good agreement between data and fits is obtained also by using the Varshni's model (eq. 2.3). It should be noticed that $(E_b - a)$ is the energy of the band gap at $T = 0\,K$ ($E_g(0)$) and not that of the PL peak, which red-shifts by an amount determined by the temperature and the exciton binding-energy. The three transitions display the same thermal shrinkage, as it appears from the experimental data and is confirmed by the very close values of the fitting parameters a and Θ reported in the first three rows of table 2.2. Interestingly, a same temperature behavior of the three optical transitions have already been observed in wide-gap bulk WZ compounds as ZnO [148], CdS [158], CdSe [159], and GaN [160]. Since WZ InP does not exist in the bulk form, our measurements first report that the A, B, and C transitions display an identical temperature dependence also in small band-gap WZ compounds. Thus, this behavior seems to be a general

fit.

Optical transitions	$E_g(0)\,(eV)$	$a\,(meV)$	$\Theta\,(meV)$
A WZ NWs	1.500 ± 0.002	45 ± 2	238 ± 9
B WZ NWs	1.540 ± 0.005	50 ± 5	250 ± 20
C WZ NWs	1.680 ± 0.020	54 ± 30	290 ± 80
ZB NWs	1.423 ± 0.003	50 ± 4	260 ± 10
ZB bulk	1.422 ± 0.002	54 ± 2	265 ± 7

Table 2.2. Values of the fitting parameters obtained from the fits of eq. 2.4 to the experimental data shown in fig. 2.12. $E_g(0)$ is the band gap energy at $T = 0\,K$. a and $k_B\Theta$ are phenomenological quantities associated to the strength of the electron-phonon interaction and to an average phonon-energy, respectively.

feature of WZ compounds, independent of band-gap energy and material form, NWs or bulk.

Now it will be discussed the intriguing temperature dependence of the main optical-transitions in WZ and ZB InP-NWs and ZB bulk-InP determined in ref. [60] on the ground of PL measurements. Therein, the temperature dependence of WZ InP-NWs was similar to that of ZB bulk-InP but different from that of ZB InP-NWs, in contrast with present results obtained by PLE measurements (and other results in the literature). In order to determine the reason of that discrepancies, PL studies as a function of temperature have been performed on ZB and WZ InP-NWs grown by VLS and a ZB epilayer[6]. Eq. A.4, where both excitonic and band-to-band contributions to the PL line shape were taken into account, was then fitted to each PL spectrum, as shown in figs. 2.11.b) and .c) in the case of WZ InP-NWs. It should be noticed that a crossover in the relative intensity between the exciton and the band-to-band contributions occurs in the range $T = 90 \div 250\,K$. That crossover hinders an accurate determination of the thermal variation of the band-gap energy from the simple red-shift of the PL peak-energy. The results of our fits of the PL data are shown in fig. 2.12.b). White open-squares, black diamonds, and gray triangles denote, in the order, $E_{gap,WZ}$ and $E_{gap,ZB}$ in NWs, and $E_{gap,ZB}$ in bulk material as determined by PL. Blue circles, instead, are the $E_{gap,WZ}$ data determined by PLE and reported in panel a). The $E_{gap,ZB}$ data in bulk material (gray triangles) are downward shifted by $10\,meV$ for sake of clarity. PL data for $T = 10$ and $30\,K$, where a reliable line shape fitting could not be obtained because of the presence of defect states, are missing. The solid black-lines are fits of eq. A.4 to the data. First of all, the perfect agreement between the energy shift of the WZ band-gap obtained by PL and PLE highlights the excellent quality of the PL results and confirm that this temperature shift does not depend on the way it has been determined, by PL or PLE. Moreover, the same thermal shrinkage is obtained also in the case of the ZB crystal structure, both in the NWs and bulk form, contrary to ref. [60] results. Therefore, the thermal behaviour of the band-gap energy in InP does not depend on the material crystal form (NW vs bulk) nor on the crystal phase (WZ vs ZB). It is worth pointing out that the fitting parameters found for the ZB epilayer match well those previously found [161, 162], confirming once again the high accuracy of our

[6]Some of these PL-spectra will be shown in the section 2.4

approach.

The quite strong similarity between the dependence on temperature of the fundamental band gap in the WZ and ZB phases can be accounted for by the corresponding similarity between the main mechanisms ruling the band-gap variation with temperature, namely, the lattice expansion and electron-phonon interaction. As described in section 1.3, the four first-nearest neighbors and nine of the twelve second-nearest neighbors in both the WZ and ZB crystal-phase are at identical crystallographic sites. This turns into a local electronic environment very similar in the two crystal-phases, with comparable WZ and ZB crystal-potentials ruling the lattice thermal expansion. Moreover, a rather similar electron-phonon interaction is expected in WZ and ZB crystals due to their similar phonon-dispersion curves [141, 163]. This is consistent with previous theoretical and experimental works highlighting the absence of a major role played by the crystal phase in determining some relevant thermal properties of NWs [163, 164].

2.4 Hot carrier in NWs

Carrier temperature, as well as band-gap energy, is one of the most relevant parameters to be extracted from PL spectra. Heat management mechanisms play, indeed, a pivotal role in driving the design of NW-based devices. In particular, the rate at which charge carriers cool down after an external excitation crucially affects the efficiency of solar cells [165], lasers [166], and transistors [167]. Any possible difference between carrier and lattice temperatures highlights extremely out of equilibrium conditions, usually referred to as hot carrier effect. That effect is not usually observed in continuous wave PL measurements where a steady-state population of carriers in thermal equilibrium is established by carrier relaxation times much shorter than recombination times. Therefore, optically generated hot carriers in NWs and bulk materials have been to date studied mainly by ultra-fast optical spectroscopy under intense excitation [168, 169] -the most common technique used to address the cooling down of photo-generated carriers. In order to study the possible presence of hot carriers in semiconductor NWs under the *quasi-equilibrium* conditions typical of continuous-wave excitation, PL spectra have been taken here as a function of temperature in all our InP samples (WZ and ZB NWs and a ZB epilayer). Then, each PL spectrum has been fitted by including all the contributions to the PL line-shape considered by eq. A.4 [133].

In figures 2.13.a) and .b), PL spectra collected from two single WZ NWs grown by SAE and drop-casted on silicon substrates are reported as a function of lattice temperatures (T_L) ranging from 90 to $310\,K$. The SEM images from which the NW diameters $d = 125\,nm$ (panel a) and $d = 700\,nm$ (panel b) were determined are shown in panel c). The temperature evolution of the spectra of the two NWs resembles that observed on an ensemble of NWs grown by VLS and shown in figure 2.11: the band gap red-shifts and the B band appears to increase for increasing temperatures, as a result of an increase in the thermal population of high-energy states. However, the B band in the $d = 125\,nm$ NW is more intense than that in the $d = 700\,nm$ NW and its weight at $T_L = 310\,K$ even exceeds that of band A, thus pointing to a quite high carrier-temperature in this narrow sample.

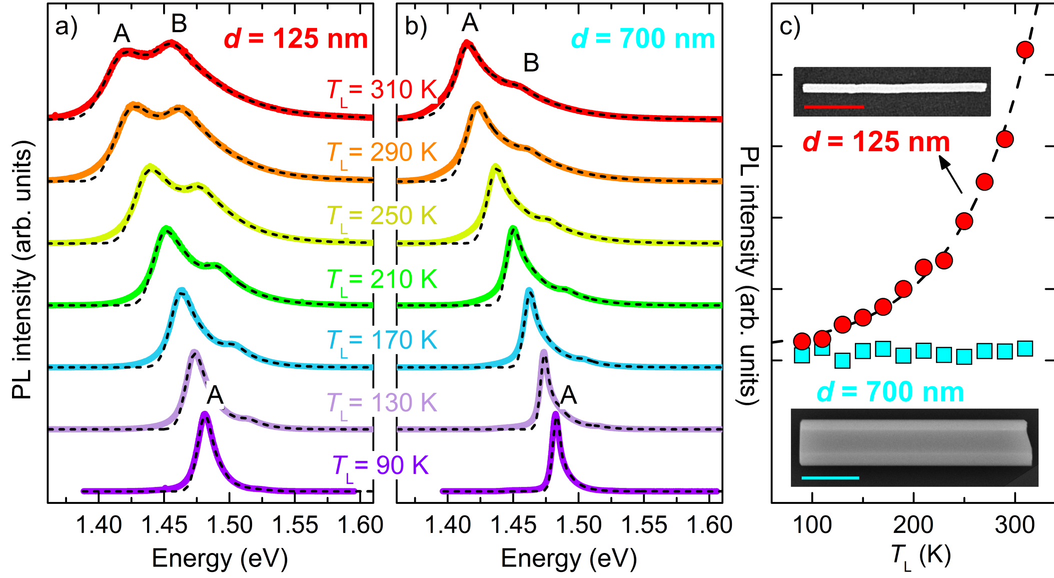

Figure 2.13. μ-PL spectra (thick coloured lines) taken at different lattice temperatures T_L on representative single WZ NWs grown by SAE and lying on a Si substrate. a) $d = 125\,nm$ at power density $P = 1.14\,kW/cm^2$; b) $d = 700\,nm$ at $P = 0.51\,kW/cm^2$. Dashed black-lines are fits of eq. A.4 to the spectra; the small mismatch between data and fits on the low-energy side is due to contributions from defect states not considered in the fits. c) Difference between carrier and lattice temperatures, $\Delta T = T_C - T_L$, as a function of T_L for the NWs shown in panel a) (red circles) and b) (light-blue squares). The dashed line for $d = 125\,nm$ is an exponential fit. SEM images of those two NWs are also shown in the panel; scale bar is $1\,\mu m$. After ref. [133].

Each PL spectrum has been reproduced by a fit of eq. A.4 to the data, as done in figure 2.11. More details on the fitting procedure will be given in subsection 2.4.1. The fitting carrier temperatures are shown in panel c). Therein, the *thermal budget* ΔT, namely, the difference between carrier and lattice temperature ($T_C - T_L$), is shown as a function of the lattice temperature (T_L). Remarkably, the results between the two single NWs are quite different. In the thick NW ($d = 700\,nm$), the thermal budget (light-blue squares) is almost zero for each lattice temperature: charge carriers recombine after having fully transferred their excess kinetic energy to the lattice, via phonons emission, as in a bulk semiconductor. On the contrary, in the thin NW ($d = 125\,nm$) the thermal budget increases with increasing lattice temperature (dashed line is an exponential fit to data): the conversion of kinetic energy into heat is less efficient than that in thick NW, therefore carriers recombine before they are fully relaxed. This finding is remarkable: in NWs whose diameter is small enough, hot carriers are observed under *continuous-wave* laser-excitation, namely, in steady-state *quasi-equilibrium* conditions. It is worth pointing out that all characteristics, but the diameter, of the two NWs investigated here are very similar because these NWs belong to a same class, as described in section 2.2

An important clarification concerning the lattice temperature should be given now. It is well-known that laser beams focused through microscope objectives may lead to high power-densities and act as local heat sources, with an ensuing increase

in the lattice temperature. Therefore, a tight control of T_L during our experiments was essential to exclude an increase in T_C due to a trivial lattice heating. The thermal dependence of the fundamental band-gap energies (E_g) in WZ and ZB InP, which have been determined in 2.3.3, allowed us an independent check of T_L from the line-shape analysis of each PL spectrum. The uncertainty in the estimation of E_g varies from $0.1\,meV$ (at $90\,K$) to $1\,meV$ (at $310\,K$). This leads to an error on the estimation of T_L ranging from $0.5\,K$ (at $90\,K$) to $3.0\,K$ (at $310\,K$), which is smaller than the symbol size in Figure 2.13.c). In the following measurements, all the lattice temperatures estimated by the fitting procedure very well agree with those measured by the sample thermometer.

2.4.1 Dependence of carrier temperatures on NW diameter and lattice temperature

Similar PL studies have been performed on other classes and typologies of NWs in order to investigate the dependence of the hot-carrier effect on the NW morphology. Figure 2.14 shows PL spectra (cyan thick-lines) taken at $T = 310\,K$ on three different single InP-NWs drop-casted on silicon substrates (panels a,b,c) and on an InP bulk (panel d). Panel a) shows a PL spectrum collected from a single kinked-NW ($d = 74\,nm$) that likely broke up during the drop-casting process, thus allowing us to measure a $1.5\,\mu m$-long WZ-tip without spurious PL contributions of the ZB base. A high carrier temperature ($498\,K$) has been determined by the fitting procedure, as also supported by a B-band weight that exceeds that of the A band (even the third recombination-band C is observed, because of a high carrier-temperature that sizably increases the population of the related valence-band) Panel b) shows a PL spectrum collected from a different single kinked NW ($d = 139\,nm$) that broke up, thus allowing us to measure a $\sim 1.5\,\mu m$-long ZB base without PL spurious contributions of the WZ tip. Panel c) shows a PL spectrum of a WZ NW grown by SAE and similar to the $d = 335\,nm$ NWs whose spectra are reported in fig. 2.13. Lastly, panel d) shows a macro-PL spectrum from a InP bulk epilayer.

Each contribution to the PL line-shape, as obtained by fits of eq. A.4 to the PL spectra, is reported in figure 2.14. In particular, contributions from the $n = 1$ exciton ground state are given by blue-filled areas, from the $n = 2$ exciton-states are shown by cyan-filled areas, and from band-to-band recombinations are indicated by orange-filled areas. The sum of all those contributions is given in each panel by thin, black dashed-lines, which very well reproduce the PL spectra of all different NWs. In the least-square fitting procedure the parameters were: the relative amplitudes of the different contributions; the transition energies $E_{g,i}$; the carrier temperatures in the Boltzmann functions; the full widths at half maximum of the broadening functions[7]. The exciton binding energy $R_{eff,i}$ for the WZ PL-emission has been calculated in the hydrogenic effective-mass approximation, as explained in 2.3.3. The value determined in 2.3.1 from the PL line-shape analysis of the InP epilayer was used, instead, for the R_{eff} of ZB InP.

Results in fig. 2.14 confirm previous results shown in fig 2.13. Indeed, the hot-carrier effect seems to be strongly dependent on the NW diameter rather than on

[7]We have arbitrarily used Lorentzian or Gaussian functions to optimize the fits.

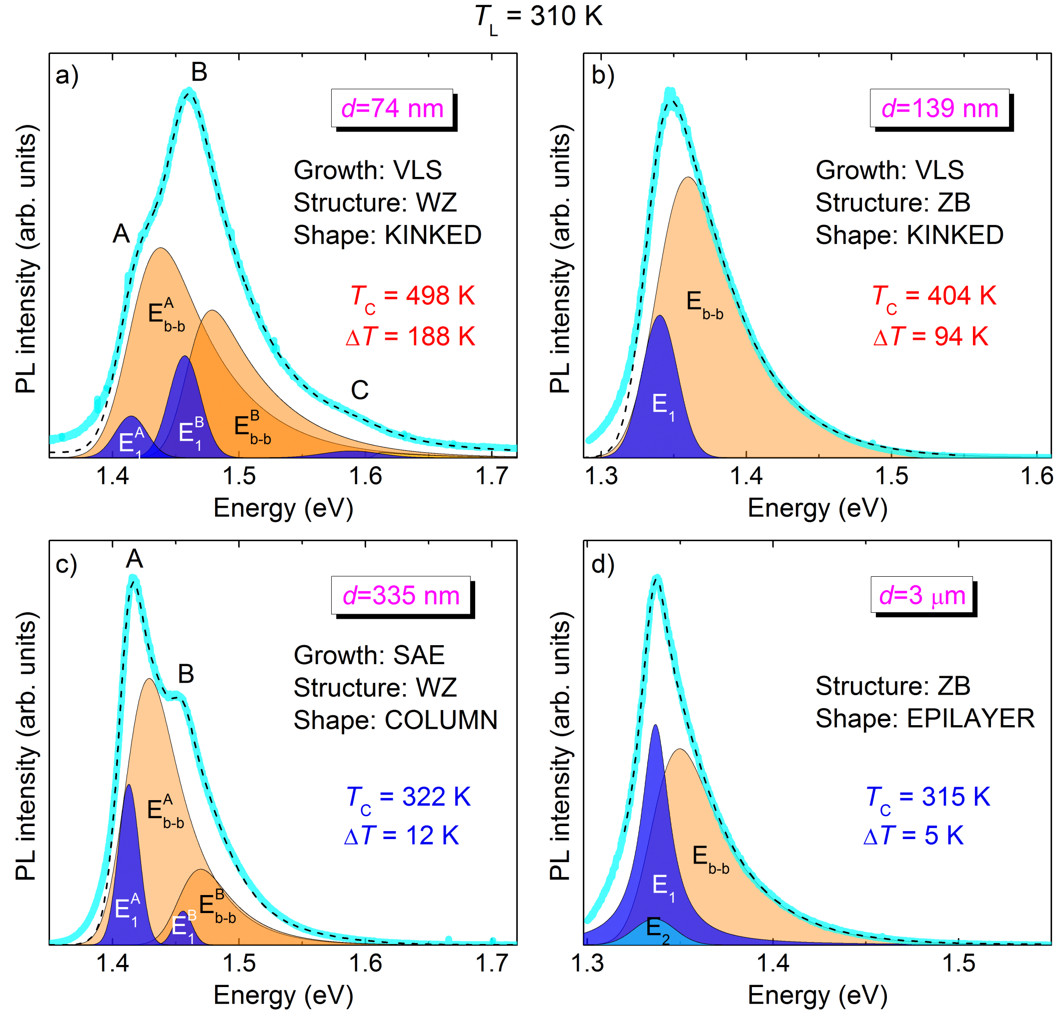

Figure 2.14. μ-PL spectra (thick cyan-lines) taken at $T = 310\,K$ on single InP NWs lying on Si substrates (panels a, b, and c) and on an InP epilayer (panel d). Power densities: a) $P = 12.7\,kW/cm^2$; b) $P = 20.4\,kW/cm^2$; c) $P = 0.7kW/cm^2$; d) $P = 0.7\,W/cm^2$. Dashed black-lines are best fits of eq A.4 to the data. The various contributions to the spectra are indicated by blue-filled areas for exciton transitions E_n ($n = 1$ for the ground state and $n = 2$ for the first excited state) and by orange-filled areas for band-to-band transitions E_{b-b}. T_C and ΔT values resulting from the fits are given in each panel. The superscripts A, B, and C associate those contributions to the different transitions involved in the case of WZ NWs. After ref. [133].

other NW characteristics, such as the growth method or crystal phase. In addition, the small thermal-budget values, $\Delta T < 15\,K$ at $T_L = 310K$, given by the two WZ NWs grown by SAE with $d = 335\,nm$ (fig. 2.14.c)) and $d = 700\,nm$ (fig. 2.13.b)) point to a threshold diameter ($\sim 300\,nm$) above which the hot carriers disappear. To address in more detail the amount of thermal budget as a function of the NWs diameter, ΔT values were measured at $T_L = 290\,K$ for all the InP NWs described in 2.2. The epilayer was measured with the macro-PL setup. μ-PL measurements on single NWs were performed on all SAE samples and on the VLS NWs with

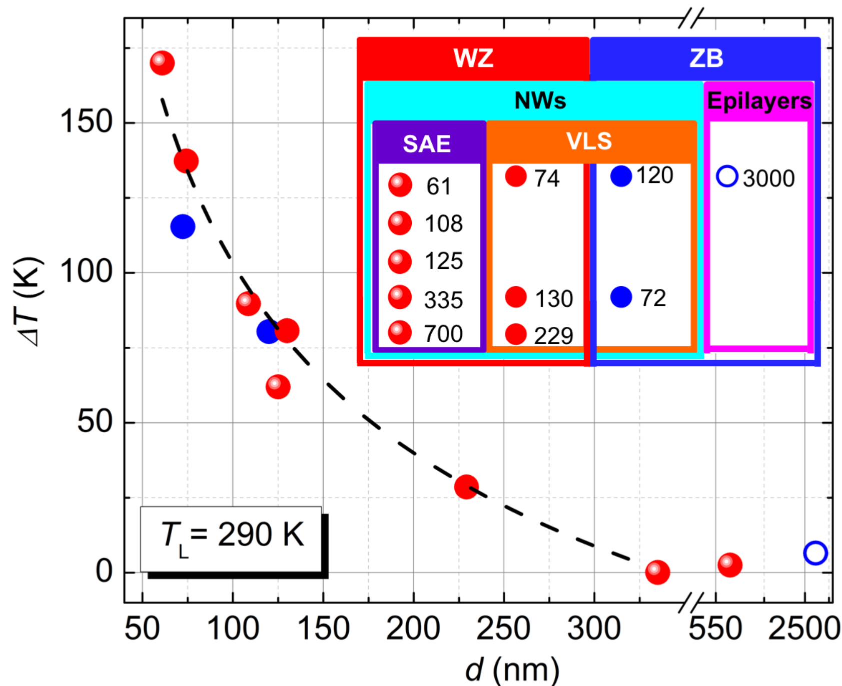

Figure 2.15. Thermal budget $\Delta T = T_C - T_L$ as a function of the diameter for all InP samples described in section 2.2. ΔT was determined by a quantitative analysis of the PL spectra (recorded at $T_L = 290\,K$) via eq. A.4. Notice the x-axis break from 350 to 550 nm and the semilog scale after the break. Error bars for ΔT and d are smaller than the symbol sizes. The dashed line is a hyperbolic fit to the $d < 350\,nm$ data. The characteristics of the investigated samples are summarized in the inset, where numbers are diameters in nm. After ref. [133].

$d = 74$ and $120\,nm$. Macro-PL measurements were made, instead, on ensembles of VLS-grown NWs with $d = 72$, 130, and $229\,nm$. $d = 130\,nm$ NWs were vertically standing on their growth substrate, while $d = 72\,nm$ and $d = 229\,nm$ NWs were mechanically transferred on a Si substrate. Ensembles of SAE NWs with $d = 335\,nm$ and $d = 700\,nm$ were measured also in macro-PL and ΔT values equal to those found in the single wire measurements were obtained. All measured ΔT values are reported in figure 2.15 as a function of the NW diameter (for the epilayer, its thickness was used) and confirm the results shown in fig. 2.14: the thermal budget ΔT at fixed lattice temperature depends *only* on the NW diameter, more precisely it goes as $1/d$. This behavior is independent of the experimental configuration and of any other NW characteristics, such as NW shape, crystal structure, and growth method. Lastly, the guess of a critical diameter above which the thermal budget vanishes is confirmed by ΔT approaching zero above $d \sim 330 nm$.

As anticipated in fig. 2.13, ΔT increases *exponentially* for increasing lattice temperature. To support that behavior, the dependence of the carrier thermal-budget on lattice temperature has been thoroughly investigated in other samples. Figure 2.16 shows ΔT as a function of T_L for InP samples with WZ (panel a) and ZB (panel b) crystal-structures. In the hot-carrier regime ΔT increases exponentially with increasing T_L in all WZ and ZB NWs samples, as it does in fig. 2.13. All the

experimental data but the epilayer are reproduced by an exponential fit $\Delta T(T_L) = C \times e^{D \cdot T_L}$ (dashed black-lines in the figure), where C and D are free parameters. Within the group of NWs with the same crystal structure, a smaller diameter leads to a greater increase in ΔT at each lattice temperature, namely, to greater C values. In WZ structures, for instance, C varies from $0.3 \pm 0.2\,K$ to $7.1 \pm 5.9\,K$ when d decreases from 229 to $74\,nm$. On the other hand, the values of D are similar in NWs with the same crystal structure, with a value in WZ only slightly greater than that in ZB. As an example, in the inset ΔT vs T_L is shown in a semilog scale for WZ (red circles) and a ZB (blue circles) samples with similar diameters ($\sim 70nm$). The WZ dependence on T_L has a slope ($D_{WZ} = (10.0 \pm 2.6) \times 10^3\,K^{-1}$) slightly greater than the ZB one ($D_{ZB} = (7.5 \pm 1.5) \times 10^3\,K^{-1}$), possibly due to the different crystal structures of the two phases.

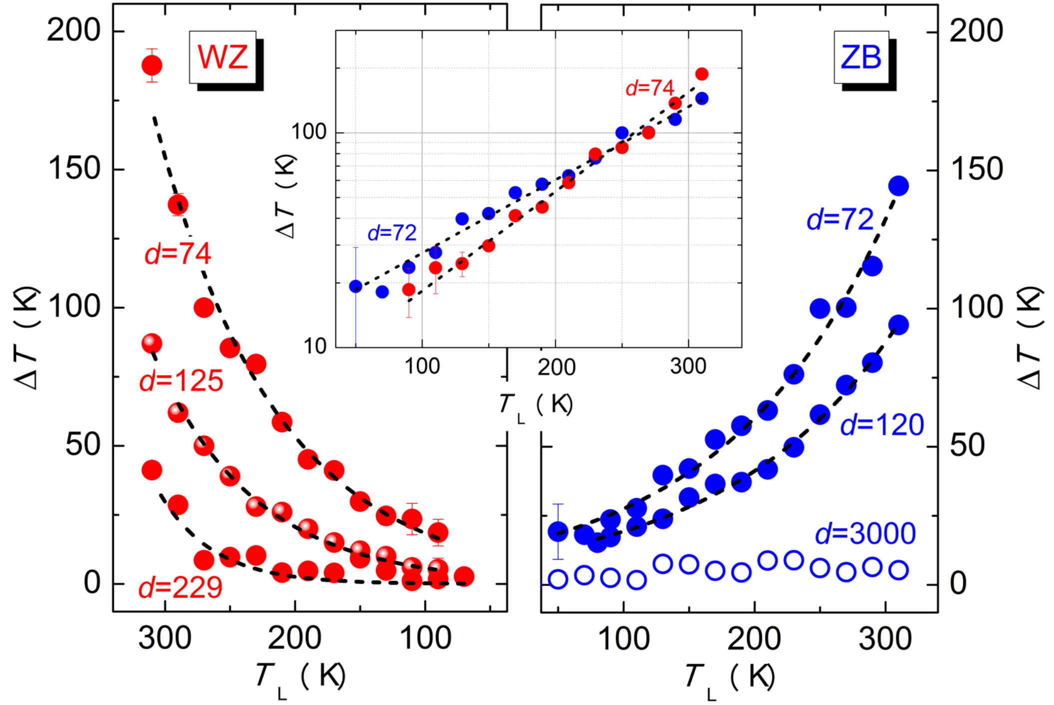

Figure 2.16. $\Delta T = T_C - T_L$ vs T_L for NWs with a WZ (a) and ZB (b) structure. Black dashed-lines are exponential fits to the data. The inset shows ΔT vs T_L on a semilog scale for a sample with WZ structure ($d = 74\,nm$, red circles) and a sample with ZB structure ($d = 72\,nm$, blue circles). After ref. [133].

The likely physical reasons for the presence of hot carriers in NWs under the quasi-equilibrium conditions typical of our measurements will be now discussed. As already anticipated, hot carriers have been observed to date only as a transient occurrence in ensembles of NWs highly excited by femto-second laser pulses. As an example, in polytypic InP NWs characterized by small diameters, room temperature PL measurements have determined carrier temperatures higher than the lattice temperature even after tens of ps, an effect ascribed to the crystal disorder produced by the crystal phase mixing [168]. Interestingly, in those thin NWs the thermal budgets extrapolated to time scales of order of ns are consistent with those estimated

in the *politypism-free* samples investigated in the present thesis. Therefore, the small NW-diameter could be at the heart of the hot-carrier effect found in ref. [168]. Hot carriers have been found also by low-temperature transient Rayleigh scattering in InP and GaAs under high excitation [169]. That effect was accounted for by hot phonons that would have likely led to an electron-hole plasma-temperature higher than that of the lattice. Even such an out-of-equilibrium phonon population cannot explain the results found in the present thesis under steady-state conditions and low excitation power that prevent the generation of a high number of photo-generated carriers and, in turns, of phonons emitted during carrier relaxation. Moreover, no change in the carrier temperature has been found in our measurements in vertically standing (horizontally lying) NWs for an increase in the excitation power density of a factor of 100 (14), which excludes a hot-phonon contribution to present results. Finally, the band gap energy did not vary with power excitation, thus implying the absence of a laser induced lattice-heating [133].

Another explanation of a hot-carrier effect could be a reduction of carrier lifetime in NWs. Indeed, it has been demonstrated that the carrier recombination time (τ_{NW}) in NWs depends on the NW diameter [170]:

$$\frac{1}{\tau_{NW}} = \frac{1}{\tau_{bulk}} + \frac{4S}{d}, \tag{2.5}$$

where τ_{bulk} is the carrier lifetime in the bulk material, S is the surface recombination velocity, and d the NW diameter. Therefore, whenever the NW diameter is small enough that the surface recombination velocity leads to τ_{NW} values shorter than or comparable to the carrier relaxation time ($1 - 100\,ps$, [171]), one falls in the phonon-assisted thermalization time-scale where hot carrier effects could be observed since electrons and holes might not have time enough to release their excess energy to the lattice. Time resolved PL measurements have been then performed at $T = 290\,K$ on three arrays of NWs grown by SAE with diameters equal to 125, 335, and $700\,nm$ in order to find out whether carrier recombination times were close to the ps time-scale. Fits of single-exponential decays gave carrier lifetimes equal to $\tau_{NW} = 0.82 \pm 0.01\,ns$ for $d = 125\,nm$, $\tau_{NW} = 1.39 \pm 0.01\,ns$ for $d = 335\,nm$, and $\tau_{NW} = 1.98 \pm 0.01\,ns$ for $d = 700\,nm$. Although τ_{NW} decreases monotonically with decreasing d, as expected, it is always too long to be comparable with carrier relaxation times, even in the thinner NW. Therefore, it cannot account for the hampered heat-dissipation we have reported on [133].

In summary, all usual explanations of the hot carrier effect do not apply to present results because in our samples hot phonons are negligible and carriers do have time enough to dissipate the excess energy provided by the laser excitation. Therefore, the reduced heat dissipation observed here in small NWs should be ascribed either to a reduced carrier-phonon interaction or to an inhibited phonon-emission, which calls for further theoretical investigations. However, it is worth pointing out that thermal conductivity (κ) measurements on ZnO NWs [172] and InAs NWs [173] evidenced that κ decreases with decreasing NW diameter, thus prompting an experimental phenomenology that parallels the diameter dependence of T_C. On the ground of this similarity, we suggest that the mechanisms that impede heat flow (i.e., dissipation) in NWs play a major role also in preventing photo-generated carriers from releasing their excess energy by phonons.

A reduced NW thermal conductivity as compared to the bulk one is usually ascribed to a phonon scattering by various elements [84, 88, 174, 175] and to a suppression of available phonon-modes in 1D due to a modified phonon density-of-states. Since phonon confinement can be excluded in our case because of the NW thickness ($d_{min} = 60\,nm$) [174], phonon-scattering processes should explain our results. Usually, those processes are divided in temperature-independent interactions with surface, impurities, roughness, and line defects [172, 176] and in temperature-dependent phonon-phonon and umklapp processes. The observation of a dependence of hot carriers on NW diameter points to the NW surface itself as the most effective phonon-scattering element, as if the phonons that are mainly involved in the relaxation of photo-generated carriers were those whose mean free path is comparable to the NW diameter. As a matter of fact, the rate of boundary scattering of phonons depends on the inverse of the NW diameter [176]. Within this picture, the smaller the diameter, the hotter the carriers are (because of a scattering-induced suppression of the phonons diffused by boundaries).

On the other hand, the drastic reduction in the thermal conductivity for $T_L > 150\,K$ observed in ref. [172, 176] has been ascribed to an increase in umklapp and phonon-phonon scattering-rates with increasing lattice-temperature. We can only qualitatively compare our exponential increase of ΔT with T_L to the reduction in thermal conductivity with T_L, as done for the mechanism envisaged for the dependence of T_C on the inverse of d. Nevertheless, such a purely exponential dependence on lattice temperature was never predicted [176] or found [172]. Thus, our experimental findings should stimulate detailed theoretical studies of the awkward temperature dependent interplay between carrier-relaxation processes as well as of the main mechanisms that hinder a plain dissipation of the carrier kinetic-energy.

2.4.2 Homostructures based on single NW as promising photothermoelectric device

The hot carrier effect, as anticipated before, can be most welcome in photovoltaic applications or in photo-thermoelectric devices. The photo-thermoelectric effect consists in a light-induced temperature-difference, ΔT, between the extremes of a device that drives a current and produces a voltage via the Seebeck effect. This effect has been widely investigated in two dimensional materials [177, 178, 179] and NWs [180, 181]. Although a temperature gradient is most commonly established in the crystal lattice, a gradient in the carrier temperature for fixed lattice temperature has been recently achieved, with ΔTs higher than in the former case [180]. Since it has been shown that heat conduction in the lattice should not contribute to establish a thermal equilibrium among carriers, μ-PL measurements in a same single, unbroken kinked-NW have been performed in order to verify if a difference in the temperatures of carriers photoexcited either in the ZB or WZ NW regions -which differ for crystal structure and *NW diameter*- could be established and maintained.

Figure 2.17 shows PL spectra from a single, unbroken kinked-NW drop-casted on a silicon substrate, as the one displayed in figure 2.8.b). The red (blue) line refers to PL spectra acquired on the WZ (ZB) region at $T_L = 300\,K$ with an excitation power $P_{exc} = 1\,kW/cm^2$. Black solid lines are fits of eq. A.4 to the data for the carrier-temperatures (and thermal-budgets) shown in the figure. T_C in the thinner

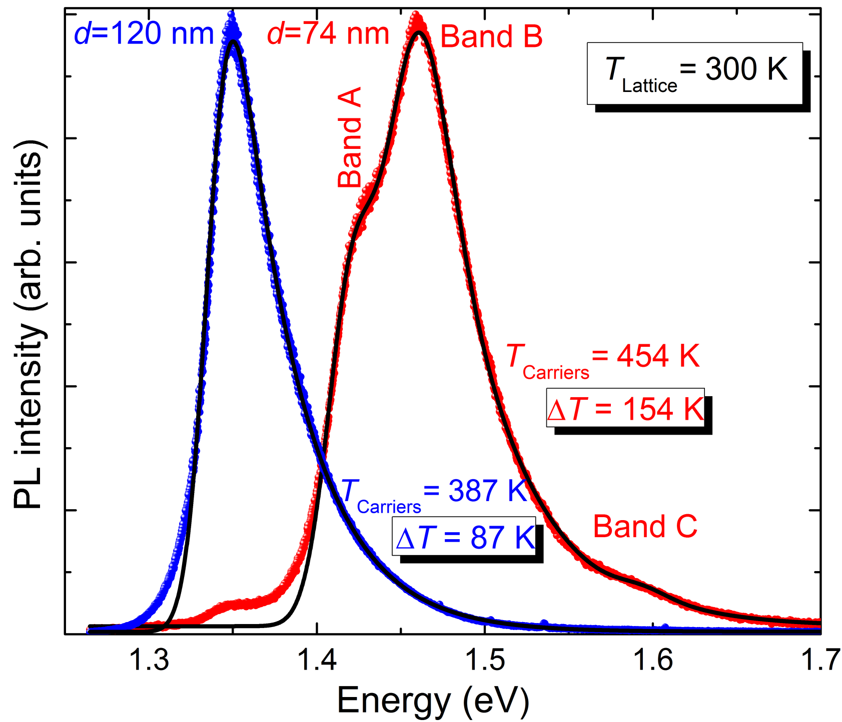

Figure 2.17. Room temperature PL-spectra collected from the WZ (red) and ZB (blue) region of a single, intact kinked-NW drop-casted on a silicon substrate (a SEM image of this NW is shown in fig. 2.8). ZB emission is visible on the low-energy side of the WZ PL-spectrum. Black dashed lines are fits to the data from which the reported carrier temperatures and thermal budgets were obtained.

WZ part of the NW ($d = 74\,nm$) is higher than in the thickest ZB part ($d = 120\,nm$), in agreement with previous results, in particular with those reported in fig. 2.16. Most interestingly, the carrier temperatures in the two NW segments differ by as much as $70\,K$ *despite the lattice temperature is the same in the WZ and ZB regions*. These preliminary promising and surprising results point toward a great relevance of long-living hot-carriers for NW-based photovoltaic and thermoelectric applications and triggered us to apply two metallic contacts at the two extremes of a single kinked NW in order to perform photo-thermoelectric experiments, still in progress.

Chapter 3

Magneto-photoluminescence studies on wurtzite InP nanowires

In this chapter, the transport and spin properties in WZ InP-NWs grown by SAE are assessed by magneto-PL experiments. Studies of the diamagnetic shift (B up to $29\,T$) of free-exciton states and impurity levels allowed us to disentangle the Coulomb interaction from the dynamics of oppositely charged carriers and, thus, to determine the electron and hole effective-masses separately. The same applies to the carrier gyromagnetic factor. Magnetic fields were applied along different crystal orientations (parallel or perpendicular to the WZ $\hat{c}$-axis) in order to highlight any possible difference in carrier motion or spin properties.

The first section of this chapter is devoted to a brief review of the effects of magnetic field on the energy and symmetry of exciton recombination in WZ crystals, as well as of free-electron-to-acceptor and donor-to-acceptor transitions. As a matter of fact, a detailed discussion is required to fully understand the role of the different physical parameters that take part in the diamagnetic shift and Zeeman splitting effects, in particular with regards to PL recombination-bands like those reported in fig. 2.5.a).

In the second section of this chapter, a quantitative analysis of the diamagnetic shift allow us to separately determine the electron and hole effective-masses and their dependence with respect to the angle their motion form with the WZ $\hat{c}$-axis. The results thus obtained are compared with existing theoretical predictions, with which only a partial agreement is found. Conversely, our findings show trends surprisingly very similar to those experimentally found in other WZ *bulk-materials.*

In the third section of this chapter, the spin properties are discussed. The experimental results well agree with a theoretical model based on a 8×8 $\vec{k} \cdot \vec{p}$ Hamiltonian, which includes spin-orbit-coupling terms. Furthermore, for B parallel to the NW axis and $B > 10\,T$, the exciton Zeeman splitting shows a marked non-linearity. This finding is explained in terms of a field-dependent hole gyromagnetic-factor ($g_h^{\parallel}$) due to the mixing between Landau levels originating from the heavy- and light-hole valence-bands of the WZ Brillouin zone.

3.1 Magnetic-field effects on optical transitions

As shown in figure 2.5.a) and discussed in section 2.3.1, the PL spectrum of WZ NWs grown by SAE results from several recombination bands, which have allowed us to determine separately the effective masses and spin properties of both electrons and holes. In this section, we briefly describe the models accounting for the energy dependence on magnetic fields of these optical transitions: *i*) free-exciton, FE, recombination; *ii*) free-electron to neutral-acceptor, (e, A^0), transition; *iii*) neutral-donor to neutral-acceptor, (D^0, A^0), transition.

3.1.1 Free-exciton recombination in WZ crystals

The symmetry properties of the WZ crystal-structure have been discussed in 1.3. Here, we focus on the exciton ground-state, namely, the A exciton and on its dependence on magnetic fields. We neglect the influence of B and C excitons on the A exciton because the energy separation between these states ($> 40\,meV$) is greater than their binding energies ($< 10\,meV$) (otherwise, interactions between exciton states should be taken into account, as it has been done in other WZ compounds [182]). Exciton levels reflect the symmetries of the involved conduction- and valence-bands, as well as the symmetries of the exciton hydrogenic-state in the center of mass. By following group-theory arguments, the exciton ground-states for A transition at Γ point are given by [43, 183]:

$$\Gamma_{9V} \otimes \Gamma_{7C} = \Gamma_5 \oplus \Gamma_6. \tag{3.1}$$

Two exciton states, each one twofold degenerate, characterize the A exciton levels. The Γ_5 states possess total (spin + orbital) angular-momentum projection along the z axis (J_z^{tot}) equal to ± 1. It turns into an optical allowed transition and usually it is called *bright* exciton, as it can be understood in terms of a Bloch basis-set of valence ($u_V^{\pm}$) and conduction ($u_C^{\pm}$) bands [43, 184]: Γ_5 is a linear combination of $u_V^+ u_C^-$ and $u_V^- u_C^+$ functions, where electron and hole spins are always antiparallel. The linear combination of $m_{j,h} = \pm 3/2$ hole-states and $m_{j,e} = \pm 1/2$ electron-states leads to a total momentum projection:

$$m_{j,exc} = \pm \left(| \pm \frac{3}{2} | - | \pm \frac{1}{2} | \right) = \pm 1. \tag{3.2}$$

The Γ_6 states involve the same linear combination but with the electron spins interchanged: Γ_6 is a linear combination of $u_V^+ u_C^+$ and $u_V^- u_C^-$ functions, where electron and hole spins are always parallel. This leads to a total momentum projection $m_{j,exc} = \pm 2$, namely, to a forbidden optical transition, and it is usually called *dark* exciton.

In absence of external perturbations, the A exciton displays three main features:

- It is split by the analytic part of the short-range exchange-term into a dipole-forbidden Γ_6-state, with energy E_6, and in a dipole-allowed Γ_5-state, with energy E_5. Γ_5 levels are optically allowed only for light-polarization perpendicular to the $\hat{c}$ axis ($\epsilon \perp \hat{c}$).

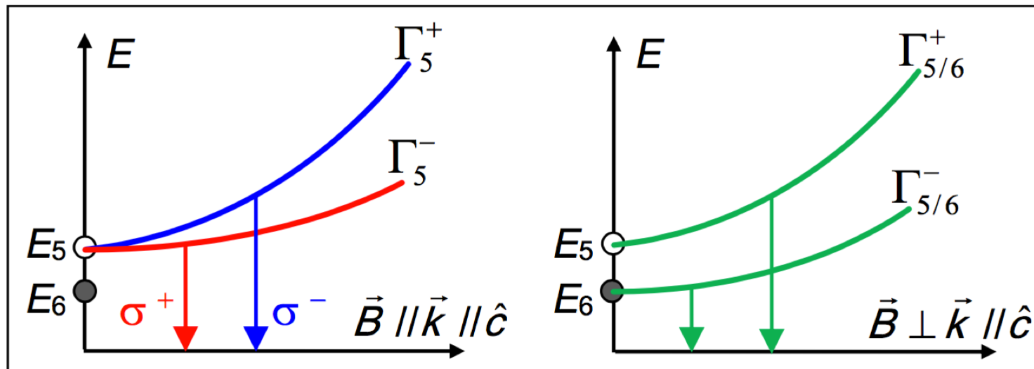

Figure 3.1. Magnetic-field dependence of the A exciton levels in a WZ crystal phase. The curves mimic the effect of the diamagnetic shift and Zeeman splitting on the A exciton levels: $\vec{B}\|\hat{c}$, namely, Faraday configuration, in the left part of the figure; $\vec{B}\perp\hat{c}$, namely, Voigt configuration, in the right part of the figure; in both cases $\vec{k}\|\hat{c}$. The vertical arrows indicate exciton recombinations toward the system ground-state. In the Faraday configuration, the emitted photons are circularly polarized. In the Voigt configuration, the emitted photons are not polarized. After ref. [134]

- The energy difference (Δ_{56}) between the Γ_5 and Γ_6 energy levels is given by the analytic part of the short-range exchange-interaction and depends on the system we are dealing with. It can range from hundreds of μeV in bulk systems ($120\,\mu eV$ in GaN [184] and $200\,\mu eV$ in CdS [185]) to tens of meV in nanocrystals. In the latter case, it depends on the nanostructure size and can lead to the observation of a five-level exciton *fine-structure* [186].

- If the exciton wave-vector is perpendicular to the $\hat{c}$ axis, the non-analytic part of the electron-hole exchange-interaction ($\Delta_{LT} = \Gamma_{5L} - \Gamma_{5T}$) splits the twofold degenerate Γ_5 states into a transverse (Γ_{5T}) and a longitudinal (Γ_{5L}) component with respect to the $\hat{c}$ axis. The energy separation between the two states can vary from $0.08\,meV$ in ZB GaAs [187] to $1\,meV$ in WZ GaN [184]. The Γ_5 levels are still degenerate, instead, for an exciton wave-vector parallel to the $\hat{c}$ axis.

In section A.1, we have briefly reviewed the theory behind the diamagnetic shift (ΔE_d) and the Zeeman splitting (ZS) of excitons. Here, we will describe the effect of a magnetic field on the A exciton states in two experimental configurations: Voigt ($\vec{B}\perp\vec{k}\|\hat{c}$) and Faraday ($\vec{B}\|\vec{k}\|\hat{c}$) [182, 185, 188]. We point out that all our measurements have been carried out with the light wave-vector parallel to the $\hat{c}$ axis. Therefore, the Γ_5 state is twofold degenerate.

As explained in section A.1, the extent and functional variation of the diamagnetic shift with B depends mainly on the relative strength between the *magnetic energy* (gauged by $\hbar\omega_c$) and the *exciton binding-energy* (R_{eff}). In WZ InP, the ratio between these two energies is $\gamma = \hbar\omega_c/R_{eff} = 0 \div 18$ for $B = 0 \div 29T$. Therefore, the numerical methods described in section A.1 have been used in this intermediate-field regime to reproduce the diamagnetic-shift data. The B-induced energy-variation of the A exciton is depicted in figure 3.1 for different field orientations with respect to the WZ $\hat{c}$-axis.

$$\vec{B}\|\vec{k}\|\hat{c}, \quad \text{Faraday configuration}$$

A magnetic field parallel to the $\hat{c}$ axis does not affect the crystal symmetry and does not mix (Γ_5) bright and (Γ_6) dark excitons. Therefore, only (Γ_5) exciton levels can be observed. The B dependence of the exciton energy sketched in the left part of fig. 3.1 is quantitatively described by:

$$E_5^{\pm}(B) = E_5(0) + \Delta E_{d,\|}(B) \pm \frac{1}{2}|g_{e,\|} - g_{h,\|}|\mu_B B, \tag{3.3}$$

where the last term accounts for the Zeeman splitting and g_h and g_e are the hole and electron g-factors, respectively. $\Delta E_{d,\|}(B)$ is the exciton diamagnetic-shift for $\vec{B}\|\hat{c}$ and it depends on $\mu_{exc}^{\perp}$ and ϵ_r. In the Faraday geometry, the Zeeman-split states possess a well-defined chirality and can be spectroscopically distinguished by circularly polarized-light filtering.

$$\vec{B} \perp \vec{k}\|\hat{c}, \quad \text{Voigt configuration}$$

A magnetic field perpendicular to the $\hat{c}$ axis lowers the crystal symmetry and mixes bright and dark excitons, thus creating two $\Gamma_{5/6}$ states with total energies (see right panel in fig. 3.1):

$$E_{5/6}^{\pm}(B) = E_6(0) + \frac{1}{2}\Delta_{56} + \Delta E_{d,\perp}(B) \pm \frac{1}{2}\left[\Delta_{56}^2 + g_{e,\perp}^2\mu_B^2 B^2\right]^{\frac{1}{2}}. \tag{3.4}$$

$\Delta E_{d,\perp}(B)$ is the exciton diamagnetic-shift for $\vec{B} \perp \hat{c}$. It depends on $\mu_{exc}^{\perp,\|}$ [189] and ϵ_r. For $B = 0\,T$, $E_{5/6}^{-} = E_6$ (dark exciton) and $E_{5/6}^{+} = E_6 + \Delta_{56} = E_5$ (bright exciton). $E_{5/6}^{\pm}(B)$ cannot be resolved by polarized light measurements because Γ_5 and Γ_6 excitons are mixed and $\vec{B} \perp \vec{k}$,. Thus, it is very difficult to trace the Zeeman-split states in this geometrical configuration, unless the bands are very narrow as in the case of free excitons at low temperature. Clearly, the Zeeman splitting is roughly linear only if $\Delta_{56} << g_{e,\perp}\mu_B B$.

Magneto-PL measurements in WZ crystals allow the determination of the dependence of the $\Gamma_{5/6}$ states on magnetic field, when performed in the $\vec{B} \perp \hat{c}$ configuration, and of the $\Gamma_5^{\pm}$ states, in the $\vec{B}\|\hat{c}$ configuration. A quantitative reproduction of data by eq. 3.3 (3.4) permits to estimate the exciton g-factor $|g_{e,\|} - g_{h,\|}|$ and the exciton reduced-mass $\mu_{exc}^{\perp}$ in a plane perpendicular to the $\hat{c}$ axis (the exciton g-factor $g_{e,\perp}$ and the exciton reduced-mass $\mu_{exc}^{\perp,\|}$ in a plane containing the $\hat{c}$ axis).

3.1.2 Free-electron to neutral-acceptor transition

At zero magnetic field, the energy of the free-electron to neutral-acceptor recombination is given by:

$$E_{(e,A^0)} = E_{CB} - E_A, \tag{3.5}$$

where E_{CB} is the energy of the conduction band minimum, E_A is the acceptor energy level, and the energy zero is set at the top of the valence band. In presence of a magnetic field B, the conduction band is split into quantized sub-bands, labeled

Landau levels, as described in section A.1. If the (e, A^0) recombination involves the lowest Landau level ($n = 0$), its energy, averaged over spin-split levels, shifts according to:

$$E_{(e,A^0)}(B) = E_{CB}(B = 0) - E_A(B = 0) + \frac{e\hbar}{2m_e}B - \Delta E_A(B), \tag{3.6}$$

where $\Delta E_A(B)$ is the energy shift of the acceptor level under the applied magnetic field. Free electrons in the CB interact with the neutral acceptor impurities through a negligibly small Coulomb force (namely $R \longrightarrow 0$ and $\gamma = \hbar\omega_c/R_{eff} >> 1$). Therefore, their energy dependence on B is given by $e\hbar B/(2m_e)$, namely, by that of the first CB Landau level [190]. $\Delta E_A(B)$ can be neglected due to the deep character of the acceptor levels (i.e., binding energy $\sim 40\,meV$). As an example, $\Delta E_A(B = 19\,T) = 0.075\,meV$ for carbon acceptors in GaAs [191], because the infinite effective- mass of the impurity levels results into a dispersion-less character in k-space [192, 193]. Therefore, eq 3.6 directly gives the effective mass of free electrons. The electron motion along different directions can be addressed by applying the magnetic field perpendicular or parallel to the $\hat{c}$ axis.

The Zeeman splitting of (e, A^0) is ruled by both the electron g-factor and the impurity-related hole g-factor. In ZB GaAs, the Zeeman splitting of (e, C^0) results in four split states [191]. Two states are due to the heavy-hole character, the other two states to the light-hole character of the carbon levels. Indeed, in ZB crystals heavy and light holes are degenerate at the Γ point. The Zeeman splitting depends on the involved hole character:

$$\Delta E^{\pm}(B) = E(\sigma^+) - E(\sigma^-) = \begin{cases} (-g_e + 3g_{hh,A})\mu_B B & \text{for heavy holes;} \\ (g_e + g_{lh,A})\mu_B B & \text{for light holes.} \end{cases} \tag{3.7}$$

Here $g_{hh,A}$ is the g-factor related to the carbon levels with total angular momentum $J = 3/2$, whereas $g_{lh,A}$ is related to the carbon levels with total angular momentum $J = 1/2$. The splitting into heavy- and light-hole valence-band states is great in InP WZ crystals (of the order of $40\,meV$). Therefore, only the valence band levels related to the heavy holes rule the Zeeman splitting in the (e, A^0) transition.

3.1.3 Neutral-donor to neutral-acceptor transition

At zero magnetic field, the energy of the neutral-donor to neutral-acceptor recombination is given by:

$$E_{(D^0,A^0)} = E_D - E_A + \frac{e^2}{4\pi\epsilon r_{D,A}}, \tag{3.8}$$

where E_D is the energy of the donor level, ϵ is the material absolute dielectric constant, $r_{D,A}(B)$ is an effective, average distance of donor-acceptor pairs for which the transition probability is maximum, and the energy zero is set at the top of the valence band. The field dependence on magnetic field of the (D^0, A^0) transition energy, averaged over spin-split levels, is given by:

$$E_{(D^0,A^0)}(B) = E_B(B = 0) - E_A(B = 0) + \Delta E_D(B) - \Delta E_A(B) + \frac{e^2}{4\pi\epsilon r_{D,A}(B)}, \tag{3.9}$$

where $\Delta E_D(B)$, the shift of the donor level energy with B, can be evaluated by numerical methods [194, 195]. Its estimated values are sizably greater than zero because of the shallow character of the donor states (i.e., binding energy $\sim 5\,meV$), in contrast with the $\Delta E_A(B)$ case [194]. $r_{D,A}(B)$ is an effective average-distance of the donor-acceptor pairs that depends on B via the hole effective-mass. For increasing B, the orbit of the impurity-localized carriers, which depends on the hole effective mass, shrinks thus favoring the weight of less distant pairs in $r_{D,A}(B)$ [196]. However, a quantitative estimate of this effect (and, thus, of m_h) requires an exact knowledge of the impurity densities as well as of the dependence of $r_{D,A}$ on B [196]. Although these stringent requirements impede a reliable determination of the hole effective mass via eq 3.9, a discrimination between (e, A^0) and (D, A^0) transitions can be made. A linear diamagnetic shift is expected, indeed, for the free-electron to neutral-acceptor transition, whereas a quadratic-like diamagnetic shift is expected for the neutral-donor to neutral-acceptor transition because of the non-null Coulomb interaction between donor-acceptor pairs. The same considerations developed in the previous section hold for the Zeeman splitting states, provided g_e is substituted by g_d.

3.2 Values of the electron and hole effective-masses

Magneto-PL spectroscopy is still a scarcely employed technique to address the electronic properties of semiconductor NWs. To the best of our knowledge, magneto-PL has been used in: GaAs/AlAs core-shell NWs, to reveal the nature of excitons and high-density p-type modulation doping in a single wire [197, 198]; WZ GaN, to study the exciton fine structure [199]; Mn-doped II-VI NWs, to study the $sp-d$ coupling induced by Mn atoms [200, 201, 202]. Only in InGaAs NWs [55] and WZ/ZB quantum disks in GaAs NWs [203], magneto-PL was used to measure the carrier effective-mass. Those mass values are essential for the design of NW-based devices strongly dependent on carrier mobility, such those aimed at photovoltaic or thermoelectric applications. In particular, the knowledge of carrier-mass anisotropy with respect to crystallographic directions is quite relevant for the engineering of NW-based devices. Finally, the energy diagram of novel, interesting one-dimensional homo-structures depends not only on E_{gap} but also on the electron and hole effective-mass [204] whenever the lattice structure varies along the NW growth-axis [205, 206].

In the previous section and in the appendix A.1, we have shown the suitability of magneto-PL to determine the carrier effective-masses. To date, only one work has reported the exciton reduced-mass in WZ InP, while no one has measured separately the electron and hole effective-mass. We will now present a review of theoretical predictions of carrier effective-mass in WZ InP, together with our experimental results [134].

3.2.1 Theoretical predictions

Carrier effective-masses in WZ-InP have been calculated in references [42, 44, 45, 47, 132, 204]. The estimated values are summarized in the first four rows of table 3.1. In the first four rows, the calculated effective-masses of electrons (Γ_{7e}) and holes (Γ_{9h}) are reported in units of the free-electron mass m_0. $m^{\parallel}$ and $m^{\perp}$ indicate,

InP WZ	[204]		[42]	[47]	[132]	[44]	[45]
$m(\Gamma_{7e}^{\perp})$	0.073(LDA)	0.065 (EP)	0.088	0.09		0.15	0.118
$m(\Gamma_{7e}^{\parallel})$	0.064	0.058	0.105	0.092		0.09	0.095
$m(\Gamma_{9h}^{\perp})$	0.14	0.13	0.158	0.148	0.1	0.19	0.209
$m(\Gamma_{9h}^{\parallel})$	1.25	0.97	1.273	1.06	1.1	0.13	1.065
$\mu_{exc}^{\perp}$	0.048	0.043	0.057	0.057		0.084	0.075
$\mu_{exc}^{\parallel}$	0.061	0.055	0.097	0.097		0.053	0.087
$\Delta m_{e}^{\perp,\parallel}$	1.14	1.12	0.84	0.98		1.67	1.24
$\Delta m_{h}^{\perp,\parallel}$	0.112	0.134	0.124	0.140	0.091	1.46	0.196

Table 3.1. Rows 1-4: Carrier effective-masses (in unit of the free-electron mass) as theoretically calculated for the Γ_{7V} electron- and Γ_{9V} hole-state. Different approaches have been used: transferable empirical-pseudopotentials, EP (ref. [42, 204]); density functional theory, DFT, within the local density approximation, LDA (ref. [44, 204]); $k \cdot p$ approach within DFT (ref. [45]); extended-basis tight-binding ([47]); full-potential linearized-augmented plane-wave method plus LDA (ref. [132]). Rows 5-6: Calculated values of the exciton reduced-mass parallel and perpendicular to the $\hat{c}$ axis. Rows 7-8: Anisotropy degree with respect to the WZ $\hat{c}$-axis of the electron and hole effective-masses, $\Delta m_{e,h}^{\perp,\parallel} = m_{e,h}^{\perp}/m_{e,h}^{\parallel}$, as estimated from rows 1-4.

respectively, the masses corresponding to the carrier motion in a direction parallel or perpendicular to the WZ $\hat{c}$-axis. In rows $5-6$, the exciton reduced-masses parallel and perpendicular to the $\hat{c}$ axis are calculated by applying Eq. A.3 to the corresponding electron and hole masses. In rows $7-8$, the anisotropy degrees of the electron and hole effective-masses ($\Delta m_{e,h}^{\perp,\parallel} = m_{e,h}^{\perp}/m_{e,h}^{\parallel}$), as measured with respect to the WZ $\hat{c}$-axis, are reported.

Although the calculated values are quite scattered, likely because of the different theoretical approaches used, some common trends are found. As far as the anisotropy between different crystallographic directions is concerned, a general agreement is found between the values calculated for electron and holes by different models, with the exception of refs. [44] and [45] (see the last two raws of table 3.1). However, EP calculations performed in ref. [204] and [42] predict opposite anisotropies for the electron effective-mass (see seventh row of table), while tight-binding calculations give a nearly isotropic electron effective-mass [47]. Moreover, LDA results in ref. [44] give $m_e^{\perp} > m_e^{\parallel}$, in accordance with EP and LDA results in ref. [204] and $k \cdot p$ results in ref. [45], but with an anisotropy degree much greater than those evaluated there.

3.2.2 Experimental results

Magneto-PL measurements have been performed on WZ NWs grown by SAE, whose excellent crystal quality has been demonstrated in section 2.2 and typical PL spectra have been shown in section 2.3.1. Therein, all the observed recombination bands have been ascribed to optical transitions whose magnetic-field dependence has been described in section 3.1.1. It should be pointed out that a good structural and

optical quality of the samples and a uniform NW orientation are required to achieve well-defined Faraday- and Voigt-geometries in magneto-PL measurements.

The number of NWs probed in each magneto-PL spectrum is about 100, as estimated from the NW-array density and the laser spot-size. Measurements were carried out at two temperatures, $T = 4.2$ and $77\,K$, in order to highlight the dependence on B of different spectral components. In both Faraday and Voigt configurations, the PL collection and laser directions were antiparallel to each other and both directed along the NW growth-axis (corresponding to the WZ $\hat{c}$-axis). In these experimental configurations, PL can be resolved by measurements in circular polarization only in the Faraday configuration ($\vec{B}\|\vec{k}\|\hat{c}$). The circular polarization of emitted light was analyzed by using a liquid-crystal variable-retarder followed by a linear polarizer with fixed axis, in order to make all measurements insensitive to the polarization response of the optical setup. The results obtained on $d = 650\,nm$ NWs will be shown. Those results, which are very similar to those found in other NWs with different diameters and excitation power density, are independent of the investigated region of the NW ensemble [134].

The $(D^0, C^0)/(e, C^0)$ energy region of PL spectra taken at $B = 0$ and $29\,T$ on WZ NWs grown by SAE with $d = 650\,nm$ is shown in figure 3.2.a). Measurements were performed at $T = 4.2\,K$ with $\vec{B}$ parallel to the emitted light wave-vector and to $\hat{c}$ (Faraday configuration). Only σ^+ polarization is shown for the sake of clarity. Circular-polarization luminescence filtering highlights a clear Zeeman splitting, to be discussed in section 3.3. Only the diamagnetic-shift results will be discussed now, although the Zeeman splitting will be duly taken into account in the data analysis and interpretation. At $B = 0\,T$, where the (D^0, C^0) intensity overwhelms the (e, C^0) intensity, the two bands are not distinguishable as explained in section 2.3.1. However, a diamagnetic shift of the (e, C^0) band greater than that of the (D^0, C^0) allowed us to disentangle the contributions of these two bands, as shown in the $29\,T$ spectrum.

The detailed magnetic-field dependence of the two bands shows up clearly from the second derivative of the magneto-PL spectra, as shown in fig. 3.2.b). The differential spectra highlight spectral features, such as shoulders, whose exact energy can be hardly determined from a direct inspection of the PL spectra [197]. Two different trends with magnetic field are observed: the (e, C^0) energy shifts linearly with magnetic fields, while the (D^0, C^0) energy follows a quadratic-like dependence, in particular at low fields ($B < 15\,T$, see circles). Moreover, the energy shift of the (D^0, C^0) band between 0 and $29\,T$ is smaller ($11.9\,meV$) than that of the (e, C^0) band ($18.5\,meV$). Both results are due to an extent of the Coulomb interaction between the donor-acceptor pairs dynamics much greater in the (D^0, C^0) than in the (e, C^0) transition, consistently with eqs. 3.9 and 3.6 and previous findings [207]. The (e, C^0) data are reproduced by eq. 3.6 [solid line in panel b)], where the Zeeman-splitting effect has been also taken into account. By imposing $\Delta E_A(B) = 0$, one obtains $m_e^{\perp} = 0.091\,m_0$, which is the first direct determination of the electron effective-mass of WZ InP. Since this value is related to the carrier motion in a plane perpendicular to the $\hat{c}$ axis, this mass is indicated as $m_e^{\perp}$.

The $B = 0$ and $29\,T$ spectra in the FE energy-region are shown in fig. 3.2.c). At $B = 0\,T$, the FE resonance exhibits a splitting into an upper (U) and a lower (L) component that originates from an exciton scattering with donors, as explained in the

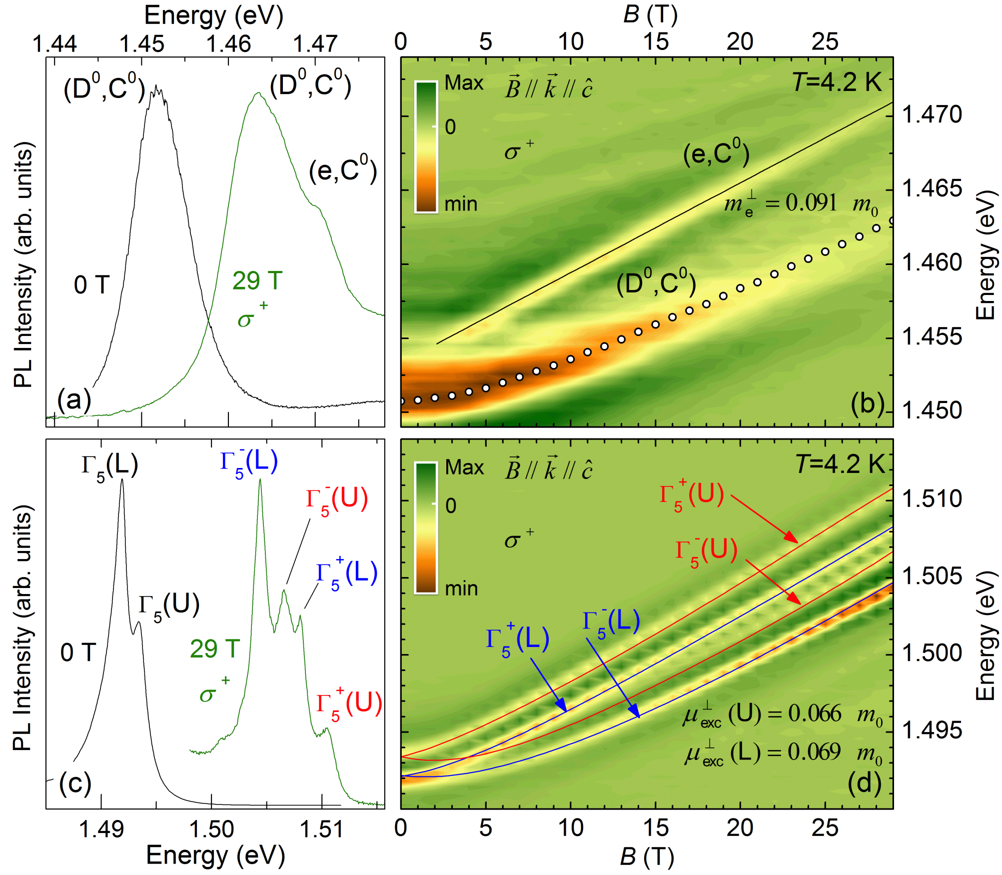

Figure 3.2. a) $T = 4.2\,K$ PL-spectra of the counterclockwise (σ_+) circularly-polarized light emitted in the Faraday configuration ($B=0$ and $29\,T$) by $650\,nm$-diameter InP-NWs grown by SAE. Only the energy region of the (D^0, C^0) and (e, C^0) transitions is displayed. The (e, C^0) appears for $B = 29\,T$ as a shoulder on the high-energy side of the PL spectrum. b) Contour plot of the second derivative of the PL spectra taken from 0 to $29\,T$ in the same energy-region of (a). The color scale represents the magnitude of the second derivative. Symbols indicate the peak energy of the (D^0, C^0) band. The solid line is a fit of eq. 3.6 to the (e, C^0) data from which the electron effective-mass $m_e^\perp$ has been determined. c) Same as (a) but in the FE energy-region. The various exciton components are indicated with the pertinent group symmetry ($\Gamma_5^\pm$) of magneto-excitons in WZ. + and − symbols indicate the Zeeman split components. d) Same as (b) but in the FE energy-region. Arrows point to different FE components. The solid lines are fits of eq. 3.3 to the data (the exciton reduced-mass values $\mu_{exc}^\perp$ derived from the fits are reported). After ref. [134]

discussion of fig. 2.7. Each of those components undergoes a Zeeman splitting under the applied magnetic-field, as clearly appears at $B = 29\,T$. Those components are labeled $\Gamma_5^\pm(U/L)$ as for the WZ-crystal terminology introduced in section 3.1.1. The " + " and " − " superscripts refer, respectively, to components with counterclockwise, σ_+, and clockwise, σ_-, circular polarizations. The magnetic-field dependence of those states can be better understood in fig. 3.2.d) where the second-derivative spectrum is shown as a function of B. In particular, $\Gamma_5^+(L)$ and $\Gamma_5^-(U)$ cross one another at $B \sim 5\,T$, where a careful line-shape analysis was required to extrapolate

the field dependence of the energy of these two components (a similar crossing was reported in bulk WZ GaN) [184]. The solid lines give the best fits of eq. 3.3 to the diamagnetic shift of each exciton state [1]. The obtained values of the exciton reduced-masses are reported in the same fig. 3.2.d). In the Faraday configuration ($\vec{B}\|\hat{c}$), the involved carrier moves in a plane perpendicular to the WZ lattice $\hat{c}$-axis ($\mu_{exc}^{\perp}$). The value of the carrier effective-mass for a motion in a plane containing the $\hat{c}$-axis can be determined, instead, by steering $\vec{B}$ perpendicular to the NW growth-axis, as shown in figure 3.3.

The $B = 0$ and $29\,T$, $T = 4.2\,K$ PL-spectra of the light emitted in the Voigt configuration ($\vec{B} \perp \vec{k}\|\hat{c}$) are shown in the impurity energy-range in figure 3.3.a). The array of $650\,nm$-diameter InP-NWs is the same discussed in fig. 3.2. The spectra are dominated by the (D^0, C^0) recombination, while the (e, C^0) transition is barely observed as a shoulder in the $29\,T$ spectrum. In the Voigt configuration, circular polarization filtering did not affect the PL spectra, as expected and discussed previously. The differential magneto-PL spectra are displayed in fig. 3.3.b). The peak energy of the (D^0, C^0) transition, which dominates at all fields, shows a quadratic-like behavior typical of Coulomb-correlated electron-hole pairs; see symbols superimposed on the (D, C^0) transition. The dominant spectral weight of the (D, C^0) band impedes an unambiguous fitting of eq. 3.6 to the peak energy of the (e, C^0) transition, which is also observed and indicated in the figure. Hence, a precise determination of $m_e^{\perp,\|}$, namely, of the mass of electrons moving in planes containing the $\hat{c}$ axis, was not possible. However, it is possible to recognize that the linear diamagnetic shift of the (e, C^0) band is greater than that of the (D^0, C^0) band. The line superimposed on the (e, C^0) band is plotted according to eq. 3.6 with an electron effective-mass $m_e^{\perp,\|}$ equal to that derived from magneto measurements performed in the same Voigt configuration at $T = 77\,K$, where only the (e, C^0) band is present (to be discussed in the following).

Let now consider the FE spectral-region. The FE PL-spectra at $B = 0$ and $29\,T$ are compared in fig. 3.3.c). At high fields, four different lines appear clearly. The attribution of the BE line to a bound exciton will be discussed in the following. The other three lines are due to different free-exciton components, whose evolution with magnetic field is shown by the contour plot of the differential spectra in fig. 3.3.d), where the attribution of these lines is also reported. In the Voigt configuration, the U and L exciton components blue-shift and split, but no intensity and line-shape dependence on light circular-polarization is observed, consistently with the Voigt configuration. The solid lines are fits of eq. 3.4 to the peak energy of the $\Gamma_{5/6}^{-}(L)$ and $\Gamma_{5/6}^{-}(U)$ states, which are the only ones observed at all magnetic fields. The obtained mass values are reported in panel d). $\mu_{exc}^{\perp,\|}$ is the exciton reduced-mass as obtained from electron- and hole-masses given by the cyclotron effective-mass tensor[2] [209]:

$$m_{e,h}^{\perp,\|} = \sqrt{m_{e,h}^{\perp} \times m_{e,h}^{\|}} \quad \text{and} \quad \mu_{exc}^{\perp,\|} = \left[\frac{1}{m_e^{\perp,\|}} + \frac{1}{m_h^{\perp,\|}}\right]^{-1}. \tag{3.10}$$

[1]In the fitting procedure, we set the values of the dielectric constant measured in InP ZB at $T = 5\,K$, $\epsilon_r = 11.76$ [208], in both the Faraday and Voigt configuration.

[2]We have assumed an isotropic carrier effective-mass in the plane orthogonal to $\hat{c}$.

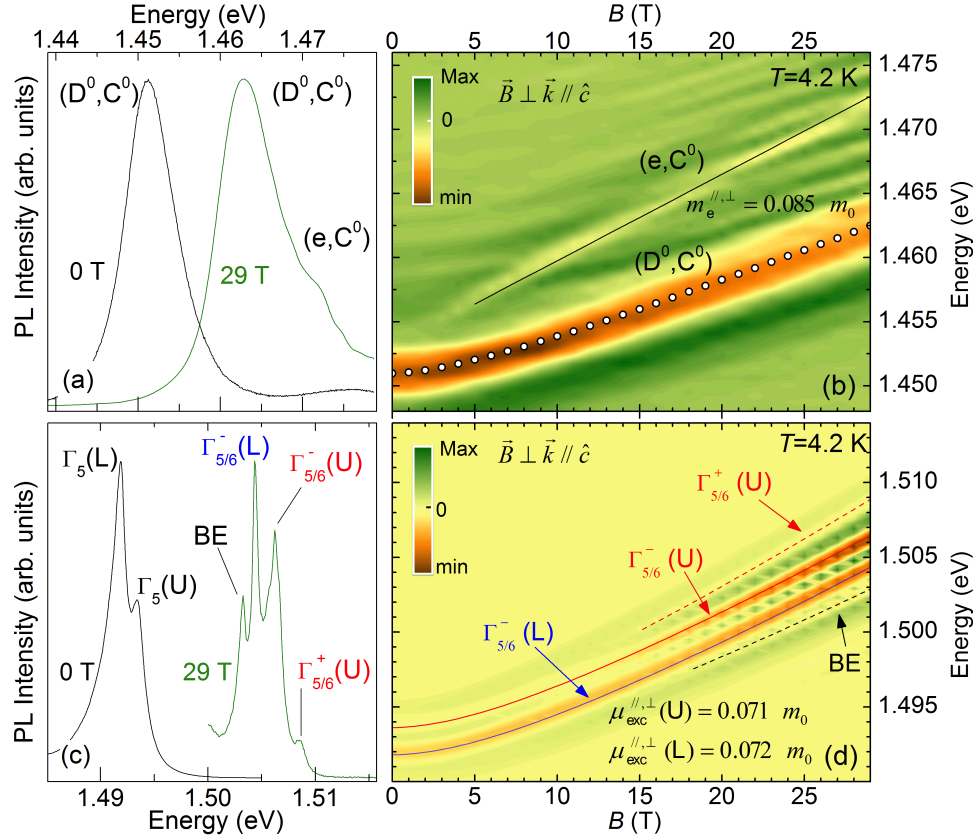

Figure 3.3. a) $T = 4.2\,K$ PL-spectra of the light emitted in the Voigt configuration (B=0 and $29\,T$) by $650\,nm$-diameter InP-NWs grown by SAE. Only the energy region of the (D^0, C^0) and (e, C^0) transitions is displayed. The (e, C^0) appears for $B = 29\,T$ as a shoulder on the high-energy side of the PL spectrum. b) Contour plot of the second derivative of the PL spectra taken from 0 to $29\,T$ in the same energy-region of (a). The color scale represents the magnitude of the second derivative. Symbols indicate the peak energy of the (D^0, C^0) band. The solid line is superimposed on the (e, C^0) band according to eq 3.6 with an electron effective-mass $m_e^{\perp,\parallel}$ equal to that derived in the following. c) Same as (a) but in the FE energy-region. The various exciton components are indicated with the pertinent group-symmetry ($\Gamma^{\pm}_{5/6}$) of magneto-excitons in WZ. + and − symbols indicate magnetic-field split-components. BE indicates a bound-exciton transition. d) Same as (b) but in the FE energy-region. Arrows point to different FE components. The solid lines are fits of eq. 3.4 to the data (the exciton reduced-mass values $\mu^{\perp}_{exc}$ derived from the fits are reported). Dashed lines highlight the spectral contribution from BE and $\Gamma^+_{5/6}(U)$ states, which are observed only for $B > 15\,T$. After ref. [134]

The BE attribution is validated by the comparison of the B-induced energy-shift of the free-exciton states with that of the BE transition. In the $B = 15 \div 29\,T$ interval, the average rate of energy shift is equal to $r = 0.48$, 0.52, and $0.54\,meV/T$ for the BE, $\Gamma_{5/6}(L)$, and $\Gamma_{5/6}(U)$ excitons, in the order. The r value for the BE transition points to a localization degree of the involved electron-hole pair greater than that of the exciton states as a direct consequence of the large Coulomb interaction caused by the impurity at which the exciton is bound to. The present results agree with

growth technique	$\mu_\perp$	$\mu_{\perp,\parallel}$
VLS [58]	0.068	0.072
SAE (this thesis)	0.069 (L)	0.072 (L)
	0.067 (U)	0.071 (U)

Table 3.2. Values of the exciton reduced-mass (in units of m_0) determined under different field-configurations and in different types of InP NWs. The mass uncertainty is equal to $0.001\,m_0$. $\mu_\perp$ and $\mu_{\perp,\parallel}$ were measured in the Faraday and Voigt configuration, respectively.

those previously found in GaAs, where bound excitons showed a diamagnetic shift smaller than that of the FE [210].

The FE reduced masses in Voigt and Faraday configurations have already been measured in WZ InP-NWs grown by VLS [58], see first row of table 3.2. In those measurements, the U and L components could not be resolved because magneto-PL was performed at $77\,K$. Table 3.2 reports also the values of the exciton reduced-mass derived by an average over various measurements performed on NW arrays with different diameters (last two rows). An excellent agreement is found between the two sets of data, which supports the general validity of our results and their independence of the NW morphology and/or size. We point out that the heavier character of the L component with respect to that of the U component is likely due to the different k-dispersion of the two energy branches around the Γ critical point [145, 146, 147].

Summarizing, at low T the *exciton reduced-mass* of WZ InP-NWs grown by SAE has been determined in a plane containing the WZ $\hat{c}$ axis and in a plane perpendicular to it. Instead, only the free *electron-mass* perpendicular to the WZ $\hat{c}$-axis has been determined. Therefore, magneto-PL experiments at high temperature have been performed in order to fully disentangle the electron and hole masses as well as the mass values along different crystallographic directions. Indeed, at $77\,K$ the (D^0, C^0) band is fully ionized because of the small binding energy of donors ($\sim 5meV$) and only the (e, C^0) recombination is observed.

The magnetic-field evolution of the (e, C^0) band at $T = 77\,K$ under Faraday and Voigt configurations is displayed in figure 3.4.a) and 3.4.b), respectively. In the Faraday geometry, the (e, C^0) band blue-shifts and splits with increasing B. A similar shift is observed, but no line splitting is found, in the Voigt configuration under $\sigma_\pm$ filtering, consistently with the WZ hexagonal-symmetry. The diamagnetic shift of the (e, C^0) band in the Faraday configuration is shown in fig. 3.4.c). For $B < 7\,T$, the recombination energy does not change, while it increases linearly for $B \geq 7\,T$. The absence of a diamagnetic shift below a critical field is due to scattering mechanisms that prevent the closure of the cyclotron orbit and the establishment of the corresponding Landau level [211]. The slope of the spin-averaged energy of the (e, C^0) transition is $\beta = (e\hbar/2m_e^\perp) = 0.627\,meV/T$. The same quantity displayed in panel c) is shown for the Voigt configuration (where no spin-averaging was necessary) in fig. 3.4.d). In this case also, no sizable diamagnetic shift is observed for $B < 7\,T$, while a linear dependence of the (e, C^0) peak energy on B is found at higher fields, with a slope $\beta = (e\hbar/2m_e^{\perp,\parallel}) = 0.683\,meV/T$. By following eq. 3.6, we find directly

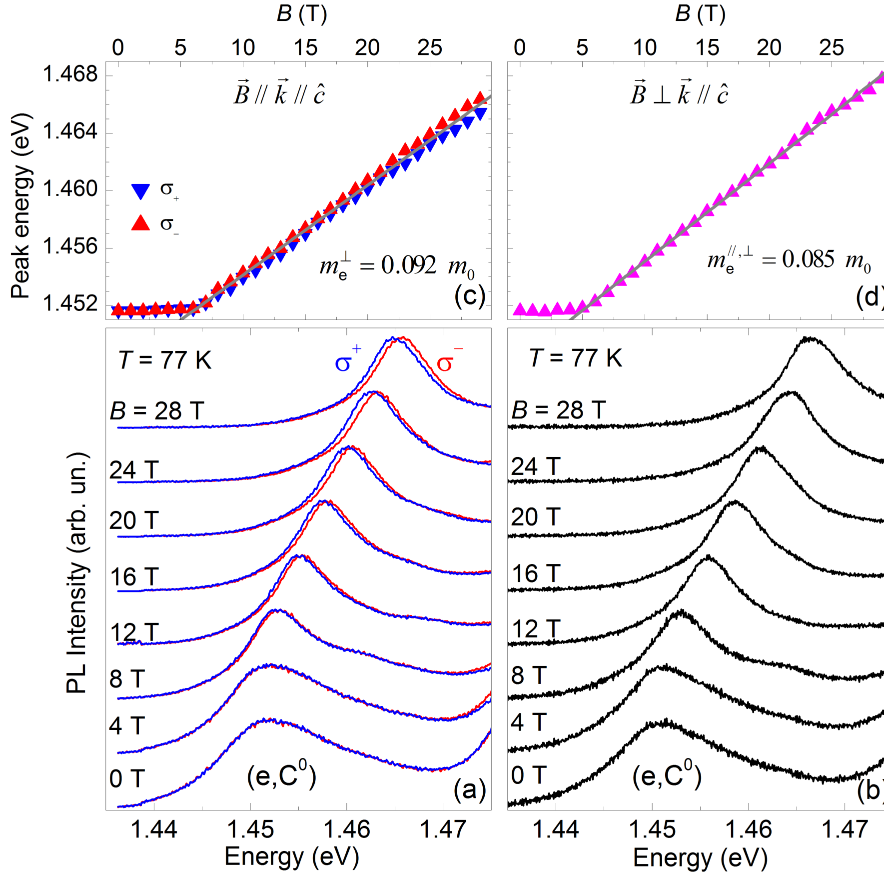

Figure 3.4. a) (e, C^0) recombination spectral-region of $T = 77\,K$ PL-spectra taken on InP NWs ($650\,nm$ diameter) grown by SAE under magnetic fields in the Faraday configuration. Blue and red lines refer to counterclockwise (σ_+) and clockwise (σ_-) circular polarization, respectively. b) The same as (a) but for the Voigt configuration, where PL is insensitive to circular-polarization filtering. c) Peak energy of the (e, C^0) band as a function of B in the Faraday configuration. Different symbols correspond to different circular polarizations, as detailed in the legend. The gray line is a fit of the first Landau level in eq. 3.6 to the Zeeman-split averaged data. The value of the electron effective-mass is indicated. d) Peak energy of the (e, C^0) band as a function of B in the Voigt configuration. The gray line is a fit of the first Landau level in eq. 3.6 to the data. The value of the electron effective-mass is indicated. After ref. [134]

$m_e^\perp = 0.092\,m_0$ and $m_e^{\perp,\parallel} = 0.085\,m_0$. It should be noticed that the value of $m_e^\perp$ found at $T = 77\,K$ is very similar to that derived at $T = 4.2\,K$. Likewise, also the exciton reduced-mass values derived at $77\,K$ are equal to those found at $4.2\,K$ (not shown here).

Analogous results have been obtained in the case of 310- and $125 - nm$ diameter NWs. By averaging over magneto-PL results obtained on arrays with different NW-diameters, the following values have been determined: $m_e^\perp = (0.093 \pm 0.001)\,m_0$, or$m_e^{\perp,\parallel} = (0.085 \pm 0.001)\,m_0$, $\mu_e^\perp = (0.068 \pm 0.001)\,m_0$, and $\mu_e^{\perp,\parallel} = (0.072 \pm 0.001)\,m_0$. Our aim is to evaluate now the hole effective-mass and decouple the electron/hole motion along the NW $\hat{c}$-axis from the carrier-motion perpendicular to the $\hat{c}$ axis.

Equation 3.10 applied to electrons easily provides $m_e^{\parallel} = (0.078 \pm 0.002)\, m_0$. In addition, $\mu_e^{\perp} = (1/m_e^{\perp} + 1/m_h^{\perp})^{-1}$ and $m_h^{\perp} = (0.250 \pm 0.016) m_0$ is found. Then, it is possible to calculate $m_h^{\perp,\parallel}$ from $\mu_e^{\perp,\parallel} = (1/m_e^{\perp,\parallel} + 1/m_h^{\perp,\parallel})^{-1}$. By applying eq. 3.10 one finally obtains $m_h^{\parallel} = (0.81 \pm 0.18)\, m_0$.

The electron and hole effective-masses (shadowed black-dots, with errors) parallel and perpendicular to the the $\hat{c}$ axis are shown in figure 3.5.a) and 3.5.b), respectively, together with the electron and hole masses in ZB InP (gray full-squares) [212]. The electron effective-mass is slightly anisotropic, with $m_e^{\parallel}$ about 20% lighter than $m_e^{\perp}$. A very different behaviour is found for the holes, whose effective-mass parallel to the $\hat{c}$-axis is more than a factor of 3 heavier than that perpendicular to this same axis. By averaging over the different directions, the carrier effective-masses in WZ InP-NWs are greater than those in ZB bulk-crystals and in good agreement with those theoretically evaluated in ref. [45, 204]; see table 3.1. A comparison between the carrier effective-masses experimentally determined in WZ InP-NWs and in other WZ compounds is also shown in figs. 3.5.a) and 3.5.b). For holes, only data for WZ GaN were found [213, 214]. For electrons, a more comprehensive comparison is shown in panel a), where data for GaN [213, 214], InN [215], and ZnO [216, 217] are displayed. Quite interestingly, a rather similar anisotropy degree, defined as $\alpha_{e,h} = m_{e,h}^{\parallel}/m_{e,h}^{\perp}$, is found in the experimental data. This fact points to a common trend, whereby the influence on the transport properties of the crystallographic characteristics is maintained in WZ crystals regardless of the material composition.

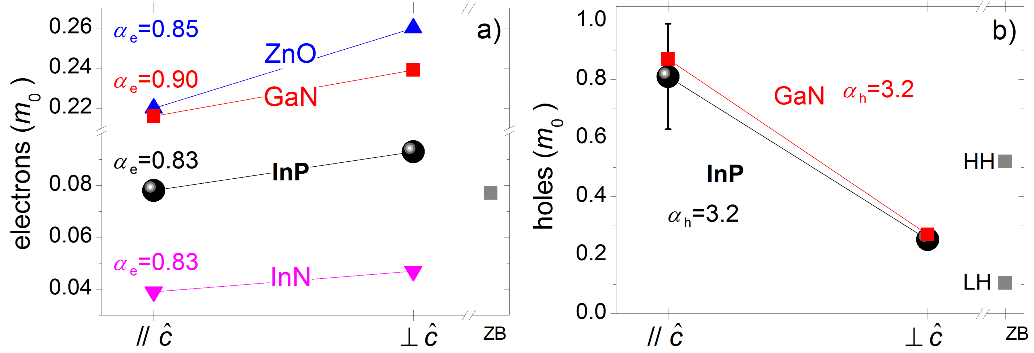

Figure 3.5. Comparison of the electron (a) and hole (b) effective-masses, as determined in this thesis (shadowed dots, with errors), with those reported in the literature for different WZ crystals. Carrier masses for parallel and perpendicular motion with respect to the WZ $\hat{c}$-axis are shown. $\alpha = m^{\parallel}/m^{\perp}$ is a measure of the carrier mass-anisotropy. The full, gray squares refer to ZB InP-bulk [212], with HH and LH labeling heavy and light holes, respectively. After ref. [134]

The above reported findings prompt valuable information on the properties of WZ NWs. Indeed, the effective mass of electrons and holes is a key parameter in the performance of devices based on charge transport, as well as in the optoelectronic properties of nano- and quantum-heterostructures. In fact, the oscillator strength and polarization degree of radiative transitions are determined by the wave-function overlap and confinement of oppositely-charged carriers, features strongly related to m [206, 218]. For instance, it has been predicted that in mixed crystal-phase

NW-superlattices, a type-II alignment between WZ and ZB can be turned into a type-I alignment depending on the NW diameter and on the hole effective-mass value [204]. The values of m_e and m_h and their dependence on the motion direction represent, finally, a stringent benchmark for theoretical models.

3.3 Carrier *g*-factors

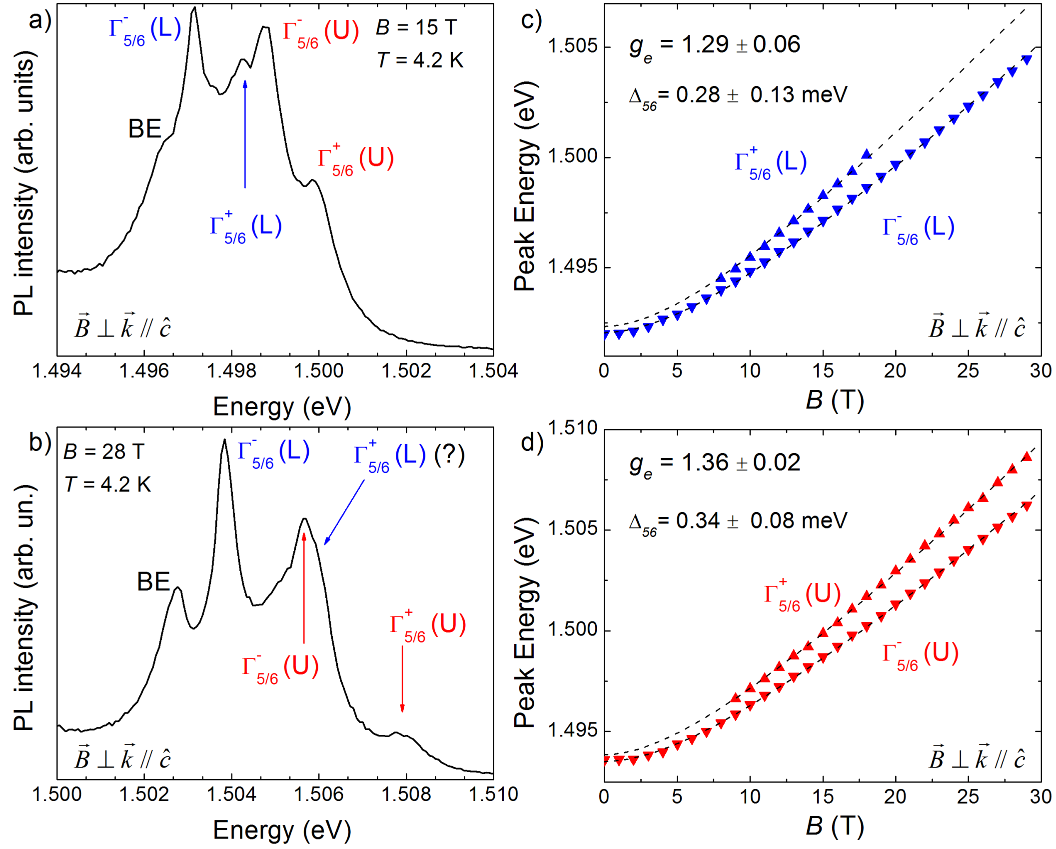

Figure 3.6. a) $T = 4.2\,K$ PL-spectra of the light emitted in the Voigt configuration ($B = 15\,T$) by $650\,nm$-diameter InP-NWs grown by SAE. The BE recombination and the various exciton components with the relative group-symmetry notation are indicated. b) Same as a) but with $B = 28\,T$. The $\Gamma^+_{5/6}(L)$ exciton-component barely appears. (c) and (d) Free-exciton energy as a function of B in the Voigt configuration for the lower and upper exciton-components, respectively. The dashed lines are fits to the Zeeman-split states of each exciton component according to the theory developed in section 3.1.1. The electron g-factors (g_e) and the energy separations Δ_{56} between Γ_5 and Γ_6 obtained by these quantitative fits are given in the figure.

The FE energy-region of a $T = 4.2\,K$ PL spectrum taken in the Voigt configuration ($B = 15\,T$) on a $d = 650\,nm$ NW-array grown by SAE is shown in figure 3.6.a). The various exciton components, each one indicated by its group symmetry notation, show up. A bound-exciton recombination is also observed, as already discussed in fig. 3.3. The PL spectrum from the same sample under the same experimental

conditions but with $B = 28\,T$ is shown in fig. 3.6.b). All the exciton components show up except for the $\Gamma^+_{5/6}(L)$ exciton-component, which is only suggested by a very weak shoulder on the high energy-side of the $\Gamma^-_{5/6}(U)$ transition. The diamagnetic shifts of the $\Gamma^{+/-}_{5/6}(L)$ states are shown as a function of B by blue up and down triangles, respectively, in fig. 3.6.c). The peak energies of $\Gamma^-_{5/6}(L)$ can be identified at all magnetic fields, while the same does not apply to the $\Gamma^+_{5/6}(L)$ peak-energies. Accordingly, the diamagnetic shift of $\Gamma^+_{5/6}(L)$ is shown only for $B = 8 \div 18\,T$, where peak energies are clearly identified. Dashed black-lines are fits of eq. 3.4 to the data, with fit parameters given by the exciton reduced-mass, the electron g-factor, and the energy separation Δ_{56} between Γ_5 and Γ_6 states. Both sets of data have been simultaneously fitted after having summed or subtracted the corresponding Zeeman-splitting term ($\pm\frac{1}{2}[\Delta^2_{56} + g^2_{e,\perp}\mu^2_B B^2]^{\frac{1}{2}}$) in eq. 3.4. The fitted electron g-factor and Δ_{56} are reported in the figure, not the exciton reduced-mass that has been already discussed in the previous section. Figure 3.6.d) shows the same as fig. 3.6.c) but for the exciton upper component, whose two split-states are shown as red up and down triangles. In this case, the energy of $\Gamma^+_{5/6}(U)$ has been detected in a range of magnetic fields ($B = 9 \div 29\,T$) wider than in the case of $\Gamma^+_{5/6}(L)$. Here also, the data of the two exciton components have been fitted all together leading to the values of electron g-factor and Δ_{56} given in the panel.

The values of g_e and Δ_{56} obtained by the two exciton components agree very well each other within the experimental errors. It should be stressed that the exciton g-factor in the Voigt configuration depends only on the electron g-factor: $g_h = g_{h,\|}\cos(\theta)$, where $g_{h,\|}$ is the component of g_h parallel to the field and θ is the angle between B and the WZ $\hat{c}$-axis [184, 219], hence, g_h is null when $\vec{B} \perp \hat{c}$. Conversely, g_e does not depend on $\cos(\theta)$[3]. An average over four different measurements (not shown), different excitation powers, and different NW diameters results in $g_e = 1.31 \pm 0.05$ and $\Delta_{56} = 0.35 \pm 0.10\,meV$. The electron g-factor agrees well with a previous experimental work [58] (where Δ_{56} could not be determined because of a lack of experimental data at low fields). Therefore, this is the first determination of the energy separation between the Γ_5 and Γ_6 exciton states in InP WZ. The obtained value is of the same order of magnitude of those found in other WZ bulk-compounds ($0.12\,meV$ in GaN [184] and $0.20\,meV$ in CdS [185]).

To the best of our knowledge, a theoretical estimate of the carrier g-factor in InP WZ has never been published. A collaboration has been established, therefore, between our group and Dr. Paulo Eduardo de Faria Junior, whose theoretical estimates of WZ-InP critical-point energies (last row in table 2.1) and carrier effective-masses and ensuing anisotropies (last column in table 3.1) agree well with our experimental results. Therefore, that theoretical method, which exploits *ab-inito* and $k \cdot p$ approaches and includes the spin-orbit coupling ref. [45], should valuably address the spin properties of WZ InP. Table 3.3 reports the calculated values of the carrier gyromagnetic-factor under different field configurations with respect to

[3]We point out that this scenario holds only in the case of NWs that approach WZ *bulk-crystals*, as in the present case. It changes completely, instead, in *fully one-dimensional* WZ nanocrystals, where the strong exchange interaction "binds" electron and hole spin-projections and impedes to consider g_h and g_e separately. In that case, the Zeeman splitting is ruled by an effective g_{exc} given by $ZS = m_S(g_{exc,\|}\cos\theta)\mu_B B$, which is null when $\vec{B} \perp \hat{c}$ (even if $g_{exc,\|} \neq 0$) [220].

Carrier	Voigt	Faraday
electron	1.29	1.61
hole	0.00	−3.05

Table 3.3. Theoretically calculated values of carrier gyromagnetic-factor determined under different field configurations with respect to the WZ $\hat{c}$-axis. The values have been calculated in the $k \cdot p$ approach including the spin-orbit coupling in the basis set of the diagonalized Hamiltonian. Courtesy of Dr. Paulo Eduardo de Faria Junior.

the WZ $\hat{c}$-axis. The agreement between experimental (1.31 ± 0.05) and theoretical (1.29) *absolute* values of g_e (the sign of g_e cannot be experimentally determined) is excellent.

Let now discuss the carrier g-factor in the Faraday configuration where the two Zeeman-split states can be well resolved by selecting the appropriate circular polarization. Figure 3.7.a) shows the FE energy-region of $T = 4.2\,K$ PL-spectra taken in the Faraday configuration ($B = 12\,T$) on a $d = 650\,nm$ NW-array grown by SAE. Black and cyan lines refer to σ^- and σ^+ circular polarization, respectively. Therein, the various exciton-components are indicated by their group-symmetry notation. Photoluminescence spectra from the same sample shown in fig. 3.7.a), with the same experimental conditions but with $B = 28\,T$, are shown in fig. 3.7.b). At variance with the Voigt experimental configuration, circularly resolved PL allows us to detect all the exciton components at each magnetic field.

The Zeeman splittings, obtained as a difference between the energies of Γ^+ states (associated to σ^+) and Γ^- states (associated to σ^-), are plotted as a function of B in fig. 3.7. c). The two sets of data, related to different excitonic components, are almost identical. The Zeeman splitting is linear for $B \leq 10\,T$ while it shows a highly non-linear behaviour at high fields, as already observed in (InGa)As NWs [55]. This non linearity, unexpected on the ground of eq. 3.3, suggests a dependence of the exciton g-factor on the magnetic field. The dashed lines are fit of eq. 3.3 to the data in the ZS linear-region ($B < 10\,T$). The values of the fitted exciton g-factors given in fig. 3.7. c). are now compared with those theoretically calculated and reported in table 3.3. The exciton g-factor in the Faraday configuration is $g_{exc} = |g_e - g_h|$, as from eq. 3.3. Therefore, $g_{exc}^{theo} = 1.61 - (-3.05) = 4.65$, in good agreement with our experimental value $g_{exc}^{exp} = 4.2 \pm 0.2$ which results from an average over seven different sets of measurements taken for different exciting powers and NW diameters.

The observed ZS non-linearity is now discussed. That non linearity was already observed in semiconductor quantum-wells [221, 222, 223, 224] and ascribed to the spin-orbit coupling between valence sub-bands. That coupling is additionally enhanced by the built-in and strain-induced electric-field, which can reach values up to $2\,MV/cm$ in such nanostructures. On the grounds of our data it can be inferred, therefore, that the hole g-factor depends on B via the coupling of valence band-states (the electron g-factor is independent on B, as verified in the Voigt configuration; see fig. 3.6). This guess is strongly supported by theoretical *ab-inito* calculations performed in ref. [45]. Therein, the envelope-function approximation was applied to the $k \cdot p$ Hamiltonian of InP WZ in order to calculate single-particle spectra under a magnetic field. Single particle data were the input to the excitonic

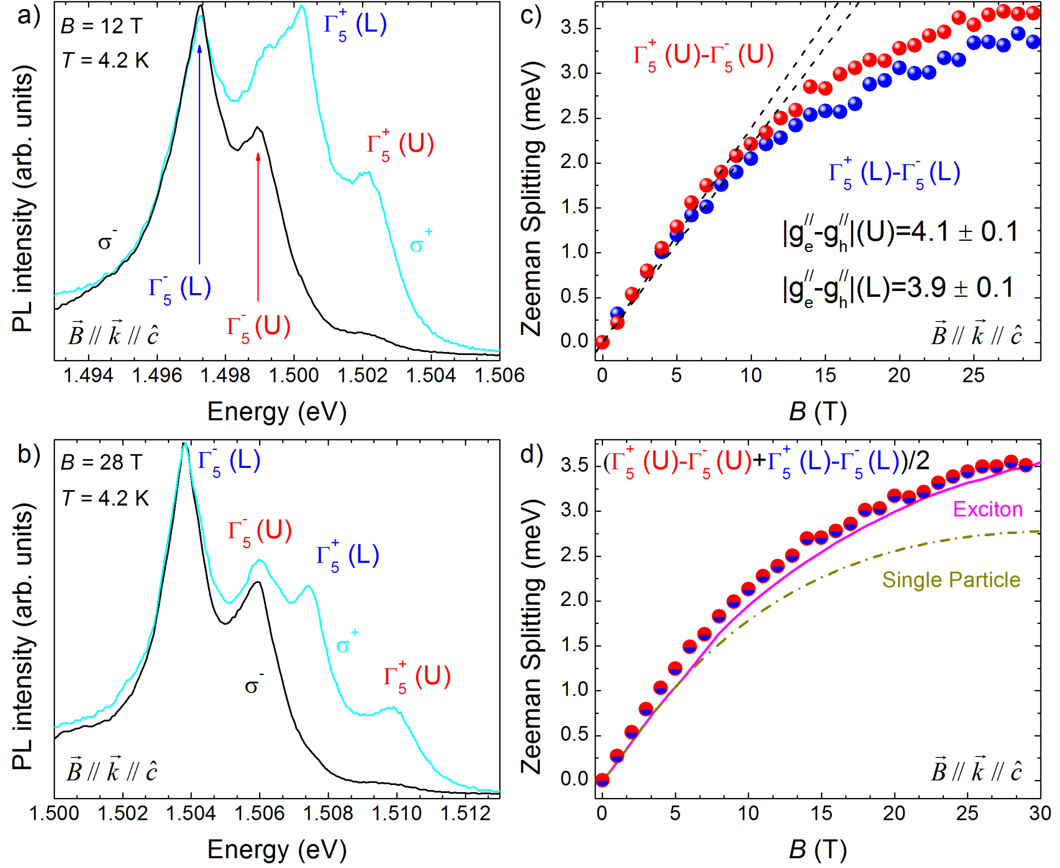

Figure 3.7. a) $T = 4.2\,K$ PL-spectra taken in the Faraday configuration ($B = 12\,T$) on a $d = 650\,nm$ NW-array grown by SAE. Black and cyan lines refer to σ^- and σ^+ circular polarization, respectively. The various exciton-components are indicated together with their group-symmetry notation. b) Same as a) but with $B = 28\,T$. c) Zeeman splitting of the upper and lower free-exciton components as a function of B. Dashed lines are linear fits to the data for $B \leq 10\,T$. The fitted exciton g-factors are reported. d) Red and blue circles are averaged Zeeman-splittings of the free-exciton components. Magenta-thick and olive dashed-dotted lines are theoretical Zeeman-splitting calculations with and without the exciton interaction, respectively.

calculations, which were performed via the effective Bethe-Salpeter equation[4]. The Zeeman splitting, as extracted by the data of the bright Γ_5 exciton states that contribute to the different PL polarized spectra, are plotted in fig. 3.7.d), where blue-red dots are the average of the upper and lower FE-components reported in fig. 3.7.c). The ZS non-linear trend is only qualitatively reproduced by a theoretical ZS prediction without an excitonic interaction; see the olive dashed-dotted line. An excellent agreement is found, instead, when the excitonic interaction is included in the theoretical model, see the thick magenta-line. In conclusion, the ZS non-linearity is due to the coupling of heavy- and light-hole bands, which increases for increasing magnetic fields, as already observed in quantum well systems.

The remnant quite small deviation of the theoretical predictions from the experi-

[4]A robust many-body formalism to treat the exciton electron-hole interaction [225].

mental data could be due to: *i*) the approximations used for the Coulomb interaction, which neglect the exchange-interaction term thus providing corrections of the order of $0.01 \div 0.05\,meV$; *ii*) the slight difference between theoretical and experimental values of the carrier effective-masses; *iii*) the few meV difference between experimental and *ab-initio* calculations of the InP WZ critical-point energies. However, it should be stressed that all quantities were calculated from an *ab-initio* model with no free parameters.

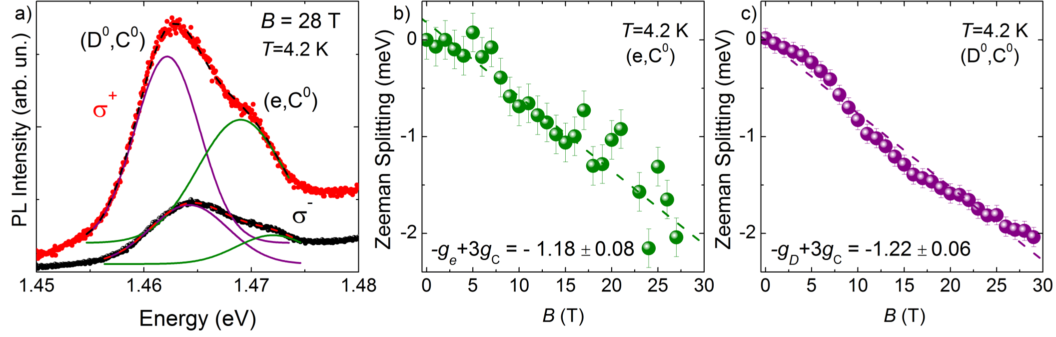

Figure 3.8. a) (D^0, C^0) and (e, C^0) energy-region of $T = 4.2\,K$ PL-spectra taken in the Faraday configuration ($B = 28\,T$) on a $d = 650\,nm$ NW-array grown by SAE. Red and black dots refer to σ^- and σ^+ circular polarization data, respectively. Dashed black and red lines are fits to the data with the (D^0, C^0) and (e, C^0) Gaussian components given by the purple and green solid lines, respectively. b) Fit (dashed line) of the (e, C^0) Zeeman-splitting as a function of B. The fitted g-factor is reported. c) Fit (dashed line) of the (D^0, C^0) Zeeman-splitting as a function of B. The fitted g-factor is reported.

We will now focus on the spin properties of the impurity-related bands. In the Voigt configuration, no meaningful information on the ZS can be obtained due to the broadness of the emission bands and the insensitivity of PL to circular polarization. Indeed, no Zeeman-split state can be observed at any field, as shown in fig. 3.4.b). Conversely, circularly polarized PL-spectra allow to highlight two different Zeeman split states in the Faraday configuration; see fig. 3.4.a)). As already discussed in section 2.3.1, that recombination band is due to PL emission from two different transitions. Therefore, at each field and for both circularly polarized PL-spectra the emission band has been de-convolved in two Gaussian peaks associated to the (D^0, C^0) and (e, C^0) recombinations. An example of the fitting procedure is shown in figure 3.8.a). Therein, the (D^0, C^0) and (e, C^0) energy-region of the $T = 4.2\,K$ PL-spectra taken in the Faraday configuration ($B = 28\,T$) on a $d = 650\,nm$ NW-array grown by SAE is shown. Black and red lines refer to σ^- and σ^+ circular polarizations, respectively. Dashed black and red lines are fits to the whole PL spectra, while purple and green solid lines are the (D^0, C^0) and (e, C^0) Gaussian components. The ZS of the (e, C^0) and (D^0, C^0) bands, calculated as the difference between peak energies of σ^+ and σ^- states at each field B, is shown in fig. 3.8.b) and fig. 3.8.c), respectively. Dashed lines are linear fits to the data.

In this Faraday configuration, the (e, C^0) ZS is linear at all fields, at variance with the *FE* ZS. Moreover, it displays an opposite circular polarization chirality with respect to FE, as evident from the negative sign of the ZS. From the linear fit and eq. 3.1.2, we obtain $-g_e + 3g_C = -(1.18 \pm 0.08)$ and $g_C = 0.04$. Indeed, the

$g_e^{\perp}$	$g_e^{\parallel} - g_h^{\parallel}$	g_C	g_D
1.31	+4.2	+0.04	1.34

Table 3.4. Summary of the experimental values of carrier gyromagnetic-factors, as determined by magneto-PL experiments.

lack in the (e, C^0) case of the non-linearity observed in the FE case, suggests that hole-like states, such as acceptors, are not contributing to the (e, C^0) ZS. Moreover, $g_e = 1.18 \pm 0.08$ if $g_C = 0$, a value very close to that experimentally determined in the Voigt configuration ($g_e = 1.31 \pm 0.05$) as well as in agreement with that theoretically calculated in the Faraday configuration ($g_e = 1.61$). A linear trend is found also for the (D^0, C^0) ZS, with a value $-g_D + 3g_C = -(1.22 \pm 0.06)$ very close to that obtained for $-g_e + 3g_C$ (1.18 ± 0.08) from the (e, C^0) ZS. Since g_C is the same in both transitions, g_e should be similar to g_D (1.34), in good agreement with theoretical and experimental investigations of the effective g-factor of donor-bound electrons in InSb [226], where the percentage difference between the g-factors of free and donor-bound electrons was less than 1%. The obtained experimental g-factors are summarized in table 3.4.

Part II

Tailoring the properties of transition metal dichalcogenide flakes

Chapter 4

Two-dimensional transition-metal dichalcogenides

Transition-metal dichalcogenides (TMDs) are layered materials with strong in-plane bonds and weak out-of-plane interactions. Their layered geometry allows an exfoliation into individual, atomically-thin layers, such as in graphite. Since the discovery of *graphene* in 2004 [227], atomically thin materials have gained much attention in the scientific community. In particular, the linear dispersion of the graphene electronic band-structure near the K point leads to mass-less Dirac fermions as charge carriers, which have provided to scientists a new and rich field for research in fundamental physic. As a matter of fact, graphene is a unique example of an extremely thin ($\sim 0.4\,nm$) electrical and thermal conductor, with high carrier mobility and surprising molecular-barrier properties [228, 229]. The lack of a forbidden gap in the graphene band-structure makes, however, this material unsuitable for opto-electronic applications. Moreover, the several ways in which the graphene forbidden gap can be opened [230] lead to an increased complexity and decreased carrier mobility. On the contrary, TMDs have a forbidden gap in the VIS-NIR spectrum and offer properties complementary to but distinct from those of graphene.

TMDs are usually indicated with the formula MX_2, where M is a transition-metal element from either group IVB (Ti, Zr, Hf, *etc.*), or group VB (*e.g.* V, Nb, or Ta), or group VIB (Mo, W *etc.*), while X is a group VIA chalcogen (S, Se, or Te). The TMD different crystalline structures will be discussed in the first section of this chapter, where a particular attention will be paid to the polytypes studied in this thesis and to a description of the electronic and vibrational properties on going from bulk to few-layer TMDs. In particular, TMDs undergo an indirect-to-direct band gap transition when the number of layers is reduced to a single X-M-X plane [231, 232].

Although mono-layer TMDs can be obtained in a number of ways, a reliable production of atomically thin 2-dimensional (2D) TMDs with uniform properties is pivotal to design devices based on these materials and exploit their novel opto-electronic properties. Therefore, a review of the different methods available for the top-down exfoliation of bulk TMDs or for the bottom-up synthesis of 2D TMDs will be given in the second section of this chapter, together with an evaluation of the

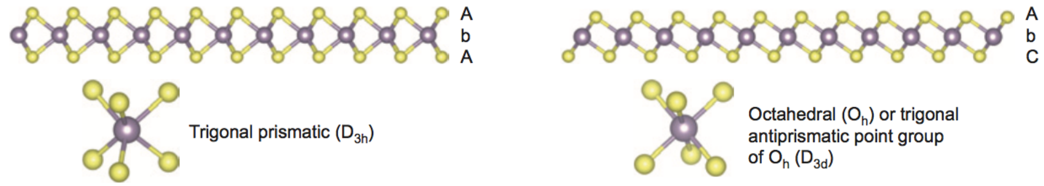

Figure 4.1. [11 – 20] section-view of a single-layer TMD with trigonal prismatic (left) and trigonal anti-prismatic (right) coordination. Atom color-code: purple, metal; yellow, chalcogen. The labels AbA and AbC represent the stacking sequence, where the upper- and lower-case letters represent chalcogen and metal elements, respectively. After ref. [233]

relative merits of these methods.

Finally, the several opportunities given by 2D TMDs in the development of technological applications will be reviewed in the last section of this chapter. The band-gap energy in the visible region of TMDs, together with their flexibility, make these materials suitable for opto-electronic applications, while their high surface-to-volume ratio makes TMDs ideal materials for sensor and detector applications. 2D TMDs are also promising as channel materials for next-generation field-effect-transistors owing to their ultrathin nature, which allows an aggressive scaling-down to atomic dimensions. Moreover, the layered structure and catalytic activity of TMDs make worthwhile their application to the fields of energy storage and production, such as lithium ion-batteries and hydrogen-evolution reaction.

4.1 Crystalline structure

Bulk VIB-VIA TMDs[1] often crystallize in a layered crystal-structure of the form X-M-X, with two layers of chalcogen atoms organized in hexagonal lattices separated by a third layer made of a hexagonal lattice of metal atoms[2]. Adjacent layers are weakly bound to each other by van der Waals forces, which has allowed an easy exfoliation of these crystals [233, 234]. The intra-layer M-X bonds are, instead, strong and predominantly covalent in nature. Bulk TMDs form in a variety of polytypes, which differ in the stacking order and metal-atom coordination. Metal atoms have always a coordination number equal to 6 and are bound to six nearest neighbors chalcogen atoms either in a trigonal prismatic coordination (D_{3h}, see left part of fig. 4.1) or in a trigonal anti-prismatic coordination[3] (D_{3d}, see right part of fig. 4.1). Coordination is ruled by the bond ionicity as given by the electronegativity difference between metal and chalcogen atoms. Trigonal anti-prismatic coordination is preferred in more ionic compounds, since it maximizes the distance between negatively charged chalcogen-atoms. On the other hand, the overlap between metal and chalcogen wave-functions is optimized in a trigonal prismatic coordination, which is typically found in more covalent compounds.

[1]From now on referred to as VI-VI TMDs.

[2]From now on the MX_2 trilayer will be considered as a single layer whose typical thickness is $6 \sim 7$Å.

[3]Sometimes referred to as an octahedral coordination.

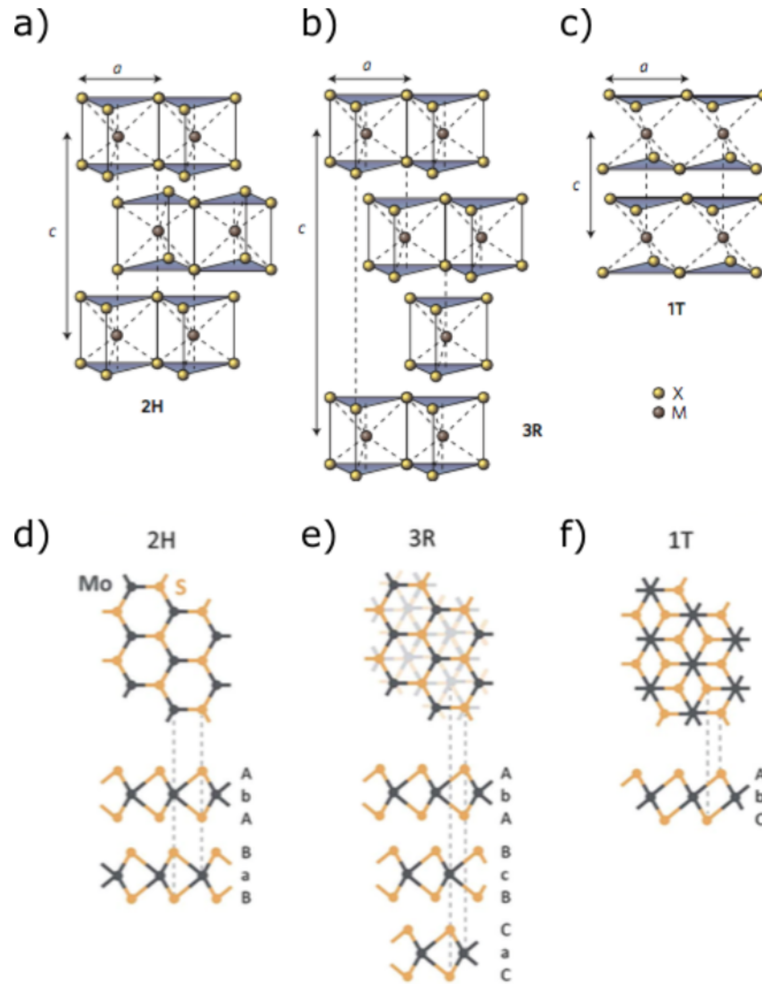

Figure 4.2. Schematics of 3-D structural polytypes of TMDs: 2H (a), 3R (b), and 1T (c). The chalcogen atoms (X) are colored yellow, the metal atoms (M) are colored grey. The stacking index c indicates the number of layers in each stacking order. Schematics top views and lateral views of structural polytypes: 2H (d), 3R (e), and 1T (f). The *abc* notation is also reported. After ref. [234, 235]

Bulk TMDs exhibit a wide variety of polytype structures because an individual MX_2 monolayer (made of three stacked layers of atoms, X–M–X) can be in anyone of the two coordination described above. Moreover, polytypes can differ for the stacking order of each MX_2 monolayer. This new degree of freedom is usually accounted for by the *abc* notation[4] shown in the top part of fig. 4.1. In that scheme, *a,b,c*[5] denote the only three different positions that can be occupied by atoms both in the sandwiched layer and in the stacking sequence. The most common polytypes are 2H, 3R, and 1T, where the letters stand for hexagonal, rhombohedral, and trigonal, in the order, and the digit indicates the number of X–M–X units in the unit cell (namely, the number of layers in the stacking sequence). The schematic 3-D crystal-structures

[4]A similar discussion has been made in section 1.3 to describe polytypism in NWs.
[5]The capital and lower case letters denote chalcogen and metal atoms, respectively.

	MoS_2	WS_2	$MoSe_2$	WSe_2
a(Å)	3.160	3.154	3.288	3.286
c(Å)	12.294	12.362	12.920	12.976

Table 4.1. Values of the lattice parameters of MoS_2, $MoSe_2$, WSe_2, and WS_2 bulk crystals in the 2H polytypes. The increase in the atomic radius of X results in an increase in the lattice parameters. From ref. [239, 240]

of those polytypes are illustrated in figures 4.2a), b), and c). In figures 4.2d), e), and f), the top- and side-view polytype schemes are displayed. There, the dashed lines show how the top views and the lateral views match with each other. Those polytypes can be differentiated using several techniques, including high-resolution transmission-electron-microscopy [236] and Raman spectroscopy [237].

In this thesis, group VI-VI TMDs, such as MoS_2, WS_2, $MoSe_2$, and WSe_2, have been studied. Among those TMDs, almost all the compounds are naturally stable either in the 2H or 3R polytype form (both with trigonal prismatic-coordination), while the 1T phase (with trigonal anti-prismatic coordination) is metastable and is rarely observed [238]. Our samples are mechanically exfoliated by bulk-samples with a 2H crystal-structure analogous to that of wurtzite InP NWs described in section 1.3. The only difference is given by the number of atoms per crystal primitive cell: 2 in the InP NWs, $n3$ (n=1, 2, 3 depending on polytype) in the bulk VI-VI TMDs. Therefore, the 2H unit-cell and the Brillouin zone are similar to those reported in fig. 1.6 for the WZ bulk crystals. The a and c lattice parameters of the 2H unit-cell, shown in figure 4.2.a), are reported in table 4.1 for all the compounds studied in this thesis. In the monolayer regime, in which the Brillouin zone is defined only in two dimensions (neglecting the existence of three planes in a X-M-X monolayer), there are, instead, 3 atoms per primitive cell (and a 1H polytype corresponds to the 2H polytype in 3 dimensions). Those differnces in the crystal structures result in differences in the electronic and vibrational properties, which will be the subject of the two next subsections.

4.1.1 Band structure

As anticipated, semiconductor TMDs undergo to a indirect-to-direct band-gap transition on going from the bulk to the monolayer regime [241, 242]. That experimental evidence has been demonstrated by *ab-initio* calculations of the electronic band-structure of several TMDs [231, 241, 243]. Figure 4.3 shows the band structures of bulk and few layers (4L, 2L, and 1L) MoS_2 calculated by density-functional-theory within a generalized gradient approximation [241]. There, it is shown that the energy of the direct transition at the Brillouin zone K point barely changes with layer thickness. Conversely, the energy of the indirect transition from the Γ point in the valence band to the valley along the Γ-K direction in the conduction band (Q critical point) increases monotonically as the number of layers decreases. Remarkably, the indirect transition-energy in the monolayer limit becomes so high that the material turns into a 2-D direct band-gap semiconductor.

A knowledge of which M and X atomic orbitals contribute to the band structure

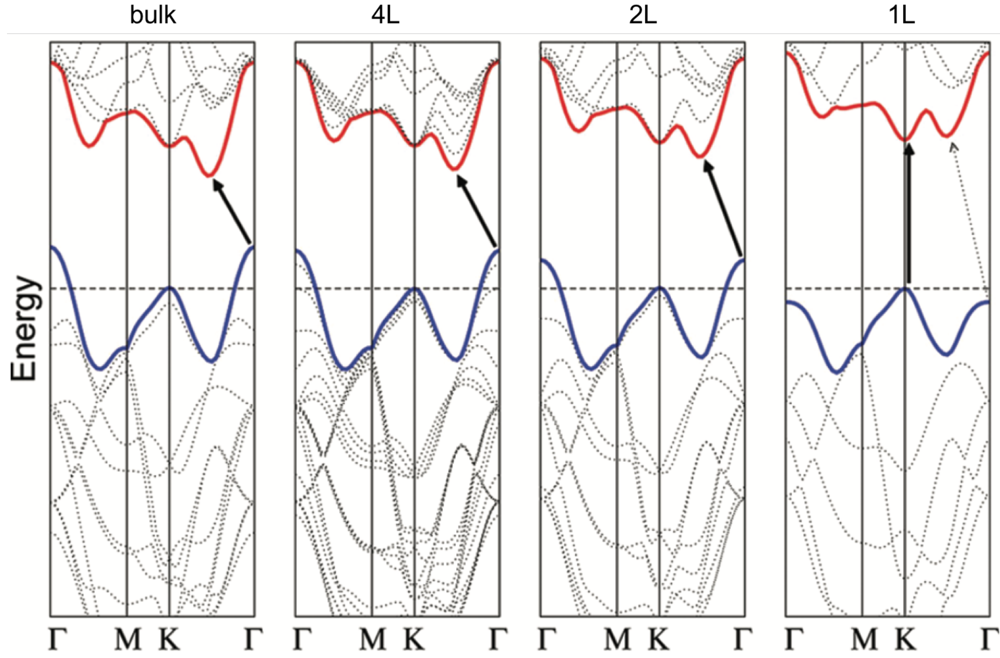

Figure 4.3. From left to right: band structures as calculated by density-functional-theory in bulk, quadri-layer (4L), bi-layer (2L), and mono-layer (1L) MoS_2. The horizontal dashed lines represent the energy of the valence-band maximum at the K point. The red and blue lines represent the conduction- and valence-band edges, respectively. The energy of the indirect band-gap (dashed arrow in the 1L panel) is greater than that of the direct band-gap (solid arrow) only in the case of a monolayer MoS_2. After ref. [241]

at K, Q, and Γ points is required in order to understand the physical origin of the indirect-to-direct transition. DFT calculations have shown that the conduction-band states at the K point are due mainly to d orbitals localized on the M atoms, which are located in the middle of the X–M–X layer-sandwiches and relatively unaffected by the interlayer coupling. Thus, as the number of layers changes, the direct states near the K-point are relatively unchanged. On the contrary, the states near the Γ point are due to combination of anti-bonding p_z-orbitals on the chalcogen atoms and d orbitals on metal atoms. Those orbitals give rise to some weak interlayer coupling as well as to a surface reconstruction with an ensuing significant shift of the Γ-Q transition to high energy in the monolayer limit of the TMD thickness [241, 242, 244]. As a consequence, direct band gaps of VI-VI TMDs are typically $\sim 50\%$ greater the indirect gaps of their bulk counterparts [243], as shown in table 4.2. Therein, theoretical calculations of bulk and monolayer band-gap energies are reported for the four compounds studied in this thesis.

Another interesting property of the VI-VI TMD band-structures is the intriguing physics of spin- and valley-coupling in the monolayer limit [246, 247], which is due to a strong TMD spin-orbit coupling and non centrosymmetric nature. In bulk MX_2, Kramer's degeneracy leads to $[E^{\uparrow}(\vec{k}) = E^{\downarrow}(\vec{k})]$, where $E(\vec{k})$ is the carrier energy in a generic $\vec{k}$ point of the BZ and $\uparrow$ ($\downarrow$) are the particle spins. This degeneracy condition is established by the combination of time-reversal symmetry $[E^{\uparrow}(\vec{k}) = E^{\downarrow}(-\vec{k})]$

	MoS_2	WS_2	$MoSe_2$	WSe_2
Bulk E_{Gap} (eV)	0.75 [243]	0.89 [243]	0.80 [243]	0.97 [243]
Monolayer E_{Gap} (eV)	1.89 [243]	2.05 [243]	1.58 [243]	1.61 [243]
	2.02 [245]	1.98 [245]	1.72 [245]	1.63 [245]

Table 4.2. Theoretical calculations of MoS_2, WS_2, $MoSe_2$, and WSe_2 band gap energies in the bulk and monolayer regime. Calculations have been performed via density-functional-theory within the local-density-approximation in ref. [243], via the frozen-core-projector augmented-wave method within the Heyd-Scuseria-Ernzerhof hybrid functional in ref. [245].

and inversion symmetry $[E^{\uparrow}(\vec{k}) = E^{\uparrow}(-\vec{k})]$. Those conditions are satisfied in bulk TMDs whose space-group symmetry, D^4_{6h}, is inversion symmetric. In the monolayer limit, however, the crystal symmetry reduces to D^1_{3h} and the inversion symmetry is explicitly broken: taking the M atom as the inversion center, an X atom will be mapped onto an empty location. This turns into a spin splitting of degenerate states, except for $\vec{k}$ points with special symmetry in the BZ.

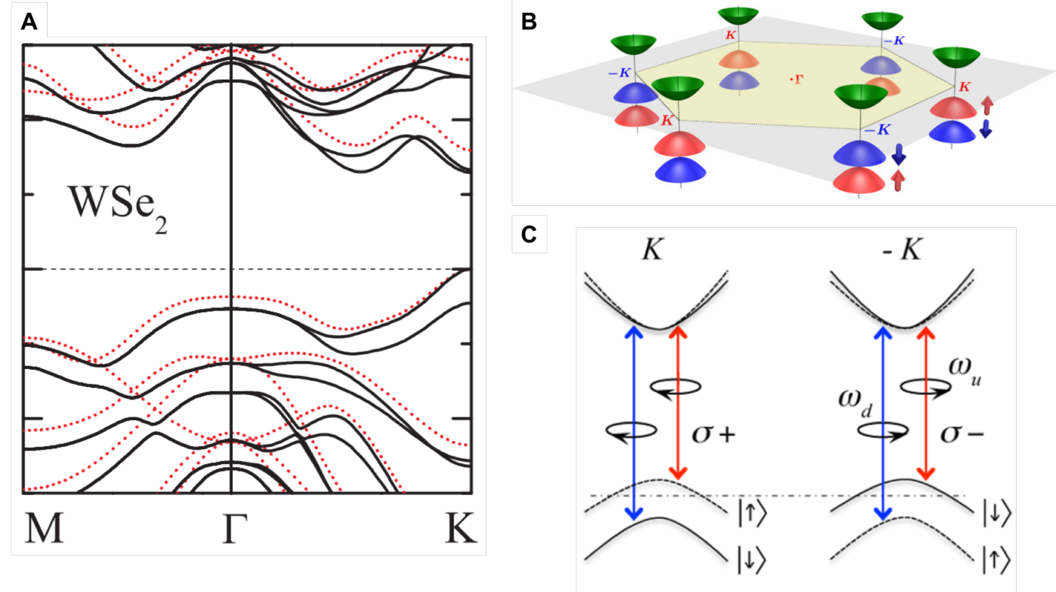

Figure 4.4. a) Theoretical band structures of the WS_2 monolayer with (solid line) and without (dotted line) the spin-orbit interaction. b) Schematic drawing of the band structure at the band edges located at the K points. c) Valley- and spin-dependence of the optical transition selection-rules. Solid (dashed) curves denote bands with spin-down (-up) quantized along the out-of-plane direction. ω_u and ω_d indicate the frequencies of transitions from the two split valence-band tops to the conduction-band bottom. After ref. [246, 247]

As an example, a spin degeneracy results at the Γ point ($\vec{k} = 0$) from the time-reversal symmetry alone ($E^{\uparrow}(0) = E^{\downarrow}(0)$). A combination of time-reversal and translational symmetry results in zero splitting also at the M point, whereas the spin splitting of a general $\vec{k}$ point is determined by the time-reversal and D^1_{3h}

point-group symmetries [247]. Finally, the spin-orbit interaction in WS_2 breaks the spin degeneracy of the valence- and conduction-bands along the line $\Gamma - K$, as shown in figure 4.4.a) where the theoretical band-structures are shown with (solid line) and without (dotted line) the inclusion of the spin-orbit interaction. Therein, the spin splitting at the K point in the valence band is greater than that in the conduction band. Indeed, the atomic orbitals (d_{z^2} and p_z), which contribute more to the conduction-band minima, are perpendicular to the layer plane and play a minor role in the spin-orbit coupling [246, 247].

Another spin-orbit-coupling effect is the valley-valley coupling. The momentum valleys K and $-K$ at the opposite corners of the first Brillouin zone are not equivalent since their spin splittings are opposite, as shown in blue and red in fig. 4.4.b) and required by the time-reversal symmetry $[E^{\uparrow}(\vec{k}) = E^{\downarrow}(-\vec{k})]$. This turns into a singular coupling between spin and valley degrees of freedom. It has been also experimentally shown that only one of the two valleys is populated by electrons when TMDs are excited with circularly polarized light [248, 249]. Conversely, circularly polarized light is emitted when those photoexcited electrons relax to the ground state, as shown in fig. 4.4.c) thus indicating that valley polarization is achieved and *preserved* during the relaxation processes and in turn suggesting that valley-based optoelectronic applications are feasible.

Lastly, another important feature displayed by monolayer TMDs is a great exciton binding-energy ($0.5 \div 1.0\,eV$) [250], which significantly influences the TMD optical properties[6].

Excitonic effects are significantly enhanced in low-dimensional materials because of a strong spatial confinement and a reduced screening effect [251]. The great binding energies of excitons in 2D TMDs (roughly two orders of magnitude greater than those in conventional semiconductors[7]) allow for the observation of excitons at room temperature. Those strong excitonic effects induce also a significant transfer of oscillator strengths from the band-to-band transitions to the fundamental 1s exciton state. A ratio between the oscillator strength of the 1s exciton state and the band-to-band transitions as high as 100 has been predicted [252]. Such a large value leads to strong light-matter interactions, which induce a strong absorbance and short radiative lifetime. Moreover, trions, namely, charged complexes between free excitons and charged particles, [253] and biexcitons, neutral complexes due to the coupling of two excitons, [254] have been observed in TMDs.

4.1.2 Vibrational properties

Lattice vibrations in crystals can be classified on the basis of the irreducible representation of their symmetry group. As anticipated previously, bulk MX_2 2H polytypes are characterized by a D^4_{6h} point group symmetry. In this scenario, lattice vibrations at Γ point are expressed by the irreducible representations of D^4_{6h} [255]:

$$\text{Bulk} \quad \Gamma = A_{1g} + 2A_{2u} + 2B_{2g} + B_{1u} + E_{1g} + 2E_{1u} + 2E_{2g} + E_{2u}, \tag{4.1}$$

[6] Exciton theory and definition are discussed in A.1

[7] See, *e.g.* , the exciton binding energies of the optical transitions in WZ InP-NWs discussed in chapter 2.

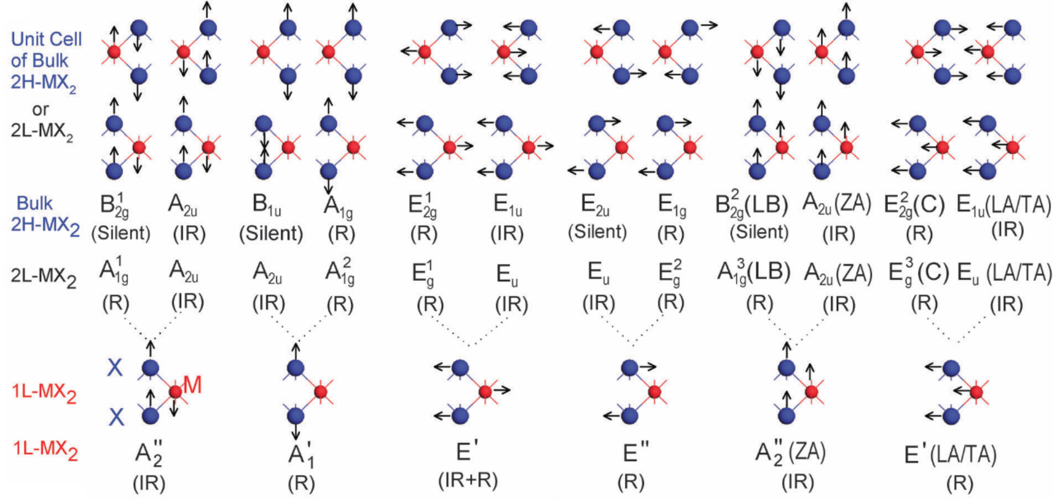

Figure 4.5. Top part: symmetry and normal displacements of each optical vibration-mode for MX_2 bulk or with an even number of layers; bottom part: same as in the top part but for monolayer MX_2. The Raman-active (R), infrared-active (IR), and both R and IR inactive (silent) modes are identified. The dotted lines show that each mode in mono-layer MX_2 is split into two modes in the bulk MX_2 of which one vibrates in-phase and the other out-of-phase. After ref. [255]

where one A_{2u} and one E_{1u} are acoustic modes, A_{1g}, E_{1g}, and E_{2g} are Raman active, another A_{2u} and E_{1u} are infrared active, and B_{2g}, B_{1u} and E_{2u} are optically inactive. Here the modes denoted by the letter E are doubly degenerate in the xy plane, because they belong to oscillations of atoms along the sandwiched layer-plane. The other letters (A and B) denote, instead, atom oscillations perpendicular to the layer plane and thus not degenerated (see top part of fig. 4.5). The 18 phonon modes (3 acoustic and 15 optical modes) are consistent with the number of atoms (6) in the primitive cell.

The aforementioned classification is valid only in the bulk limit. When the number of layers is finite that classification is no longer valid and a discrimination between odd and even number of layers is mandatory. As a matter of fact, in the case of an even number of layers the point group, D_{3d}, is characterized by the inversion symmetry i. In the case of an odd number of layers, instead, the point group, D_{3h}, is characterized by a horizontal reflection plane (σ_h) through the transition metal atom (M), which is there also in bulk MX_2. Therefore, the vibrational properties of monolayer and bulk TMDs are almost similar, as it will be clear soon. In more details, the primitive cell of monolayer MX_2 is composed of three atoms leading to nine vibrational modes at the Γ point, which on the basis of the D_{3h} symmetry are [255]:

$$\text{Monolayer} \quad \Gamma = 2A''_2 + A'_1 + 2E' + E'', \tag{4.2}$$

where one A''_2 and one E' are acoustic modes, another A''_2 is infrared active, A'_1 and E'' are Raman active, and another E' is both Raman and infrared active, as shown in the bottom part of fig. 4.5. On the contrary, in the bilayer regime there are 6 atoms per primitive cell, as in the bulk case, leading to 18 vibrational modes at the

Γ point, which on the basis of the D_{3d} symmetry are [255]:

$$\text{Bi-layer} \quad \Gamma = 3A_{1g} + 3A_{2u} + 3E_g + 3E_u, \tag{4.3}$$

where one A_{2u} and one E_u are acoustic modes, the other A_{2u} and E_u are infrared active, and A_{1g} and E_g are Raman active, as shown in in the top part of fig. 4.5. The symmetry and normal-mode displacement of each mode of either bulk or bi-layer and mono-layer MX_2 are shown in fig. 4.5, together with the respective correspondence of vibrational modes on going from mono- to bi-layer (see dotted gray lines). Indeed, each of the nine normal vibrational modes in mono-layer MX_2 splits into two corresponding modes in bi-layer and bulk MX_2.

As explained in sec. A.1, the intensity of a Raman-active mode in a crystal can be expressed by the Raman tensor and by the polarization vectors of the incoming and scattered photons via eq. A.20. Therefore, eq. A.20 establishes the selection rules for a given vibrational mode. Raman tensor of bulk, bilayer, and monolayer MX_2 are reported in ref. [255]. Because of the correlation between D_{3h} and D^4_{6h}, the bulk and mono-layer Raman tensors are equal, with similar polarization dependences of the A_{1g} (A'_1), E^1_{2g} (E'), and E_{1g} (E'') modes[8]. On this ground, in both bulk and monolayer TMDs modes parallel and perpendicular to the plane can be distinguished via polarization-resolved Raman-measurements. Indeed, modes in the XX but not in the YX configuration[9] correspond to the relative motions of the atoms perpendicular to the layer plane, namely, to A'_1 (mono-layer) or A_{1g} (bulk). On the contrary, modes in both XX and YX configurations correspond to the relative motions of the atoms within the $\hat{x}\hat{y}$ plane, namely, to E' (monolayer) or E^1_{2g} (bulk).

The frequencies of the corresponding modes in mono-layer and multi-layer MX_2 are expected to depend on the number of layers (N). In the following discussion on the high-frequency peak-evolution with N, we will simply refer to the corresponding modes as E^1_{2g} and A_{1g} in the bulk, as it is commonly done in the literature [257]. Figure 4.6.a) shows the dependence on N of the peak energies and widths for E^1_{2g} and A_{1g} in MoS_2 [255]. The two peak energies show opposite trends with decreasing thickness, see dashed lines. On the basis of a linear chain model including only van der Waals interactions, one would expect, instead, a red-shift of both peaks [258]. The unexpected trend shown by the E_{2g} mode is accounted for by the long-range Coulomb interaction due to the effective charges resulting from the relative displacement of M and X atoms. This effect considerably decreases in the few layer and bulk structures because of a significant dielectric-constant increase with N [259]. Similar differences in the frequency trends with N of E^1_{2g} and A_{1g} have been reported also in N-layer WS_2, WSe_2 [256], and $MoSe_2$ [260]. As an example, polarization-resolved Raman-measurements in N-layer WS_2 are shown in fig. 4.6.b), where it is also experimentally demonstrated that the same selection rules hold in the bulk and mono-layer regime. The mode-frequencies theoretically calculated for the four TMD compounds investigated in this thesis are reported in table 4.3. As expected, the vibrational mode frequencies red-shift for increasing atomic masses, namely, $\omega_{MoS_2} > \omega_{MoSe_2}$ and $\omega_{WS_2} > \omega_{WSe_2}$.

[8] Nomenclature in brackets refers to the notation of mono-layer modes.

[9] Here we are considering a back-scattering configuration, thus polarization vectors of light can be directed only parallel to the TMD plane along the $\hat{x}$(X) or $\hat{y}$(Y) directions.

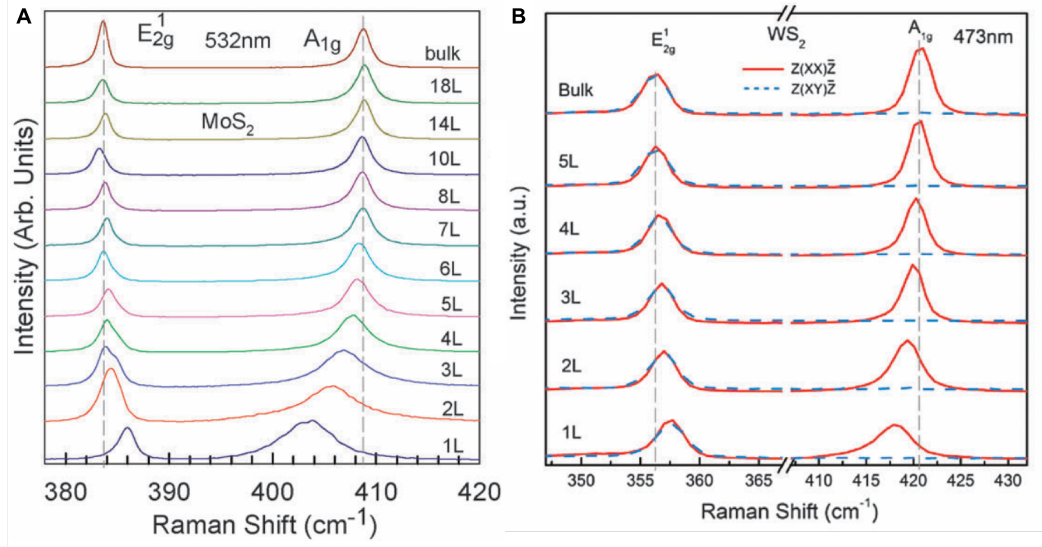

Figure 4.6. a) Raman spectra (laser excitation wavelength 532 nm) of N-layer ($N = 1 \div 8$, 10, 14, 18) and bulk MoS_2. The two grey-dashed lines indicate the position of E^1_{2g} and A_{1g} in bulk MoS_2. b) Polarized Raman spectra (laser excitation wavelength 473 nm) of $1 \div 5$ layer and bulk WS_2 in the back scattering configuration. After ref. [255, 256]

	MoS_2	$MoSe_2$	WSe_2	WS_2
Bulk A_{1g} (cm^{-1})	405.0	241.8	251.6	420.3
Bulk E^1_{2g} (cm^{-1})	380.4	283.1	247.8	357.2
Monolayer A_{1g} (cm^{-1})	402.7	240.3	250.2	418.7
Monolayer E^1_{2g} (cm^{-1})	383.6	285.3	249.4	359.2

Table 4.3. Vibrational mode frequencies as theoretically calculated for MoS_2, $MoSe_2$, WSe_2, and WS_2. Calculations have been performed by using first-principle density-functional perturbation-theory [261].

At ultra-low frequency, other vibrational modes are present in bulk or N> 2-layer TMDs. These modes, denoted in fig. 4.5 as B^2_{2g} and E^2_{2g}, are referred to as layer breathing (LB) and shear modes (C), respectively, and regard the relative motions of two X–M–X layers in a direction perpendicular (B^2_{2g}) or parallel (E^2_{2g}, twofold degenerate) to the layer plane. These modes are ruled only by van der Waals interlayer-interactions because the two single layers oscillate as they were two rigid bodies. Therefore, restoring forces are weak and the frequencies of LB modes are usually less than $\sim 100\,cm^{-1}$, while those of C modes are even smaller (less than $\sim 50\,cm^{-1}$). The traditional approach to perform very low-frequency Raman measurements involves the use of a triple spectrometer, as done by several experimental groups [258]. Other groups resort, instead, to a single monochromator coupled with volume holographic filters to prevent a low spectral throughput due to the use of three monochromators [237]. These modes are particularly relevant since from their energies it is possible to determine the exact number of layers in a

given flake. Indeed, a monatomic chain model[10] has been developed to predict the dependence of the C and LB modes on the layer thickness, in very good agreement with experimental data [258]. On the contrary, the energies of the high frequency modes slightly depend also on the specific substrate where the sample is deposited onto [255] and, thus, do not allow for a precise determination of the number of flake layers as C and LB modes do, instead.

4.2 Growth techniques

Several techniques have been developed to obtain high quality both single- and few-layer TMDs with uniform properties, which is essential for transferring the TMD new electronic and optical properties described so far into applications. As anticipated, these techniques are divided into two main categories: *top-down* and *bottom-up* approaches. Here, top-down exfoliation from bulk materials and bottom-up synthesis of TMD flakes will be shortly reviewed and the relative merits of these methods evaluated.

4.2.1 Top-down approach

Mechanical cleavage

As explained in section 4.1.1, TMDs are layered materials characterized by weak van der Waals interactions between contiguous layers. This allows for peeling atomically-thin flakes from their parent bulk-crystals by micromechanical cleavage by using an adhesive tape [227, 229, 235]. Those flakes are, then, deposited on substrates and optically identified by light interference [262] by using the same techniques developed for graphene (see fig. 4.7.a)). To date, the mechanical cleavage is one of the easiest, simplest, and most popular method to get atomically-thin flakes of layered materials. However, transmission-electron-microscopy and atomic-force-microscopy measurements made after cleavage have highlighted the presence of organic contamination from remnant tape glue [229]. Several procedures have then been developed to clean single and multilayer surfaces [229, 263]. Lastly, mechanical cleavage is useless for industrial applications because it is not scalable and lacks of a systematic control over the flake thickness and size.

Photoexfoliation

High-power laser beam can be used to remove material from a solid surface. If irradiation results in the detachment of an entire or partial layer, the process is called photoexfoliation (see fig. 4.7.b)). The unique structure of layered materials causes an anisotropic heat dissipation in the bulk crystals, which enables selective sublimation of top crystal layers. Although the early stage of this method, laser ablation has already thinned down both graphene [265] and MoS_2 [266] to monolayer thicknesses with a micro-meter scale-resolution. The process is best implemented in an inert atmosphere or in vacuum since ablation in air tends to oxidize the surface

[10]The entire X-M-X layer is treated as a single ball.

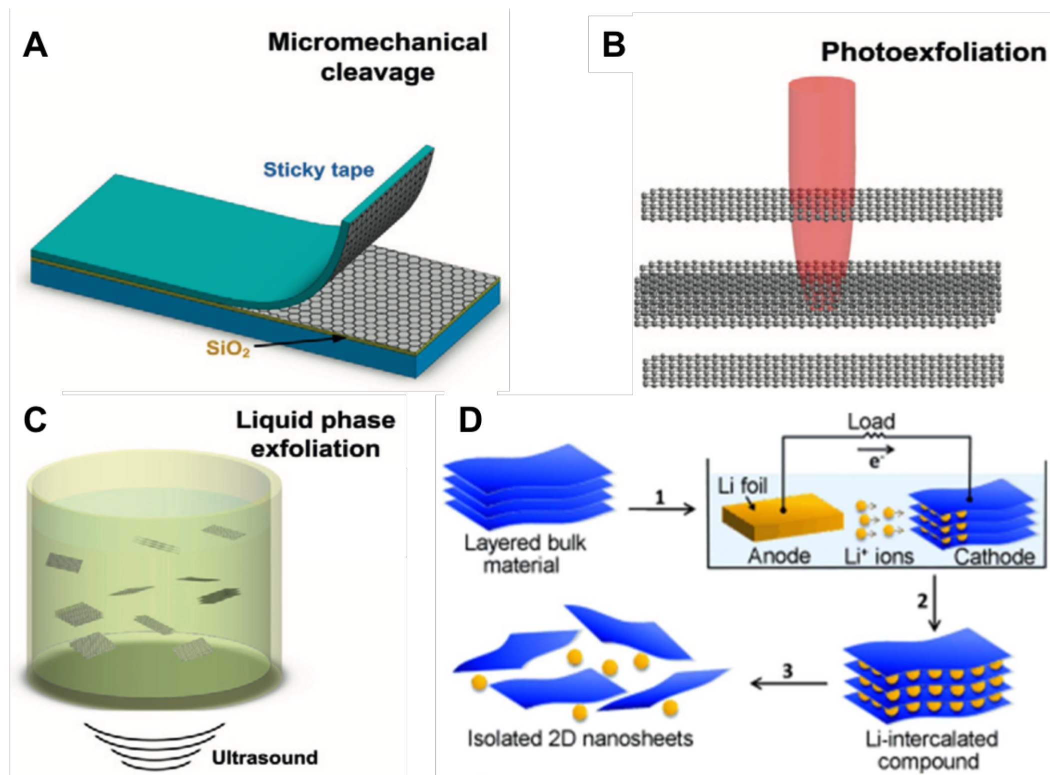

Figure 4.7. Schematic illustration of some exfoliation techniques. a) Micromechanical cleavage using an adhesive tape. b) Photo-exfoliation induced by laser. c) Liquid-phase exfoliation via ultrasonification. d) Chemical intercalation with lithium. After ref. [229, 264]

layers. Besides, the requirement for a laser raster-scanning makes challenging the scale-up of this procedure.

Liquid-phase-exfoliation

Liquid-phase-exfoliation (LPE) of TMDs, commonly used to obtain large quantities of nanosheets, is a promising technique for industrial applications. This process is generally divided in three steps:

- *Dispersion of bulk material in a solvent.* The aim of this procedure is to prevent that single flakes join together after their exfoliation. Therefore, ideal solvents to disperse single layer are those that minimize the interfacial tension $[mN/m]$ between the liquid and single flakes. Indeed, flakes tend to join together whenever their dispersion in the liquid is poor because of a high solid-liquid interfacial tension. As an example, the best solvents of graphene have surface tension $\gamma \sim 40\, mN/m$ [229], such as *benzyl benzoate*, *gamma-Butyrolactone*, and *Dimetilformammide*. However, most of those solvents are toxic. Moreover, they have high boiling points ($T_B > 450\, K$), which makes difficult their removal after exfoliation. As an alternative, low boiling point solvents, such as acetone, chloroform, and isopropanol are used, together with linear-chain surfactants

that minimize the solvent surface-tension. In any case, annealing treatments at temperature higher than that of the solvent boiling-point should to remove the solvents from the surface after LPE to ensure a clean layer surface.

- *Exfoliation by ultracentrifigation* In this step, single and multi layer exfolation from bulk occurs, see fig. 4.7.c). Ultrasounds, namely, sound waves with frequencies greater than $20\,kHz$ give rise to high- and low-pressure cycles in a liquid solution. During these cycles, the materials are exfoliated via cavitation effects, namely, formation, growth, and collapse of bubbles or voids in the liquid due to pressure fluctuations, which considerably increase the local temperature and thus lead to the exfolation of single- and multi-layer flakes [229].
- *"Purification"* In this step, exfoliated flakes are separated from un-exfoliated flakes. Thick flakes can be removed by different strategies called differential ultracentrifugation or density-gradient ultracentrifugation. In the former process, the various flakes are separated on the basis of their sedimentation rate in response to centrifugal forces acting on them. To date, this procedure is the most common separation strategy: flakes ranging from few nm to a few μm have been thus produced [229]. In the latter process, the flakes are ultracentrifugated in a preformed density-gradient medium. Then, they move along the cuvette until they reach the point where their density equals that of the surrounding liquid. However, flakes should have the same density, independently of N, thus another approach is necessary to induce a density difference: as an example, coverage of the flakes with a surfactant [229].

LPE is cheap and easily scalable, and does not require expensive growth substrates. Unfortunately, it does not allow for a high yield of monolayer sheets.

Chemical intercalation with ions

The intercalation of TMDs by ionic species also allows the layer exfoliation in liquid solution. The most used ionic specie is lithium. The typical procedure involves submerging a bulk-TMD powder in a solution of a lithium-containing compound, such as *n-butyllithium*, for more than a day to allow an intercalation of lithium ions. The intercalated material is then exposed to water, whose vigorous reaction with the intra-layer lithium atoms leads to the evolution of H_2 gas and ensuing rapid separation of the TMD layers. Such chemical exfoliation method produces gram quantities of sub-micrometer-sized single-layers, but the resulting exfoliated material differs structurally and electronically from the bulk material. In particular, for MoS_2 the process changes the electronic structure of the exfoliated nanosheets from semiconducting to metallic. The Mo atom coordination is changed from trigonal prismatic (2H-MoS_2) to trigonal antiprismatic (1T-MoS_2). Annealing at $300°\,C$ can eventually restore the Mo atom-coordination [267]. In addition, controllable lithiation of TMD crystals has been demonstrated with electrochemical process, as shown in fig. 4.7.d) [268]. Therein, a galvanic electrochemical cell was constructed with the TMD crystal as cathode and a lithium foil as anode, thus allowing for a precise control of the lithiation process in the TMD crystal by monitoring a galvanic discharge-process in the electrochemical cell. That method operates at

room temperature and requires times shorter than the previously described LPE technique.

4.2.2 Bottom up approach

The development of methods for synthesizing large-area and uniform layers is crucial for applications such as wafer-scale fabrication of electronic devices and flexible, transparent optoelectronic applications. Several methods, differing for the use of different precursors to be heated at high temperature, have been developed to grow single-layer TMDs by chemical-vapor-deposition (CVD), which enables large-scale device fabrication. In the case of MoS_2, solid precursors can be: sulphur and MoO_3 powders vaporized and co-deposited onto a nearby substrate [269]; a thin layer of Mo metal deposited onto a wafer and heated with solid sulphur [270]. Substrates dip-coated in a solution of $(NH_4)_2MoS_4$ can be also heated in the presence of a sulphur gas [271]. The film thickness is dependent on the concentration or thickness of the initial precursors, although a precise control of the number of layers can be hardly achieved over a large area.

In addition to MoS_2, other VI-VI semiconductor TMDs, such as $MoSe_2$, WS_2, and WSe_2, have been synthesized via CVD [264]. However, large-scale growth of TMD atomic layers is still challenging, which is a significant, major restraint to TMD applications. Another challenge in the synthesis of TMDs is the achievement of wafer-scale continuous films, which are often limited to a micron scale. Only recently, single flake $MoSe_2$ with an area on the millimeter scale have been synthesized [272], thus paving the way to a large-scale synthesis of single layers in industrial applications. Most importantly, it has been demonstrated that the procedures used for MoSe2 can be extended to other TMDs. However, defects formed during the growth process are the main limitation to this technique. To date, a route to mitigate the effect of defects in those TMDs remains a challenging issue, albeit post growth treatments with an organic superacid have improved the optical quality of CVD materials [273].

Also MBE allows for the growth of large-area single-layer TMDs, whose crystal quality and purity are better than those of TMDs synthesized by CVD [229]. However, as explained in section 1.2, MBE requires ultra-high vacuum conditions and is more expensive and time consuming than CVD.

4.3 Technological development of TMD based devices

Although people working in the TMD field are constantly pushing to develop new fundamental science as well as applications of TMD novel physical properties in almost all technological fields, no production-scale TMD-based device has reached the market place to date. The aim of this section is to provide a terse overview of the potential applications of TMD-based devices, whereas more thorough reviews can be found in refs. [235, 252, 274]. The four following subsections will cover applications of TMD-based devices in the field of opto-electronics, electrocatalysis, sensing, and storage applications.

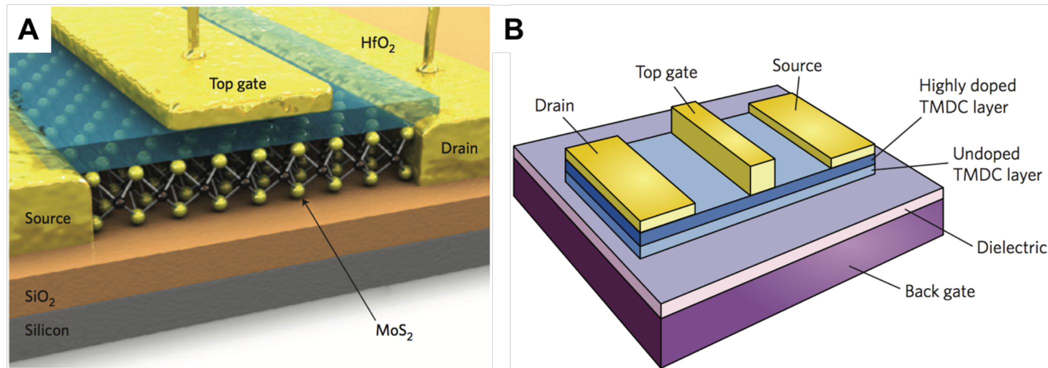

Figure 4.8. a) Schematic illustration of HfO_2-top-gated monolayer MoS_2 FET-device. b) Proposed TMD-based high-electron-mobility-transistor (HEMT) device with top-gated Schottky contact and TMD layers with different doping levels. After ref. [235]

4.3.1 Opto-electronic devices

As already discussed in the first part of this thesis, nanostructures pave the way to transistor with dimensions smaller than those presently reached with state-of-the-art processors ($22\,nm$ in length [275]). In addition, 2D semiconductor materials are easily processed and lack of short-channel effects that can hinder the device performance [235]. Among 2D materials, TMDs are very suitable for the fabrication of **logic transistors**with high carrier mobilities for fast operation, high on/off ratios (namely, the ratio of on-state to off-state conductance) for effective switching[11], high on-state and low off-state conductivities (*i.e.*, product of the charge density and mobility) for low power consumption during operation. Although graphene satisfies the conditions of a high carrier-mobility and conductivity, the lack of a forbidden gap results into a low off-state current and limits the use of graphene as a digital logic transistor. On the contrary, TMDs with a bandgap in the NIR and VIS support high on/off ratios while maintaining high carrier mobilities.

The first implementation of a top-gated field-effect-transistor (FET) based on monolayer MoS_2 was reported by Kis *et al.* [276]; see fig. 4.8.a). Therein, excellent on/off current ratio ($\sim 10^8$), n-type conduction, and room-temperature mobility greater than $200\,cm^2V^{-1}s^{-1}$ have been achieved with the implementation of a high-k dielectric (HfO_2), which gave the additional benefit of improving the mobility of the single-layer [276]. Although that MoS_2 FET will not compete with conventional III–V transistors on mobility values alone, its attractive electrical-performance characteristics, flexibility, and transparency make it a valuable candidate for low-power electronics [235]. Electron mobility can be increased by resorting to an analogue of high-electron-mobility transistors, which are conventionally fabricated from planar junctions of semiconductors with different band gaps. In those systems, the great band-gap semiconductor is highly doped whereas the one with small band-gap is nominally intrinsic. When the two layers are brought into contact, electrons move from the doped to the intrinsic layer where the impurity scattering is minimized. That device architecture could be promising for TMDs because there is a number of TMDs with different band-gap values (see table 4.2) and similar lattice

[11]For digital logic, on/off ratios of $10^4 \div 10^7$ are generally required for switches.

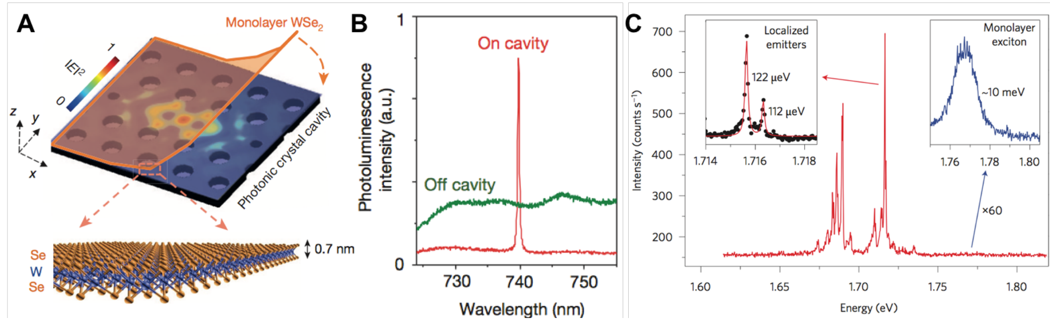

Figure 4.9. a) Schematic of a planar photonic cavity coupled with a single-layer WSe_2. The electric-field profile of the fundamental cavity-mode is embedded as a color plot. A schematic atomic structure of monolayer WSe_2 is also shown. b) PL spectra taken on (red) and off (green) the cavity region. c) PL spectrum from isolated quantum-dot-like defects in mono-layer WSe_2. PL emission from the quantum dots shows line-widths much narrower ($\sim 0.1\,meV$; left inset) than that of the free excitons ($\sim 10\,meV$; right inset). After ref. [277, 278]

constants (see table 4.1). The schematic of a TMD high-electron-mobility-transistor is shown in fig. 4.8.b) where a highly doped TMD layer is interfaced with an undoped layer [235].

The strong light-matter interaction in TMDs makes them suitable also as **photodetectors**. The TMD flexibility even allows for the achievement of photovoltaic devices that could coat buildings and curved structures. Phototransistors of almost all VI-VI TMDs have been fabricated and their potentiality has been demonstrated in devices based on both photoconduction and photocurrent[12] and for both lateral and vertical geometries [252]. In particular, single-layer MoS_2 highly sensitive photodetectors have been fabricated whose photocurrent depends on the incident light intensity, responds within $50\,ms$ to changes in light levels, and is highly stable [279]. Moreover, plasmonic effects can significantly enhance that photocurrent at wavelengths corresponding to the plasmonic-resonance of gold nanoparticles deposited on the single-layer sheet [280].

Light emitting diodes (LEDs) made of TMD p-n junctions have been also developed [252]. However, a low quantum efficiency ($\sim 10\%$ at the most) has been achieved at low temperature [281] because of the poor carrier mobility and PL quantum-yield of single-layer TMDs. On the other hand, the unique valley-dependent optical properties of TMDs (see 4.1.1) make TMDs suitable to design LEDs with controllable polarized emission: circularly polarized electroluminescence has been observed from WSe_2-based ambipolar transistors with a degree of circular polarization and handedness dependent on the relative orientation between the bias electric-field and the WSe_2 crystal [282].

The atomic thickness of 2D TMDs allows for their natural integration into photonic structures such as planar photonic crystal-cavities (see fig. 4.9.a)). Two effects occur in this coupled **TMD–cavity** system: the photonic band-gap effect and the Purcell effect. These effects lead to a significant enhancement in the

[12]Photoexcited carriers increase the device conductance, in photoconduction, while they are converted into current with the help of a built-in electric field, in photocurrent.

spontaneous emission-rate along the out-of-plane direction [252]. Due to those effects, ultralow-threshold lasing ($\sim 1\,Wcm^{-2}$ under continuous-wave pumping) in a coupled mono-layer WSe_2–cavity system has been reported and ascribed to the presence of the photonic crystal (see fig. 4.9.b)) [277]. To conclude, TMDs have shown promising application also in the field of **single photon emitters** for quantum computing. Recently, it has been demonstrated that isolated defects act as single-photon emitter in 2D WSe_2 [278]. In contrast to the broad line-widths ($\sim 10\,meV$) of free exciton emission, quantum dot-like defects exhibit very narrow ($\sim 0.1\,meV$) emission line-widths, see fig. 4.9.c). Moreover, correlation measurements have shown a photon antibunching characteristic of single-photon emitters [278]. These studies suggest exciting new opportunities offered by those single-photon emitters once embedded in atomically thin semiconductors. Besides, those emitters should be highly tunable, at variance with other solid-state single-photon emitters [252].

4.3.2 Electrocatalysis

It has been demonstrated that single-layer TMDs, in particular MoS_2 and WS_2 nanosheets, are some of the most promising non-precious electrocatalysts for **hydrogen-evolution reaction** (HER, $2H^+ + 2e^- \rightarrow H_2$). Hydrogen production (see fig. 4.10.a)) is very important because hydrogen represents one of the most promising energy sources [274]. In single-layer TMDs, two key-factors could improve HER: conductivity and active site density, whose increase would result in a higher catalytic activity. To this end, a variety of strategies have been developed to engineer functional hybrid nanomaterials based on TMD nanosheets with optimized conductivity and/or enriched active site-density [274]. As an example, it has been demonstrated that oxygen incorporation in MoS_2 nanosheets, as well as sulphur doping in $MoSe_2$, leads to an increase in the electrical conductivity, which turns into a higher catalytic activity for HER [283, 284]. Moreover, the unsaturated chalcogen-edge in TMD, induced by oxygen or sulphur introduction, is electrocatalytically active and beneficial for the HER process. It has been shown also that the 2H into 1T phase-conversion (see section 4.1) improves the HER catalytic performance, see fig. 4.10.b). As a matter of fact, an excellent electrocatalytic performance have been observed in chemically exfoliated MoS_2 nanosheets [285]. It was ascribed to the very high concentration of metallic 1T phase in the chemically exfoliated samples, which substantially improves the charge transfer kinetics of HER. Moreover, an electrochemical oxidation of the edges led to a dramatic reduction in the catalytic activity of 2H nanosheets, consistently with the oxidation of active sites for HER. On the contrary, the catalytic performance was unaffected by oxidation of 1T-phase nanosheets, thus suggesting that the active sites on 1T phase nanosheets are mainly located in the basal plane and the contribution of the 1T-phase metallic edges to the overall HER is relatively small [285], at variance with findings in 2H nanosheets.

Very recently, other processes have been developed to activate the basal plane in 2H MoS_2 nanosheets or bulk crystals[13] [286]. It was hypothesized and experimentally confirmed [286] that annealing in a hydrogen environment increases the active sites

[13] Pristine MoS_2 is predominately in the 2H crystal-phase rather than in the metallic 1T crystal-phase.

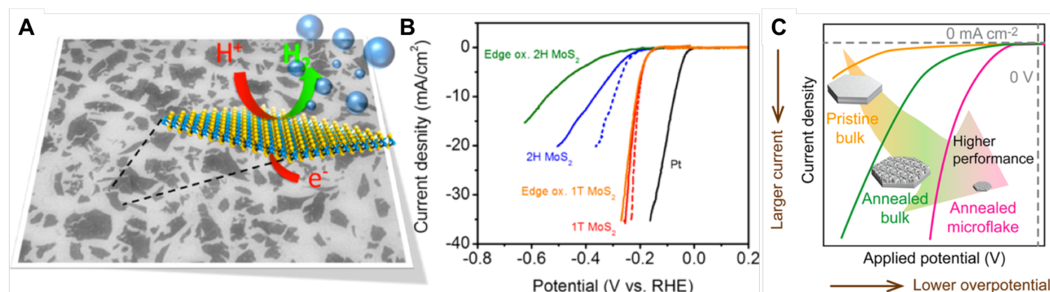

Figure 4.10. a) Schematic of hydrogen-evolution reaction on exfoliated MoS_2 single-layers. b) Polarization curves (current density vs applied potential) of 1T- and 2H-MoS_2 single-layer electrodes before and after edge oxidation. c) Schematic illustration of the polarization curves for pristine bulk MoS_2, annealed bulk MoS_2, and an annealed MoS_2 microflake. The annealing process is expected to improve the HER performance (higher current density), more dramatically for the MoS_2 microflake. After ref. [285, 286].

for HER and reduces the resistivity of the MoS_2 starting material; see fig. 4.10.c). In that process, hydrogen reacts with sulphur atoms in MoS_2 surface leading to the evolution of H_2S gas from the surface and to the formation in the (0001) plane of S-vacancies, edges, and clusters made of excess Mo-atoms. The removal of chalcogen atoms from their sites to generate edges on the basal plane is a promising mean to activate/improve the catalytic properties of other 2D materials. Finally, the highest intrinsic HER activity among molybdenum-sulphide-based catalysts was achieved by forming sulphur vacancies in the basal plane of MoS_2 2H-nanosheets by exposing the samples to a mild Ar-plasma and controlling their density by the Ar-plasma treatment-time. There, the hydrogen adsorption on the catalytic site was further increased by suitably straining the surface to achieve minima total energy for the MoS_2-H system at the S-vacancy sites [287].

4.3.3 Molecular sensing applications

TMDs are promising also in **molecular sensing** applications. As 2D materials, their high surface-to-volume ratio makes them particularly sensitive to changes in their surroundings. On exposure to gases and vapours, there can be changes such as charge transfer and doping, intercalation, and shifts in permittivity and lattice vibrations. The variations caused by the adsorbates can be detected in TMD transistor-devices electrically, by measuring the current–voltage behaviour, or optically, by changes in PL, absorption, or Raman spectra [235]. Photoluminescence would be particularly relevant in the **bio-sensing** field, where stable fluorescent markers are of importance for imaging and fluorometric measurements.

It has been demonstrated that MoS_2 FETs made by mechanically exfoliated single- to four-layer nanosheets can detect NO gas at room temperature [288]. As an example, the current response of a bilayer MoS_2 nanosheet-based FET that has been exposed to NO with concentrations ranging from 0.3 to $2\,ppm$ is shown in fig. 4.11.a). In the top right inset, the typical processes occurring in the device after NO exposure are highlighted. First, the current drops quickly for $\sim 30\,s$, then it smoothly decreases for more than 2 minutes until the saturation of NO adsorption

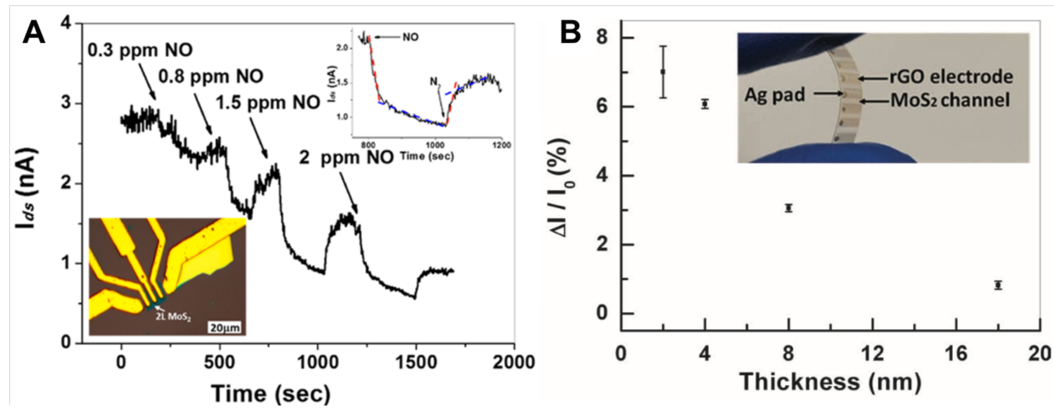

Figure 4.11. a) Real-time current-response after exposure of a bilayer MoS_2-FET to increasing concentrations of NO gas. Bottom inset: optical image of the device. Top right inset: typical adsorption and desorption processes of NO with rapid (red dashed lines) and slow steps (blue dashed lines). b) Plot of the detection sensitivity of $1.2\,ppm$ NO_2 versus the thickness of a MoS_2 film. Standard errors were obtained by measuring three devices. Inset is an optical image of the device on a polyethylene terephthalate substrate. After ref. [288, 289].

is achieved. Therein, good performances were achieved in FETs fabricated with either bi- or four-layers. On the contrary, single-layer devices presented an unstable response [288].

Furthermore, a flexible NO_2-gas sensor based on a hybrid structure made of MoS_2 covered by graphene oxide was fabricated on a polyethylene terephthalate (PET) substrate [289]; see inset in fig. 4.11.b). Therein, the dependence on the MoS_2 film-thickness of the device sensitivity towards NO_2 was also investigated, see fig. 4.11.b): the device sensitivity decreases dramatically with increasing MoS_2-film thickness, most likely because the thicker the film is, the lower the surface-to-volume ratio of the MoS_2 channel is. However, device current became unstable for thicknesses less than $4\,nm$, possibly because of not perfectly planar MoS_2 sheets. Those results point out that mechanically exfoliated multilayer MoS_2 nanosheets are promising channel materials for potential gas sensors.

4.3.4 Energy storage applications

The interlayer spacing of TMDs provides a convenient environment for the accommodation of a variety of guest species, for example Li^+ ions. *Bulk* TMDs such as MoS_2 and WS_2 have been investigated as electrode materials for **lithium ion batteries** because Li^+ ions can be easily intercalated or extracted from these materials [233]. Unfortunately, lithiation of these bulk compounds leads to structural instability during the exfoliation step, while their relatively low average-voltage and energy-density limit their potential as cathode materials. On the contrary, both *single and few* exfoliated-layers are to some extent very attractive as anodes for lithium ion-batteries. In fact, they do not suffer from the structural instability of loosely stacked bulk crystals and can accommodate easily structural changes [233].

Although the electrical conductivity of both bulk and exfoliated TMDs is too low

for the TMD effective implementation as electrodes in ion batteries, the coupling of layered TMDs with other materials, such as graphene, carbon or TiO_2 nanotubes, and Fe_3O_4 nanoparticles, may overcome this weaknesses [274]. Among those materials, graphene-based nanomaterials are the most studied and, *e.g.*, ion-battery anodes made of sheets of graphene oxide coated with few-layer MoS_2 were prepared via a hydrothermal method and investigated [290]. Thus, a high specific capacity ($\sim 1100\, mAhg^{-1}$ at a current density of $0.1\, Ag^{-1}$, even higher than that of pure MoS_2 and graphene sheets) was achieved with an excellent stability even after 100 cycles. The superior electrochemical performance of MoS_2/graphene composites as lithium ion-battery anodes was attributed to their robust composite structure and the synergistic effects between layered MoS_2 and graphene [290]. However, the unavoidable aggregation of TMD or graphene sheets during the electrode fabrication and the structure collapse during the discharging and charging process are harmful to the performance of batteries based on few-layer TMDs, whose surface area for lithium storage is also reduced with respect to the single layer case [274].

The stability after several cycles as well as the charge capacity have been improved by resorting to single-layer TMD-sheets. Recently, MoS_2 monolayers have been homogeneously embedded in carbon fibers and used as anodes for lithium ion-batteries [291]. Such a novel hybrid nanostructure exhibited a fascinating rate-performance and cycling-stability. Its initial discharge and charge capacities were 1712 and $1267\, mAhg^{\cdot 1}$ at $0.1\, Ag^{-1}$, respectively. More impressively, its capacity could be maintained at $661\, mAhg^{\cdot 1}$ even after 1000 cycles at very high current density ($10\, Ag^{-1}$). The excellent rate performance and cycling stability were ascribed to the unique nanostructure of this hybrid anode, very efficient for Li^+-ion storage because of its atomic thickness. Besides, the excellent mechanical property of carbon fibers wrapped around the MoS_2 single layer eliminates the expansion (shrinkage) problems during charging (discharging), making these structures very stable during cycling performances, at variance with multi-layer TMD-anodes. Lastly, the good conductivity and 1D character of the carbon matrix that is perfectly coupled with MoS2 sheets has allowed for an easy transport of Li^+ ions [274].

Chapter 5

Effects of hydrogen irradiation on single- and bi-layer TMDs

This chapter will be devoted to the description of the effects of hydrogen irradiation on the emission of single- and bi-layer TMDs, such as $MoSe_2$ and WSe_2. Both pristine and hydrogenated samples have been studied by means of either μ-PL or μ-Raman. In the first section of this chapter, the state of the art of VI-VI semiconductor MX_2 compounds will be presented. A wide variety of experimental results regarding MX_2 optical band-gaps obtained with different spectroscopic techniques will be summarized, together with the characteristic frequencies of the most common vibrational modes. Then, the motivations of our study will be highlighted and the use of a Kaufman source to implant hydrogen in single- and few-layer TMDs justified. A small part of the first section will be devoted to describe the investigated samples.

In the second section of this chapter, the optical properties of pristine $MoSe_2$ and WSe_2 will be investigated with room- and low-temperature results in good agreement with the existing literature. After a full characterization of each pristine flake, either single- or bi-layer, the TMD sheets have been hydrogenated, namely, irradiated with low-energy hydrogen ions by using a Kaufman source. In some cases, pristine flakes have been implanted with progressively increasing hydrogen-doses. Then, each hydrogenated flake has been investigated under the same experimental conditions used for its pre-characterization. In the single-layer regime, hydrogenation leads to a worsening of the flake optical quality and to the appearance of very sharp peaks in the forbidden band gap. Conversely, the PL-efficiency of bi-layer flakes slightly improves upon hydrogenation. Those results will be presented in the third section of this chapter. Finally, a cure for the worsening of the optical quality observed in single-layer flakes upon hydrogenation will be presented.

5.1 State of the art of MX_2 physical properties

Several experiments have been carried out to achieve an optical characterization of the electronic properties of VI-VI semiconductor TMDs[1], in the single- and multi-layer form [241, 260, 292, 293, 294, 295, 296, 297, 298]. Here, we will report

[1]From now on, we will refer to MoS_2, $MoSe_2$, WS_2, and WSe_2, as TMDs.

only low- and room-temperature data taken on single-layers deposited on SiO_2. In table 5.1, the experimental values of the optical band-gaps of MX_2 (with M=Mo,W, and X=Se,S) TMDs deposited on SiO_2 are reported (optical band-gaps instead of E_{gap} because of the huge exciton binding-energies in these systems, as already discussed in 4.1.1). The experimental values agree well between each other and with the theoretical predictions reported in table 4.2.

MoS_2	$MoSe_2$	WSe_2	WS_2
Low temperature optical band-gap (eV)			
1.92 [292] Absorp. @ $10\,K$	1.67* [293] Ref. @ $20\,K$	1.75* [298] Ref. @ $30\,K$	2.08 [296] Ref. @ $4\,K$
	1.66* [293] PL @ $20\,K$	1.74* [298] PL @ $30\,K$	2.04 [295] PL @ $4\,K$
Room temperature optical band-gap (eV)			
1.85* [241] Ref.	1.57 [260] PL	1.65 [260] PL	2.02 [297] Ref. and PL
1.83* [241] PL	1.55 [294] PL	1.66 [297] Ref. and PL	2.02[299] PL

Table 5.1. Experimental values of the optical band-gap in MX_2 TMDs, as assessed by optical spectroscopy at low (top part) and room (bottom part) temperature. The used spectroscopy techniques are: absorption (Absorp.), reflectivity (Ref.), and photoluminescence (PL). *: the differences between photoluminescence and reflectivity measurements performed in the same works (refs. [293], [298], and [241]) have been ascribed to the Stoke shift.

It is worth pointing out that the optical band-gap values sizably vary with the substrate on which the TMD sheet is deposited onto because the dielectric constant which rules the TMD giant exciton binding-energy depends on the medium surrounding the TMD single-layer. Very recently, it has been demonstrated that it is even possible to achieve a semiconductor-to-metal transition in single-layer TMDs, merely by a right choice of the substrate. Specifically, a single-layer WS_2 undergoes a semiconductor-to-metal transition when it is epitaxially grown on Ag(111) [300]. Moreover, as explained in sec. 4.1.1, the optical band gaps of TMDs depend also on the number of layers. Optical band gaps of n-layer TMDs with n$>$ 1 have not been reported in table 4.2 to avoid a piling of data in a single table. However, each PL spectra obtained from n$>$ 1-layer TMDs will be compared in due course to the existing literature.

Several experiments have been carried out to determine the frequencies of the most common vibrational modes in single- and multi-layer TMDs [256, 260, 294, 299, 301]. The experimental values of the Raman active modes of MX_2 (with M=Mo, W and X=Se, S) TMDs deposited on SiO_2 are reported in table 5.2. All the data have been taken at room temperature in a back-scattering configuration. The experimental values agree well between each other and with the theoretical predictions reported

	MoS_2	$MoSe_2$	WSe_2	WS_2
Frequencies of bulk vibrational-modes (cm^{-1})				
A_{1g}	408.7 [294] 408.6 [260]	243.0 [294] 242.5 [260]	250.8 [260]	420.5 [299]
E^1_{2g}	383.7 [294] 383.5 [260]	283.7 [294]	248.0 [260]	355.5 [299]
Frequencies of single-layer vibrational-modes (cm^{-1})				
A_{1g}	406.1 [294]	241.2 [294] 240.5 [260]	249.5 [256]	417.5 [299] 417.5 [301]
E^1_{2g}	384.7 [294]	287.3 [294] 287.2 [260]	249.5 [256]	356.0 [299] 356.0 [301]

Table 5.2. Experimental values of Raman active modes in bulk (top part) and single-layer (bottom part) MX_2 TMDs. Experimental values have been obtained at room temperature in the back-scattering configuration.

in table 4.3. It is worth pointing out that A_{1g} and E^1_{2g} frequencies in all compounds show opposite trends with respect to the variation of the number of layers, as already discussed in sec. 4.1.2. Also in table 5.2, the frequencies of vibrational modes of n-layer TMDs, with n> 1, are not reported to avoid the piling of a large amount of data in a single table. However, both mode frequencies shift monotonically with increasing number of layers on going from the single-layer to bulk TMDs.

Another important physical parameter in single-layer TMDs is the quantum-yield, which is defined in PL experiments as the ratio of number of emitted photons to number of absorbed photons. In single-layer TMDs, quantum yields ranging from 0.01% to 6% have been reported, which indicates a high density of defect states and mediocre optical quality. Those small quantum-yields have been attributed to both defect-mediated nonradiative recombinations and biexcitonic recombinations at high excitation power [242, 302, 303]. In the following, some of the methods developed to improve the TMD quantum-yield will be discussed, in particular the irradiation with low-energy hydrogen atoms.

5.1.1 Why hydrogen?

As anticipated previously, single-layer TMDs are characterized by very low quantum-yields. Those experimental evidences are quite surprising because ideal 2D systems have natural out-of-plane self-terminations, at variance with 3D materials, where terminations in the crystal lattice result in dangling bonds. Therefore, it could be expected that single-layer semiconductors should show near-unity PL quantum yield, whereas materials such as bulk GaAs require cladding layers (i.e., AlGaAs) to show a comparable performance [273]. However, several defects such as vacancies, edge- and point-defects lead to a rather low quantum-efficiency in TMD single-layer flakes. Fortunately, those single-layer TMDs also offer a unique opportunity for

defect passivation/repair because there is no distinction between bulk and surface defects, in such a way that the entire semiconductor can be accessed and perhaps repaired.

In the last four years, several chemical treatments have been developed to improve the quantum efficiency in single-layer TMDs [273, 302, 304, 305, 306]. An improvement by a factor of 3 in the excitonic emission was reported in mechanically exfoliated MoS_2 single-layers chemically treated with *2,3,5,6-tetrafluoro-7,7,8,8-tetracyanoquinodimethane* (F4TCNQ) [304]. Since the dominant PL process switched from a negative trion to an exciton recombination, that PL enhancement was ascribed to a balance of an unintentional high electron-doping in the pristine flake by a p-type chemical doping.

In mechanically exfoliated MoS_2 single-layers treated with an organic superacid (*bis(trifluoro-methane) sulfonimide*, TFSI) [302], the room-temperature PL-emission increased by a factor of 190 and a near-unity quantum-yield was achieved. Although the exact mechanism of surface defect passivation was not fully understood, it was partially ascribed to the strong protonating nature of the superacid, namely, to an easy release of hydrogen. Moreover, when $MoSe_2$, WS_2, and WSe_2 single-layers were treated with the same organic super acid [273], the defects in sulfur-based compounds were effectively passivated/repaired while those in the selenide-based materials were largely unaffected by the TFSI treatment. That different response to the chemical treatment of sulfur- and selenide-based compounds was ascribed to a drastic difference in the nature of the involved defects.

The PL emission of mechanically exfoliated MoS_2 single layers increased by a factor of 27 after a chemical treatment with low concentrations of H_2O_2 and *toluene* to form a sandwiched structure of H_2O_2/1L-MoS_2/toluene [305]. That improvement was ascribed to the p-doping character of the hydrogen peroxide. Finally, the PL of single-layer $MoSe_2$ grown by CVD increased upon an exposure to *hydrohalic acid vapors*, such as HCl, HBr, and HI [306]. In particular, the overall PL intensity of $MoSe_2$ increased by more than a factor of 30 after a HBr treatment, an increase ascribed to p-doping and/or removal of impurities.

All the aforementioned inprovements in PL efficiency were due to chemical treatments that could lead either to a p-type chemical doping or to the release of hydrogen ions. It is well known, indeed, that hydrogen passivates defects and dangling bonds in many III-V bulk-semiconductors, with an ensuing enhancement in the semiconductor optical quality [307]. Therefore, single- and multi-layer flakes were irradiated with low-energy hydrogen ions produced by a Kaufman source because:

- firstly, a Kaufman source allows an easy and precise tuning of the amount of implanted hydrogen ions, at variance with the chemical treatments described so far;

- secondly, several techniques allow a hydrogen irradiation of arbitrary samples with a space resolution of the order of tens of *nm*, by previous deposition on the sample of suitable H-opaque masks [308].

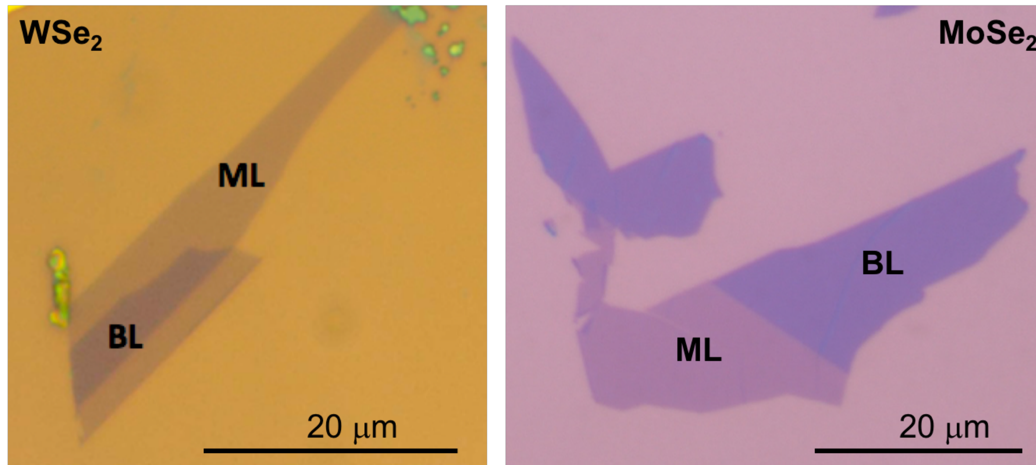

Figure 5.1. Optical microscopy images of both single- (ML) and bi-layer (BL) WSe_2 (left) and $MoSe_2$ (right) flakes. Those images were acquired with a 100× objective.

5.1.2 Investigated samples

In this thesis, mechanically exfoliated flakes of $MoSe_2$, MoS_2, WSe_2, and WS_2 have been studied. All the samples were mechanically exfoliated by 2H bulk-samples and deposited onto SiO_2/Si substrates because a simple optical model, which relies on Fabry-Perot interferometry, demonstrated that the visibility of either single- or few-layer flakes can be enhanced by choosing a proper thickness for the substrate oxide-layer [262]. Since MoS_2 and WSe_2 single-layers on 90 and 270 nm thick SiO_2 layers were optically detected [262], a SiO_2 thickness of 270 nm has been chosen to allow us a good visibility of single- and few-layer flakes.

In this chapter, only $MoSe_2$ and WSe_2 flakes exfoliated by the group of Prof. Yuerui Lu, in the *NEMS Laboratory* at *Australian National University* of Canberra, and by the group of Prof. Rinaldo Trotta, in the *Nanophotonics group* at the *Johannes Kepler University* of Linz, have been investigated. In the latter case, some single- and few-layer flakes have been identified by optical means before being capped with a thin layer of Al_2O_3 (30 nm) in order to study the effects of hydrogen irradiation and diffusion in flakes *protected* by an oxide cap-layer. It should be noticed that the capping layer itself worsens the visibility of single- and few-layer flakes. The dimensions of single-layer vary from few μm to hundreds of μm.

Typical optical-microscopy images of the studied samples acquired with a 100× objective are shown in figure 5.1. Single- (ML) and bi-layer (BL) uncapped WSe_2 ($MoSe_2$) flakes are shown in the left (right) panel. In all samples, the flake coloration varies from a transparent light blue to a more opaque dark blue with increasing number of layers.

5.2 Optical properties of pristine $MoSe_2$ and WSe_2

In this section, the number of layers and optical quality of a specific flake of pristine $MoSe_2$ and uncapped WSe_2 will be investigated by μ-Raman and μ-PL. Raman measurements, which more easily allow us to distinguish between single- and few-

layer flakes, will be discussed first. Then, a μ-PL linear map on a single-layer $MoSe_2$ will investigate the dependence of energy and intensity of FEs and trions on the position of the exciting laser beam over the flake surface. Finally, the study of the temperature dependence of the single-layer $MoSe_2$ PL will verify the FE nature of the optical recombination in TMD flakes.

5.2.1 μ-Raman investigation

The room-temperature ($T = 295\,K$) Raman spectra ($532\,nm$ laser excitation) collected from single- (blue) and bi-layer (red) uncapped WSe_2 flakes are shown in figure 5.2.a). First, single-layer Raman spectra will be discussed. A well defined peak and a high energy shoulder appear at $\sim 250\,cm^{-1}$ and $\sim 261\,cm^{-1}$, respectively. By a comparison with the literature, the sharp peak and the shoulder are ascribed, respectively, to the A_{1g} vibrational mode and to a second-order Raman mode of longitudinal acoustic phonons at the M point in the Brillouin zone, usually labeled as 2LA(M) [256, 309]; see also table 5.2. As regards the in-plane mode E^1_{2g}, polarization resolved Raman measurements demonstrated that this mode is degenerate with the A_{1g} mode in the single layer regime and shows up as a low-energy shoulder only when the number of layers increases up to 4 [256]. For the sake of clarity we do not report that mode in the figure.

In the bi-layer Raman spectra, the well defined peak ascribed to the A_{1g} mode once more appears at $\sim 251\,cm^{-1}$, namely, slightly blue-shifted with respect to single-layer case ($\sim 250\,cm^{-1}$). The high energy shoulder 2LA(M) at $\sim 259\,cm^{-1}$ red-shifts, instead, with respect to the single-layer case ($\sim 261\,cm^{-1}$). The weak peak at $\sim 309\,cm^{-1}$ is ascribed to the B^1_{2g} mode. It is due to the interlayer restoring forces, see fig. 4.5, and thus is the fingerprint of few-layer WSe_2 flakes [256, 309]. The flake bi-layer nature is confirmed by the $\sim 1\,cm^{-1}$ blue-shift of the A_{1g} and $\sim 2\,cm^{-1}$ red-shift of the 2LA(M) modes, as already reported in ref. [256].

The low-temperature ($T = 295\,K$) Raman spectra ($532\,nm$ laser excitation) collected from single- (blue) and bi-layer (red) uncapped $MoSe_2$ flakes are shown in figure 5.2.b). A well defined peak and a high energy shoulder appear in the single-layer Raman spectra at $\sim 245\,cm^{-1}$ and $\sim 252\,cm^{-1}$, respectively. By a comparison with the literature, the sharp peak and the shoulder are ascribed, respectively, to the A_{1g} vibrational mode and to the two-phonon energy of the E^2_{2g} shear mode at the M point of the Brillouin zone [294, 309, 310]; see also table 5.2. The small energy difference ($< 5\,cm^{-1}$) with the corresponding values reported in the literature is due to the different lattice temperatures in the Raman measurements, namely, $295\,K$ and $5\,K$. As explained in ref. [294, 309], temperature mainly changes the atom equilibrium-positions: the interatomic distances increase with increasing temperature, which turns into a reduction of the interatomic forces and in a red-shift of the vibrational-mode energies. As a matter of fact, a linear extrapolation to low temperature ($5\,K$) of the data shown in ref. [309, 311] gives A_{1g} energy $\sim 244.7\,cm^{-1}$, a value very close to our result ($\sim 245\,cm^{-1}$). As regards the in-plane mode E^1_{2g}, it should be observed only for Raman excitation wave-length lower than the present one ($532\,nm$) [310].

In the bi-layer Raman spectra, once more the well defined peak ascribed to the A_{1g} mode appears at $\sim 246\,cm^{-1}$, namely, slightly blue-shifted with respect

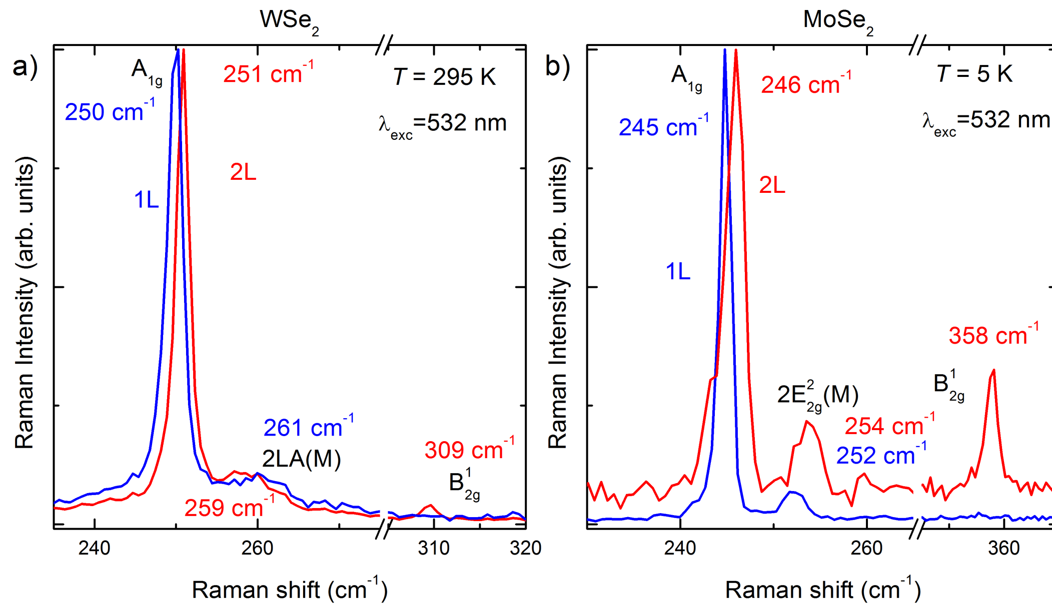

Figure 5.2. a) Room-temperature ($T = 295\,K$) unpolarized μ-Raman spectra ($532\,nm$ laser excitation) of single- (blue) and bi-layer (red) WSe_2 flakes. b) Low-temperature ($T = 5\,K$) unpolarized μ-Raman spectra ($532\,nm$ laser excitation) of single- (blue) and bi-layer (red) $MoSe_2$ flakes. The different vibrational modes are labeled following the notation discussed in sec. 4.1.2.

to single-layer case ($\sim 245\,cm^{-1}$). The high-energy E^2_{2g} shear-mode at $\sim 254\,cm^{-1}$ also blue-shifts with respect to the single-layer case ($\sim 252\,cm^{-1}$) . Once more, the fingerprint of a bi-layer regime is given by the B^1_{2g} mode at $\sim 358\,cm^{-1}$, in good agreement with previous results once the mode temperature-dependence has been taken into account [260]. The $\sim 1\,cm^{-1}$ blue-shift of the A_{1g} is consistent with previous results [260] and confirms the flake bi-layer nature. As regards the E^2_{2g} mode, its energy dependence on layer thickness is still unclear [312] and no meaningful information can be obtained from its energy variation.

The aforementioned discussion demonstrates the capability of Raman measurements to distinguish between single- and few-layer flakes, at room- and low-temperature. However, the tiny variation in the Raman vibrational-mode energies could be unsuitable in some cases, *e.g.* when a high resolution spectrometer is not available. In the next section, it will be shown that PL more than Raman measurements make it possible to easily discriminate single- from few-layer flakes, because the former are characterized by a direct band-gap transition, the latter by an indirect-gap transition.

5.2.2 μ-PL investigation

Room-temperature ($T = 295\,K$) normalized μ-PL spectra of single- (blue), bi- (red), and four-layer (olive) WSe_2 flakes ($P_{exc} = 1\,kW/cm^2$) are shown in figure 5.3.a). The single-layer spectrum shows an asymmetric band located at around $1.636\,eV$. At variance with typical room-temperature PL-spectra on III-V semiconductors, see for example PL spectra on InP NWs in the first part of this thesis, there is no Maxwell-

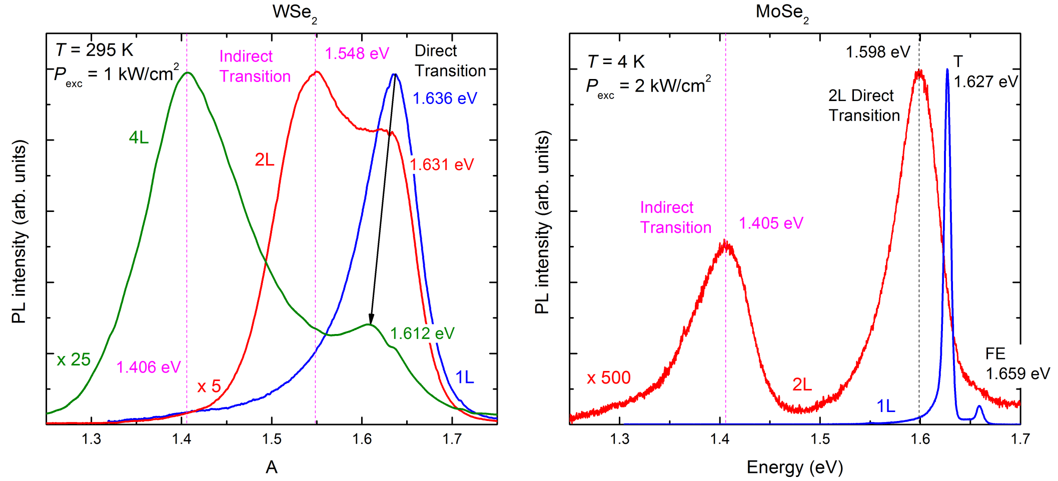

Figure 5.3. a) Room-temperature ($T = 295\,K$) normalized μ-PL spectra of single- (blue), bi- (red), and four-layer (olive) WSe_2 flakes ($P_{exc} = 1\,kW/cm^2$). The evolution of the direct band gap is highlighted by a black arrow, while the positions of the indirect band-gaps are denoted by purple dashed-lines. b) Low-temperature ($T = 5\,K$) normalized μ-PL spectra of single- (blue), and bi-layer (red) $MoSe_2$ flakes ($P_{exc} = 2\,kW/cm^2$). All the recombination bands in both bi- and single-layer regime are highlighted. Intensity factors are reported in both panels.

Boltzmann high-energy tail in these spectra because FEs in single-layer TMDs are not ionized, even at room temperature, and, therefore, band-to-band recombination does not sizably contribute to PL spectra. The presence of a low-energy tail, on the other hand, could be ascribed to surface bound-excitons, as already found in ref. [260]. Notice that small deviations of our results from those reported in table 5.1 are mainly due to different environments among samples caused by adsorbates or potential variations at the SiO_2/flake interfaces [260].

Two broad bands show up in the bi- and four-layer spectra. The high-energy shoulders ($\sim 1.631\,eV$ and $\sim 1.612\,eV$ for the bi- and four-layer cases, respectively) are due to direct transitions, whose energy is expected to slightly increase for decreasing number of layers, as described in sec. 4.1.1 and experimentally demonstrated [297]. On the other hand, the most intense peaks are ascribed to the indirect recombination bands, whose change in energy with increasing number of layers is fairly big, as already found in the literature [297]. Lastly, the indirect character of the optical band gap in bi- and four-layer flakes is confirmed by a progressive reduction of the PL intensity, even up to a factor of 25 in the four-layer case.

Low-temperature ($T = 5\,K$) normalized μ-PL spectra of single- (blue) and bi-layer (red) $MoSe_2$ flakes ($P_{exc} = 2\,kW/cm^2$) are shown in figure 5.3.b). The single-layer spectrum shows two sharp peaks. Similarly to previous attributions of the experimental peak energies in almost all single-layer TMDs, the most intense peak at $1.627\,eV$ is ascribed to a FE recombination, the weakest peak at $1.659\,eV$ is attributed, instead, to a trion (T) recombination [292, 293, 295, 298, 313, 314]. The energy difference between these two peaks ($\sim 32\,meV$) is equal to the trion binding-energy. In those previous works, the T recombination was ascribed to a negatively charged complex, namely a $e^- - h^+ - e^-$ triplet, because the electron

density exceeds the hole density in single-layer flakes. That n-type doping originates from an interaction of the substrate with the TMD flake, with an ensuing transfer of electrons from the former to the latter [276, 292]. The negative nature of the T recombination has been further confirmed by its suppression as a result of a chemically induced p-doping of TMD single-layers [304]. Finally, the asymmetrical low-energy broadening of the T peak is mainly due to defect recombination bands and bound excitons [295, 298].

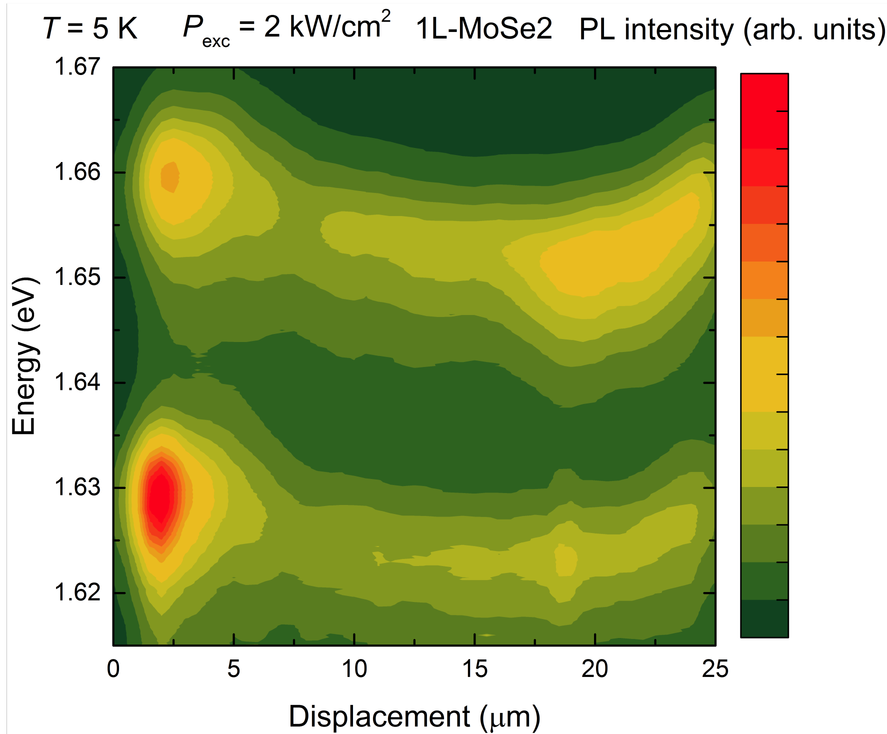

Figure 5.4. Contour plot of a linear μ-PL map acquired on a $MoSe_2$ single-layer flake at $T = 5\,K$ ($P_{exc} = 2\,kW/cm^2$). The relative displacement of the linear map is reported in the abscissa, the energy and intensity of each PL spectrum are reported, respectively, in the ordinate and in a color scale. Only the FE and T energy-region are shown.

The bi-layer spectrum shows two relatively broad recombination bands. As in the case of the WSe_2 bi-layer, the most intense band at $1.627\,eV$ is assigned to a direct transition, the weaker band at $1.405\,eV$ is attributed, instead, to an indirect transition. The $\sim 61\,meV$ red-shift of the direct transition on going from the single- to the bi-layer flake and the energy difference between indirect and direct transitions ($\sim 190\,meV$) resemble previous findings [313]. The emission intensity of the bi-layer flake decreases by a factor of $\sim$ 500 with respect to that of the single-layer flake, namely, much more than what observed in the WSe_2 case. This might be due to a difference in the oscillator strengths of the indirect transitions or to the energy separation between the direct and indirect emission energies in the two TMDs. The latter in WSe_2 is $\sim 90\,meV$, namely, much smaller than that energy separation in

$MoSe_2$ ($\sim 190\, meV$). Thus, the population of hot carriers that transiently occupy the direct band-edge at the K point in bilayer WSe_2 could be higher than that in bilayer $MoSe_2$ [297].

Another intriguing effect observed in single-layer TMDs, namely, the dependence of the energy and intensity of the FE and T recombination on the position over the flake of the exciting laser-beam will be now discussed. A contour plot of a linear μ-PL map, as taken on a $MoSe_2$ single-layer flake at $T = 5\, K$ ($P_{exc} = 2\, kW/cm^2$), is shown in figure 5.4. The energy and intensity of each PL spectrum in the map are shown in the ordinate and in the color scale, respectively, while the relative displacement of the exciting laser beam is given in the abscissa. Only the FE and T energy-regions are shown. The map has been taken along the cyan line reported in the inset of fig. 5.5.b). Therein, the $0\, \mu m$ position corresponds to the left diamond point, while the right diamond point corresponds to a $25\, \mu m$ displacement. Both the energy and intensity of the FE and T recombinations depend on the sample spot where PL emission is collected from. The FE and T energies and intensities move in parallel, namely, both peaks red-shift or blue-shift and decrease or increase at the same sample spots, as it can be better understood at a glance by looking at the data shown in figure 5.5. In panel a), the energy variation of the FE and T PL-peaks are shown, while the intensity variation of these same peaks are shown in panel b). The intensity values have been obtained by integrating over an energy range of $10\, meV$ centered on the corresponding PL peaks. Both peaks red-shift and their PL intensity decreases when the laser beam moves toward the center of the flake ($\sim 17\, \mu m$). The PL intensity at the map edges, especially at the "*free*" edge, *i.e.* the left edge in the optical image in the inset of fig. 5.5.b), is greater than that at the map centre. At the left map edge, at variance with the right map edge, the single-layer is not followed by a multi-layer flake, which in the optical image is characterized by a white coloration and almost null PL efficiency, but rather by a "*free-space*" region.

These effects have already been observed and tentatively explained in several experimental works performed in CVD grown [299, 306] and mechanically exfoliated [314, 315] single-layer TMDs. The most common hypotheses about the cause of those effects are:

- the environment surrounding the sample varies because of adsorbates at the SiO_2/flake interface [260];
- localized strains vary over the flake surface due to wrinkles (strained regions) in the flake itself [314, 315];
- lattice defects over the flake surface could generate local electric-fields, localize excitons, and create inhomogeneities in the exciton binding energy [299];
- n-type doping changes over the flake surface [306].

Contrary to our results, no correlation between the energy and intensity variations has been observed in refs.[260, 314, 315], where the first two hypotheses were made. In ref. [299], where the third hypothesis was made, the PL intensity at the flake edges was found to be greater than in the flake center, while the PL peak red-shifts at the edges (once again contrary to our results). Those observations were ascribed to a variation of the exciton binding-energy over the flake surface. In

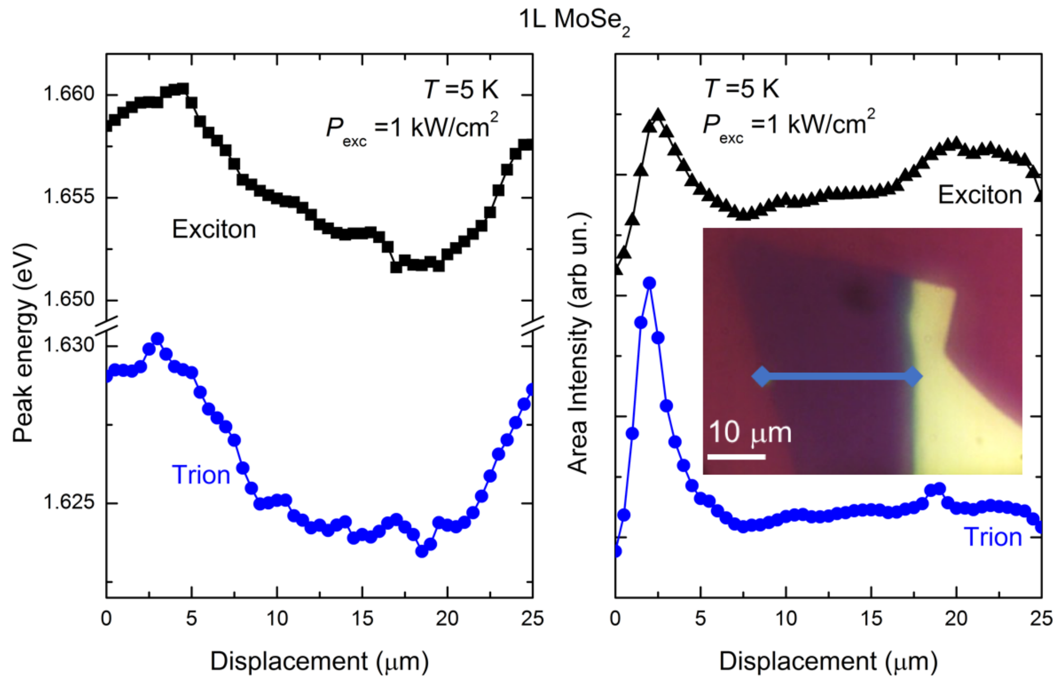

Figure 5.5. a) Peak energy of FE (black dots) and T (blue dots), as obtained by the linear map shown in fig. 5.4, versus the relative exciting laser-beam displacement. b) Area intensity of FE (black dots) and T (blue dots), as obtained by the same linear map, versus the relative laser-beam displacement. The inset is an optical image of the single-layer studied. The cyan line shows the region where the map has been acquired.

particular, the regions of highest exciton binding-energy (and thus lowest-energy PL emission) correspond to minima in an effective FE potential with an ensuing exciton accumulation and high PL intensity. Finally, an intensity increase and a peak-energy blue-shift at the flake edges, rather than in their center, of the FE peak was found in ref. [306], where the last hypothesis has been made, in agreement with our results. It is important to stress here that PL has to be collected from the same points in pristine and hydrogenated flakes whenever a comparison between those two results should be made, especially as regards the PL intensity.

Finally, the temperature dependence of the PL emission of a single-layer $MoSe_2$ flake is shown in figure 5.6. At low temperature, the normalized PL spectra ($P_{exc} = 2\,kW/cm^2$) are dominated by a trion contribution that quickly quenches with increasing temperature because of its relatively low binding-energy ($\sim 30\,meV$) and, for $T > 170\,K$, becomes negligible with respect to the FE contribution. The lack of a Maxwell-Boltzmann high-energy tail in the PL spectra suggests that the FEs are not ionized, even at room temperature, as usually observed in TMD single-layers because of the high exciton binding-energy ($\sim 0.5\,eV$); see also fig. 5.3.a). Finally, the overall PL intensity drops by a factor of ~ 300 for a temperature increase from 5 to 300 K (not shown here). In panel b), the PL peak-energy of both FEs and Ts is shown as a function of lattice temperature by blue and green dots, respectively. As commonly done in the literature [293, 313], the equation reported in the figure [316] has been fitted to the dependence on temperature of the FE and T energy.

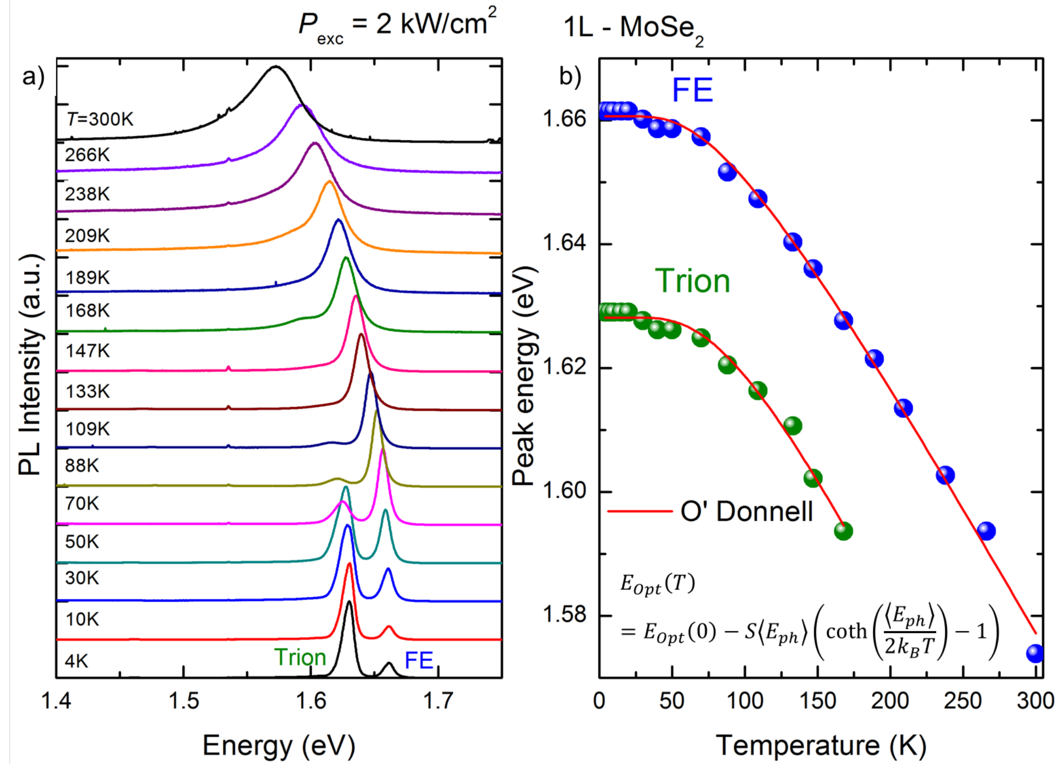

Figure 5.6. a) Normalized PL spectra of mono-layer $MoSe_2$ ($P_{exc} = 2\,kW/cm^2$) taken at lattice temperatures ranging from 4 to $300\,K$. FE and T emissions are highlighted. b) FE (blue dots) and T (green dots) PL peak-energy versus lattice temperature. Red lines are fits of the equation reported in the bottom part of the figure to the data.

In that equation, $E_{opt}(0)$ is the ground-state transition-energy at $T = 0\,K$, S is a dimensionless coupling constant, and $< E_{Ph} >$ is an average phonon energy. The fitted values are reported in table 5.3 together with other previous findings [293, 313]. A good agreement between our and previous results is found.

5.3 Optical properties of hydrogenated $MoSe_2$ and WSe_2

The effect of hydrogen irradiation over $MoSe_2$ and WSe_2 TMDs will be now discussed. Room-temperature PL spectra ($P_{exc} = 0.4\,kW/cm^2$) taken on *a same* point of a single-layer WSe_2 flake before and after successive hydrogen irradiations are shown in figure 5.7.a). Notice that the FE energy in the pristine PL spectrum varies by $\sim 15\,meV$ with respect to that taken in a *different* flake, see the blue PL spectrum in fig. 5.3.a). Moreover, it should be reminded that the FE energy depends on the specific point probed over the flake surface; see fig. 5.4 and the relative discussion. Hydrogen irradiations were performed at $T = 150°\,C$ with low-energy ($20\,eV$) protons generated by a Kaufman source; see sec. A.3. The red PL spectrum was taken after irradiation with an impinging H^+ dose equal to $H_0 = 10^{15}\,protons/cm^2$, the blue spectrum after a successive irradiation with an impinging H^+ dose equal to $5H_0$. The PL efficiency progressively worsens for increasing H^+ dose, with a worsening by

	Free Exciton			Trion	
	This thesis	[293]	[313]	This thesis	[293]
$E_{opt}(0)\ (eV)$	1.661	1.657	1.656	1.628	1.625
S	2.47	1.96	2.23	2.95	2.24
$< E_{Ph} >\ (meV)$	22	15	19	24	15

Table 5.3. Fitting parameters entering the equation for the temperature dependence of the free-exciton and trion energies reported in fig. 5.6.

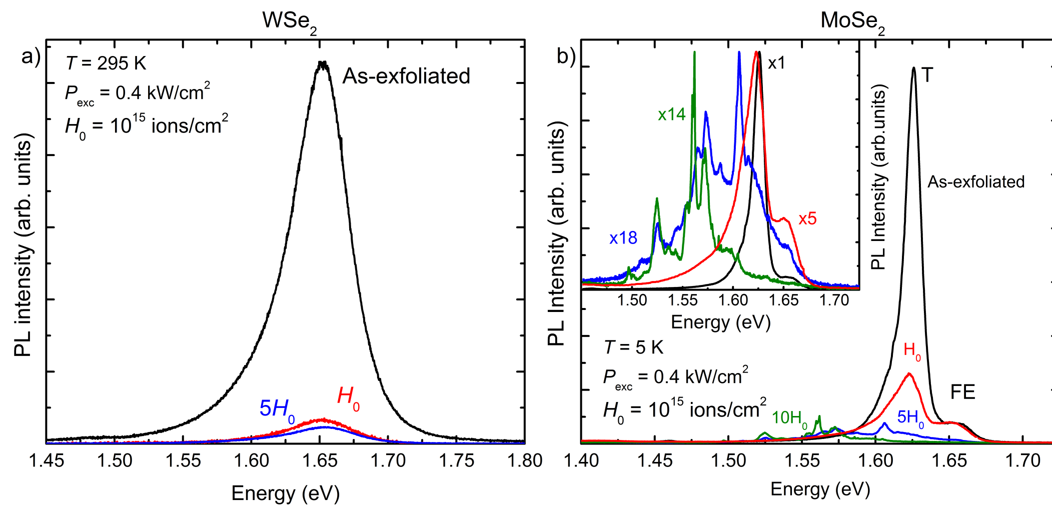

Figure 5.7. a) Room-temperature PL spectra ($P_{exc} = 0.4\,kW/cm^2$) of single-layer WSe_2 before and after successive hydrogen irradiations. b) Low-temperature ($T = 5\,K$) PL spectra ($P_{exc} = 0.4\,kW/cm^2$) of a same single-layer $MoSe_2$ before and after successive hydrogen irradiations. The inset shows the same spectra after having been normalized (normalization factors are reported).

a factor of 20 of the PL integrated intensity of the pristine flake with respect to that of the $6H_0$ $(5 + 1\,H_0)$ hydrogenated flake. Apart from that PL-intensity reduction, no other effect is observed after hydrogen irradiation, with a constant energy for the FE emission.

Different effects are observed at low temperature, as shown in figure 5.7.b). Therein, the PL spectra of a single-layer taken before and after successive hydrogen irradiations are shown. The pristine PL spectrum is similar to the blue one shown in fig. 5.3.b) but for broader T and FE emissions. The other PL spectra were taken on the same point of a same single-layer $MoSe_2$ flake after additive hydrogen irradiations, more precisely: H_0, $5H_0$, and $10H_0$ for the red, blue, and olive PL spectra, in the order. A progressive worsening of the PL efficiency for increasing H^+ dose was observed also in this case, with a maximum decrease by a factor of 14 in the PL integrated intensity of the $16H_0$ $(10+5+1\,H_0)$ hydrogenated sample with respect to the pristine sample. Moreover, the T and FE recombinations are progressively depleted in favor of multiple sharp emissions at energies lower than those of the FE and T bands, as it can be better seen in the inset where PL spectra are separately

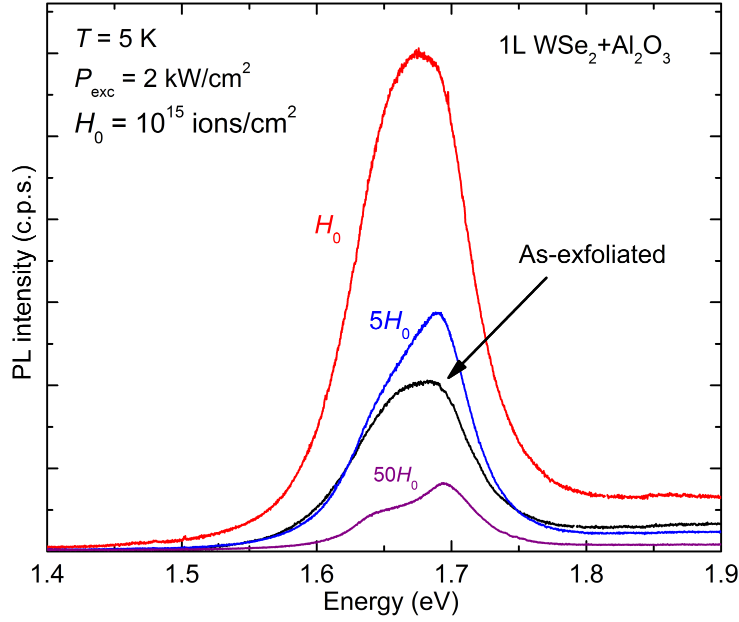

Figure 5.8. $T = 5\,K$ PL spectra ($P_{exc} = 2\,kW/cm^2$) of a capped single-layer WSe_2 before and after successive hydrogen irradiations.

normalized. Those extremely sharp peaks (FWHM$< 1\,meV$) are ascribed to the formation of bound excitons localized on impurities or defects likely due to the hydrogenation process. As a matter of fact, similar PL spectra have already been observed in pristine TMD flakes and ascribed to crystal structure imperfections that act as efficient carrier trapping centers as well as sources of single-photon emission provided these imperfections are suitably isolated [317, 318].

The TMD PL-efficiency decreased upon hydrogenation with a Kaufman source, both at low and room temperature, while it increased upon acid chemical treatments, as discussed in sec. 5.1.1. The main difference between our hydrogenation method and those reported in the literature is the way by which protons are *sent* to the sample. Since it is known that energetic-hydrogen irradiation can damage the surface of III-V bulk-semiconductors, one can speculate that present negative results are due to a mechanical damage of the single-layer surface, namely, of the TMD mono-layer itself.

To support the hypothesis of a surface mechanical damage induced by proton irradiation, a $30\,nm$ oxide cap-layer of Al_2O_3 was deposited on a single-layer WSe_2 flake. That flake was then investigated by PL at low-temperature ($P_{exc} = 2kW/cm^2$) before and after progressive hydrogenation, as shown in figure 5.8. The pristine PL spectrum shows a broad recombination band at $\sim 1.681\,eV$, an energy widely different from the FE energies reported in table 5.1. This difference is due to the different environment, an oxide capping layer instead of air, that surrounds the single-layer flake: the free-exciton binding-energy, and thus the PL peak energy, can be dramatically modified by changes in the surrounding dielectric medium [250, 300, 319]. On the other hand, low-energy ($20\,eV$) proton irradiations of the capped flake similar to those reported in fig. 5.7, namely, H_0 (red spectrum) and

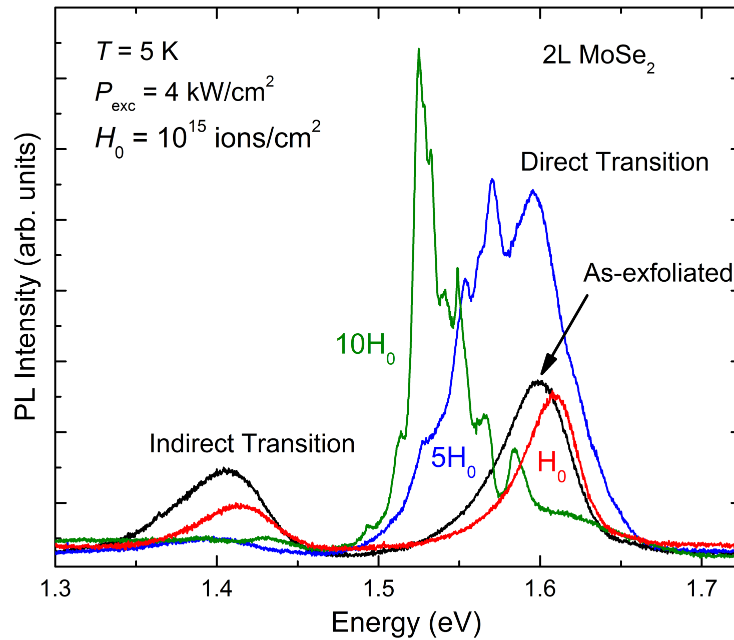

Figure 5.9. $T = 5\,K$ PL spectra ($P_{exc} = 4\,kW/cm^2$) of a bi-layer $MoSe_2$ before and after successive hydrogen irradiations.

$5H_0$ (blue spectrum), led to an initial factor of 3 increase in the overall PL intensity for the H_0 dose, followed by a decrease for the $5H_0$ dose. The purple spectrum was taken, instead, from the same flake irradiated with a $50H_0$ dose of $100\,eV$ impinging protons. In that case, the overall PL intensity decreased with respect to that of the pristine flake, namely, the results found in the uncapped flake were recovered even in the capped flake. Those results suggest that the oxide capping layer prevents the surface damage from the *physical act of H^+ bombardment*, at least for low-energy hydrogen-beams, absorbing a large part of the ion kinetic and thermal energy. Thus, protons come *gently* in contact with the flake, as in the chemical treatments, and may saturate non-radiative recombination centers without damaging the flake surface.

Lastly, the effect of hydrogen irradiation on a bi-layer $MoSe_2$ flake is reported in figure 5.9. The PL spectrum of the pristine bi-layer flake resembles the red one displayed in fig. 5.3.b). The other $T = 150°\,C$ PL-spectra were taken from the *same* point of the *same* bi-layer flake after successive hydrogen irradiations with low energy ($20\,eV$) protons. Irradiated hydrogen doses were H_0, $5H_0$, and $10H_0$ for the red, blue, and olive PL spectra, in the order. The intensity of the PL emission related to the indirect band-gap at $\sim 1.4\,eV$ monotonously decreases for increasing H^+ doses, almost vanishing at the highest dose. Conversely, the PL intensity of the high-energy direct band-gap initially increases ($5\,H_0$ dose) then it decreases ($10\,H_0$ dose). At the same time the peak center-of-mass red-shifts and sharp peaks appear at the highest doses (5 and $10H_0$). The latter are ascribed to the formation at high H doses of crystal defects on which excitons and carriers are trapped to, as in the single-layer case. These results suggest that hydrogen irradiation of bi-layer TMDs may even improve their optical efficiency like the first layer was acting as a cap protecting-layer, at variance with what reported in the uncapped single-layer regime,.

Finally, results similar to those described here have been reported very recently in few-layer MoS_2 uncapped flakes (2-, 3-, and 4- layers). Therein, proton irradiation causes a substantial ($> 10\times$) suppression of the room-temperature indirect band-gap emission and an approximately 2-fold increase in the direct band-gap emission. Those results, which are very similar to those presented here, were ascribed to some decoupling of the layers after proton irradiation [320].

Chapter 6

Hydrogen filling of bulk TMD domes induced by proton irradiation

In this chapter, the effects of hydrogen irradiation of n-layer ($n > 10$) TMD flakes will be presented. It will be shown that our hydrogenation procedure favors unique conditions for the production and accumulation of molecular hydrogen one or few mono-layers beneath the crystal surface of all the bulk MX_2 compounds investigated (M=Mo, W and X=S, Se). The hydrogen molecules thus produced coalesce to form bubbles. This leads to a localized swelling of one (or few) X-M-X planes with an ensuing creation of atomically thin domes filled with H_2. In the first section of this chapter, an atomic-force-microscopy investigation of these new kind of nanostructures will be presented. Furthermore, the mechanism by which domes form will be investigated and the evidence of molecular hydrogen inside the domes will be provided.

In the second section of this chapter, the new fascinating properties of that domes will be presented. Indeed, those domes show a strong light emission well above room temperature and can store H_2 indefinitely. In some cases, it will be shown that the dome PL-emission is even more efficient than that observed in single-layer flakes and that domes are one-layer-thick. Finally, μ-PL resolved in circular-polarization as well as AFM measurements will be reported. In the third section of this chapter, it will be shown that domes can be produced with the desired density, well-ordered positions, and a footprint size tunable from the nanometer to the micrometer scale. These results suggest that domes can be a template for the manageable and durable mechanical and electronic structuring of two-dimensional materials.

6.1 Domes formation in bulk TMDs

A multi-layer WS_2 flake has been irradiated at $T = 150°C$ with low-energy ($20\,eV$) protons using a Kaufman source, see sec. A.3. An optical microscopy image of that flake, acquired with a 50× objective, is shown in figure 6.1. The impinging H^+ dose is equal to $H_d = 8 \times 10^{16}\, protons/cm^2$. Circular spots spread out uniformly over the flake surface with diameters ranging from less than one to several micrometers.

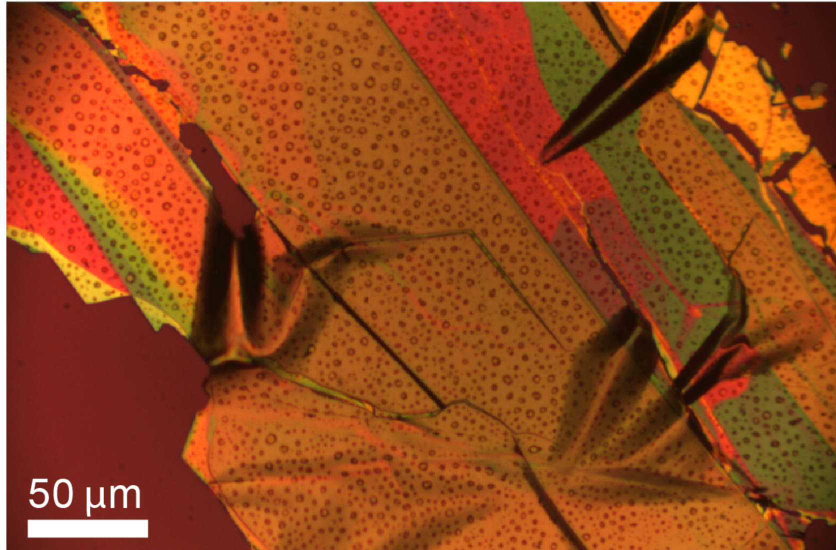

Figure 6.1. Optical microscopy image taken on a multi-layer WS_2 flake after irradiation with a proton dose $H_d = 8 \times 10^{16}\, protons/cm^2$. Round-shaped domes appear over all the flake surface.

It should be stressed that the flake surface was completely flat before the hydrogen treatment, but for few debris due to the mechanical exfoliation procedure. First, an atomic-force microscopy investigation of these new features, hereafter referred to as domes, will be presented. Then, the physical origin of the dome production upon hydrogen irradiation will be accounted for.

6.1.1 AFM investigation

An AFM image of a region of the multi-layer WS_2 flake displayed in fig. 6.1 is shown in figure 6.2.a). Therein, round-shaped domes protruding from the flake surface appear clearly. Those domes have an average footprint diameter $d = (1.43 \pm 0.12)\, \mu m$, a maximum height $h_m = (0.23 \pm 0.02)\, \mu m$, and display a virtually-perfect spherical-shape; see also figure 6.3. It is important to note that domes form almost everywhere and with the same average dimensions and density, independently of the layer thickness. As an example, the bottom part of the AFM image is characterized by a number of layers lower than that of the top, but it displays almost the same dome average-dimension and density.

The average dome-size can be controlled by varying the irradiated proton-dose, as illustrated in fig. 6.2.b). There, nanometer-sized structures with average $d = (164 \pm 40)\, nm$ and $h_m = (25.6 \pm 5.6)\, nm$ are obtained for a hydrogen dose equal to $H_d = 1 \times 10^{16}\, protons/cm^2$, namely, a dose height times smaller than that of fig. 6.2.a). Moreover, uniform and perfectly circular domes are obtained at this low H dose, at variance with the image displayed in fig. 6.2.a) for high H dose where coalescence of more domes into a single dome may lead to the formation of *irregular* multi-dome ensembles.

An AFM image of a single dome formed after H^+-irradiation of bulk WS_2 is shown in fig. 6.3.a), where the perfect circular shape of the dome is highlighted.

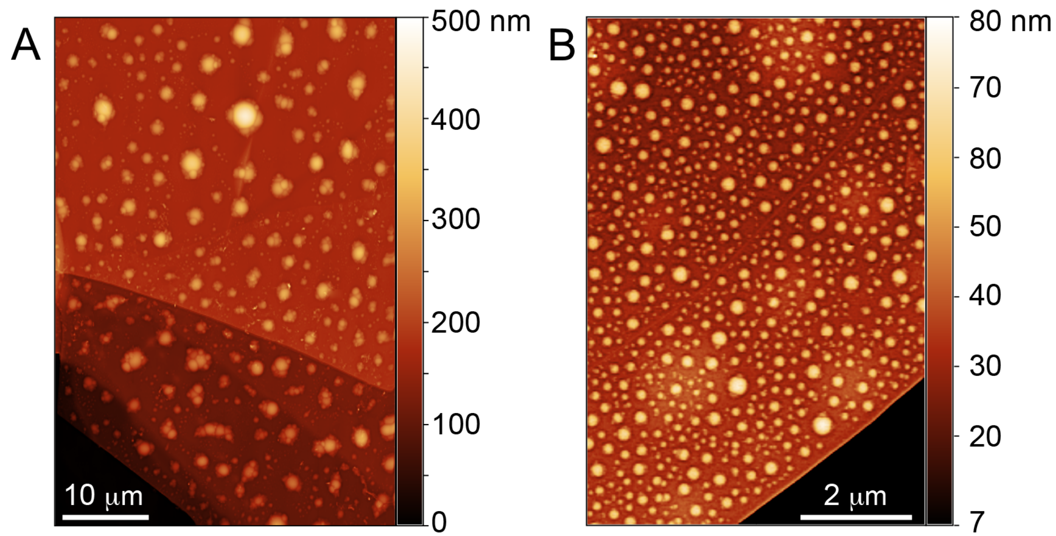

Figure 6.2. a) AFM image of a region of the multi-layer WS_2 flake shown in fig. 6.1. Round-shaped domes protrude from the flake surface after H^+ irradiation. b) AFM image of a bulk WS2 flake H^+-irradiated with a dose 8 times smaller than that of a).

This can be better perceived in fig. 6.3.b), where h_m (the maximum height of the domes with respect to their base) and d (the footprint diameter of the domes) are defined. In fig. 6.3.b), the AFM height profiles taken along the blue and red lines indicated in fig. 6.3.a) show that the AFM height profiles are independent of the directions along which they have been taken.

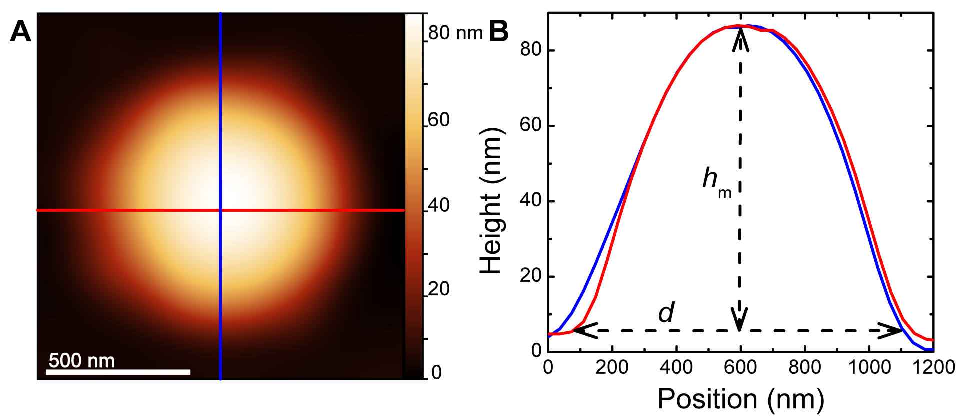

Figure 6.3. a) 2D AFM image of a single dome formed after H^+-irradiation of a multi-layer WS_2 flake. The spherical shape of the dome can be appreciated. Red and blue lines represent scan lines along which the profiles displayed in b) have been taken. b) AFM height profiles of the dome displayed in a), taken along two mutually perpendicular directions. Thick dashed lines define the geometrical meaning of h_m and d. Notice the very low aspect ratio of the dome.

So far, only results on multi-layer WS_2 flakes have been shown. However, domes form in each MX_2 material, as shown in figure 6.4. Therein, 3-dimensional (3D) AFM images of every MX_2 bulk compound investigated in this thesis and treated

under a same irradiation process (impinging dose equal to $5 \times 10^{16}\, protons/cm^2$) are displayed. Each AFM map has been recorded on an area equal to $5 \times 5\, \mu m^2$. The values close to the top of each dome give the maximum height of that dome. The significant size variations observed upon the considered compound will be the object of future studies. Till now, the dome dimensions of tungsten based compounds seem to be bigger than those of the correspondent molybdenum compounds. Furthermore, the average dome dimensions decrease with increasing chalcogen atomic number in compounds with the same transition metal.

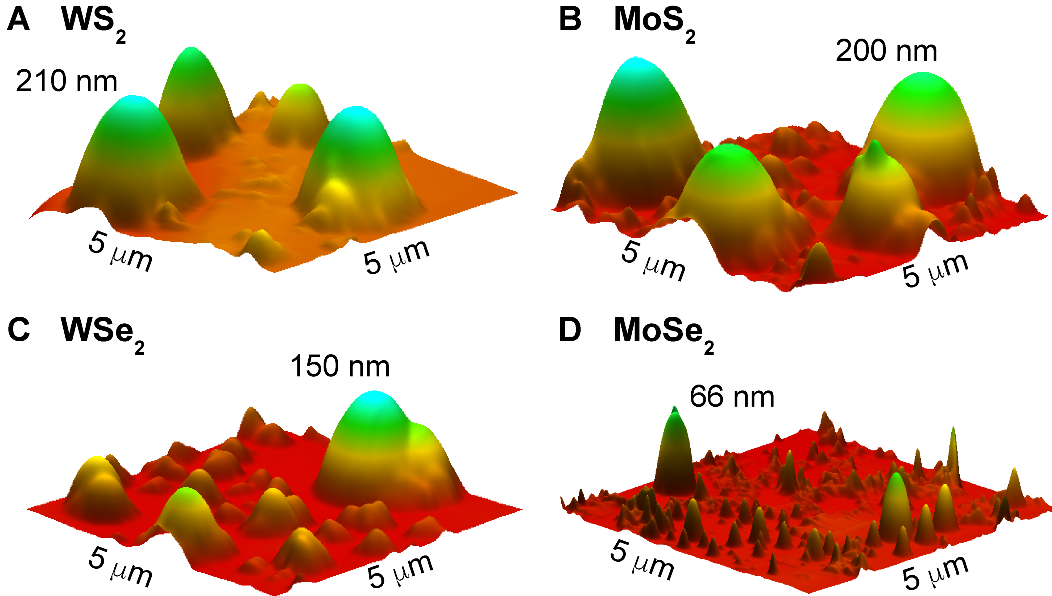

Figure 6.4. 3D AFM images of TMD bulk samples after H^+ irradiation with an impinging dose equal to $5 \times 10^{16}\, protons/cm^2$ (the samples were treated under the same irradiation conditions). Each AFM map was recorded on an area equal to $5 \times 5\, \mu m^2$. The values close to the top of each dome give the maximum height of that dome.

Finally, we stress that dome formation is exclusively due to the interaction of multi-layer flakes with protons. No effect was found in samples exposed to molecular hydrogen or ionized helium atoms, which suggests a prominent role of protons in the dome formation. In the next subsection, the dome physical origin will be discussed.

6.1.2 Is there something inside the domes?

Information on the nature of domes is provided by a study of their evolution with temperature. The room-temperature ($T = 300\, K$) and low-temperature ($T = 4\, K$) optical microscopy images of a bulk WS_2 sample irradiated with $H_d = 8 \times 10^{16}\, protons/cm^2$ are shown in figures 6.5.a) and 6.5.b), respectively. At $T = 300\, K$, many circular fringes, whose origin will be discussed in the following, appear in the domes. At low temperature, instead, the domes disappear and the sample surface looks flat, but for some debris due to the mechanical exfoliation procedure.

The insets in fig. 6.5.c) illustrate some sudden dome bulge (within $10\, mK$ at most, namely, our experimental resolution) at about $T = 30\, K$. The transition

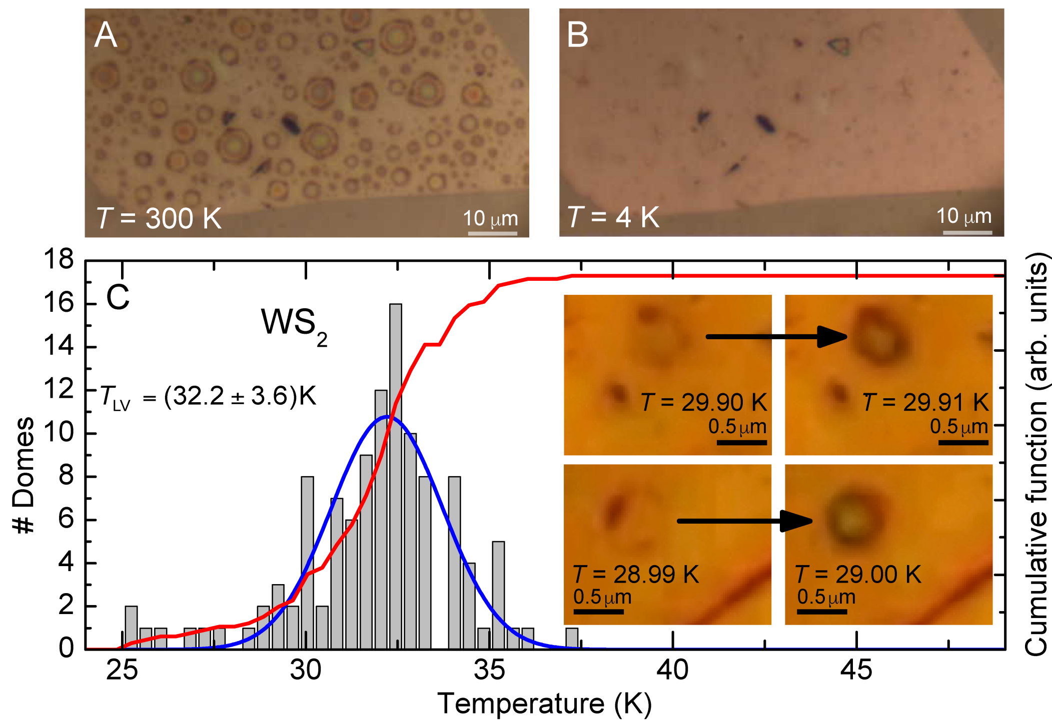

Figure 6.5. a) $T = 300\,K$ optical microscopy image of a H^{+}-irradiated ($H_d = 8 \times 10^{16}\,protons/cm^2$) WS_2 sample. b) Same as a) but for $T = 4\,K$. c) Histogram of the transition temperature T_{LV} at which domes appear (left axis). The blue line is a Gaussian fit to the data. The red line is the histogram cumulative function (right axis). The insets are optical microscopy images of two domes taken at two temperatures near to the transition temperature and differing by $10\,mK$. The arrows highlight the regions where the domes are formed.

temperature depends slightly on the dome considered, as shown by the histogram and the corresponding cumulative function in the main part of fig. 6.5.c). Therein, each bin reports the number of domes that swell out at a specific temperature. An average transition temperature $T_{LV} = (32.2 \pm 3.6)\,K$ has been estimated from the investigation of more than 120 WS_2 domes. That temperature value is close to that of the critical temperature of H_2 $(33.18\,K)$[1]. It suggests, therefore, the presence of molecular hydrogen inside the domes: when the temperature is low (high) enough, H_2 liquefies (boils) and the domes deflate (inflate) at the same position on the sample, regardless of the temperature arrow. The presence of any other substance liquefying near those low temperatures,*e.g.* helium, neon, *etc* should be excluded: high vacuum conditions ($P = 10^{-7}\,mbar$) are achieved in the hydrogenation chamber before a hydrogen flow is introduced in the camera and a dynamic pressure of $P = 10^{-4}\,mbar$ is established.

Finally, according to the H_2 phase diagram [321] and to the estimated average liquid-vapor transition-temperature of $32.2\,K$, a dome internal pressure $P_{int} =\sim 10\,atm$ has been evaluated. Thus, the colored rings characterizing the large domes

[1]The critical temperature of a substance is defined as the temperature above which vapor of the substance cannot be liquefied, no matter how much pressure is applied.

in fig. 6.5.a) can be ascribed to Newton's rings caused by the interference of the light reflected inside the H_2-filled spherical domes [322].

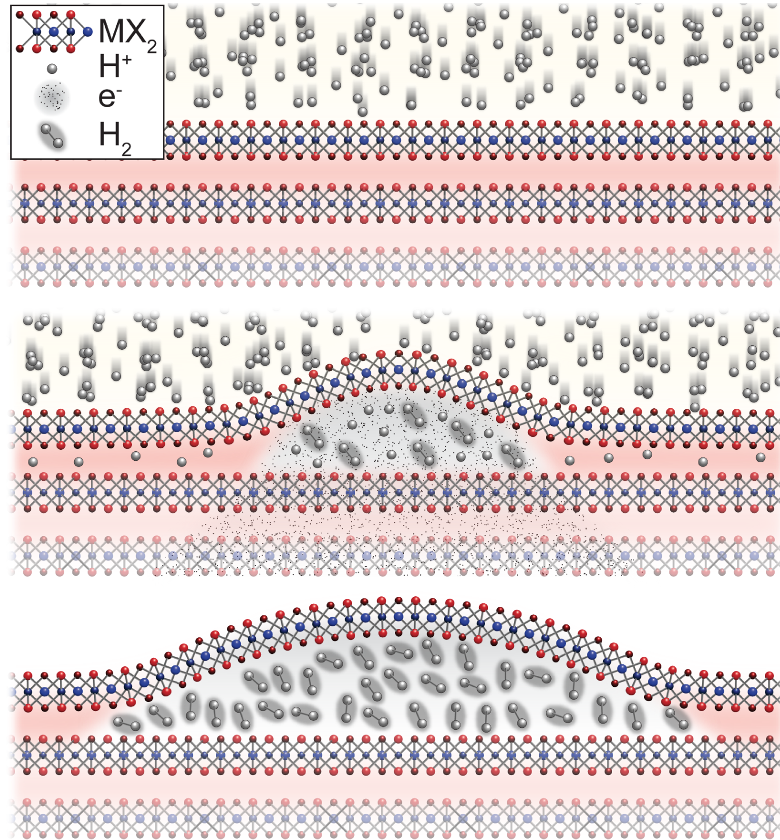

Figure 6.6. Sketch of the process steps leading to the dome formation by a local blistering of TMD surface layers. Top: protons impingement on the flake surface. Middle: proton-electron interaction below the first surface mono-layer to form neutral atomic and molecular hydrogen. Bottom: blistering of a thin dome.

The process ruling the formation of molecular hydrogen beneath one or a few atom-thin layers will be now tentatively explained, although further studies are necessary, in particular to understand the role played by the crystal composition. In the proton irradiation process, a fraction of the protons impinging on the MX_2 surface (top part of figure 6.6) are confined in between two X-M-X layers. Therein, the catalytic activity of TMDs [286, 287, 323] triggers the formation of molecular hydrogen according to the $2H^+ + 2e^- \rightarrow H_2$ reaction, where the electrons e^- are supplied by the ground contact (middle part of fig. 6.6). The build-up of H_2 molecules, stored just beneath the MX_2 surface, leads to a local blistering of one or few X-M-X layers and eventually to the dome formation (bottom part of fig. 6.6). The above scenario is supported by previous studies showing that thermal protons do not diffuse through X-M-X planes, thus favoring a H_2 storage [324, 325]. Another proof of the catalytic role played by TMDs in the dome formation will be provided in sec. 6.3.

6.2 Light emission from domes

The most intriguing effect of dome formation is the PL emission from the domes themselves. An optical image of the multi-layer WS_2 flake displayed in fig. 6.1 and exposed to an external excitation in the configuration described in sec. A.1 is shown in figure 6.7.a). Therein, the sample exhibits a strong PL emission in the red wave-length region ($\lambda \sim 690\,nm$), which is totally unexpected for an indirect-gap bulk WS_2, as discussed in section 4.1.1. The top right inset shows the same sample in the absence of laser excitation (this optical image is taken at a lower magnification of the image displayed in fig. 6.1). The bottom left inset shows how a PL emission shaped like perfect circles originates from the domes. The orange boxes in the figure highlight the region from where the AFM image displayed in fig. 6.2.a) has been acquired.

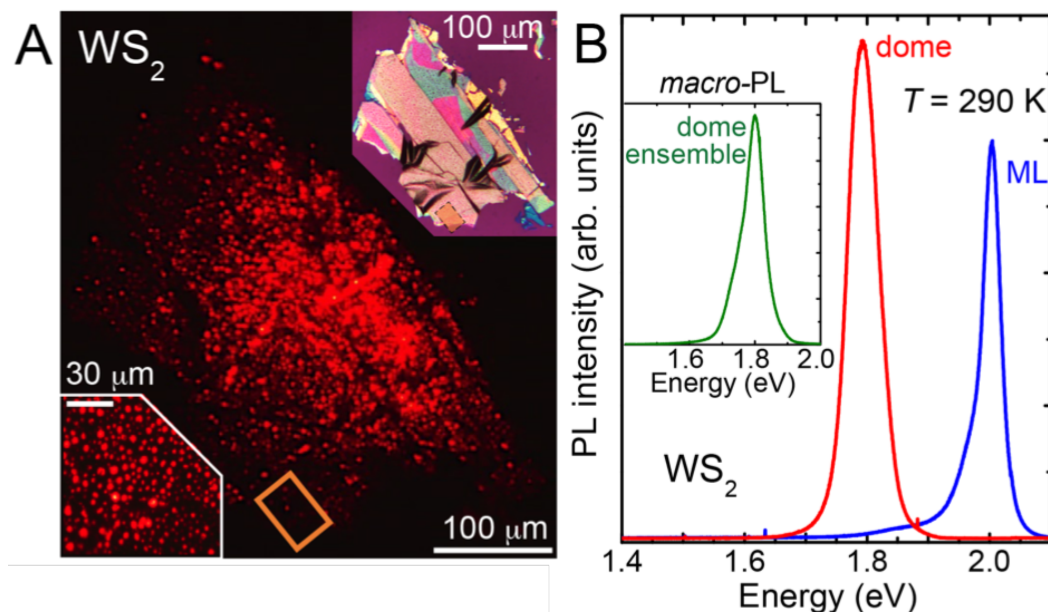

Figure 6.7. a) Optical microscopy image of the laser-excited red luminescence of a bulk WS_2 flake irradiated with a proton dose $H_d = 8 \times 10^{16}\,protons/cm^2$ and shown in fig. 6.2.a). The top-right inset shows the same sample in the absence of a laser excitation. The bottom-left inset is a zoomed-in image of the main picture showing the round shape of the emitting spots. Orange rectangles highlight the region from where the AFM image displayed in fig. 6.2.a) has been acquired. b) μ-PL spectrum of a dome (red line) singled out from the ensemble displayed in a). The blue line is the PL spectrum of a WS_2 mono-layer flake. The inset shows the macro-PL spectrum of an ensemble formed by ~ 2500 domes.

The spectral composition of the light produced by one dome (singled out from the ensemble shown in fig. 6.7.a)) is provided by the μ-PL spectrum shown in fig. 6.7.b). The luminescence of an untreated WS_2 mono-layer measured under the same excitation/collection conditions is also shown for comparison. The energy of the PL peak (corresponding to the free-exciton recombination) of the WS_2 dome is $\sim 200\,meV$ lower than that of the single-layer because of the biaxial strain

on the dome spherical-surface [326, 327], as it will discussed in the following. In addition, the PL intensity of the dome is greater than that of the WS_2 mono-layer, as systematically observed for dome diameters $\geq 1\mu m$. No major additional line-width broadening is observed when many of such domes are measured all together, as demonstrated by the macro-PL spectrum acquired from an ensemble of ~ 2500 domes and shown in the inset of fig. 6.7.b). This result suggests that PL dome-emission is almost uniform and no variation of the PL peak-energy from dome-to-dome is expected. The reason behind this experimental evidence will be discussed in the following.

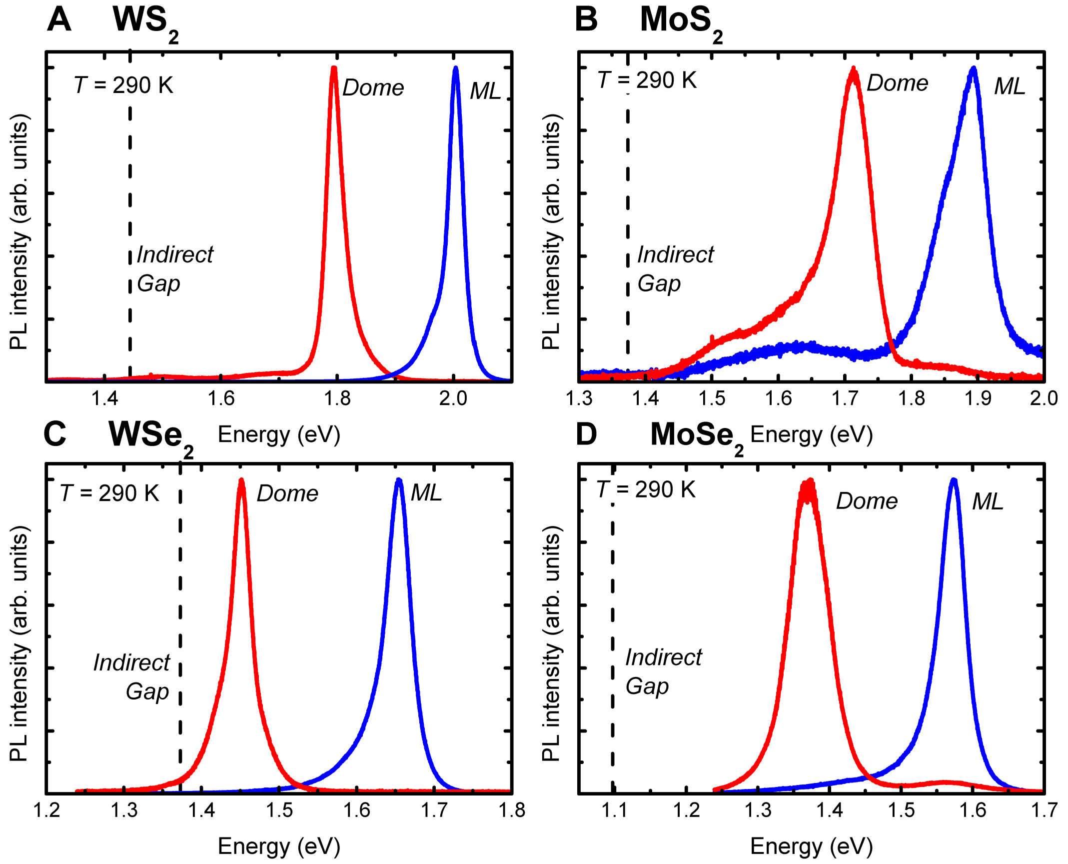

Figure 6.8. Room temperature μ-PL spectra of single domes formed on four MX_2 compounds (red lines) [and corresponding to the AFM images in fig. 6.4] after H^+ irradiation with an impinging dose $H_d = 5 \times 10^{16}\, protons/cm^2$. The emissions from mono-layers of the same compound (blue lines) are also shown, for comparison purposes. The excitation power density is equal to $30\, W/cm^2$. The dashed lines indicate the energy of the indirect gap in the bulk material. Each spectrum is separately normalized.

Dome PL-emission is not a peculiar characteristic of WS_2 but rather a general phenomenon independent of the specific MX_2 compound. The room-temperature μ-PL emissions ($P_{exc} = 30\, W/cm^2$) from single domes of each MX_2 compound investigated in this thesis (red lines) and their corresponding mono-layer PL emissions (blue lines) are shown in figure 6.8. Therein, each spectrum is separately normalized for the sake of clarity and the dashed lines indicate the energy of the indirect gaps

of the bulk materials. For each compound, the energy shift of the PL peak between the dome and the mono-layer varies between 180 meV (MoS_2) and 210 meV (WS_2). As in the WS_2 case, those shifts are due to the biaxial strain exerted on the dome spherical surface. Notice that the narrowest PL spectra are shown by the tungsten-based compounds, mirroring at some extent what happens in the mono-layer case. All the aforementioned findings demonstrate that indirect-gap bulk MX_2 compounds can be turned into *efficient light emitters* without the size restrictions typically affecting exfoliated flakes or samples grown by chemical vapor deposition: exfoliated or CVD grown flakes have typical sizes ranging from tens to hundreds of micrometers, while few millimeter flakes have been hydrogenated with eye-naked PL-observation.

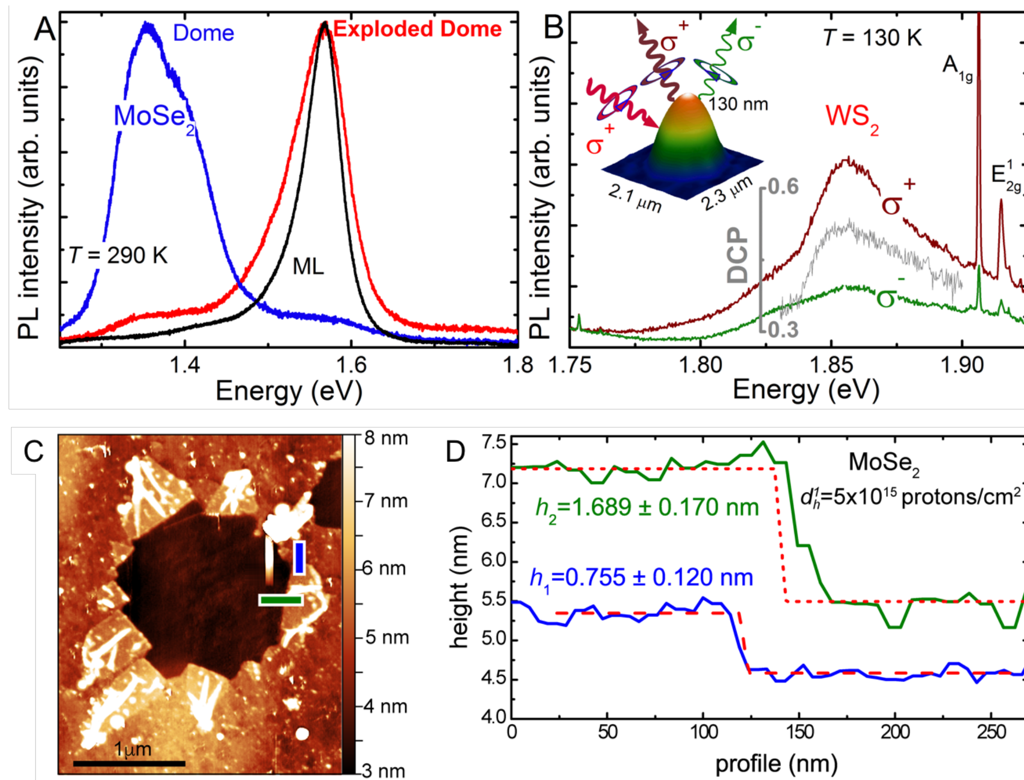

Figure 6.9. a) Room temperature μ-PL spectra recorded on: an as-formed $MoSe_2$ dome (blue line), the edges of the dome after its explosion (red line), a reference mono-layer $MoSe_2$ flake (black line). The dome was obtained with a hydrogen dose $H_d = 5 \times 10^{15}\, protons/cm^2$. b) Circular-polarization-resolved μ-PL spectra of a WS_2 dome (whose AFM image is shown in the inset) excited by a σ^+ 632.8 nm laser line. The resulting degree of circular polarization is shown by a grey line. Raman lines of in-plane $E^1_{2g}(\Gamma)$ and out-of-plane $A_{1g}(\Gamma)$ modes are also visible. c) 2D AFM image taken on the exploded $MoSe_2$ dome whose PL spectra are shown in 6.9.a). d) AFM-profile measurements taken along the green and blue bars highlighted in 6.9.c). Red dashed lines are fits of an edge function to the data. The blue line refers to the step from a patch around the pristine dome footprint to the area outside the dome, while the green line refers to the step from this same patch to the area inside the dome.

The high dome radiative-efficiency (in some cases even higher than that of single-layers) suggests that the dome peel should be made of a single X-M-X plane.

That educated guess is supported by the data shown in figure 6.9.a). Therein, μ-PL measurements of a $MoSe_2$ dome[2] are shown before (blue line) and after (red line) having been exposed for $\sim 10\,s$ to a focused laser beam ($4\,kW/cm^2$). The ensuing increase in the H_2-gas temperature led to the expansion of the bubble and hence to its explosion. The μ-PL data acquired at the edges of the exploded dome nearly overlap those of a reference $MoSe_2$ single-layer flake (black line). That evidence strongly supports a single-plane-thin dome-peel, as further well confirmed by the AFM image collected from the dome region after the dome explosion and shown in fig. 6.9.c). The crater replacing the dome footprint should have a depth equal or close to that of one of the patches from which the dome was build up before its explosion. The blue [green] curve in fig. 6.9.d), taken along the blue [green] bar highlighted in fig. 6.9.c), is a measurement of the difference in the heights of one of those patches and that of the area outside [inside] the dome. That curve is well fitted by a step function of $(0.76 \pm 0.12)\,nm$ [$(1.69 \pm 0.17)\,nm$], namely, a value close to that of a single [double] Se-Mo-Se plane ($0.7\,nm$) [$(1.4\,nm$].

Finally, the guess of a dome-peel made of a single X-M-X layer has been further confirmed by circular-polarization-resolved μ-PL measurements performed by using a linearly polarized He-Ne laser as excitation source ($\lambda_{exc} = 632.8\,nm$). An achromatic quarter-wave plate was placed just before a $50\times$ objective to obtain a circularly polarized excitation of the sample and prevent any mirror-induced elliptical distortion. The PL emission was then analyzed as a function of its circular polarization degree by exploiting the same achromatic quarter-wave plate and a combination of a variable retarder half-wave plate followed by a linear polarizer. Those measurements, when performed on a single WS_2 dome whose 3D AFM image is shown as inset in fig. 6.9.b), demonstrate that the light generated by the exciton recombination in a single WS_2 dome is circularly dichroic, with a degree of circular polarization (DCP) $> 50\%$ at $T = 130\,K$, as shown by the gray line in the same fig. 6.9.b). This is an intrinsic property of the hexagonal symmetry of the first Brillouin zone of single-layered TMDs, as explained in sec. 4.1.1 and shown in figure 6.10.a). Therein, the light generated by the exciton recombination in a single-layer MoS_2 flake results to be circularly dichroic, with a DCP value ($\sim 60\%$ at $T = 130\,K$) comparable to that of the single WS_2 dome shown in fig. 6.9.b). The choice of a MoS_2 single-layer (with an energy gap corresponding to $650.7\,nm$ at $T = 130\,K$) is dictated by the necessity to have nearly resonant excitation to better observe a circular polarization dichroism, a condition not satisfied in the case of a WS_2 *single-layer*. Therefore, this measurement strongly supports our hypothesis of a dome-peel thickness equal to a single X-M-X layer.

Although single-layer domes are encountered more often, two- or even more-layer thick domes have been also observed, as shown in figs. 6.10.b), c), and d). Fig. 6.10.b) shows circular-polarization-resolved μ-PL measurements performed on a single WS_2 dome different from that of fig. 6.9.b). The resulting DCP at the free-exciton energy is about 5%, which suggests that the dome under consideration should be thicker than a monolayer. It should be pointed out that the PL efficiency in the case of dome peels greater than one layer is likely enhanced by the built-in

[2]The multi-layer flake where the dome formed was treated with a hydrogen dose $H_d = 5 \times 10^{15}\,protons/cm^2$.

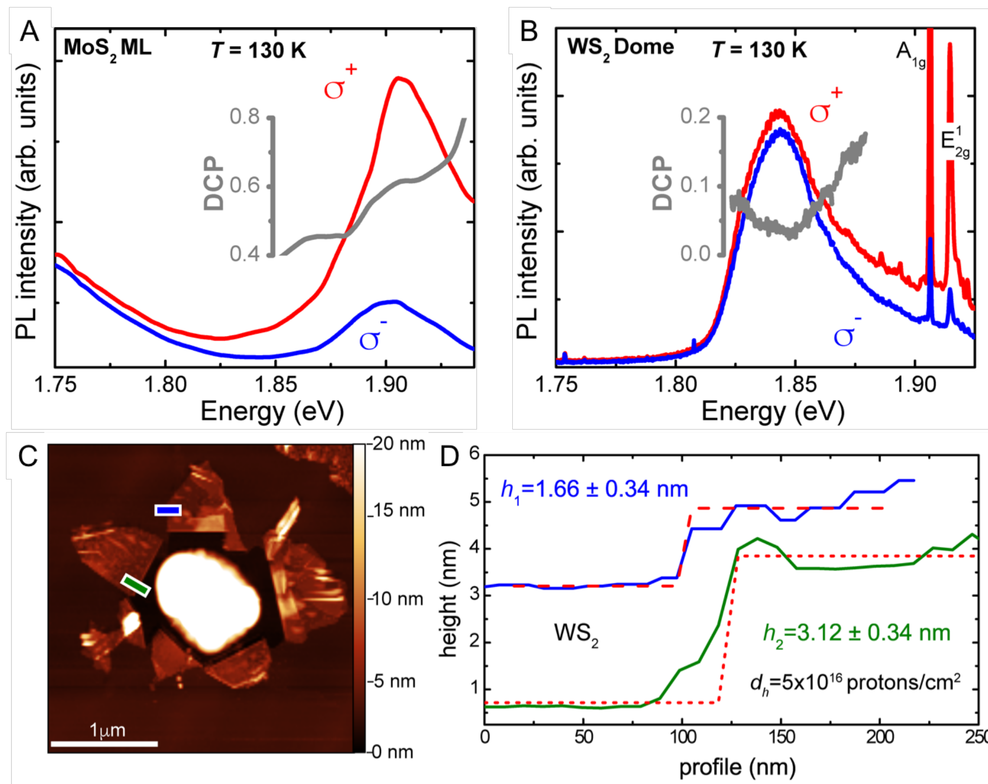

Figure 6.10. a) μ-PL spectra at $130\,K$ of a MoS_2 mono-layer excited by a σ^+ circularly polarized $632.8\,nm$ laser. The emission spectra were filtered by $\sigma^\pm$ polarization resulting in the degree of circular polarization (DCP) shown by the grey line. b) Same as a) but on a WS_2 single dome. c) 2D AFM image taken on an exploded dome of a WS_2 multi-layer flake containing another dome inside (Russian-doll like). The sample was exposed to a hydrogen dose 10 times greater than that of the sample described in fig. 6.9.c), which accounts for the presence of one dome inside the other. d) AFM profile measurements taken along the green and blue bars highlighted in fig. 6.10.c). Red dashed-lines are fits of an edge function to the data. The blue line refers to the step from the patch around the pristine dome footprint to the area outside the dome, while the green line refers to the step from this same patch to the area inside the dome.

tensile strain, as already observed in ref. [328]. Moreover, the red-shift of the PL peak-energy on going from one-layer thick to two-layer thick domes ($< 20\,meV$) is small and comparable to that observed on going from one- to two-layer WS_2 flakes [297]. Figure 6.10.c) shows an AFM image of an exploded WS_2 dome in a multi-layer flake treated with a hydrogen dose 10 times greater than that of the sample described in fig. 6.9.c), which could lead to a second dome inside the exploded one (Russian-doll like). In this case, the crater replacing the dome footprint has a depth almost equal to that of a double S-W-S layer ($\sim 1.7\,nm$). Moreover, the patches around the pristine dome-footprint (from which the dome itself was build up before its explosion) have also that same thickness. This claim is based on the AFM measurements shown in fig. 6.10.d). Therein, the blue [green] curve, taken along the blue [green] bar highlighted in fig. 6.10.c), is a measurement of the difference in the height of one of those patches and that of the area outside [inside] the dome.

That curve is well fitted by a step function of $(1.66 \pm 0.34)\,nm$ $[(3.12 \pm 0.34)\,nm]$, namely, a value very close to that of two [four] S-W-S planes $(1.7\,nm)$ $[3.4\,nm]$.

We would like to stress that a hydrogen-induced blistering in thin film Mo/Si coatings has been observed with a hydrogenation procedure similar to that used here [329]. Therein, cross-sectional transmission-electron-microscopy has shown that blistering occurs mainly via either single- or bi-layer detachments. Moreover, no layer detachment at deeper interfaces, *i.e.* tri- or more layers beneath the surface, has been observed. Those results surprisingly resemble the present ones, although they have been found in a physical system totally different from the one investigate here.

The shift of the PL peak on going from the mono-layer to the dome regime will be now discussed. As anticipated, all the compounds investigated here exhibit an almost constant red-shift ($\sim 200\,meV$) to be accounted for by a biaxial strain exerted on the dome itself. Following Hencky's model for circular, pressurized sheets, the biaxial strain produced at the center of the domes is [326, 330]:

$$\epsilon = \left(\frac{h_m}{R}\right)^2 f(\nu) = \left(\frac{h_m}{R}\right)^2 \frac{b_0(\nu)(1-\nu)K(\nu)^{2/3}}{4}. \tag{6.1}$$

R is equal to $d/2$, and b_0 and K depend only on the Poisson ratio $\nu = C_{12}/C_{11}$, where C_{12} and C_{11} are two independent elastic constants of the specific material we are dealing with. The values of ν for all the materials investigated are listed in table 6.1.

	MoS_2	$MoSe_2$	WSe_2	WS_2
ν	0.249	0.239	0.192	0.217

Table 6.1. Poisson's ratio ν of the compounds investigated in this thesis [331].

The values of b_0, K (and thus of $f(\nu)$), as obtained for all the investigated compounds by an interpolation between the values reported in the literature [326, 330, 332], are listed in table 6.2.

	MoS_2	$MoSe_2$	WSe_2	WS_2
b_0	1.702	1.698	1.680	1.689
K	3.386	3.35	3.192	3.274
$f(\nu)$	0.721	0.725	0.736	0.729

Table 6.2. b_0, K, and $f(\nu)$ values of the compounds investigated in this thesis.

The amount of strain exerted on the MX_2 domes has been evaluated by applying eq. 6.1 to the values of the squares of the maximum height (h_m^2) and radius (R^2) of more than 300 domes investigated by AFM. The results shown in figure 6.11 by blue squares, red circles, green triangles, and olive hexagons refer to $MoSe_2$, WS_2, MoS_2, and WSe_2 domes, in the order. Once the values of $f(\nu)$ for each materials have been taken into account, the strain values have been obtained by linear fits (black thin-lines) to the data. The difference in the ϵ values (from 2.4% in $MoSe_2$

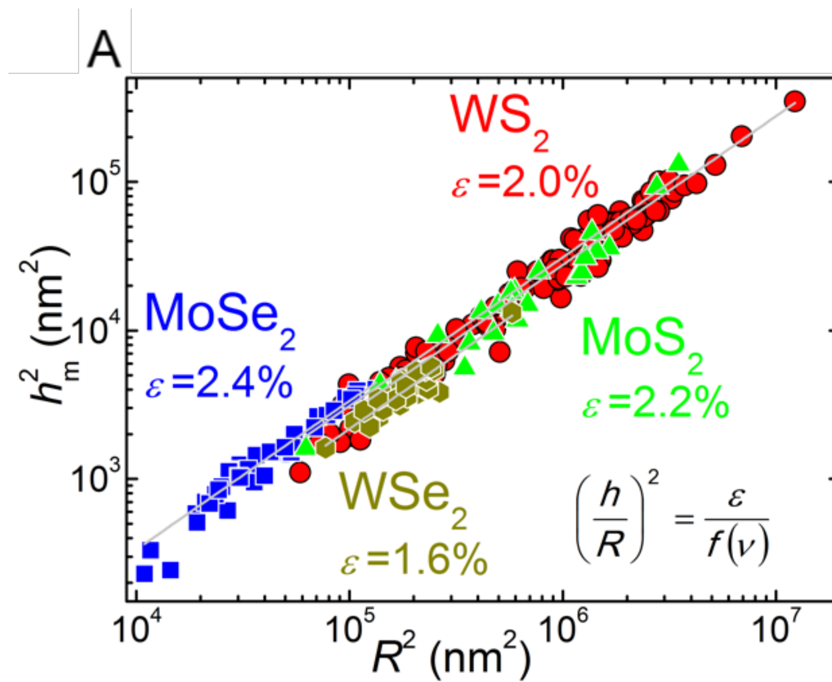

Figure 6.11. a) Square of the maximum height (h_m^2) vs. radius squared (R^2) of the MX_2 domes. The linear fit of equation 6.11 (reported in the figure) to the data provides the dome biaxial tensile strain ϵ.

to 1.6% in WSe_2) are due to the different material elastic properties. The value of $-95\,meV/\%$ found in WS_2 flakes under biaxial strain [333] and of $-105\,meV/\%$ reported in MoS_2 single-layers [334] agree well with the energy red-shifts between the dome PL-spectra and the single-layer ones, reported in fig. 6.8, and the biaxial strain values determined here. Since the PL band of an ensemble of dome does not exhibit a broadening greater than that shown by a single dome, as shown in fig. 6.7.b), all the domes in a given TMD are subjected to the same amount of strain, independently of their size. Finally, the dome PL-emission is broader than that of a mono-layer ($\sim$ a factor 2, see fig. 6.7.b)), because the spatial resolution ($\sim 1\,\mu m$) of our μ-PL can only provide measurements averaged over a (whole) dome surface where the strain varies, as it will be shown in fig. 6.12.

Most interestingly, dome sizes and shapes are determined by the competition between several physical quantities: the van der Waals attraction between TMD layers, the elastic energy needed to deform the crystal, and the free energy of the molecular gas inside the dome. Nevertheless, the ratio h_m/R found here is independent of the dome size over more than one order of magnitude. Moreover, it depends only slightly on the dome TMD: $h_m/R = 0.15 \pm 0.01$ in WSe_2, 0.16 ± 0.02 in WS_2 and MoS_2, and $h_m/R = 0.18 \pm 0.02$ in $MoSe_2$. Similarly, in ref. [335] AFM measurements have demonstrated that the shape of graphene and MoS_2 domes exhibit a universal scaling. Those results, theoretically predicted on the ground of a model based on the theory of elasticity of membranes, have been explained in term of a balance between the dome internal pressure and the elastic properties of its shell [335].

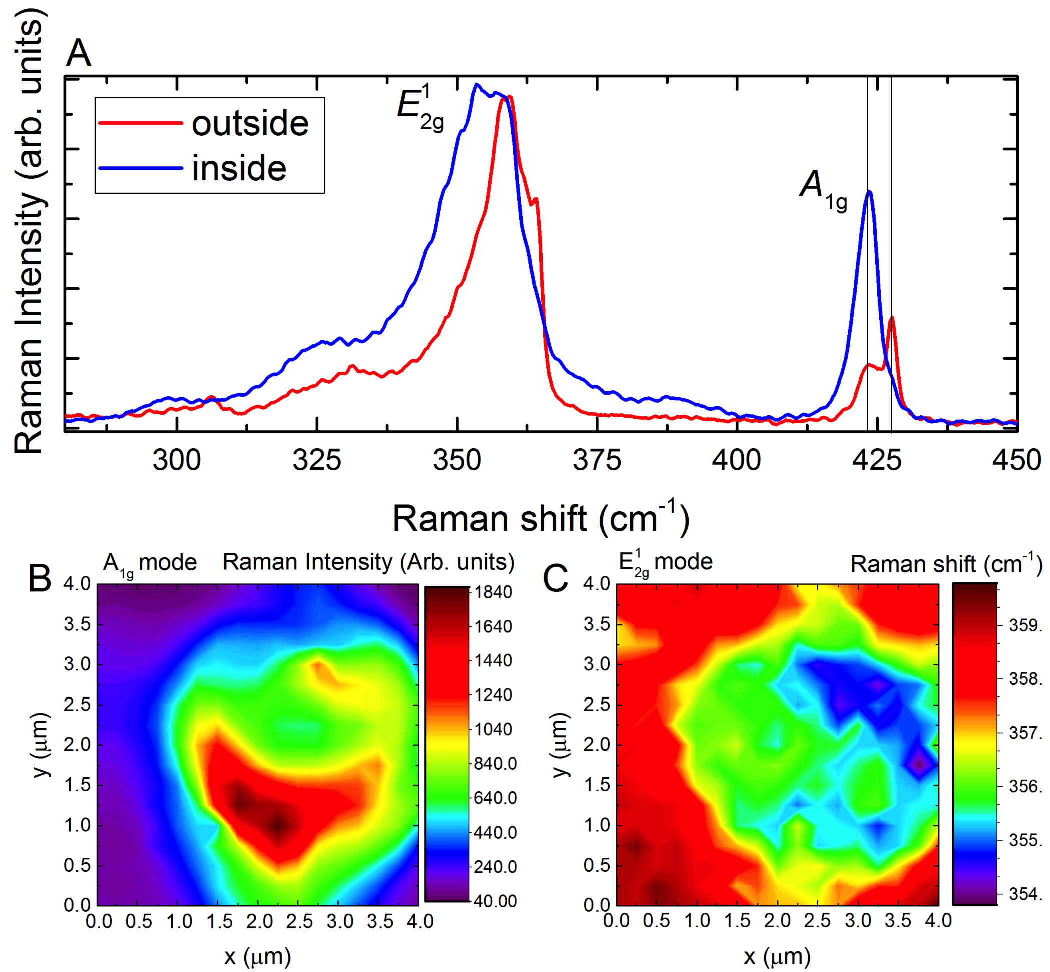

Figure 6.12. c) μ-Raman spectra taken inside (blue line) and outside (red line) the dome perimeter. The two Raman peaks are denoted following the notation in sec. 4.1.2. b) 2D μ-Raman map of the Raman intensity of the A_{1g} vibrational mode over a dome surface. c) 2D μ-Raman map of the Raman shift of the E^1_{2g} vibrational mode over a dome surface.

The μ-Raman spectra taken with a 50× objective outside (red line) and inside (blue line) a hydrogenated ($H_d = 8 \times 10^{16}\, protons/cm^2$) WS_2 dome formed on a multi-layer flake are shown in figure 6.12.a). In the blue spectrum, the A_{1g} and E^1_{2g} vibrational modes are observed at $\sim 423.5\, cm^{-1}$ and $\sim 355.5\, cm^{-1}$, in partial disagreement with the values reported in the literature for mono-layer WS_2 flakes, see table 5.2. This suggests that the dome peel is made by more than one layer and/or that some contribution to Raman scattering come from the multi-layer flake just beneath the dome. However, since only the vibrational-mode-energy variations over the dome surface are of interest here, and not the absolute mode energies, only these variations will be compared here. In the red spectrum, the E^1_{2g} mode is blue-shifted by $\sim 3\, cm^{-1}$ with respect to the peak shown in the blue spectrum, while the A_{1g} is split into two components, one at the same energy as in the blue spectrum, the other one at $\sim 427.5\, cm^{-1}$. The energy difference between these two

peaks ($\sim 4\,cm^{-1}$) is that usually reported when single- and few-layer WS_2 Raman spectra are compared [336]. Therefore, the low-energy component of the A_{1g} doublet is ascribed to the Raman emission from the dome peel, the high-energy component is ascribed, instead, to Raman emission from the multi-layer flake beneath the dome. This attribution is confirmed by the 2D map of the μ-Raman *intensity* of the $\sim 423.5\,cm^{-1}$ A_{1g} component shown in fig. 6.12.b). Therein, the intensity of the $\sim 423.5\,cm^{-1}$ A_{1g} Raman peak over a $4 \times 4\,\mu m^2$ region of the dome surface is shown. The Raman intensity increases by almost three orders of magnitude in moving from the outside to the dome center. On the other hand, nothing can be gathered about the asymmetrical shape of the Raman intensity, which requires a further study.

The expected strain variations over the dome surface are now discussed. It is known from the literature that the strain only slightly affects the energy of the A_{1g} vibrational mode. It strongly modifies, instead, the energy of the E^1_{2g} vibrational mode [336], whose variations over the dome surface are shown in fig. 6.12.c). Therein, a 2D map of the *Raman shift* of that mode, as taken over a $4 \times 4\,\mu m^2$ region of the dome surface, is shown. Also in that map the circular shape of the dome can be appreciated, exactly in the same position as in fig. 6.12.b), thus confirming that the two modes originate from a common dome. An abrupt red-shift of $\sim 3\,cm^{-1}$ is observed when approaching the dome contour. At the same time, the mode energy smoothly changes by $\sim 2\,cm^{-1}$ over the dome surface, thus confirming that the strain varies over the dome surface (asymmetrically, as in the case of the mode-intensity variations shown in fig. 6.12.b)). Finally, the *absolute* values of Raman shift ($\sim 3 \div 5\,cm^{-1}$) are comparable with a biaxial strain exerted over the dome surface equal to ($1.5 \div 2.4\%$), in good agreement with the results shown in fig. 6.11.

6.2.1 Temperature investigation

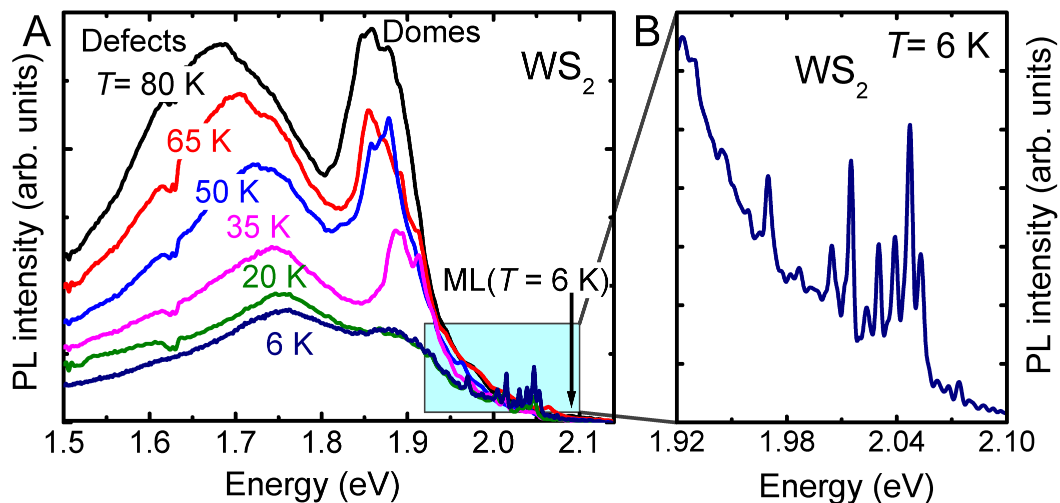

Figure 6.13. a) μ-PL spectra taken from $T = 6\,K$ to $T = 80\,K$ in an external excitation configuration on an ensemble of about 50 WS_2 domes. b) $T = 6\,K$ zoomed-in μ-PL spectrum of the energy region highlighted by the azure rectangle in panel a)

In figure 6.5, on the average the domes disappear below $\sim 32\,K$ because of a

molecular hydrogen gas-liquid transition. The evolution from $T = 6\,K$ to $T = 80\,K$ of μ-PL spectra taken over about 50 WS_2 domes in the external excitation configuration described in sec. A.1 is shown in figure 6.13.a). Below the critical temperature of the molecular-hydrogen phase-diagram ($\sim 33\,K$), sharp peaks appears at an energy below that typical of free-excitons in WS_2 monolayers ($2.1\,eV$, see black arrow), as better shown in the zoomed-in μ-PL spectrum in fig. 6.5.b). These sharp lines are most likely due to the emission of localized excitons in wrinkled patches formed after the deflation of the domes and the subsequent folding of the dome peel [314]. The broad emission band at lower energy in fig. 6.5.a) is mainly due to emission from defects. Above the hydrogen critical temperature ($\sim 33\,K$), the dome emission at $1.9\,eV$ begins to appear, which suggests a strong correlation between the dome optical properties and the temperature-evolution of the dome morphology.

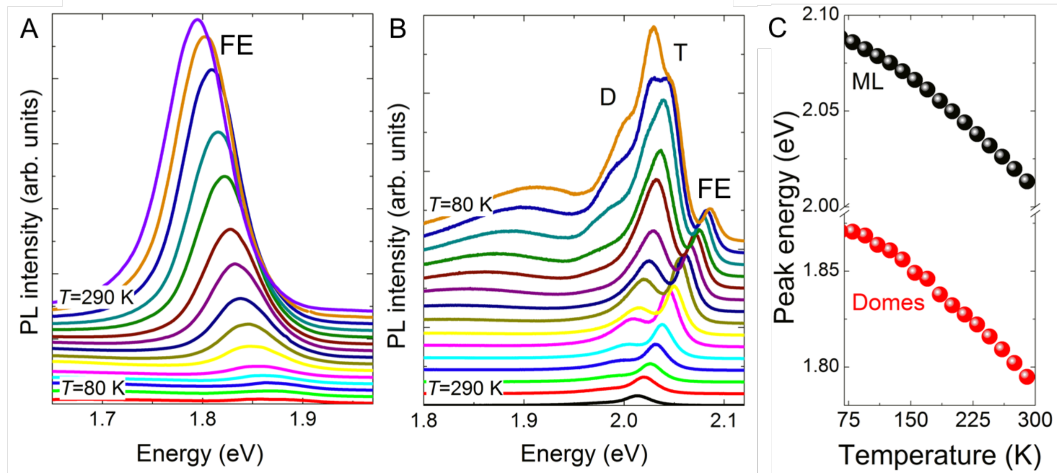

Figure 6.14. a) Free-exciton temperature-dependent μ-PL spectra taken in an external excitation configuration on an ensemble of about 50 WS_2 domes. b) Same as a) for a mono-layer WS_2 flake but with an inverted temperature evolution. In this case, charged exciton (T) and defect-related transitions (D) are found in addition to the FE recombination. c) Temperature dependence of the FE recombination-energy for WS_2 domes and a mono-layer.

Quite surprisingly, the overall PL intensity increases with increasing temperature, in contrast to what is usually observed in semiconductor materials (see sections 2.3 and 5.2.2), as better appreciated in figure 6.14. Therein, the μ-PL spectra of an ensemble of WS_2 domes and of a WS_2 single-layer taken from $80\,K$ to room temperature ($290\,K$) in steps of $15\,K$ in the external excitation configuration described in sec. A.1 are shown in fig. 6.14.a) and b), respectively. At variance with the single-layer case, the dome luminescence-intensity increases steadily, at least up to room temperature. This is due to an increasing emitting surface of the dome, whose diameter increases with temperature because of the expansion of the HS_2 gas. Furthermore, the dome emission is dominated by the free-exciton recombination, while the single-layer emission displays several contributions related either to charged excitons (T) and other defect-related bands (D). This marked difference is likely due to the decoupling of the domes from the substrate, which should act as a source of free charges and impurities in single layers, as reported in ref. [337]and in sec. 5.1.

On the other hand, the very close temperature dependence of the free-exciton energy in the single-layer and dome regime, shown in fig. 6.14.c), indicates that the strain in the curved WS_2 domes does not vary with temperature, in agreement with theoretical predictions in ref. [335]. Therein, a h_m/R ratio constant with temperature has been guessed on the ground of free-energy considerations. Preliminary interferometry results, not shown here and based on the study of the Newton rings[3], have permitted to determine h_m at various temperatures. Those results point to a h_m/R ratio constant with temperature, thus strengthening the hypothesis of a surface-dome strain independent of temperature.

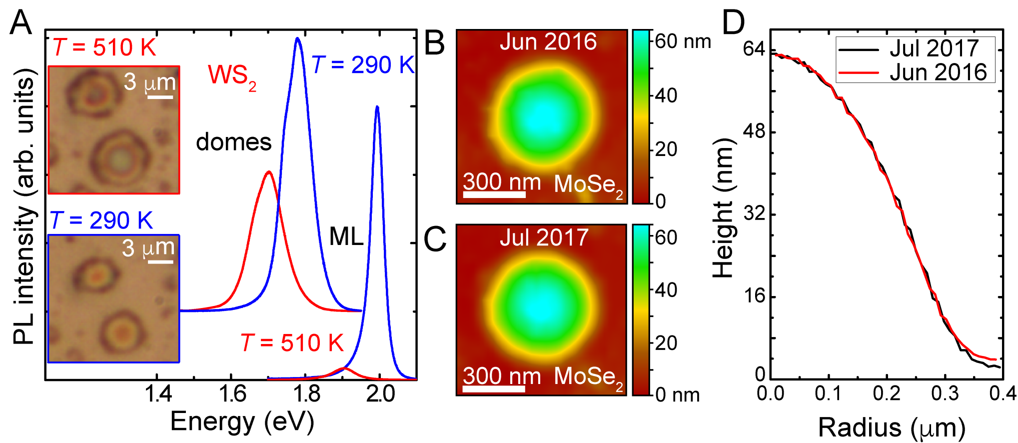

Figure 6.15. a) Room temperature (blue lines) and $T = 510\,K$ (red lines) μ-PL spectra taken on an ensemble of about 100 WS_2 domes and on a WS2 mono-layer. Insets: optical microscopy images of domes taken at the same temperatures as PL. The different dome coloration at different Ts results from different conditions for light constructive interference (Newton's rings) due to the H_2 expansion. b) AFM image of a single $MoSe_2$ dome. c) AFM image of the same dome as in b) after 13 months. d) Height profiles of the two AFM images taken on a same dome at an interval of 13 months.

To conclude, it should be stressed that the domes persist up to $T = 510\,K$ at least. Moreover, in contrast with the mono-layer case, dome light-emission is strong and thermally stable also above room temperature (see figure 6.15.a)). The dome morphology is long durable and stable as well, as illustrated by the AFM images in figs. 6.15.b) and .c) and by the corresponding height profiles shown in fig. 6.15.d), where it is shown that the dome shape does not change after 13 months. This assure also a long hydrogen storage with large areal density over unlimited surface regions of bulk TMDs, in contrast with findings in graphene [338] and MoS_2 inflated membranes [339]. Therein, indeed, the membranes remained inflated for a short period because of gas diffusion through the foreign substrates on which the membranes were laid down or through imperfect membrane seals. This is not the case of present H_2-containing structures, where hydrogen diffusion through the TMD bulk/layers is strongly inhibited [324]. The latter results highlight the high dome robustness and durability, which are key parameters to assess the dome potential for

[3] A technique similar to that employed in ref. [322] to determine the height of suspended graphene membranes

applications.

6.3 Tailoring the size, density, and position of domes

MX_2 domes are stand-alone and can be easily handled thanks to the parent substrate on which they form. At variance with other techniques aimed at obtaining inflated ordered structures [326, 327], MX_2 domes do not need specially designed devices and substrates that may limit their manageability. It has been demonstrated that durable bubbles may form owing to the accidental incorporation of contaminant gases between mono-layers and their supporting substrates [335]. However, those bubbles lack spatial ordering and high density. Conversely, many practical uses of these structures would require that their size, density, and position are precisely controlled.

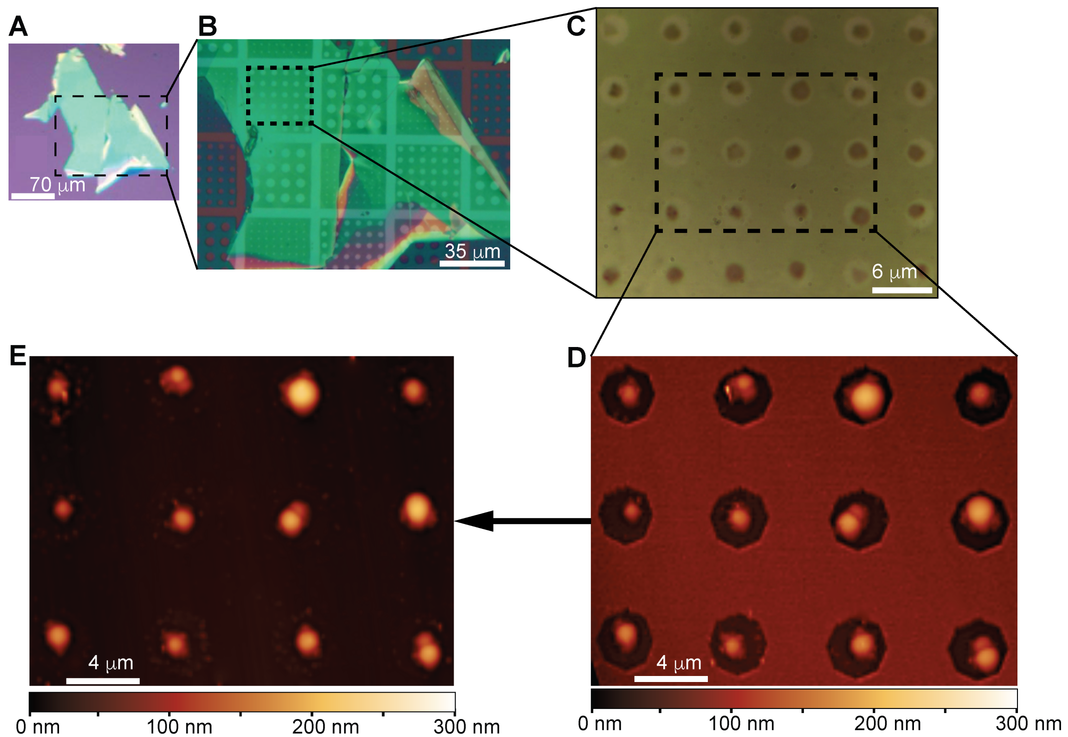

Figure 6.16. Steps of the formation of ordered dome arrays: optical image of the pristine flake (a), after the deposition of the desired H-opaque mask (b), and after the hydrogenation procedure (c). AFM image before (d) and after (e) removal of the H-opaque mask.

To that end, the procedure schematically depicted in figure 6.16 was followed. TMD flakes with suitable dimensions were identified by optical microscopy; see fig. 6.16.a). Then a H-opaque mask with an array of $5\,\mu m$ equally spaced octagonal openings with different diameters ($D = 1$, 3, and $5\,\mu m$) was realized on the sample by electron-beam lithography, as reported in ref. [308] and in sec. A.3; see fig. 6.16.b). After hydrogenation (H^+ dose equal to $H_d = 4 \times 10^{16}\,protons/cm^2$), domes formed in the flake regions not covered by the H-opaque mask; see fig. 6.16.c). Then,

the dome morphology was investigated by atomic-force-microscopy, see fig. 6.16.d), and the H-opaque mask was removed; see fig. 6.16.e). The HSQ chemical etching does not attack the formed domes, leaving the sample as it was before the chemical treatment.

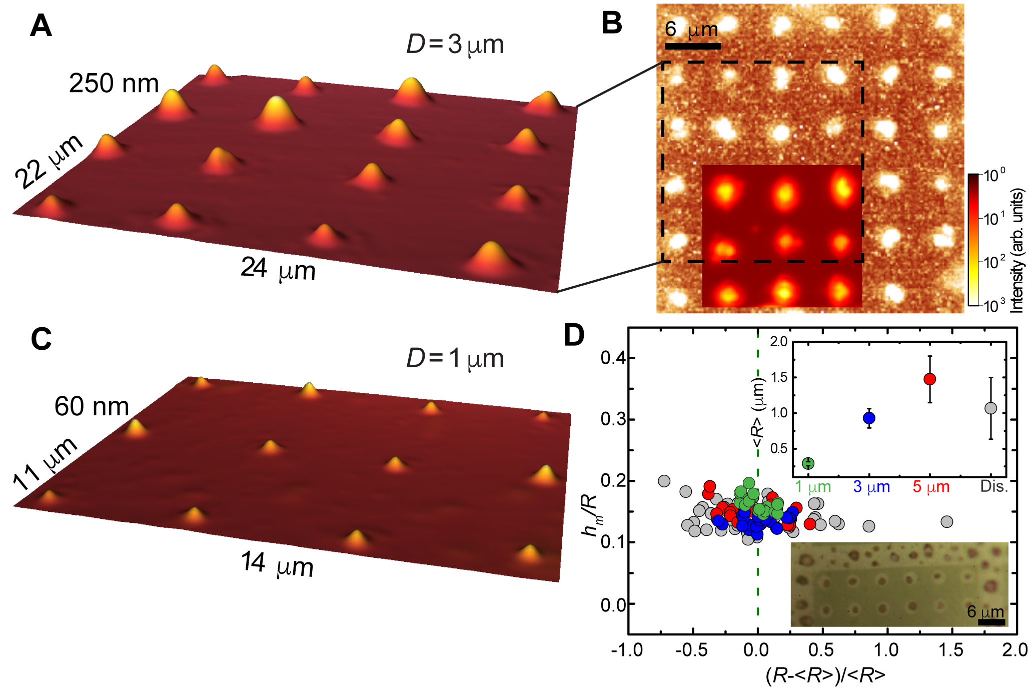

Figure 6.17. 3D AFM image of an array of $D = 3\,\mu m$ WS_2 domes obtained by H^+ irradiation through a suitable H-opaque mask, later removed by a HSQ chemical etching. An aspect ratio (10:1) between the horizontal and vertical scales is applied. b) Room temperature PL imaging of the same array of domes shown in a). The bottom-left inset is a μ-PL mapping (detection wavelength equal to 689 nm) of a portion of the same array. c) 3D AFM image of an array of $D = 1\,\mu m$ domes formed in the same process used for the domes shown in a). d) Dependence of the h_m/R ratio vs. the normalized deviation of the dome footprint radius from the pertinent average value $< R >$ shown with a color code in the top-right inset. The domes are grouped into different subsets depending on their random or ordered formation (see the optical image in the bottom inset). The size distribution of ordered domes is narrower than that of randomly formed domes.

The successful output of that procedure can be verified in figure 6.17. The AFM 3D image of a WS_2 sample subjected to the above summarized process (dose $H_d = 4 \times 10^{16}\, protons/cm^2$, mask openings $D = 3\,\mu m$) is displayed in fig. 6.17.a), where the achievement of neatly arranged single domes with average $d = (1.86 \pm 0.14)\,\mu m$ and $h_m = (0.13 \pm 0.02)\,\mu m$ is shown. Moreover, the PL signal emitted by the array, taken in the external excitation configuration and shown in fig. 6.17.b), is as good as the one observed in the random formed domes; see fig. 6.7. The dome high optical-quality is confirmed by the inset in the bottom-left part of fig. 6.17.b), where a μ-PL mapping (recorded at the exciton emission energy of $1.8\,eV$ from the same array and excited by a $532\,nm$ laser) is overlapped to the PL imaging.

The dome dimensions can be engineered too by varying the opening size. The AFM 3D image of an array of domes, fabricated by using a mask with $D = 1\,\mu m$ and irradiated together with the $D = 3\,\mu m$ array shown in fig. 6.17. a), is shown in fig. 6.17.c). Therein, the achievement of a neatly arranged array of single domes ($d = (0.58 \pm 0.03)\,\mu m$ and $h_m = (0.047 \pm 0.004)\,\mu m$ average values) is demonstrated. The dispersion of the dome dimensions as a function of the mask opening size has been then investigated (the color code of the opening diameters is given in the top inset of fig. 6.17.d)). The ratio (h_m/R) between the maximum height, h_m, and the footprint radius, R, of the domes versus $(R- < R >)/ < R >$, namely, the percentage deviation of each dome footprint radius from the average value $< R >$, is shown in the main part of fig. 6.17.d). The data are grouped into randomly-formed (gray dots) and ordered dome subsets (blue, red, and green dots), all obtained during the same proton irradiation process ($H_d = 4 \times 10^{16}\, protons/cm^2$), as shown in the bottom inset. The size distribution of the domes formed by the lithographic approach is remarkably narrower than that of the randomly formed domes. Furthermore, the size distribution gets even narrower with decreasing the dome size, a feature to be further investigated. Finally, in the ordered arrays, the average dome volume $[V = \pi h_m/6(3R^2/4 + h_m^2)]$ scales as $V = A \times S^\gamma$ with the surface area ($S = 0.25\pi D^2$) available to the $2H^+ + 2e^- \rightarrow H_2$ reaction, which supports the dome formation as a catalysis-driven process. Moreover, the value obtained for γ (3/2) points out the right proportionality between a volume ($[l^3]$) and a surface ($[l^2]$), thus validating once again the assumption of a catalytic role of TMD materials for the production of molecular hydrogen.

To conclude, we point out that a control of the dome position and size over large areas is valuable in many other situations. Indeed, the high flexibility featured by the dome fabrication-method prompts a means to engineer, via strain fields, pseudo-magnetic field superlattices in TMD single-layers and thus to create the conditions for the generation of dissipation-less electrical currents [340, 341, 342]. Most importantly, the domes themselves can be employed as a template to modulate the curvature (and hence the electronic properties) of other 2D materials, such as graphene, h-BN, and phosphorene, deposited on top of TMD bulk samples before proton irradiation.

Conclusions

In this thesis, we have investigated the electronic properties of InP NWs both in the WZ and ZB crystal-phases and tailored the electronic and morphological properties of single- and multi-layer MX_2 flakes by means of hydrogen irradiation. We summarize here the main results of our work. As regards InP NWs:

- We have reported a detailed investigation of the A, B, and C band-gap energies in WZ InP nanowires from low ($10\,K$) to room ($290\,K$) temperature. A quantitative reproduction of both PLE and PL measurements allowed us to establish that the A, B, and C optical transitions show a same thermal shrinkage with increasing temperature. This result highlights that the thermal properties of WZ materials have a same general trend, independently of either crystal bond-polarity or energy-gap. Indeed, the same reduction in the A, B, and C transition-energies for increasing temperature has been found also in other hexagonal compounds, such as GaN, ZnO, CdS, and CdSe. Moreover, studies of the temperature dependence of the band-gap energy in ZB InP-NWs and bulk InP have shown that the thermal shrinkage of the WZ phase is similar to that found in ZB materials. The negligible difference in the thermal properties of the WZ/ZB crystal-phases is ascribed to the great similarity in the phonon-dispersion curves and lattice thermal-expansions shown by the two phases. On this ground, important quantities related to heat transfer and dissipation in the NW lattice are expected to be independent of the NW crystal-phase. This is important, for instance, in discriminating which NW structural characteristics matter most in the reduced thermal-conductivity usually exploited in NW-based thermoelectric devices.

- We have reported a detailed study, performed by continuous-wave PL and μ-PL, of the thermalization properties of photogenerated carriers in InP NWs with different structural and morphological characteristics. By a quantitative reproduction of the PL spectra, we found the signatures of carrier temperatures largely exceeding that of the lattice (hot carriers). Specifically, the difference between those two temperatures increases dramatically (from 0 up to $190\,K$) with increasing lattice temperature (from 80 to $310\,K$) and decreasing NW diameter (from 700 to $60\,nm$), independently of all the other NW characteristics (growth method, crystal structure, and NW shape). Usually, hot carriers survive for only few *ps* after excitation. Instead, this phenomenon persists here in a steady-state regime, most likely because the large surface-to-volume ratio of small-diameter NWs hampers the achievement of a thermal equilibrium between carriers and lattice via phonon emission. On the other hand, hot

carriers live long enough ($\sim 1\,ns$) to ensure their interaction with phonon modes, thus confirming that the hot-carrier effect is an intrinsic feature of thin NWs. The ability of charge carriers to harvest a thermal budget for the long times probed by steady-state PL spectroscopy (and at temperatures useful for practical devices) could be of great significance for photovoltaic and thermoelectric applications. Moreover, the observation of a temperature gradient in homostructures based on two NWs with different diameters paves the way for promising photo-thermoelectric experiments, which is to be the subject of future studies.

- We have investigated the response of different optical transitions of wurtzite InP-NWs to changes in magnetic-field intensity and orientation. Via a quantitative analysis of the diamagnetic shift of the free-exciton and free-electron-to-neutral-acceptor transitions at different temperatures, we have determined the values of the effective mass of electrons and holes in WZ NWs, which result to be heavier than their counterparts in ZB crystals. The use of magnetic fields applied parallel or perpendicular to the WZ $\hat{c}$-axis of the NWs has provided significant information about the dynamics of carriers along different directions. Specifically, the electron effective-mass changes from $m_e^{\|} = (0.078 \pm 0.002)\,m_0$ in a direction parallel to $\hat{c}$ to $m_e^{\perp} = (0.093 \pm 0.001)\,m_0$ perpendicularly to $\hat{c}$. A much large anisotropy is found for holes, whose effective mass is $m_h^{\|} = (0.81 \pm 0.18)\,m_0$ in a direction parallel to $\hat{c}$ and reduces by more than a factor of three $[m_h^{\perp} = (0.250 \pm 0.016)\,m_0]$ perpendicularly to $\hat{c}$, a behavior opposite to that found for electrons. Notice that these findings are similar to those reported in other WZ materials in bulk form (*e.g.* GaN, InN, and ZnO), which highlights the existence of a general trend. Our results offer appropriate inputs for the engineering of the electronic properties of quantum heterostructures and novel crystal-phase homostructures. As an example, the knowledge of the carrier-mass anisotropy in WZ NWs is pivotal in the design of NW solar cells, in which the choice of either radial or axial junctions strongly depends on that parameter.

- The Zeeman splitting has been reproduced for both the free-exciton and impurities transitions by the equation valid in WZ crystals for magnetic fields both parallel and perpendicular to the WZ $\hat{c}$-axis. This quantitative analysis allowed us to determine the carrier g-factors for several $\vec{k} - \hat{c}$ configurations. The results thus obtained were compared with theoretical predictions made in the framework of $k \cdot p$ theory. As expected, a circular dichroism between the two Zeeman-split states has been observed only in the $\vec{k} \| \hat{c}$ configuration. In the Faraday configuration, a non-linear trend in the exciton Zeeman-splitting has been found, which has been ascribed to the interaction between heavy- and light-hole states of the WZ structure. That trend has been also confirmed by theoretical simulations that included excitonic effects. We stress that a precise knowledge of the carrier g-factors and how they can be manipulated is necessary to implement NWs in spintronic devices.

As regards 2D TMDs:

- We have performed a detailed investigation of the effects of low-energy hydrogen irradiation upon single- and bi-layer $MoSe_2$ and WSe_2 flakes. A complete characterization of the optical properties of single- and bi-layer flakes has been reported, and the achieved results have been compared with the existing literature. In the single-layer regime, it has been shown that the free-exciton recombination-energy strongly depends on the environment surrounding a single-layer flake. Then, each pre-characterized flake has been treated with increasing hydrogen doses. In the single-layer regime, a decrease in the PL efficiency was observed both at room and low temperature upon hydrogenation because of a flake surface-damage. That proton detrimental activity has been strongly reduced by depositing an oxide capping layer on the flake. That capping decreases the proton energy to roughly thermal values and allows a gentle contact of protons with the flake without affecting the proton saturation of non-radiative recombination centers. Moreover, sharp PL-peaks ($FWHM < 1\,meV$) were found at low temperature after hydrogen irradiation. Those peaks have been ascribed to the formation of defect centers, which are valuable candidates as single-photon emitters. In the bi-layer regime, instead, hydrogenation increases the PL efficiency up to a factor of 3. At the highest H doses, the indirect band-gap recombination vanishes and sharp peaks appear in the PL spectra, too. Further studies as a function of the number of flake layers and of different work conditions, such as proton energy, process temperature, *etc.*, are required to investigate the phase diagram of this fascinating process.

- We have shown that hydrogenation of bulk (number of layers greater than ~ 10) $MoSe_2$, MoS_2, WSe_2, and WS_2 results in the formation of a new kind of nanostructures. Indeed, our process favors the production of molecular hydrogen just beneath either one or few X-M-X planes. This results in a local blistering of the TMD surface-plane, which turns into the formation of perfectly circular domes that emit light (in most cases more efficiently than the single-layer counterparts) well above room temperature (up to $\sim 500\,K$). All those domes are characterized by a same aspect ratio (~ 0.15) -namely, the ratio between the dome maximum height and the dome footprint- independently of the dome size, from the nanometer to micrometer scale, and only slightly material dependent. Atomic-force-microscopy and polarization-resolved μ-PL measurements provided experimental evidence that the dome peel is only one-layer thick. Moreover, it has been shown that domes are durable, stable, and robust: atomic-force-microscopy images performed on the same dome at a 13-months interval display no variation in the dome morphology. A temperature study performed on an ensemble of about fifty domes has highlighted that the dome PL-intensity increases with increasing temperature, due to an increase in the dome volume, and that the dome aspect-ratio is constant with temperature. Indeed, the dependence on temperature of the band-gap energy is the same for domes and single-layers, thus suggesting a constant strain value over the dome surface. Finally, a receipt to get ordered domes with defined size and density has been provided. It consists in the deposition over the surface of a multi-layer flake of a H-opaque mask made by electron-beam-lithography and having circular openings with different diameters, followed by hydrogen implantation. After

the dome formation, the mask have been removed via chemical etching without affecting the dome morphological and optical properties. By this procedure, the formation of neatly arranged domes has been proved. The hypotheses regarding hydrogen production have been confirmed by the proportionality found between the dome volume and the area of the surface available for the chemical reaction. However, other investigations are needed to draw a complete picture of those new nanostructures. As an example, scanning near-field optical microscopy experiments will allow for the investigation of the strain variation over the dome surface. At the same time, an atomic-force-microscopy investigation below the liquid-gas phase-transition will show how the domes deflate or inflate and how the peels fold after the dome deflation. On the other hand, scanning-tunneling-microscopy will address the possible existence of very high pseudo-magnetic fields, as already observed in graphene nano-bubbles. Finally, the potential of ordered domes to be a template for deforming other 2D materials, such graphene, boron nitrides, and so on, should be investigated, too.

Appendix A

Experimental details

In this chapter, we give an overview of the experimental techniques, mainly optical spectroscopy, used in this work. Theory of optical spectroscopy is treated in the first section. Photoluminescence (PL), a well-established technique to address the electronic properties of semiconductor nanostructures, is described together with its main variation, PL excitation (PLE) spectroscopy, which mimics to some extent absorption spectroscopy. The effect of a constant magnetic field on PL spectroscopy is discussed and a way to get insights on carrier effective masses and gyromagnetic factors from magneto-PL spectra is highlighted. Finally, Raman spectroscopy, which allows one to get information about the lattice properties of solids, is described.

In the second section, the experimental setups used in the course of this thesis (macro-PL/PLE, micro-($\mu-$) PL/Raman, magneto-PL) are thoroughly described. The third section is devoted to the description of the post-growth technique used to implant hydrogen and of the lithographic process for engineering hydrogen incorporation in semiconductor nanostructures. In the last section, the atomic force microscopy, which allows an insight into the morphology of two dimensional materials, is described.

A.1 Optical spectroscopy

Optical spectroscopy is largely used for the study of the interaction between matter and electromagnetic radiation. In principle, four possible light beams can be studied and analysed in this interaction: light reflected from the surface, light transmitted through the medium, light scattered or emitted by the medium. Obviously, the simultaneous measurement of all of those four light beams is almost impossible. Moreover, the matter response-function to the electromagnetic radiation is wide spread all over the electromagnetic spectrum making usually impossible to record all the information simultaneously. Several different optical spectroscopy techniques have been developed along the course of science, especially as regards the studies of the opto-electronic properties of crystalline solids. Some techniques are more suitable for the study of metals (*e.g.*, *reflectivity*) whereas *absorption* is more suitable to probe the electronic structure of semiconductor materials. Nevertheless, absorption cannot be used to study nanostructures grown (*e.g.*, nanowires) or deposited (*e.g.*, two-dimensional films) on opaque substrates. Therefore, luminescence spectroscopy

has gained much more value to investigate such nanostructures. This section is devoted to the description of the optical spectroscopies used in this thesis.

Photoluminescence (PL)

Generally speaking luminescence from a medium occurs when this medium emits a photon after having been brought into an excited state and subsequently relaxed to the ground state. If the electromagnetic radiation results from heating, we speak of black-body radiation. Instead, when the external excitation promoting luminescence is electrically driven, as in light emitting diodes, we talk about *electro-luminescence*, or driven by a high energy electron beam, as in a scanning electron microscope, we talk about *cathodo-luminescence*, or is a light beam, as in our case, we talk about *photo-luminescence* (PL). The luminescence process can be divided in three main steps:

- ***Excitation***: An external perturbation increases the population of the system excited states. In a PL experiment, a laser source at fixed energy, at or above the band gap of the semiconductor, usually promotes extra electrons (e^-) from the valence band (VB) to the conduction band (CB) thus leaving holes (h^+) in the VB in excess with respect to thermal equilibrium.

- ***Relaxation***: Extra electrons and holes relax toward the minimum of the CB and the maximum of the VB, respectively throughout scattering, firstly with optical and then acoustic phonons.

- ***Emission***: The relaxed electron-hole pairs recombine radiatively emitting a photon of energy typically lower than that of the exciting photon, and the system returns to its ground state.

The step sequence is determined by different time scales: carrier relaxation to the lowest energy states takes place in few *ps* whereas carrier recombination occurs typically after few *ns*. Therefore, PL is a powerful tool to investigate the energy of the forbidden band gap or of shallow defects in the band gap due to crystal imperfections and impurities (whose low density hinders their detection in absorption experiments).

Several recombination processes can occur in a PL experiment, some of which are sketched in figure 1.1. In an *ideal* semiconductor with no crystal defects and impurities, the only possible recombination is the band-to-band recombination. Therein, electrons and holes relaxed to the conduction and valence band extrema recombine emitting a photon whose energy gives the minimum energy difference (band-gap energy) between the two bands (assuming that the Coulomb interaction can be neglected, as in InSb [344]; see fifth panel in fig. 1.1). However, in almost all III-V semiconductors, the excitonic interaction[1] is not negligible and thus the emitted photons will have an energy equal to that of the band gap minus the exciton binding energy (see fourth panel in fig. 1.1). In a *real* semiconductor, instead, the

[1] A complete description of the exciton quasi-particle will be given in A.1.

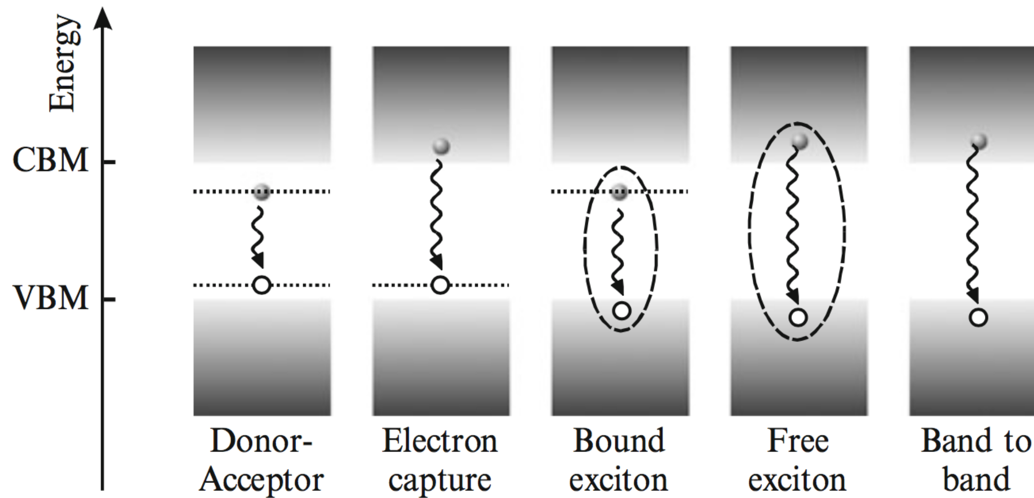

Figure 1.1. Main radiative recombination processes observed in PL experiment. VB and CB are indicated as grey areas, whereas horizontal dotted lines in the band gap mark impurity levels. Electrons (holes) are indicated by dark-shaded (hollow) dots. Undulated arrows indicate radiative recombinations and dashed circles highlight the presence of Coulomb interactions [343].

emission from energy levels in the band gap, and due to intrinsic or extrinsic[2] defects, is detected at an energy lower than that of the energy gap by an amount equal to the defect binding energy (see first and second panels in fig. 1.1). Moreover, excitons can bind to an impurity (or other defects in the material (see third panel in fig. 1.1). In that case, recombination occurs from a bound exciton (BE) and its energy is lower than that of a free exciton (FE). Photogenerated carriers can also recombine via non-radiative processes where the photon energy is fully converted into heat. Typical non-radiative channels are given by multi phonon emission, Auger effects, and recombination at surface defects. The competition between all these recombination mechanisms leads to a polychromatic PL spectrum that must be resolved in wavelength to gather information on the electronic properties of the materials under investigation.

Photoluminescence experiments can be carried out under different perturbations: light excitation, lattice temperature, static magnetic field, and strain. The first two perturbations are the most employed to discriminate between intrinsic (e.g., FE and band to band) or extrinsic (e.g., electron to acceptor, BE, ecc.) recombinations. As regards light excitation, each spectral feature has a different power dependence. For increasing excitation power, the emission from localized structural defects and impurities, usually in a relative small number, progressively saturates while the relative weight of emission from intrinsic states increases. Similarly, for increasing lattice temperature localized states are progressively ionized (the deeper the state, the higher the ionization temperature) and their emission decreases in favor of that from intrinsic excited states with an ensuing asymmetrical high energy broadening

[2]Extrinsic defects are due to the presence of foreign chemical species into the semiconductor materials, *e.g.*, acceptor and donors. Intrinsic defects are due, instead, to structural and crystal defects such as vacancies, dislocation, surface states, etc.

of the emitted spectra. Finally, the overall PL intensity decreases with increasing temperature, because of the thermal activation of non-radiative recombination centers.

Photoluminescence spectroscopy is mainly limited by the material optical quality: low quality or indirect band-gap materials, with weak oscillator strengths, are almost impossible to characterize by PL. On the other hand, PL is a non invasive and non destructive powerful technique to probe semiconductor nanostructures with direct gap. It does not require a specific sample preparation or a strict environment control or complex experimental setup. Therefore, PL can give insight into several physical properties in a simple and fast way whenever the optical quality of the investigated materials is good enough.

PL excitation (PLE)

Photoluminescence excitation (PLE) is a technique complementary to PL that mimics absorption [345]. One of the main PL limits is the difficulty to probe and study states at energies higher than the band gap, because of the rapid thermalization of photogenerated carriers. Photoluminescence excitation, instead, can probe those excited states, thus forming together with PL a complete tool to study the semiconductor optoelectronic properties. Moreover, PLE is crucial in the study of nanostructures grown or deposited on opaque bulk substrate where conventional absorption measurements are challenging or even impossible.

In a PL experiment, the excitation energy (E_{exc}) is kept fixed while the emitted light is recorded as a function of detection energy (E_{det}). In a PLE experiment, instead, E_{det} is kept fixed (close to a sample PL resonance) while E_{exc} is varied from just above E_{det} to higher energies. The relationship between PL intensity ($I_{PL}(E_{exc}, E_{det})$) and excitation intensity ($I_{exc}(E_{exc})$) highlights the similarities between absorption and PLE:

$$I_{PL}(E_{exc}, E_{det}) = I_{exc}(E_{exc}) \cdot P_{abs}(E_{exc}) \cdot P_{rel}(E_{exc}, E_{det}) \cdot P_{em}(E_{det}), \qquad \text{(A.1)}$$

where the probabilities Ps indicate the three different steps which occur during a PL experiment, as described in subsec. A.1. More precisely, assuming the top of VB as the zero of energy:

- $P_{abs}(E_{exc})$ is the probability that a photon having energy equal to E_{exc} is absorbed by the sample;

- $P_{rel}(E_{exc}, E_{det})$ is the probability that photogenerated carriers relax from conduction and valence band-states whose energy difference is equal to E_{exc} towards states where this difference is E_{det};

- $P_{em}(E_{det})$ is the probability that $e^- - h^+$ pairs will recombine radiatively after the relaxation process by emitting a photon of energy (E_{det}).

In a PLE experiment, P_{em} is fixed at $P_{em}(E_{det}$. On the other hand, $P_{abs}(E_{exc})$ is proportional to the absorption coefficient and thus to the material joint density of states (JDOS). Therefore, a PLE spectrum, defined as I_{PL}/I_{exc}, is analogous to an absorption one provided that $P_{rel}(E_{exc}, E_{det})$ does not depend on E_{exc}. In particular,

the approximation $dP_{rel}/dE_{exc} \sim 0$ is robust for E_{det} coincident or near critical points, where the JDOS exhibits sharp features. On the contrary, that approximation is no longer valid whenever there are channels of preferential relaxations between different states of the band structure. Therefore the choice of an E_{det} that minimizes the dependence of $P_{rel}(E_{exc}, E_{det})$ on E_{exc} is mandatory, if meaningful information on the absorption coefficient should be obtained from a PLE spectra.

Excitons

Photogenerated electrons and holes feel a mutually attractive Coulomb potential under which they may form an $e-h$ bound state in analogy with the well known hydrogen-atom case, whose heavy proton is replaced by a much lighter hole. The energy of the new quasi-particle, called *exciton*, is the lowest among those of the semiconductor excited states [345].

In almost all III-V semiconductors, where the strong screening of the Coulomb potential by valence-band electrons results in a large dielectric constant, the $e-h$ pairs are weakly bound and the exciton is known as *Wannier* exciton [346]. In the effective mass approximation, electrons and hole are free particles moving in a crystal whose lattice potential renormalizes the electron and hole (effective) masses. Within that approximation, the exciton motion can be solved as in any two particle system (*e.g.*, the hydrogen atom), by a decomposition in two subsystems. The one, namely, the *center of mass* motion, consists of a free particle moving inside the crystal with mass $M = m_e^* + m_h^*$ and wave-vector $\vec{K} = \vec{k}_e + \vec{k}_h$. The other, namely, the *relative* motion of the two particles around the center of mass under the effect of the Coulomb potential, results in an energy spectrum identical to that of the hydrogen atom. The bound states are identified by the principal quantum number $n = 1, 2, 3, etc.$ and the orbital quantum number $l = 0, 1, 2, etc.$. Then, the discrete exciton energy levels and their related orbital radii are:

$$E_{exc}(n) = \frac{\mu_{exc}}{2}\left(\frac{e^2}{4\pi\epsilon\hbar n}\right)^2 = \frac{R_{eff}}{n^2}, \quad r_{exc}(n) = \frac{4\pi\epsilon\hbar^2 n^2}{\mu_{exc}e^2}, \tag{A.2}$$

where

$$\mu_{exc} = \frac{m_e m_h}{m_e + m_h} \tag{A.3}$$

is the exciton reduced mass, $\epsilon = \epsilon_r \epsilon_0$ is the static dielectric constant of the material, and R_{eff} is the *exciton effective Rydberg*, namely, the binding energy of the exciton ground state. The continuum states correspond, instead, to free electrons and holes moving in the crystal under the influence of a Coulomb potential that modifies the free carrier wave-functions as accounted for by the *Sommerfeld factor* [347].

The intensity of PL spectra is directly proportional to the absorption coefficient via the principle of detailed balance:

$$I_{PL}(E) \propto \alpha(E) f(E), \tag{A.4}$$

where $f(E)$ is a suitable statistical function accounting for the thermal population of excited states by photoexcited carriers. In all undoped semiconductors, the Fermi level at zero absolute temperature is in the middle of the energy gap, usually far away

from the VB and CB band extrema. Therefore, the Maxwell-Boltzmann distribution-function may often replace the Fermi-Dirac function. However, a detailed description of the exciton wave-function is mandatory for a duly reproduction of an ideal PL spectrum, where the only contributions to emission come from intrinsic states (FE and band-to-band). The absorption coefficient is directly related, indeed, to the wave-function of the states involved in the transition via the *Fermi golden rule*. Following the work of Elliot [348], it is possible to write the exciton wave-functions for both the bound and unbound states in terms of radial and angular components:

$$\Phi_{nlm}(\vec{r}) = R_{nl}(r)Y_{lm}(\theta,\phi), \tag{A.5}$$

where m is the magnetic quantum number. For the bound levels, $R_{nl}(r)$ are the *associated Laguerre polynomials* and $Y_{lm}(\theta,\phi)$ are the *spherical harmonic functions*. For the unbound levels, the angular components are always the same whereas the radial components are now given by the *Coulomb wave-functions*. Once the wave-functions are known, the matrix elements of the Fermi golden rule can be evaluated.

In the dipole approximation, $\vec{K} = 0$ and only direct transitions are allowed. The absorption coefficient for transitions from the ground state to the excited states is given by two main terms: the term due to the discrete energy spectrum of the exciton, characterized by sharp transitions, and the term due to transition to the continuum states (band-to-band) corresponding to ionized excitons. Therefore the absorption coefficient is given by [155]:

$$\alpha(\hbar\omega) = \frac{4\pi e^2|M_{c-v}|^2}{cn\omega m_0^2}\left\{\frac{1}{a_B^3}\left[A_x(E_G - R_{eff} - \hbar\omega) + \sum_{n\geq 2}\frac{1}{n^3}A_b(E_G - R_{eff}/n^2 - \hbar\omega)\right]\right.$$
$$\left. + \left(\frac{2\mu}{\hbar^2}\right)^{\frac{3}{2}}\frac{\sqrt{R_{eff}}}{2}\int_{E_G}^{\infty}\frac{A_b(E-\hbar\omega)}{1 - exp\left[-2\pi\sqrt{R_{eff}/(E-E_G)}\right]}\,dE\right\}, \tag{A.6}$$

where the term between square brackets represents the contribution from the exciton, the term in the second row, due to transitions to the continuum states, includes the Coulomb interaction, and the exponential term inside the integral is the Sommerfeld factor. It can be demonstrated that the absorption term due to the continuum state recovers its well known formulation, $\alpha(\hbar\omega) \sim \sqrt{\hbar\omega - E_{gap}}$ for $E >> R^*$. The functions $A_{x,b}(E)$ take into account the several broadening effects that can occur during absorption[3], while $|M_{c-v}|^2$ takes into account the various selection rules, which depend on the group symmetry of the material crystal-phase.

Figure 1.2, which shows the optical absorption spectrum of GaAs at low temperature in the exciton energy region, depicts most of the spectral features described so far [349]. The sharp peaks labeled as $n = 1, 2, 3$ correspond to the first terms of the FE discrete energy spectrum, while absorption for $n > 3$ merges with that due to the continuum states. The exact values of the energy gap is determined by extrapolating the excitonic series to $n = \infty$. Recombinations due to excitons bound to some neutral donor are also detected and labeled as $(D^0 - X)$.

[3]In the case of broadening due to inhomogeneous phenomena, a Lorentzian function is the best choice, while for homogeneous phenomena a Gaussian function should be preferred.

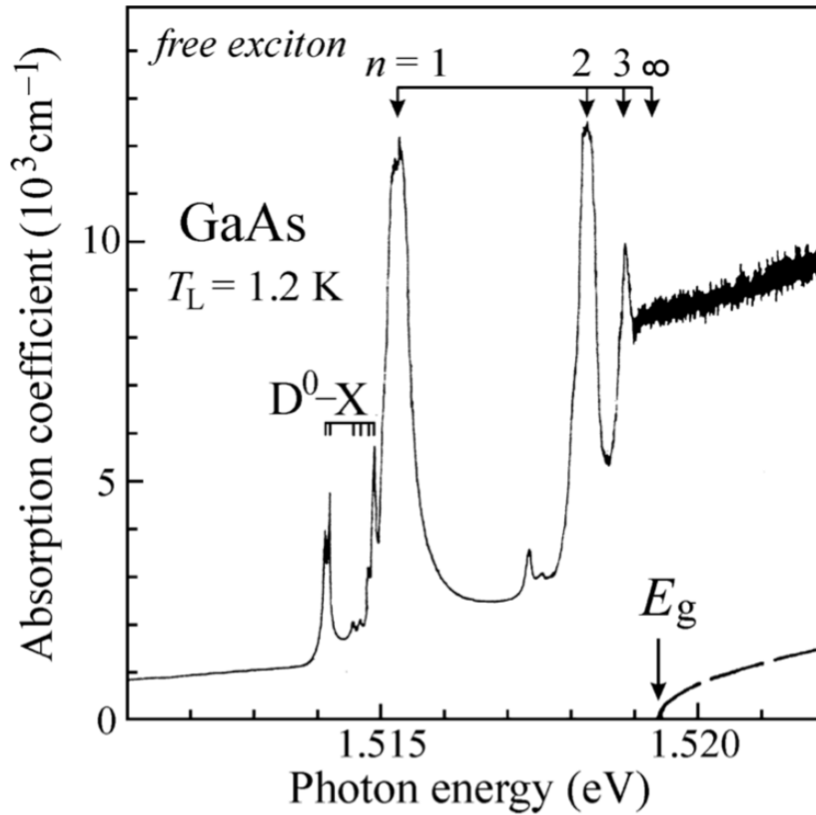

Figure 1.2. Absorption spectra close the band gap of ZB GaAs at $T_L = 1.2\,K$. The discrete energy spectrum of the free exciton is clearly visible, along with other extrinsic features due to a bound exciton. Recombination from continuum states is also visible. The dashed line at the bottom represent the theoretical shape of the absorption edge [349].

Magneto-PL

As anticipated in sec. A.1, PL experiments can be carried out under different external perturbations. Magnetic fields, in particular, can provide a valuable information about carrier effective masses and *Lande* gyromagnetic-factors as magnetic fields $\vec{B}$ affect energies and degeneracies of the states involved in optical transitions. In order to quantify those effects, several factors should be taken into account, the most important of which is the ratio between the $\vec{B}$ intensity and the Coulomb interaction in the electron-hole pair.

The Coulomb energy-scale is given by eq. A.2, the effective exciton Rydberg, which can be rewritten in terms of the hydrogen Rydberg as:

$$R_{eff}[eV] = \frac{R_y \mu[m_0]}{\epsilon_r}, \tag{A.7}$$

where $R_y = 13.6eV$ and m_0 is the electron mass in a vacuum. The magnetic energy scale is given, instead, by the cyclotron frequency, which is given in eV units by:

$$\hbar\omega_c[eV] = \frac{\hbar eB}{\mu} = \frac{1.16 \cdot 10^{-4} B[T]}{\mu[m_0]}. \tag{A.8}$$

A dimensionless parameter γ weights the relative intensity between the two effects:

$$\gamma = \frac{\hbar\omega_c}{2R_{eff}}. \tag{A.9}$$

Two straightforward approximations can be made to get analytical solutions of the Schroedinger equation for magneto-PL spectra in the opposite limits of $\gamma >> 1$ or $\gamma << 1$, while only a numerical solution can be found for $\gamma \sim 1$.

In the effective mass approximation, the Schroedinger equation for a carrier moving in a semiconductor in presence of an external potential is given by [345]:

$$(H_0 + U)\Phi(\vec{r}) = E\Phi(\vec{r}). \tag{A.10}$$

H_0 is the crystal one-electron Hamiltonian where all the effects of the crystal periodic potential are summarized by the effective mass, and U is an external perturbation (e.g., a magnetic field or a Coulomb interaction between electron-hole pairs). The effects of a magnetic field $\vec{B}$ are taken into account by the minimal substitution: the carrier momentum becomes $\hbar\vec{k} = \vec{p} + e\vec{A}$ where $\vec{A} = 1/2(\vec{B} \times \vec{r})$ is the vector potential. Finally, by neglecting the carrier spin the Hamiltonian of an exciton in a static magnetic field $\vec{B} = (0, 0, B)$ in the Landau gauge ($\nabla \cdot \vec{A} = 0$) is given by [350]:

$$\left[-\frac{\hbar^2}{2\mu}\nabla_r^2 - \frac{e^2}{4\pi\epsilon_r\epsilon_0\vec{r}} + \frac{e}{2}\left(\frac{1}{m_e} - \frac{1}{m_h}\right)\vec{B} \cdot \vec{L} + \frac{e^2B^2}{8\mu}(x^2 + y^2) + \right.$$
$$\left. + \frac{e}{2}(\vec{V} \times \vec{B}) \cdot \vec{r}\right]\phi(\vec{r}) = \left[E - \frac{\hbar^2K^2}{2(m_e + m_h)}\right]\phi(\vec{r}). \tag{A.11}$$

Here, r is the relative distance between the electron and the hole, $\vec{L}$ is the angular momentum associated to the relative motion of the $e-h$ pair, $(x^2 + y^2)$ is the square of the orbital exciton radii perpendicular to $\vec{B}$, $\vec{V}$ is the velocity of the exciton center of mass, and the right hand side contains the kinetics energy of the exciton center of mass where $\vec{K}$ is the center of mass momentum. The presence of a magnetic field introduces in the Hamiltonian a term proportional to B^2 and two linear terms in $\vec{B}$: one accounts for the effect of the Lorentz force on the exciton center of mass (last term in the left hand side), the other, instead, is the orbital Zeeman effect (third term in the left hand side).

The Zeeman effect takes into account the splitting induced by a magnetic field on states having different projections (m_J) of the total angular momentum ($\vec{J}$) along $\vec{B}$. For a certain value of $\vec{J}$, sum of the orbital ($\vec{L}$) and spin ($\vec{S}$) angular momenta, a $2J + 1$ degenerate energy level is split into $2J + 1$ states, whose energy depends on m_J, the magnetic field intensity, and the carrier gyromagnetic factor. In eq. A.11, the carrier spin can be taken into account by adding the spin Zeeman-splitting (ZS) term to the Hamiltonian part:

$$ZS = \frac{\mu_B}{\hbar} g_{exc} \vec{B} \cdot \vec{S}, \tag{A.12}$$

where $\mu_B = 5.8 \cdot 10^{-3} meV/T$ is the Bohr's magneton and g_{exc} is the exciton g-factor. The exciton ground state has $\vec{L} = 0$, thus the only contribution to the ZS is due to the exciton g-factor. Therefore, the ZS term adds to the energy of each exciton level an amount which is positive (negative) if the exciton spin is parallel (antiparallel) to the $\vec{B}$ direction in the case of a positive exciton g-factor.

By observing eq. A.11, it is clear that a solution of the Schroedinger equation is rather complex and an analytical solution does not exist. In the following, the cases for very high, very low, and intermediate values of γ will be discussed together with the related different formulations of eq. A.11.

High fields, $\gamma >> 1$

For high magnetic fields ($\gamma >> 1$), the Coulomb interaction between electron-hole pairs can be neglected and the solution for the Hamiltonian is given by $1/2m(\vec{p}+e\vec{A})^2$, as it can be easily obtained. In the case of nondegenerate semiconductors with parabolic dispersion for the CB and VB and spherical symmetry along the Γ point, the energy dispersion relations are [345][350]:

$$E_{c,v}(k_z, n) = E^0_{c,v} \pm \left(n + \frac{1}{2}\right) \frac{\hbar e B}{m_{e,h}} \pm \frac{\hbar^2 k_z^2}{2m_{e,h}}, \tag{A.13}$$

where $E^0_{c,v}$ is the unperturbed bottom (top) of the conduction (valence) band, and the plus (minus) sign refers to the conduction, c, (valence, v) case. The conduction and valence band states are split in a series of quantized energy levels identified by the quantum number $n = 0, 1, 2...$, called *Landau levels* (LLs) and depicted in fig. 1.3. It should be noticed that also the conduction (valence) band ground state is up- (down-) shifted by an amount of energy equal to the zero point energy of the harmonic oscillator ($1/2\hbar eB/m_{e,h}$). This turns in a linear increase of the energy gap with increasing magnetic fields (*linear diamagnetic shift*). The magnetic field introduces also a modification of the density of states of the conduction and valence bands. Each LL is highly degenerate and its density of state mimics that of a one-dimensional system. Indeed, the density of states at zero absolute temperature is infinite at the edge of each sublevel.

For what concerns the ZS, electron and hole states are independently Zeeman split, if the exciton interaction can be neglected. Usually, the CB is split in two levels because predominantly s-type and thus $\vec{L} = 0$, $\vec{S} = 1/2$ and $\vec{J} = 1/2$, whereas the VB is split in four levels because predominantly p-type and therefore $\vec{L} = 1$, $\vec{S} = 1/2$ and $\vec{J} = 3/2$.

Low fields, $\gamma << 1$

In the limit of very weak fields, the Coulomb interaction cannot be neglected. However, all the terms due to magnetic field of eq. A.11 can be considered as a perturbation. If only terms up to B^2 are considered, the energy correction

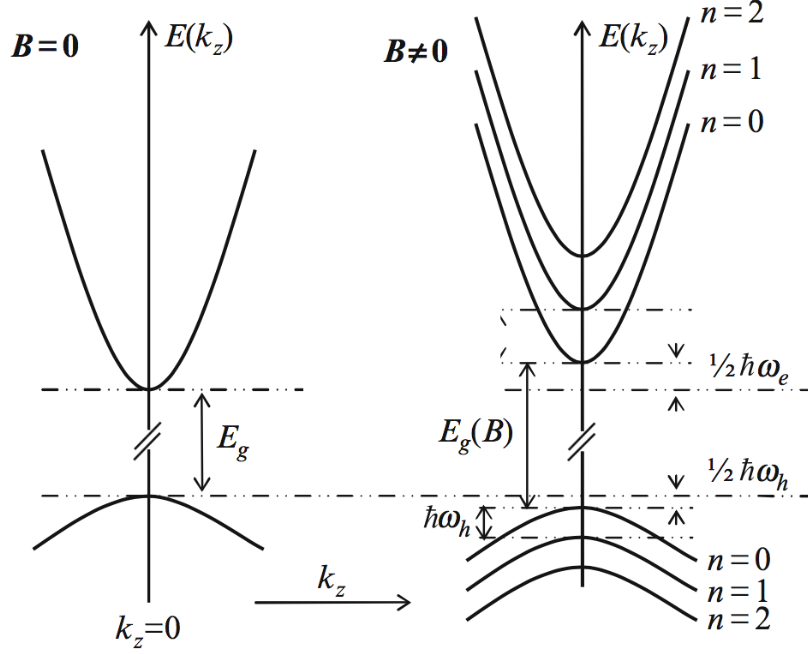

Figure 1.3. Diagram of the energy bands of a semiconductor in absence [left] and presence [right] of an external magnetic field. The magnetic field is directed parallel to the z direction. [343]

$(\Delta E_{Tot}(B))$ to the unperturbed exciton ground state is [351][352]:

$$\Delta E_{Tot}(B) = \Delta E_D + ZS = \frac{e^2B^2}{8\mu_{exc}}\langle 0|x^2 + y^2|0\rangle \pm \mu_B g_{exc}\vec{B}\cdot\vec{S}, \tag{A.14}$$

where the matrix element is related to the square of the exciton Bohr radius perpendicular to $\vec{B}$. The first part, ΔE_D, is related to a *quadratic diamagnetic shift* of the exciton energy-levels and the second term, ZS, is related to the Zeeman effect on the exciton levels. Eq. A.14 is very frequently used to gain insight into the dimension of the exciton wave-function, provided the exciton reduced mass is known. This is very useful in the case of nanostructures such as quantum dots, where the dimensions are usually lower than the bulk exciton Bohr-radius, and, therefore, the size of the exciton wave-function is rarely known.

Intermediate fields, $\gamma \sim 1$

In the case of $\gamma \sim 1$, which holds for almost all III-V semiconductors, perturbative approaches cannot be employed and the Coulomb interaction term cannot be neglected. Nevertheless, a numerical solution, which relies on symmetry considerations, has been found. It holds for any semiconductor and for any magnetic field intensity [195] [353]. Eq. A.11 has an axial symmetry along z and is invariant under space inversion, therefore the wave-function has definite parity and z-projection of the angular momentum. Moreover, allowed electromagnetic dipole transitions for band-edge emission involve an initial state whose envelope wave-function does not vanish at the origin [345]. This implies that the wave-function can be expressed as a

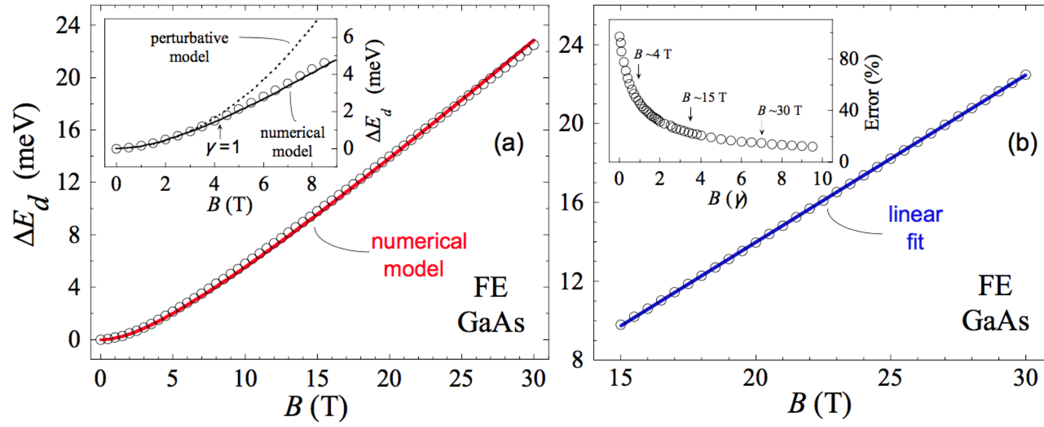

Figure 1.4. a) FE diamagnetic shift (open circles) measured in bulk GaAs from 0 to 30 T by averaging over the Zeeman split components. The red solid line is a fit to the data according to eq. A.15. The inset shows a comparison at low fields (B < 9 T) between the fit via eq. A.15 (solid line) and fit via eq. A.14 valid for $\gamma << 1$. (b) Same data displayed in (a) in the 15-30 T range. The blue solid line is a fit of the Landau level (LL) model to the data. The inset shows the percentage error on the estimate of μ_{exc}, as obtained by the LL model, as a function of the magnetic field in units of γ [343].

linear combination of spherical harmonics with null or even angular momentum and that the eigenvalue problem can be solved by a numerical calculation with a linear combination of spherical harmonics. The resulting exciton diamagnetic shift can be approximated by a ninth degree polynomial of B with known coefficients A_j[4]

$$\Delta E_D(B) = 13.6\frac{\mu_{exc}}{m_0\epsilon_r^2}\sum_{j=1}^{9} A_j\left[4.26\cdot 10^{-6}\frac{\epsilon_r^2}{(\mu_{exc}/m_0)^2}B\right]^j, \qquad \text{(A.15)}$$

which can be used to get the exciton reduced mass from the diamagnetic shift, provided ϵ_r is known. The total energy variation of the exciton ground-state energy with respect to the zero field case is given by:

$$\Delta E_{Tot}(B) = \Delta E_D + ZS = \Delta E_D \pm \mu_B g_{exc}\vec{B}\cdot\vec{S}. \qquad \text{(A.16)}$$

The difference between the numerical model and the models discussed so far is highlighted in figure 1.4, where the diamagnetic shift for bulk GaAs, as obtained by averaging over the Zeeman splitting, is shown. In fig. 1.4.a, the red solid line is a fit to the data via eq. A.15 which gives $0.053\,m_0$ for the exciton reduced mass, in good agreement with previous results [354]. In the inset, a comparison between the numerical calculation of eq. A.15 and the perturbative approach of eq. A.14 is shown. For $\gamma = 1$ (which for bulk GaAs occurs at $B = 4.3\,T$), the perturbative approach holds and the experimental data are well reproduced below $B = 4\,T$. An exciton radius equal to $12\,nm$ is obtained, a value close to the one obtainable within the exciton hydrogen-model. However, the quadratic model deviates more and more from the experimental data for magnetic fields increasing above $B = 4\,T$.

[4] $A_1 = 0.017; A_2 = 0.494; A_3 = -0.236; A_4 = 7.88\times10^{-2}; A_5 = -1.73\times10^{-2}; A_6 = 2.43\times10^{-3}; A_7 = -2.09\times10^{-4}; A_8 = 1.01\times10^{-5}; A_9 = -2.06\times10^{-7}$

The limit of high fields is shown in fig. 1.4.b) where the same data of fig. 1.4.a) are plotted from $B = 15\,T$ to $B = 30\,T$. In that magnetic field region, the LL approximation holds and data can be reproduced by a linear fit. Nevertheless, this fit leads to a value of the exciton reduced mass slightly larger than the expected value ($\mu_{exc} = 0.07\,m_0$). Indeed, $\gamma \sim 7$ at $B = 30\,T$, as reported in the inset, and thus the regime $>> 1$ is not yet reached and the LL approximation is not completely valid. The inset in fig. 1.4.b) shows the percentage error in the estimate of μ_{exc} in the LL approximation: the linear approximation is more and more valid for magnetic fields increasing to $\gamma >> 1$.

Raman

Raman spectroscopy allows an investigation of the material vibrational modes by inelastic light scattering. In a semiclassical model, it can be explained as follows. An electromagnetic (EM) wave interacting with a medium induces a dipole moment $\vec{P}$ equal to the product of the polarizability α. The latter depends on the atomic nuclei position Q and chemical bond nature, times the EM field $\vec{E}$ and is described by a 3×3 tensor. Under the approximation of small displacements of the atomic nuclei around their equilibrium position, the polarizability can be expanded as a Taylor series for small Q:

$$\alpha = \alpha_0 + \left(\frac{\partial \alpha}{\partial Q}\right)_0 Q + \frac{1}{2}\left(\frac{\partial^2 \alpha}{\partial Q^2}\right)_0 Q^2 + O(Q^3). \tag{A.17}$$

The crystal periodicity leads to normal modes for the lattice vibrations, whose energy levels are given by the phonon dispersion curves. The atomic nuclei displacements are given by:

$$Q_q = Q_q^0 \cdot e^{-2\pi i(\vec{q}\cdot\vec{r} - \omega_q t)}, \tag{A.18}$$

where Q_n^0, ω_q, and $\vec{q}$ are the amplitude, frequency, and wavevector, in the order, of a normal mode. The EM incident field produced, *e.g.*, from a laser can be expressed as $\vec{E} = \vec{E}_0 e^{2\pi i(\vec{k}\cdot\vec{r} - \omega t)}$, where $\hbar\omega$ and $\vec{k}$ are, respectively, the energy and the wavevector of the EM wave. By limiting the polarizability expansion to the first order, the dipole moment becomes:

$$\vec{P} = \vec{E}_0 \alpha_0 e^{2\pi i(\vec{k}\cdot\vec{r} - \omega t)} + \frac{1}{2}\vec{E}_0 \sum_q \left(\frac{\partial \alpha}{\partial Q_q}\right)_0 Q_q^0 e^{2\pi i\left[(\vec{k}\pm\vec{q})\cdot\vec{r} - (\omega \pm \omega_q)t\right]}, \tag{A.19}$$

where the first term is the elastic Rayleigh scattering at the same energy of the incident beam and the second term accounts for the inelastic Raman scattering. The light can be scattered at lower frequency $\omega - \omega_q$ (*Stokes*) with propagating direction $\vec{k} - \vec{q}$ or at higher frequency $\omega + \omega_n$ (*anti-Stokes*) with propagating direction $\vec{k} + \vec{q}$.

A true comprehension of the Raman effect requires the quantum calculation of the differential cross-section via the scattering-matrix and perturbation theory. The differential cross section is given by:

$$\frac{d\sigma}{d\Omega} = |\vec{e}_s \cdot R \cdot \vec{e}_i|^2, \tag{A.20}$$

where $\vec{e}_{i,s}$ are the polarizations of the incident and scattered photons and R is the scattering matrix. The latter is the spatial-temporal Fourier-transform of the correlation function polarizability-polarizability and it is a 3×3 matrix with the details of the radiation-matter interaction. The reader should refer to [355] for a more exhaustive description of the quantum theory of the Raman effect.

Albeit the quantum theory of the Raman scattering provides selection rules and intensity of the scattered light, this scattering is mainly governed by energy and momentum conservation, as highlighted in eq. A.19. Those conservations require that $\vec{k} = \vec{k}_s \pm \vec{q}$, where $\vec{k}_s$ is the wave vector of the scattered light, and $\hbar\omega = \hbar\omega_s \pm \hbar\omega_q$, where $\hbar\omega_s$ is the energy of the scattered light. Therefore, Raman scattering probes only phonons close to the center of the Brillouin zone. Finally, it should be noticed that the rate of Stokes and anti-Stokes scatterings are different. Indeed, a phonon is emitted in a Stokes process, independently of phonon population. Conversely, a phonon is absorbed in an anti-Stokes process at a rate that depends on phonon population and therefore decreases for decreasing lattice temperature T.

A.2 Optical experimental setup

Micro and macro photoluminescence setup

The main experimental results of the present thesis have been obtained by macro-(M) or micro-(μ) photoluminescence measurements where the dimension of the focused laser-beam spot is on the order of hundreds of μm or nm, respectively. $\mu-$PL allows measurements of single nanostructures, while M-PL allows one to get information about an ensemble of nanostructures, thus avoiding statistically non-relevant effects due to the details of single nanostructures. Figure 1.5 shows a top-view diagram of the M-PL setup employed in the thesis. The laser excitation is provided by a diode pumped solid-state laser (*Coehrent* Verdi V-8). The active medium is a neodymium-doped yttrium-vanadate ($Nd : YVO_4$) which emits photon at $1064\,nm$. A type-I non linear lithium-triborate (LBO) crystal halves the wave-length emission to $532\,nm$ by second harmonic generation. The resulting output beam is linearly polarized perpendicular to the optical table. The output power of the laser can be tuned up to $8\,W$ with a stability better than 1% after a warm up of ten minutes. Neutral filters (NF) and polarisers (P) are used to finely tune the laser excitation power. An interference narrow-band ($\pm 3\,nm$) filter (IF_1) centered at the laser wave-length removes the spurious laser-cavity fluorescence.

The laser beam is focused on the sample by a lens (L_1) and two mirrors (M_1, M_2). The lens focal length ($25\,cm$) reduces the laser-beam spot on the sample to $200\,\mu m$. Mirror M_2 is as small as possible in order to minimize the PL signal losses in the backscattering configuration where the laser beam and PL-signal wave-vectors are anti-parallel; see fig. 1.5. The laser exciting power is measured in front of the cryostat window by a Si photodiode calibrated in wavelength.

Samples are mounted inside a *Edwards* closed-cycle He cryostat made up of a Coolstar 2/9 coldhead and a Cryodrive compressor interconnected by high and low pressure He gas lines. High pressure He provided by the compressor expands inside the coldhead and returns at low pressure to the compressor. While expanding, He gas cools the coldhead whose cold finger is in thermal contact with the sample

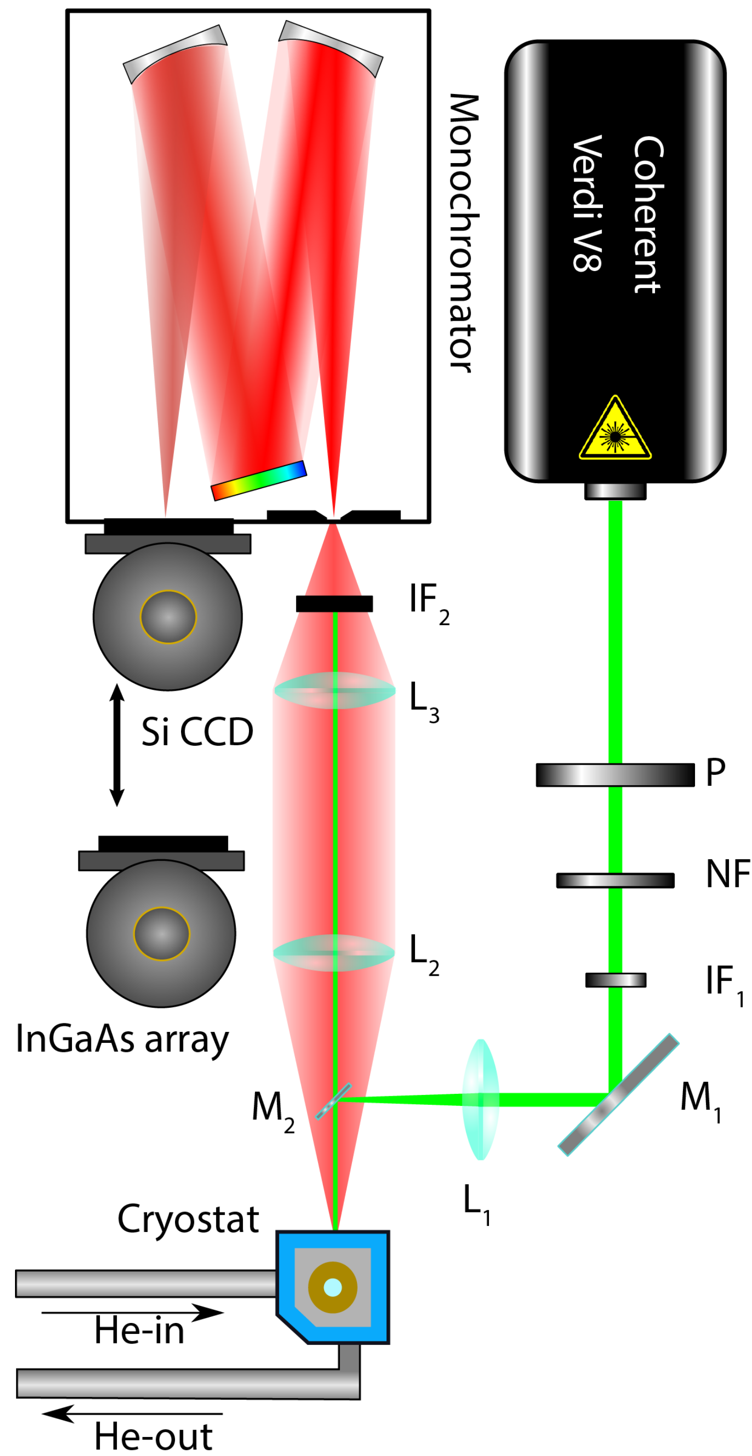

Figure 1.5. Top-view schematic of the experimental setup employed in M-PL experiment. M_i, L_i, and IF_i denote mirrors, lens, and optical filters, respectively. NF denotes neutral filters and P denotes polarisers.

[356]. Within the sample chamber, high-vacuum (HV) conditions ($\sim 10^{-6}\,Torr$) are maintained by a turbo-molecular pump in series to a rotative pump. Samples are

glued with conductive silver paint to a polished Cu vertical sample-holder, which warrants an efficient thermal contact. The sample temperature is varied from $10\,K$ to $310\,K$ by an Oxford Instruments ITC4. This instrument controls an electric current flowing into a resistor embedded in a Cu column on which the sample holder is screwed. A temperature control within $0.1\,K$ is achieved by a feedback relying on a proportional-integral-derivative circuit driven by a four-wire Rh-Fe resistance thermometer, also embedded in the Cu column.

The isotropic PL emission is collimated by a lens (L_2) (focal distance equal to $25\,cm$). Another lens (L_3) (focal distance of $50\,cm$) focuses the collimated PL emission on the entrance slit of a monochromator. The *F-number*[5] of the focusing lens is matched to that of the monochromator in order to fill exactly the monochromator grating and thus maximize energy resolution -while minimizing spurious stray light and signal losses. A razor edge filter (IF_2) with wavelength cut-off at $535\,nm$ is placed in front of the monochromator slit to prevent the reflected laser beam to enter into the monochromator as well as avoid contributions from higher orders of the diffracted light.

The PL signal is frequency resolved by an *Acton* Spectra Pro 750 monochromator in a Czerny-Turner configuration, with two concave mirrors (focal length of $75\,cm$). The first mirror collimates the PL broad signal to the grating which disperses the light to the second mirror. Then, the second mirror focuses the dispersed light on the exit slit where a suitable detector converts the collected light into an electrical signal. Three different diffraction gratings (300 and 600 grooves/mm with blaze at 1 μm and 1200 grooves/mm with blaze at 0.5 μm) are mounted on a rotating turret driven by a stepping motor, thus allowing a remote control of wavelength scan and grating switch. The wavelength resolution is directly proportional to the grating groove-density.

Multichannel detectors are used to detect the dispersed polychromatic PL spectra. A silicon charged coupled device (CCD) of *Princeton instruments* Spec 10:100 BR allows a quick acquisition ($\sim\ ms$) of portions of PL spectra in the $400 - 1100\,nm$ energy range. The device, cooled down to $-120°C$ by liquid nitrogen to reduce the thermal noise, is made of 1340×100 pixels. The pixel size ($20 \times 20\,\mu m$) is the ultimate limit to the device's resolution ($\Delta\lambda = 2.2 \times 10^{-3} nm$ for a 1200 grooves/mm grating). An (InGa)As linear array made of 512 pixels, each one of size $50 \times 50\,\mu m$, is cooled down to $-100°C$ by liquid nitrogen to detect PL spectra in the $900 - 1500\,nm$ energy range. The system resolution is $\Delta\lambda = 5.5 \times 10^{-3} nm$ for a 1200 grooves/mm grating, because of a pixel size greater than that of the CCD.

Figure 1.6 shows the side-view of the μ-PL setup employed in this work. A sub-micrometer resolution is obtained by using microscope-objectives with long working-distance and high numerical-aperture (N.A.) that focus a laser beam - emitted by the same source as in the M-PL setup and sent to the samples by a beam splitter (BS in the figure). Four different objectives are mounted on the rotating turret of the microscope: a 20× (N.A=0.4), 50× (N.A=0.5), 100× (N.A=0.8) *Olympus* LMPLanFL objectives (the first two objective optimized in the VIS range and the latter one in the NIR range) and a 100× (N.A=0.75) *Zeiss* LD EC Epiplan

[5]The *F-number* of an optical system is defined as the ratio between the lens focal length and the diameter of the light spot on the lens surface.

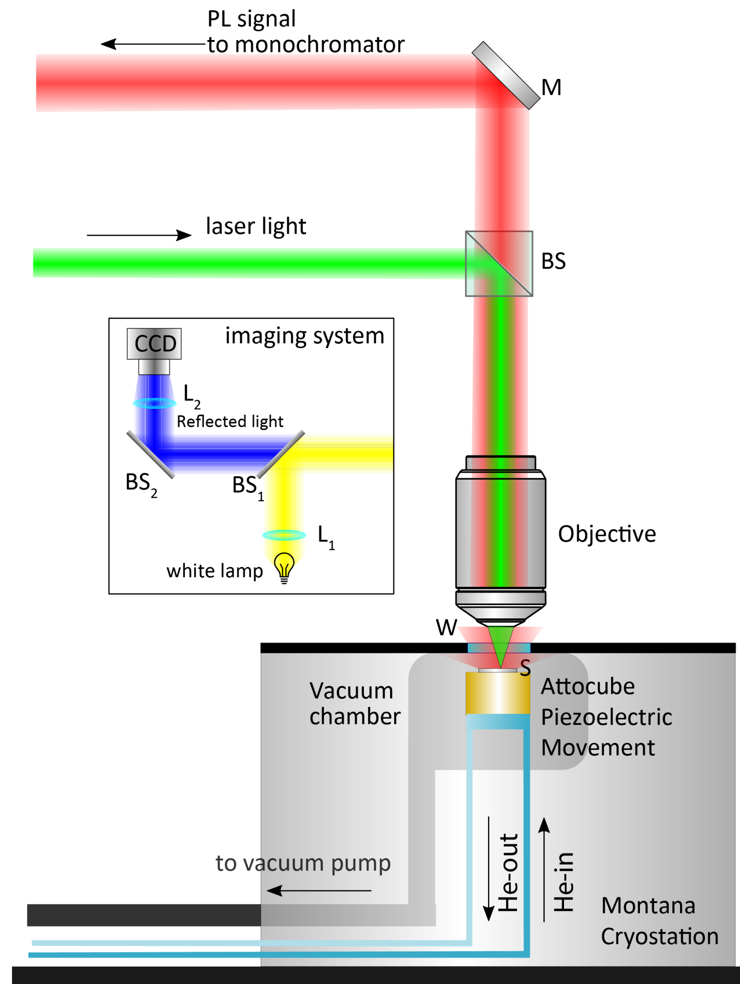

Figure 1.6. Side-view schematic of the experimental setup employed in μ-PL experiment. M, BS, W, and S denote mirror, beam splitter, window, and sample holder, in the order. The imaging system is reported in the inset. Here L_i and BS_i denote lens and beam splitters.

NeoFluar objective optimized in the VIS range. The laser beam can be focused to a diffraction limited spot (around 600 nm) by the 100× objectives. Sometimes, a different excitation configuration, denoted as *external excitation*, was used. In that configuration, not shown in the figure, a 200 μm laser spot is focused onto the sample by a 20 cm focal length lens and the emitted light is collected by a microscope objective. The sample PL signal (red beam in fig. 1.6) is collected by the same objective employed to focus the laser beam in the backscattering geometry.

A confocal geometry (not sketched in the figure) is also used to collect the signal with a spatial resolution as high as possible. In a confocal geometry, a pinhole aperture is placed exactly at the focal plane between two lenses with a same focal distance [357]. The pinhole width can be varied from 10 to 100 μm to limit the collection of light coming from regions surrounding the excitation laser-spot. The PL collimated emission is then sent, via a mirror M, to a 10 cm focal length lens that focuses the PL on the entrance slit of the same monochromator used in the M-PL

setup. The same IF_2 filter removes the reflected laser beam from the PL signal and the same detectors are used to analyze the dispersed PL signal.

Samples are glued with a silver paint to a sample holder placed inside a a closed-cycle He cryostat (*Montana instruments* optical Cryostation). The cryostation mode of operation is the same of the M-PL cryostat with the only variant of two in-series expansion-chambers, instead of one, to reduce the lowest achievable temperature ($T_{min} = 4.5\,K$) and the vibrational instability ($< 5\,nm$, peak to peak) produced by the He expansion. Within the sample chamber, a high-vacuum (HV) ($\sim 10^{-7}\,Torr$) is achieved by a cryopump that traps molecules in cold activated carbon adsorbers. As in the M-PL setup, the temperature can be stabilized (between 4.5 K and 350 K) by modulating the frequency of the helium cycle and applying a variable voltage to a heat controller. The sample holder is mounted on the top of three planar *Attocube* piezoelectric-motors. Two of them (ANPx101) allow sample-holder steps in the $x - y$ plane as short as $50\,nm$ along distances on the order of $1\,cm$, the other one (ANSxy100) allows steps shorter than $1\,nm$ in a $x - y$ plan area of $40 \times 40\mu m$. Finally, exactly the same system is used to do μ-Raman measurements.

The inset in fig. 1.6 shows a scheme of the imaging system. The white light of a halogen lamp is collimated by a lens L_1 and sent by a beam splitter BS_1 to a microscope objective (the same used in mu-PL) that focuses the white light onto the sample surface. The light reflected back by the sample surface is collected by that same objective, sent through BS_1 and by a beam-splitter BS_2 to a lens L_2 that forms a sample image on a *IDS uEye industrial* CCD. The imaging system is placed between the microscope objective and the beam splitter from which the laser beam comes from. This system can be moved easily and rapidly to switch from the imaging to the spectroscopy acquisition-procedure.

Photoluminescence excitation setup

Figure 1.7 shows the top view sketch of the setup in a M-PLE experiment. The tunable excitation source required for PLE experiments is provided by a *Coherent* Model 890 passive lasing system pumped by the Verdi V8 previously described. The active medium is a titanium-doped sapphire (Al_2O_3:Ti) crystal (Ti:Sa). The output frequency is changed by rotating a birefringent Lyot filter by an electrically-driven piezoelectric inchworm PS. By using three different sets of mirrors, the Ti:Sa can lase in the wave-length range from 690 nm to 1090 nm. The output power can be as high as 1 W at high pump intensity ($\sim 8W$). The Ti:Sa crystal (refractive index n = 1.76) is terminated by a surface at Brewster-angle ($\Theta_B = 60.4°$) in order to minimize reflection losses and to provide a polarized output (perpendicular to the optical table in this setup).

At the laser output neutral filters finely tune the excitation power intensity recorded at each wavelength. A beam splitter (BS_1) switches 8% of the laser beam to a power meter (PM) equipped with a Si (for VIS range) or (InGa)As (for NIR range) photodiode calibrated in wavelength. A following beam splitter (BS_1) reflects 5% of the laser beam to a Michelson interferometer (WM) to accurately measure wave-lengths in real time ($\Delta\lambda < 0.1\,nm$). The measured wavelength-value is recorded by the control system and used to normalize the PL signal to the system calibration-curve and to drive the Ti:Sa laser inchworm.

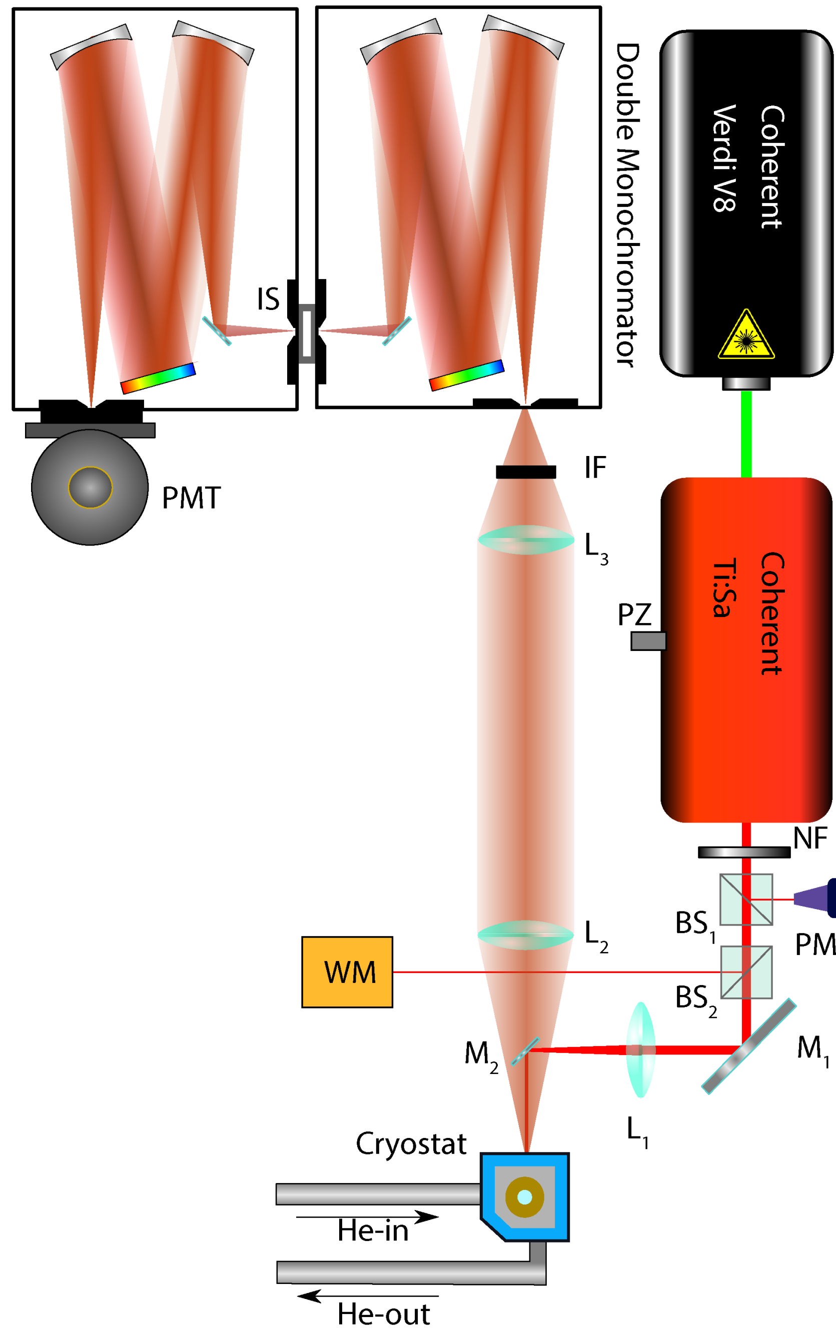

Figure 1.7. Top-view schematic of the experimental setup used in M-PLE experiment. M_i, L_i, and BS_i denote mirrors, lens, and beam splitters, in the order. PM, WM, IF, IS, NF, and PMT label power meter, wavelength meter, optical filter, intermediate slit, neutral filter, and photomultiplier tube, in the order. PS is a piezoelectric inchworm used to change the wave-length emission of a Ti:Sa laser.

As in the M-PL setup, the exciting laser beam is steered to the samples inside the cryostat by two mirrors (M_1 and M_2) and focused by the lens (L_1). Sample holder is rotated by 30° to prevent collection of the reflected laser light. The PL

signal is collected as in M-PL. Two identical 75 cm monochromators are connected in series through an intermediate slit (IS), with mechanical components working in tandem as to select the same wavelength. This experimental configuration allows a doubling of the maximum achievable spectral resolution and a stray-light reduction.

Single channel detectors are used to measure the PL intensity at fixed energy while varying the laser excitation energy, as required in a PLE experiment. A *Hamamatsu* R943 photomultiplier tube (PMT), used in single photon counting mode, provides the extremely sensitive and low-noise detection needed for low signal intensities, as it is often the case in the double-monochromator configuration. A Cs-activated GaAs photocathode extends the NIR PMT response to $\sim 880\,nm$. At longer wave-lengths, the PMT response falls down abruptly, as its photoelectric response does. The PMT is thermoelectrically cooled to $-30°C$ to reduce the intrinsic electronic noise.

Magneto-photoluminescence

All the PL measurements under magnetic fields have been performed at the High Field Magnet Laboratory at the Radboud University of Nijmegen, in the Netherlands. M-PL and $\mu-$PL setups under magnetic fields are similar to those described in section A.2. PL is excited by a frequency-doubled $Nd:YVO_4$ laser focused by a long focal-length objective (spot diameter $\sim 10\,\mu m$) or short focal-length objective (spot diameter $\sim 1\,\mu m$). PL is collected in a backscattering configuration (namely, laser and PL wave-vectors are always anti-parallel) by a same objective. The collected signal is focused by a lens on the entrance slit of a 30 cm long monochromator and detected by either a Si CCD or an InGaAs array, both cooled at liquid-N_2. The monochromator is equipped with 150, 300, and 1200 grooves/mm gratings. The samples are glued by silver paint on a sample holder mounted in a liquid-N or liquid-He bath cryostat. The cryostat is placed in a water-cooled *Florida* Poly-Bitter type resistive magnet with a maximum static field $\vec{B}$=30 T [358]. The magnetic field direction is fixed and the sample holder can be mounted into the cryostat in two possible configurations with respect to $\vec{B}$. In the *Faraday* configuration, PL wave-vector ($\vec{k}$) and $\vec{B}$ are parallel. In the *Voigt* configuration, instead, $\vec{k}$ is made perpendicular to $\vec{B}$ by a small 45° mirror inside the cryostat. A typical Bitter resistive magnet uses conventional electrical currents to generate high magnetic fields [361]. Figure 1.8a shows a sketch of the principle behind Bitter magnets. As in the case of a solenoid, where a current travelling through coils generates an intense magnetic field in the center of the solenoid itself, in a Bitter magnet the current flows through hundred of copper discs[6] piled one atop the other. The conductive discs are separated each other by insulators plates inserted at strategic spots in order to block all possible shortcuts and ensure that the current takes the longest possible path, as highlighted by the red line in fig. 1.8a(if the electrical current could find the shortest route to complete its journey from the top of the magnet coil to the bottom, the magnet performance would be very poor). The disc stacking-sequence is designed to maximize the carried current (the greater the current, the greater the

[6]Depending on the specifications of the magnet, 1 mm-thick holed discs may be made of pure copper, an excellent conductor, or of a copper alloy (Cu-Be, Cu-Zr, or Cu-Ag).

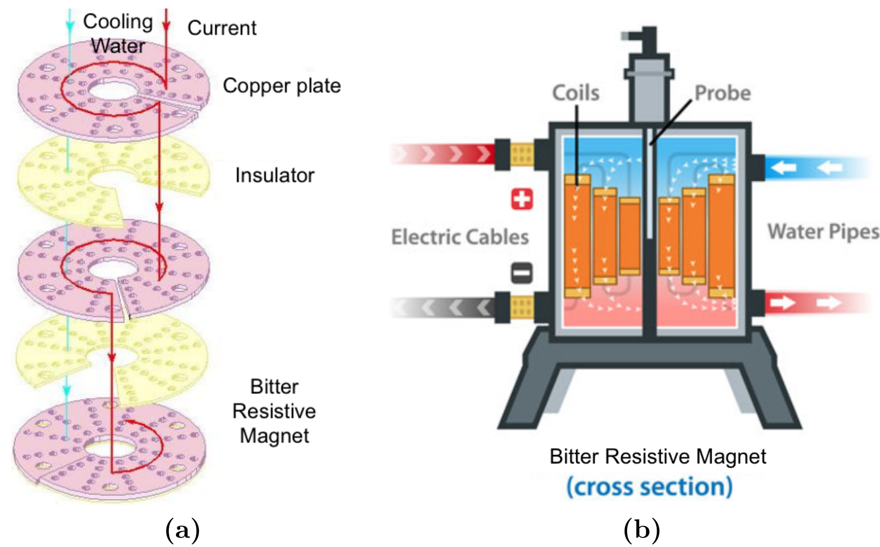

(a) (b)

Figure 1.8. a) Schematic principle of a Bitter resistive magnet. Large holes host the rods needed to align a series of parallel Cu disks whereas small holes in these same discs allow water to flow throughout and cool down the discs. Insulating discs separate groups of bitter turns [359]. b) Illustration of coils stacked as Russian dolls in the magnet. Electric connections and cold water pumping through the coil are highlighted [360].

magnetic field it generates) while minimizing the chance of disc melting by Joule effect.

Large round holes accommodate rods (not shown) that keep the metal plates in place, while narrowest elongated holes let huge amounts of cold water flow through the magnet, see cyan line in fig. 1.8a. Almost 15.000 liters of de-ionized water at $10°C$ are sent per minute inside the coil to avoid the quick melting of magnets into copper puddles.

A group of intermixing insulator and metallic discs stacked in a flat or helical way, called *magnet turn*, is the building block of the magnet. Usually, a turn is made of 4 to 16 Bitter plates along with one or more insulators, each turn being one loop in the current path through the magnet. Several magnet turns can be placed one inside the other, as shown in the side-view in fig. 1.8b, and run in series: the current spirals down the innermost coil first, then works its way up the next one, passing through the largest coil last. There are 3 coils in our magnet. The sample is mounted at the base of a cryostat tube which is placed at the center of the magnetic field (denoted as probe in fig. 1.8b).

A.3 Post-growth hydrogen-implantation and electron-beam lithography

In the present PhD thesis, hydrogen has been post-growth implanted into samples in order to study its effects on the electronic and optical properties of transition metal dichalcogenides (see part II of this thesis). Hydrogen post-growth incorporation in a crystal can be achieved by a hydrogen plasma at low-power density or by an ion

gun with a *Kaufman source* [362]. A schematic representation of the hydrogenation chamber is given in figure 1.9

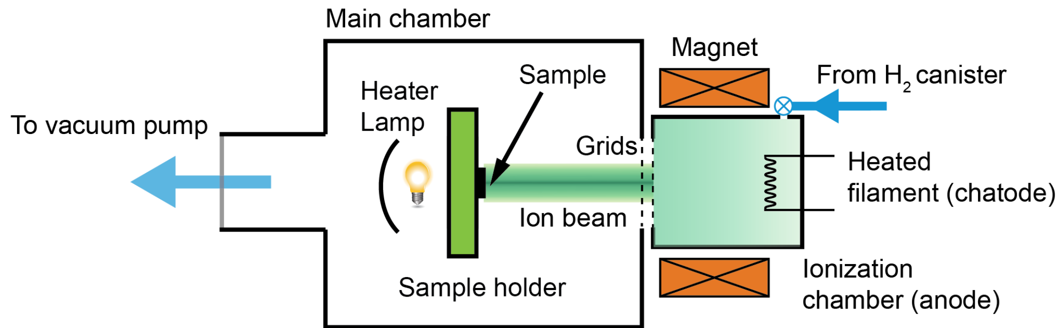

Figure 1.9. Schematic illustration of the hydrogenation chamber with a Kaufman ion-beam source.

At the start of each implantation, the whole chamber is pumped by a turbo-molecolar pump down to a pressure of $\sim 1 \times 10^{-6}\, mbar$ to minimize contamination from foreign atomic species. A constant flux equal to 30 scc per second of molecular hydrogen (H_2), equivalent to a dynamic hydrogen atmosphere of $\sim 2 \times 10^{-4}\, mbar$, is maintained throughout the irradiation process in the *main chamber*. In the *ionization chamber* the molecular hydrogen is dissociated and ionized into protons by scattering with electrons emitted from a hot tungsten filament (*cathode*) and accelerated towards the wall of the chamber (*anode*). A couple of *magnets* spirals the electron trajectories to enhance the H-ionization cross-section. A set of graphite grids negatively charged accelerate protons towards the main chamber, thus generating a beam with a Gaussian profile ($\sigma \sim 2,5\, cm$ for a grid potential of -100 eV). Then, in the main chamber the proton beam hits the sample, which is electrically grounded to neutralize the impinging protons. Since the sample sizes are smaller than the beam profile, a uniform irradiation of each treated sample is ensured. Low ion-beam energies ($10 \div 100\, eV$) are used to reduce the mechanical damage of the sample surface.

The samples are glued by silver paint on a metallic *sample holder* that can be heated up to $600°C$ by two $650\, W$ *halogen lamps*. A thermocouple mounted beneath the sample holder provides a feedback to the power supply of the two lamps to regulate the temperature with a precision of $\pm 1°$. The same system can be used also to perform *thermal annealing* up to $600°C$ in a vacuum.

Various parameters, such as filament current, grid difference-voltage, and H_2 flux permits to vary with high accuracy the ion current impinging onto the samples, as measured by a *Faraday cup* placed in front of the samples. Ion current (I) and exposure time (Δt) determine the hydrogen dose d_H sent to the sample:

$$d_H(cm^{-2}) = \frac{\Delta t[s] \cdot I[\mu A/cm^2]}{1.6022 \cdot 10^{-13}[C]}. \tag{A.21}$$

Typical exposure times varied from few minutes to several hours leading to impinging hydrogen doses ranging from $10^{15}\, ions/cm^2$ to $10^{19}\, ions/cm^2$. In order to achieve a

spatially controlled hydrogen implantation, some of the samples have been patterned with arrays of H-opaque masks at the electron-beam-lithography (EBL) facility of the CNR Institute of Photonics and Nanotechnologies in Rome. Electron-beam lithography is a powerful technique to design a nanoscale pattern onto the surface of a sample with an extremely high spatial resolution (down to 10 nm [363]). In the EBL process, a focused electron beam is scanned onto the surface of a sample previously covered with a thin layer of an electron sensitive material (resist). Electrons change the solubility of the resist in an appropriate developing solvent, thus allowing a selective removal of the resist. A resist can be either positive or negative: in the former case the resist solubility increases after exposure to the electron beam, leading to a chemical removal of the exposed areas, while in the latter case the resist solubility decreases and the non-exposed areas are chemically etched away.

Here, a hydrogen silesquioxane (HSQ) negative e-beam resist [364] was used, because of its property to be H-opaque under the irradiation conditions used. A *Vistec* EPBG 5HR system working at 100 kV was the EBL facility. The main steps in the spatial control of the hydrogen implantation are the following:

- *Resist deposition.* The sample surface is covered with a liquid solution of a HSQ resist, after its thermalization at room temperature for 30 minutes. Then the sample is spun for a few minutes at $3500\,rpm$ in order to produce a uniformly $80\,nm$ thick resist layer.

- *Exposure and development.* The electron beam (electron dose of $300\,\mu C/cm^2$) is scanned across the sample in order to write a pattern of ordered arrays of octagonal openings with maximal diameters of 1, 3, and 5 μm and inter-feature spacing of $3\,\mu m$. After exposure, the resist is developed with an aqueous solution of tetramethyl ammonium hydroxide at 2.4%.

- *Hydrogen implantation.* Patterned samples are hydrogenated via the procedure described above (hydrogen doses ranging from $1 \cdot 10^{16}\,ions/cm^2$ to $7 \cdot 10^{16}\,ions/cm^2$ at $T = 150\,K$).

- *H-opaque mask removal.* HSQ masks are removed by chemical etching in an aqueous solution that does not attack the surface of the treated samples (potassium borates at $5 - 15\%$ and potassium hydroxide at 2%).

A.4 Atomic force microscopy

A morphological characterization of transition-metal dichalcogenides-flakes has been performed by *atomic force microscopy* (AFM). AFM belongs to a wide family of microscopy techniques called *scanning probe microscopies* (SPMs). An SPM is defined as a microscopy where a very sharp (under ideal cases, atomically sharp) probe-tip cemented on the top of a cantilever slightly contacts or is very close[7] to the surface of the sample to be investigated. While the probe tip scans over the surface, the interaction of the tip with the sample, which gives rise to tunneling currents in a scanning tunneling microscopy, or interaction forces in AFM, causes

[7] A few nm or less

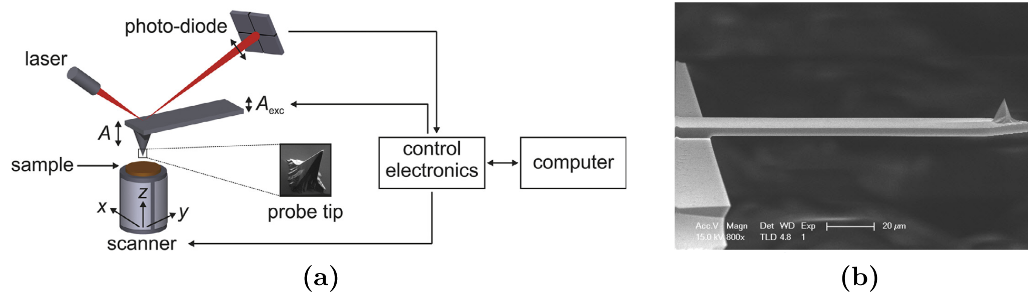

(a) (b)

Figure 1.10. a) Schematic drawing of a typical AFM setup. A piezoelectric scanner controls the relative tip-sample position with picometer precision, while the deflections of the cantilever with an integrated probe tip are detected by the deflection of a laser-beam. A computer controls the electronics for tip-sample positioning, data acquisition, and the feedback loops. For dynamic AFM operations, the cantilever base is excited with an amplitude A_{exc}, resulting in an oscillation of the probe tip with amplitude A [365]. b) Scanning-electron-microscopy (SEM) image of a cantilever with an integrated probe tip similar to that used in this work [366].

tiny vertical displacements of the cantilever. In turns, these displacements lead to angular deflections, measured by a 4-quadrant photo-detector, of a laser beam impinging on the cantilever top. Feedback loops are used to keep fixed certain physical parameters (*e.g.*, interaction forces or surface-tip distance) leading to the acquisition of high-resolution topographic maps of the sample surfaces. In particular, in an AFM the probe tip interacts with the sample via van der Walls forces, to which tip and surface atoms are subjected. Therefore, the precise detection of interaction forces acting between the tip and the sample surface at close separations is the key principle behind AFM. Morphology images are obtained via feedback loops which hold constant the interaction force, and thus the distance between probe tip and surface.

The main components of an AFM set-up are displayed in figure 1.10a and are identified as follow [367]

- *Piezoelectric scanners.* Piezoelectric movements with an expansion coefficient of the order of $0.1\,nm/V$, which allow the movement of the sample in the $x-y-z$ space with pm-scale precision. Unfortunately, piezoelectric movements are subjected to nonlinearities including hysteresis and creeps, which often limit the AFM field of view to $100 \times 100\,\mu m$.

- *Force sensing element.* It consists of a micro-fabricated cantilever[8] with an integrated, sharp tip; see fig. 1.10b. The cantilever acts as a soft spring (spring constant $k = 0.01 \div 100\,N/m$), which is deflected in response to the force interaction (F) between the tip and the sample surface by an amount d via the Hooke law ($F = -k \cdot d$). Deflections of the force sensor are detected via a laser beam reflected from the cantilever and collected on a four quadrant photo-diode.

[8]It can be made of Si, SiO_2, or Si_3N_4, with a length on the order of a few hundreds of μm

- *Feedback control.* A control electronic is implemented to maintain fixed the intensity of interactive forces between tip and sample during the raster-scan over the sample. It controls the z-component of the piezoelectric scanner in order to adjust the tip-sample distance according to the Hooke law. In the meanwhile, it records these movements to generate a 3-dimensional image of the sample surface.

AFM is commonly operated in three distinct modes: the *static* mode (frequently referred to as *contact mode*), and two *dynamic* modes, where the force sensor oscillates at (*tapping mode*) or near (*non-contact mode*) its resonance frequency using a piezoelectric element with excitation amplitude A_{exc}.

In the *static* mode, the cantilever slightly touches the sample surface and undergoes a repulsive force. Therefore, it bends whenever its spring constant is smaller than the interaction between the probe-tip and the sample surface. The feedback loop maintains a constant force between the probe and the sample. A tracking and recording of the vertical displacements the piezoelectric scanner leads to the acquisition of topographical maps with nm resolution. However, despite its operational simplicity contact mode AFM can destroy the samples surfaces, while topography images are usually affected by unwanted lateral forces.

The *dynamic* mode requires ultra high vacuum condition to have the best surface images. In that mode, the cantilever oscillates near its resonance frequency with an amplitude of the order of a few nm in the non-contact mode or of tens of nm in the tapping mode. In the former case, the probe does not contact the sample surface, whereas in the latter case the probe lightly “taps” on the sample surface during its scanning and contacts the surface at the bottom of its oscillations. However, in both cases the system detects variations in the resonance frequency or vibration amplitude whenever the tip approaches the sample surface. Indeed, the cantilever can be thought as a simple, driven harmonic oscillator. Therefore, the feedback loop must maintain constant the oscillation amplitude in the *dynamic* mode, thus allowing the acquisition of a surface image. Albeit AFM in the *dynamic* mode is more time consuming than that in the *static* mode, it has several advantages as regards high resolution mapping of samples that can be easily damaged. Moreover, in the non-contact mode the probe lifetime is rather extended.

In this thesis, a *Bruker* dimension icon SPM system, with a Nanoscope V controller[9], and a *Veeco* Digital Instruments Dimension D3100 system, with a Nanoscope IIIa controller[10], were used in the tapping mode with monolithic silicon probes (nominal tip curvature radius of $5 - 10\,nm$ and force constant of $40\,N/m$).

[9]Located at the Research Center on Nanotechnology Applied to Engineering of Sapienza (CNIS)

[10]Located at CNR Institute of Photonics and Nanotechnologies in Rome

Publications and conferences

Papers in international peer-reviewed journals

1 A. Zilli , M. De Luca, D. Tedeschi, H. A. Fonseka, A. Miriametro, H. H. Tan, C. Jagadish, M. Capizzi, and A. Polimeni. *Temperature Dependence of Interband Transitions in Wurtzite InP Nanowires.*
ACS Nano, **9** (4), 4277-4287 (2015).

2 D. Tedeschi, M. De Luca, H. A. Fonseka, Q. Gao, F. Mura, H. H. Tan, S. Rubini, F. Martelli, C. Jagadish, M. Capizzi, and A. Polimeni. *Long-lived Hot Carriers in III-V Nanowires.*
Nano Letters, **16** (5), 3085-3093 (2016).

3 M. Valentini,C. Malerba, F. Menchini, D. Tedeschi, A. Polimeni, M. Capizzi, and A. Mittiga. *Effect of the order-disorder transition on the optical properties of Cu2ZnSnS4.*
Applied Physics Letters, **108** (21), 211909-211914 (2016).

4 D. Tedeschi, M. De Luca, A. Granados Del Aguila, Q. Gao, G. Ambrosio, M. Capizzi, H. H. Tan, P. C. M. Christianen, C. Jagadish, and A. Polimeni. *Value and anisotropy of the electron and hole mass in pure wurtzite InP nanowires.*
Nano Letters, **16** (10), 6213-6221 (2016).

5 H. A. Fonseka, A. S. Ameruddin, P. Caroff, D. Tedeschi, M. De Luca, F. Mura, Y. Guo, M. Lysevych, F. Wang, H. H. Tan, A. Polimeni, and C. Jagadish. *InP-$In_xGa_{1-x}As$ core-multi-shell nanowire quantum wells with tunable emission in the 1.3–1.55 μm wavelength range.*
Nanoscale, **9** (36), 13554-13562 (2017).

6 D. Tedeschi, E. Petroni, M. Felici, G. Pettinari, S. Sennato, C. Zhang, Y. Lu, and A. Polimeni.*Proton-driven patterning of bulk transition metal dichalcogenides for light generation, mechanical modulation, and hydrogen storage.*
under review in Nature Nanotechnology (2017)

International conferences (in bold the name of the presenting author)

1 **M. De Luca**, A. Zilli, D. Tedeschi, F. Mura, H. A. Fonseka, S. Mokkapati, H. H. Tan, L. M. Smith, C. Jagadish, M. Capizzi e A. Polimeni. *Light absorption*

in Wurtzite-phase InP Nanowires
Poster presentation at the III-V Nanowire Photonics (Bad Honnef, March 2015).

2 **D. Tedeschi**, M. De Luca, A. Zilli, H. A. Fonseka, Q. Gao, F. Mura, H. H. Tan, C. Jagadish, M. Capizzi, and A. Polimeni. *Dependence of hot carrier effect on the diameter of InP nanowire*
Poster presentation at the III-V Nanowire Photonics (Bad Honnef, March 2015).

3 **D. Tedeschi**, M. De Luca, H. A. Fonseka, Q. Gao, F. Mura, H. H. Tan, C. Jagadish, M. Capizzi e A. Polimeni *What is the NW electron temperature?*
Poster presentation at *PULSE* summer school (Porquerolles, September 2015).

4 **D. Tedeschi**, M. De Luca, H. A. Fonseka, Q. Gao, F. Mura, H. H. Tan, C. Jagadish, M. Capizzi, and A. Polimeni *Hot carrier in InP nanowires*
Oral presentation at the 101 Congresso Nazionale Societa' Italiana di Fisica (Roma, September 2015).

5 M. De Luca, A. Zilli, H. A. Fonseka, D. Tedeschi, F. Mura, S. Mokkapati, A. Miriametro, H. H. Tan, C. Jagadish, M. Capizzi, and **A. Polimeni** *Polarized Light Absorption in Wurtzite InP Nanowires*
Poster presentation at the Nanowires 2015 Conference (Barcelona, October 2015).

6 **M. De Luca**, D. Tedeschi, H. A. Fonseka, Q. Gao, F. Mura, H. H. Tan, C. Jagadish, M. Capizzi, and A. Polimeni *Nanowires Are Not So Cool*
Oral presentation at the Nanowires 2015 Conference (Barcelona, October 2015).

7 **D. Tedeschi**, E. Petroni, M. Felici, G. Pettinari, S. Sennato, S. Albano, C. Zhang, Y. Lu, C. Jagadish, M. Capizzi, A. Polimeni *Light emission in hydrogenated mono-, bi-, and multi-layer* $MoSe_2$
Poster presentation at the European Materials Research Society Spring Meeting (Lille, May 2016).

8 **D. Tedeschi**, M. De Luca , A. Granados del Aguila, H. A. Fonseka, F. Mura, M. Capizzi, H. H. Tan, P. C. M. Christianen, C. Jagadish, A. Polimeni *Optical studies of a single crystal-phase homostructured InP nanowire*
Poster presentation at the Nanowire Week Meeting (Lund, May 2017).

9 **D. Tedeschi**, M. De Luca , P. E. Faria Junior, A. Granados del Aguila, Q. Gao, J. Fabian, M. Capizzi, H. H. Tan, P. C. M. Christianen, C. Jagadish, A. Polimeni *Spin and transport properties of electrons and holes in InP wurtzite nanowires assessed by magneto-optical measurements and k.p calculations*
Oral presentation at the Nanowire Week Meeting (Lund, May 2017).

10 **D. Tedeschi**, M. De Luca , P. E. Faria Junior, A. Granados del Aguila, Q. Gao, J. Fabian, M. Capizzi, H. H. Tan, P. C. M. Christianen, C. Jagadish, A. Polimeni *Spin and transport properties of electrons and holes in InP wurtzite*

nanowires assessed by magneto-optical measurements and k.p calculations
Oral presentation at the FisMat 2017 conference (Trieste, October 2017)

Bibliography

[1] X. Duan, Y. Huang, *et al.*, “Indium phosphide nanowires as building blocks for nanoscale electronic and optoelectronic devices,” *Nature*, vol. 409, no. 6816, pp. 66–69, Jan. 2001.

[2] R. Wagner and W. Ellis, “Vapor-liquid-solid mechanism of single crystal growth,” *Applied Physics Letters*, vol. 4, no. 5, pp. 89–90, 1964.

[3] M. Yazawa, M. Koguchi, *et al.*, “Heteroepitaxial ultrafine wire-like growth of InAs on GaAs substrates,” *Applied Physics Letters*, vol. 58, no. 10, pp. 1080–1082, June 1991.

[4] ——, “Effect of one monolayer of surface gold atoms on the epitaxial growth of InAs nanowhiskers,” *Applied Physics Letters*, vol. 61, no. 17, pp. 2051–2053, 1992.

[5] X. Duan and C. M. Lieber, “General synthesis of compound semiconductor nanowires,” *Advanced Materials*, vol. 12, no. 17, p. 298, 2000.

[6] V. G. Dubrovskii, N. V. Sibirev, *et al.*, “Growth kinetics and crystal structure of semiconductor nanowires,” *Physical Review B*, vol. 78, no. 23, p. 235301, Dec. 2008.

[7] Q. Gao, D. Saxena, *et al.*, “Selective-Area Epitaxy of Pure Wurtzite InP Nanowires: High Quantum Efficiency and Room-Temperature Lasing,” *Nano Letters*, vol. 14, no. 9, pp. 5206–5211, Aug. 2014.

[8] M. Law, J. Goldberger, *et al.*, “SEMICONDUCTOR NANOWIRES AND NANOTUBES,” *Annu. Rev. Mater. Res.*, vol. 34, no. 1, pp. 83–122, July 2004.

[9] T. Mårtensson, C. P. T. Svensson, *et al.*, “Epitaxial III- V nanowires on silicon,” *Nano Letters*, vol. 4, no. 10, pp. 1987–1990, 2004.

[10] M. Björk, B. Ohlsson, *et al.*, “One-dimensional steeplechase for electrons realized,” *Nano Letters*, vol. 2, no. 2, pp. 87–89, 2002.

[11] F. Qian, S. Gradečak, *et al.*, “Core/Multishell Nanowire Heterostructures as Multicolor, High-Efficiency Light-Emitting Diodes,” *Nano Letters*, vol. 5, no. 11, pp. 2287–2291, Nov. 2005.

[12] J. Wallentin, J. M. Persson, *et al.*, “High-Performance Single Nanowire Tunnel Diodes,” *Nano Letters*, vol. 10, no. 3, pp. 974–979, Mar. 2010.

[13] O. Hayden, R. Agarwal, *et al.*, “Semiconductor nanowire devices,” *Nano Today*, vol. 3, no. 5-6, pp. 12–22, Oct. 2008.

[14] K. Pemasiri, M. Montazeri, *et al.*, “Carrier Dynamics and Quantum Confinement in type II ZB-WZ InP Nanowire Homostructures,” *Nano Letters*, vol. 9, no. 2, pp. 648–654, Feb. 2009.

[15] S. A. Fortuna and X. Li, “Metal-catalyzed semiconductor nanowires: a review on the control of growth directions,” *Semiconductor Science and Technology*, vol. 25, no. 2, p. 024005, Feb. 2010.

[16] B. Tian, T. Cohen-Karni, *et al.*, “Three-Dimensional, Flexible Nanoscale Field-Effect Transistors as Localized Bioprobes,” *Science*, vol. 329, no. 5993, pp. 830–834, Aug. 2010.

[17] S. R. Plissard, I. van Weperen, *et al.*, “Formation and electronic properties of InSb nanocrosses,” *Nature Publishing Group*, vol. 8, pp. 859–864, Oct. 2013.

[18] K. A. Dick, “A review of nanowire growth promoted by alloys and non-alloying elements with emphasis on Au-assisted III–V nanowires,” *Progress in Crystal Growth and Characterization of Materials*, vol. 54, no. 3-4, pp. 138–173, Sept. 2008.

[19] R. Adelung, O. C. Aktas, *et al.*, “Strain-controlled growth of nanowires within thin-film cracks,” *Nature Materials*, vol. 3, no. 6, pp. 375–379, May 2004.

[20] N. Wang, Y. Cai, *et al.*, “Growth of nanowires,” *Materials Science and Engineering: R: Reports*, vol. 60, no. 1-6, pp. 1–51, Mar. 2008.

[21] Y. Wu and P. Yang, *Direct Observation of Vapor−Liquid−Solid Nanowire Growth*. American Chemical Society, Mar. 2001, vol. 123.

[22] S. Hashimoto, J. Takeda, *et al.*, “Formation of InP and InGaAs Air-Hole Arrays on InP(111) Substrates by Selective-Area Metal–Organic Vapor Phase Epitaxy,” *Japanese Journal of Applied Physics*, vol. 47, no. 5, pp. 3354–3358, May 2008.

[23] J. Johansson, B. A. Wacaser, *et al.*, “Growth related aspects of epitaxial nanowires,” *Nanotechnology*, vol. 17, no. 11, p. S355, 2006.

[24] P. Caroff, J. B. Wagner, *et al.*, “High-Quality InAs/InSb Nanowire Heterostructures Grown by Metal–Organic Vapor-Phase Epitaxy,” *Small*, vol. 4, no. 7, pp. 878–882, 2008.

[25] Dick, Kimberly A and Caroff, Philippe and Bolinsson, Jessica and Messing, Maria E and Johansson, Jonas and Deppert, Knut and Wallenberg, L Reine and Samuelson, Lars, “Control of III–V nanowire crystal structure by growth parameter tuning,” *Semiconductor Science and Technology*, vol. 25, no. 2, p. 024009, Feb. 2010.

[26] G. Patriarche, F. Glas, *et al.*, “Wurtzite to zinc blende phase transition in GaAs nanowires induced by epitaxial burying,” *Nano letters*, vol. 8, no. 6, pp. 1638–1643, 2008.

[27] S. Paiman, Q. Gao, *et al.*, “The effect of V/III ratio and catalyst particle size on the crystal structure and optical properties of InP nanowires,” *Nanotechnology*, vol. 20, no. 22, p. 225606, 2009.

[28] S. Assali, I. Zardo, *et al.*, “Direct band gap wurtzite gallium phosphide nanowires,” *Nano letters*, vol. 13, no. 4, pp. 1559–1563, 2013.

[29] H. I. T. Hauge, M. A. Verheijen, *et al.*, “Hexagonal silicon realized,” *Nano letters*, vol. 15, no. 9, pp. 5855–5860, 2015.

[30] F. Glas, J.-C. Harmand, *et al.*, “Why Does Wurtzite Form in Nanowires of III-V Zinc Blende Semiconductors?” *Physical review letters*, vol. 99, no. 14, pp. 146 101–4, Oct. 2007.

[31] R. Leitsmann and F. Bechstedt, “Surface influence on stability and structure of hexagon-shaped III-V semiconductor nanorods,” *Journal of Applied Physics*, vol. 102, no. 6, p. 063528, 2007.

[32] T. Akiyama, K. Sano, *et al.*, “An empirical potential approach to wurtzite–zinc-blende polytypism in group III–V semiconductor nanowires,” *Japanese journal of applied physics*, vol. 45, no. 3L, p. L275, 2006.

[33] V. Dubrovskii and N. Sibirev, “Growth thermodynamics of nanowires and its application to polytypism of zinc blende III-V nanowires,” *Physical Review B*, vol. 77, no. 3, p. 035414, 2008.

[34] J. Johansson, J. Bolinsson, *et al.*, “Combinatorial Approaches to Understanding Polytypism in III–V Nanowires,” *ACS Nano*, vol. 6, no. 7, pp. 6142–6149, July 2012.

[35] M. Stiles and D. Hamann, “Electron transmission through silicon stacking faults,” *Physical Review B*, vol. 41, no. 8, p. 5280, 1990.

[36] J. Bao, D. C. Bell, *et al.*, “Optical properties of rotationally twinned InP nanowire heterostructures,” *Nano letters*, vol. 8, no. 3, pp. 836–841, 2008.

[37] A. L. Moore, S. K. Saha, *et al.*, “Phonon backscattering and thermal conductivity suppression in sawtooth nanowires,” *Applied Physics Letters*, vol. 93, no. 8, p. 083112, 2008.

[38] P. Caroff, K. A. Dick, *et al.*, “Controlled polytypic and twin-plane superlattices in III–V nanowires,” *Nature nanotechnology*, vol. 4, no. 1, pp. 50–55, 2009.

[39] N. Akopian, G. Patriarche, *et al.*, “Crystal phase quantum dots,” *Nano letters*, vol. 10, no. 4, pp. 1198–1201, 2010.

[40] M. Murayama and T. Nakayama, “Chemical trend of band offsets at wurtzite/zinc-blende heterocrystalline semiconductor interfaces,” *Physical Review B*, vol. 49, no. 7, p. 4710, 1994.

[41] J. L. Birman, “Polarization of fluorescence in CdS and ZnS single crystals,” *Physical Review Letters*, vol. 2, no. 4, p. 157, 1959.

[42] A. De and C. E. Pryor, “Predicted band structures of III-V semiconductors in the wurtzite phase,” *Physical Review B*, vol. 81, no. 15, p. 155210, 2010.

[43] W. R. Lambrecht, A. V. Rodina, *et al.*, “Valence-band ordering and magneto-optic exciton fine structure in ZnO,” *Physical review B*, vol. 65, no. 7, p. 075207, 2002.

[44] F. Bechstedt and A. Belabbes, “Structure, energetics, and electronic states of III–V compound polytypes,” *Journal of Physics: Condensed Matter*, vol. 25, no. 27, p. 273201, 2013.

[45] P. E. F. Junior, T. Campos, *et al.*, “Realistic multiband k · p approach from ab initio and spin-orbit coupling effects of InAs and InP in wurtzite phase,” *Physical Review B*, vol. 93, no. 23, p. 235204, 2016.

[46] Z. Zanolli, F. Fuchs, *et al.*, “Model GW band structure of InAs and GaAs in the wurtzite phase,” *Physical Review B*, vol. 75, no. 24, p. 245121, 2007.

[47] J.-M. Jancu, K. Gauthron, *et al.*, “Type II heterostructures formed by zinc-blende inclusions in InP and GaAs wurtzite nanowires,” *Applied Physics Letters*, vol. 97, no. 4, p. 041910, 2010.

[48] Y. E. Kitaev, A. Panfilov, *et al.*, “Electron state symmetries and optical transitions in semiconductor superlattices: I. grown along the [001] direction,” *Journal of Physics: Condensed Matter*, vol. 9, no. 1, p. 257, 1997.

[49] J. L. Birman, “Some selection rules for band-band transitions in wurtzite structure,” *Physical Review*, vol. 114, no. 6, p. 1490, 1959.

[50] J. Wang, M. S. Gudiksen, *et al.*, “Highly polarized photoluminescence and photodetection from single indium phosphide nanowires,” *Science*, vol. 293, no. 5534, pp. 1455–1457, 2001.

[51] A. Maslov and C. Ning, "Radius-dependent polarization anisotropy in semiconductor nanowires," *Physical Review B*, vol. 72, no. 16, p. 161310, 2005.

[52] H. Ruda and A. Shik, "Polarization-sensitive optical phenomena in semiconducting and metallic nanowires," *Physical Review B*, vol. 72, no. 11, p. 115308, 2005.

[53] ——, "Polarization-sensitive optical phenomena in thick semiconducting nanowires," *Journal of applied physics*, vol. 100, no. 2, p. 024314, 2006.

[54] L. D. Landau, J. Bell, *et al.*, *Electrodynamics of continuous media.* elsevier, 2013, vol. 8.

[55] M. De Luca, A. Polimeni, *et al.*, "Determination of exciton reduced mass and gyromagnetic factor of wurtzite (inga) as nanowires by photoluminescence spectroscopy under high magnetic fields," *ACS nano*, vol. 7, no. 12, pp. 10 717–10 725, 2013.

[56] M. De Luca, G. Lavenuta, *et al.*, "Excitonic recombination and absorption in In x Ga 1- x As/GaAs heterostructure nanowires," *Physical Review B*, vol. 87, no. 23, p. 235304, 2013.

[57] M. De Luca, A. Zilli, *et al.*, "Polarized light absorption in wurtzite InP nanowire ensembles," *Nano letters*, vol. 15, no. 2, pp. 998–1005, 2015.

[58] M. De Luca, A. Polimeni, *et al.*, "Magneto-optical properties of wurtzite-phase InP nanowires," *Nano letters*, vol. 14, no. 8, pp. 4250–4256, 2014.

[59] K. Li, H. Sun, *et al.*, "Tailoring the optical characteristics of microsized InP nanoneedles directly grown on silicon," *Nano letters*, vol. 14, no. 1, pp. 183–190, 2013.

[60] A. Mishra, L. Titova, *et al.*, "Polarization and temperature dependence of photoluminescence from zincblende and wurtzite InP nanowires," *Applied Physics Letters*, vol. 91, no. 26, p. 263104, 2007.

[61] H.-Y. Chen, Y.-C. Yang, *et al.*, "Polarized photoluminescence from single GaN nanorods: effects of optical confinement," *Optics express*, vol. 16, no. 17, pp. 13 465–13 475, 2008.

[62] P. Yang, R. Yan, *et al.*, "Semiconductor nanowire: what's next?" *Nano letters*, vol. 10, no. 5, pp. 1529–1536, 2010.

[63] N. P. Dasgupta, J. Sun, *et al.*, "25th anniversary article: semiconductor nanowires–synthesis, characterization, and applications," *Advanced Materials*, vol. 26, no. 14, pp. 2137–2184, 2014.

[64] J. Goldberger, A. I. Hochbaum, *et al.*, "Silicon vertically integrated nanowire field effect transistors," *Nano letters*, vol. 6, no. 5, pp. 973–977, 2006.

[65] E. C. Garnett, Y.-C. Tseng, *et al.*, "Dopant profiling and surface analysis of silicon nanowires using capacitance–voltage measurements," *Nature nanotechnology*, vol. 4, no. 5, pp. 311–314, 2009.

[66] D. Khanal and J. Wu, "Gate coupling and charge distribution in nanowire field effect transistors," *Nano letters*, vol. 7, no. 9, pp. 2778–2783, 2007.

[67] Y. Cui, X. Duan, *et al.*, "Doping and electrical transport in silicon nanowires," *The Journal of Physical Chemistry B*, vol. 104, no. 22, pp. 5213–5216, 2000.

[68] O. Wunnicke, "Gate capacitance of back-gated nanowire field-effect transistors," *Applied Physics Letters*, vol. 89, no. 8, p. 083102, 2006.

[69] V. Schmidt, S. Senz, *et al.*, "Influence of the Si/SiO 2 interface on the charge carrier density of Si nanowires," *Applied Physics A: Materials Science & Processing*, vol. 86, no. 2, pp. 187–191, 2007.

[70] X. Sun, C. Li, *et al.*, "Reductive growth of nanosized ligated metal clusters on silicon nanowires," *Inorganic chemistry*, vol. 41, no. 17, pp. 4331–4336, 2002.

[71] B. Hoex, J. Gielis, *et al.*, "On the c-Si surface passivation mechanism by the negative-charge-dielectric Al 2 O 3," *Journal of Applied Physics*, vol. 104, no. 11, p. 113703, 2008.

[72] P. Nguyen, H. T. Ng, *et al.*, "Direct integration of metal oxide nanowire in vertical field-effect transistor," *Nano Letters*, vol. 4, no. 4, pp. 651–657, 2004.

[73] S. A. Dayeh, D. P. Aplin, *et al.*, "High electron mobility InAs nanowire field-effect transistors," *small*, vol. 3, no. 2, pp. 326–332, 2007.

[74] P.-C. Chang, Z. Fan, *et al.*, "High-performance ZnO nanowire field effect transistors," *Applied physics letters*, vol. 89, no. 13, p. 133113, 2006.

[75] H. Gao, A. Fu, *et al.*, "Cleaved-coupled nanowire lasers," *Proceedings of the National Academy of Sciences*, vol. 110, no. 3, pp. 865–869, 2013.

[76] J. Xu, X. Zhuang, *et al.*, "Asymmetric light propagation in composition-graded semiconductor nanowires," *Scientific reports*, vol. 2, 2012.

[77] M. H. Huang, S. Mao, *et al.*, "Room-temperature ultraviolet nanowire nanolasers," *science*, vol. 292, no. 5523, pp. 1897–1899, 2001.

[78] X. Duan, Y. Huang, *et al.*, "Single-nanowire electrically driven lasers," *Nature*, vol. 421, no. 6920, pp. 241–245, 2003.

[79] F. Qian, Y. Li, *et al.*, "Multi-quantum-well nanowire heterostructures for wavelength-controlled lasers," *Nature materials*, vol. 7, no. 9, pp. 701–706, 2008.

[80] Y. Xiao, C. Meng, *et al.*, "Single-nanowire single-mode laser," *Nano letters*, vol. 11, no. 3, pp. 1122–1126, 2011.

[81] R. F. Oulton, V. J. Sorger, *et al.*, "Plasmon lasers at deep subwavelength scale," *Nature*, vol. 461, no. 7264, pp. 629–632, 2009.

[82] L. E. Bell, "Cooling, heating, generating power, and recovering waste heat with thermoelectric systems," *Science*, vol. 321, no. 5895, pp. 1457–1461, 2008.

[83] G. J. Snyder and E. S. Toberer, "Complex thermoelectric materials," *Nature materials*, vol. 7, no. 2, pp. 105–114, 2008.

[84] A. I. Hochbaum, R. Chen, *et al.*, "Enhanced thermoelectric performance of rough silicon nanowires," *Nature*, vol. 451, no. 7175, pp. 163–167, 2008.

[85] Y.-M. Lin and M. Dresselhaus, "Thermoelectric properties of superlattice nanowires," *Physical review B*, vol. 68, no. 7, p. 075304, 2003.

[86] F. Zhou, A. L. Moore, *et al.*, "Effect of growth base pressure on the thermoelectric properties of indium antimonide nanowires," *Journal of Physics D: Applied Physics*, vol. 43, no. 2, p. 025406, 2009.

[87] A. Ali, Y. Chen, *et al.*, "Nanowire-based thermoelectrics," *Nanotechnology*, vol. 28, no. 28, p. 282001, 2017.

[88] D. Li, Y. Wu, *et al.*, "Thermal conductivity of individual silicon nanowires," *Applied Physics Letters*, vol. 83, no. 14, pp. 2934–2936, 2003.

[89] J. Lim, K. Hippalgaonkar, *et al.*, "Quantifying surface roughness effects on phonon transport in silicon nanowires," *Nano letters*, vol. 12, no. 5, pp. 2475–2482, 2012.

[90] C. O'Dwyer, R. Chen, *et al.*, "Scientific and Technical Challenges in Thermal Transport and Thermoelectric Materials and Devices," *ECS Journal of Solid State Science and Technology*, vol. 6, no. 3, pp. N3058–N3064, 2017.

[91] Z. Fan, H. Razavi, *et al.*, "Three-dimensional nanopillar-array photovoltaics on low-cost and flexible substrates," *Nature materials*, vol. 8, no. 8, p. 648, 2009.

[92] A. Standing, S. Assali, *et al.*, "High yield transfer of ordered nanowire arrays into transparent flexible polymer films," *Nanotechnology*, vol. 23, no. 49, p. 495305, 2012.

[93] J. Wallentin, N. Anttu, *et al.*, "InP nanowire array solar cells achieving 13.8% efficiency by exceeding the ray optics limit," *Science*, vol. 339, no. 6123, pp. 1057–1060, 2013.

[94] B. M. Kayes, H. A. Atwater, *et al.*, "Comparison of the device physics principles of planar and radial p-n junction nanorod solar cells," *Journal of applied physics*, vol. 97, no. 11, p. 114302, 2005.

[95] O. L. Muskens, J. G. Rivas, *et al.*, "Design of light scattering in nanowire materials for photovoltaic applications," *Nano letters*, vol. 8, no. 9, pp. 2638–2642, 2008.

[96] D. van Dam, N. J. van Hoof, *et al.*, "High-efficiency nanowire solar cells with omnidirectionally enhanced absorption due to self-aligned Indium-Tin-Oxide Mie scatterers," *ACS nano*, vol. 10, no. 12, pp. 11 414–11 419, 2016.

[97] E. Majorana and L. Maiani, "A symmetric theory of electrons and positrons," in *Ettore Majorana Scientific Papers.* Springer, 2006, pp. 201–233.

[98] Y. Aharonov and D. Bohm, "Significance of electromagnetic potentials in the quantum theory," *Physical Review*, vol. 115, no. 3, p. 485, 1959.

[99] R. M. Lutchyn, J. D. Sau, *et al.*, "Majorana fermions and a topological phase transition in semiconductor-superconductor heterostructures," *Physical review letters*, vol. 105, no. 7, p. 077001, 2010.

[100] Y. Oreg, G. Refael, *et al.*, "Helical liquids and Majorana bound states in quantum wires," *Physical review letters*, vol. 105, no. 17, p. 177002, 2010.

[101] K. T. Law, P. A. Lee, *et al.*, "Majorana fermion induced resonant Andreev reflection," *Physical review letters*, vol. 103, no. 23, p. 237001, 2009.

[102] V. Mourik, K. Zuo, *et al.*, "Signatures of Majorana fermions in hybrid superconductor-semiconductor nanowire devices," *Science*, vol. 336, no. 6084, pp. 1003–1007, 2012.

[103] S. Gazibegovic, D. Car, *et al.*, "Epitaxy of advanced nanowire quantum devices," *arXiv preprint arXiv:1705.01480*, 2017.

[104] M. Deng, S. Vaitiekėnas, *et al.*, "Majorana bound state in a coupled quantum-dot hybrid-nanowire system," *Science*, vol. 354, no. 6319, pp. 1557–1562, 2016.

[105] S. M. Albrecht, A. Higginbotham, *et al.*, "Exponential protection of zero modes in Majorana islands," *Nature*, vol. 531, no. 7593, pp. 206–209, 2016.

[106] M. Royo, C. Segarra, *et al.*, "Aharonov-Bohm oscillations and electron gas transitions in hexagonal core-shell nanowires with an axial magnetic field," *Physical Review B*, vol. 91, no. 11, p. 115440, 2015.

[107] M. Royo, M. De Luca, *et al.*, "A review on III–V core–multishell nanowires: growth, properties, and applications," *Journal of Physics D: Applied Physics*, vol. 50, no. 14, p. 143001, 2017.

[108] E. Ribeiro, A. Govorov, *et al.*, "Aharonov-Bohm signature for neutral polarized excitons in type-II quantum dot ensembles," *Physical review letters*, vol. 92, no. 12, p. 126402, 2004.

[109] I. Sellers, V. Whiteside, *et al.*, “Aharonov-Bohm excitons at elevated temperatures in type-II ZnTe/ZnSe quantum dots,” *Physical review letters*, vol. 100, no. 13, p. 136405, 2008.

[110] M. Bayer, M. Korkusinski, *et al.*, “Optical detection of the Aharonov-Bohm effect on a charged particle in a nanoscale quantum ring,” *Physical review letters*, vol. 90, no. 18, p. 186801, 2003.

[111] M. Jung, J. S. Lee, *et al.*, “Quantum interference in radial heterostructure nanowires,” *Nano letters*, vol. 8, no. 10, pp. 3189–3193, 2008.

[112] Ö. Gül, N. Demarina, *et al.*, “Flux periodic magnetoconductance oscillations in GaAs/InAs core/shell nanowires,” *Physical Review B*, vol. 89, no. 4, p. 045417, 2014.

[113] T. Berthing, S. Bonde, *et al.*, “Intact Mammalian Cell Function on Semiconductor Nanowire Arrays: New Perspectives for Cell-Based Biosensing,” *Small*, vol. 7, no. 5, pp. 640–647, 2011.

[114] J. T. Robinson, M. Jorgolli, *et al.*, “Vertical nanowire electrode arrays as a scalable platform for intracellular interfacing to neuronal circuits,” *Nature nanotechnology*, vol. 7, no. 3, pp. 180–184, 2012.

[115] C. Xie, Z. Lin, *et al.*, “Intracellular recording of action potentials by nanopillar electroporation,” *Nature nanotechnology*, vol. 7, no. 3, pp. 185–190, 2012.

[116] F. Patolsky, B. P. Timko, *et al.*, “Detection, stimulation, and inhibition of neuronal signals with high-density nanowire transistor arrays,” *Science*, vol. 313, no. 5790, pp. 1100–1104, 2006.

[117] T. Cohen-Karni, D. Casanova, *et al.*, “Synthetically encoded ultrashort-channel nanowire transistors for fast, pointlike cellular signal detection,” *Nano letters*, vol. 12, no. 5, pp. 2639–2644, 2012.

[118] R. Gao, S. Strehle, *et al.*, “Outside looking in: nanotube transistor intracellular sensors,” *Nano letters*, vol. 12, no. 6, pp. 3329–3333, 2012.

[119] W. Zhou, X. Dai, *et al.*, “Advances in nanowire bioelectronics,” *Reports on Progress in Physics*, vol. 80, no. 1, p. 016701, 2016.

[120] W. Kim, J. K. Ng, *et al.*, “Interfacing silicon nanowires with mammalian cells,” *Journal of the American Chemical Society*, vol. 129, no. 23, pp. 7228–7229, 2007.

[121] X. Duan, R. Gao, *et al.*, “Intracellular recordings of action potentials by an extracellular nanoscale field-effect transistor,” *Nature nanotechnology*, vol. 7, no. 3, pp. 174–179, 2012.

[122] S. Perera, K. Pemasiri, *et al.*, “Probing valence band structure in wurtzite InP nanowires using excitation spectroscopy,” *Applied Physics Letters*, vol. 97, no. 2, p. 023106, 2010.

[123] E. Gadret, G. Dias, *et al.*, “Valence-band splitting energies in wurtzite InP nanowires: Photoluminescence spectroscopy and ab initio calculations,” *Physical Review B*, vol. 82, no. 12, p. 125327, 2010.

[124] M. Montazeri, A. Wade, *et al.*, “Photomodulated rayleigh scattering of single semiconductor nanowires: probing electronic band structure,” *Nano letters*, vol. 11, no. 10, pp. 4329–4336, 2011.

[125] G. L. Tuin, M. T. Borgström, *et al.*, “Valence band splitting in wurtzite InP nanowires observed by photoluminescence and photoluminescence excitation spectroscopy,” *Nano Research*, vol. 4, no. 2, pp. 159–163, 2011.

[126] T. T. Vu, T. Zehender, *et al.*, “High optical quality single crystal phase wurtzite and zincblende InP nanowires,” *Nanotechnology*, vol. 24, no. 11, p. 115705, 2013.

[127] M. H. Alouane, N. Chauvin, *et al.*, “Excitonic properties of wurtzite InP nanowires grown on silicon substrate,” *Nanotechnology*, vol. 24, no. 3, p. 035704, 2012.

[128] A. Iqbal, J. P. Beech, *et al.*, “Photoluminescence study of as-grown vertically standing wurtzite InP nanowire ensembles,” *Nanotechnology*, vol. 24, no. 11, p. 115706, 2013.

[129] S. Perera, T. Shi, *et al.*, “Illuminating the second conduction band and spin–orbit energy in single wurtzite InP nanowires,” *Nano letters*, vol. 13, no. 11, pp. 5367–5372, 2013.

[130] F. Ren, K. Wei Ng, *et al.*, “High-quality InP nanoneedles grown on silicon,” *Applied Physics Letters*, vol. 102, no. 1, p. 012115, 2013.

[131] A. Zilli, M. De Luca, *et al.*, “Temperature dependence of interband transitions in wurtzite InP nanowires,” *ACS nano*, vol. 9, no. 4, pp. 4277–4287, 2015.

[132] L. C. Dacal and A. Cantarero, “Ab initio electronic band structure calculation of InP in the wurtzite phase,” *Solid State Communications*, vol. 151, no. 10, pp. 781–784, 2011.

[133] D. Tedeschi, M. De Luca, *et al.*, “Long-lived hot carriers in III–V nanowires,” *Nano letters*, vol. 16, no. 5, pp. 3085–3093, 2016.

[134] ——, “Value and anisotropy of the electron and hole mass in pure wurtzite InP nanowires,” *Nano letters*, vol. 16, no. 10, pp. 6213–6221, 2016.

[135] S. Paiman, Q. Gao, *et al.*, “Effects of growth rate on InP nanowires morphology and crystal structure,” *Journal of Crystal Growth*, vol. 383, pp. 100–105, 2013.

[136] ——, “Growth temperature and V/III ratio effects on the morphology and crystal structure of InP nanowires,” *Journal of Physics D: Applied Physics*, vol. 43, no. 44, p. 445402, 2010.

[137] H. A. Fonseka, P. Caroff, *et al.*, “Nanowires grown on InP (100): growth directions, facets, crystal structures, and relative yield control,” *ACS nano*, vol. 8, no. 7, pp. 6945–6954, 2014.

[138] J. Wang, S. R. Plissard, *et al.*, “Reversible switching of InP nanowire growth direction by catalyst engineering,” *Nano letters*, vol. 13, no. 8, pp. 3802–3806, 2013.

[139] http://www.ioffe.ru/SVA/NSM/Semicond/InP.

[140] M. Van Weert, O. Wunnicke, *et al.*, “Large redshift in photoluminescence of p-doped InP nanowires induced by Fermi-level pinning,” *Applied Physics Letters*, vol. 88, no. 4, p. 043109, 2006.

[141] E. Gadret, M. de Lima Jr, *et al.*, “Optical phonon modes of wurtzite InP,” *Applied Physics Letters*, vol. 102, no. 12, p. 122101, 2013.

[142] Y. Chen, B. Gil, *et al.*, “Dependence of the exciton polariton reflectivity spectrum of InP upon hydrostatic pressure,” *Physica B+ C*, vol. 139, pp. 491–494, 1986.

[143] B. Skromme, G. Stillman, *et al.*, “Photoluminescence identification of the C and Be acceptor levels in InP,” *Journal of electronic materials*, vol. 13, no. 3, pp. 463–491, 1984.

[144] E. Kubota, Y. Ohmori, *et al.*, “Electrical and optical properties of Mg-, Ca-, and Zn-doped InP crystals grown by the synthesis, solute diffusion technique,” *Journal of applied physics*, vol. 55, no. 10, pp. 3779–3784, 1984.

[145] R. Benzaquen, R. Leonelli, *et al.*, “Exciton-impurity interactions in high-purity InP,” *Physical Review B*, vol. 59, no. 3, p. 1973, 1999.

[146] E. S. Koteles, J. Lee, *et al.*, “Elastic scattering of exciton polaritons by neutral impurities,” *Physical review letters*, vol. 55, no. 8, p. 867, 1985.

[147] T. Steiner, M. Thewalt, *et al.*, “Effect of neutral donor scattering on the time-dependent exciton-polariton photoluminescence line shape in GaAs,” *Physical Review B*, vol. 34, no. 2, p. 1006, 1986.

[148] H. Alawadhi, S. Tsoi, *et al.*, “Effect of temperature on isotopic mass dependence of excitonic band gaps in semiconductors: ZnO,” *Physical Review B*, vol. 75, no. 20, p. 205207, 2007.

[149] M. Cardona, “Renormalization of the Optical Response of Semiconductors by Electron–Phonon Interaction,” *physica status solidi (a)*, vol. 188, no. 4, pp. 1209–1232, 2001.

[150] Y. P. Varshni, “Temperature dependence of the energy gap in semiconductors,” *physica*, vol. 34, no. 1, pp. 149–154, 1967.

[151] L. Vina, S. Logothetidis, *et al.*, “Temperature dependence of the dielectric function of germanium,” *Physical Review B*, vol. 30, no. 4, p. 1979, 1984.

[152] H. Murotani, Y. Yamada, *et al.*, “Effects of exciton localization on internal quantum efficiency of InGaN nanowires,” *Journal of Applied Physics*, vol. 114, no. 15, p. 153506, 2013.

[153] A. Polimeni, M. Capizzi, *et al.*, “Effect of nitrogen on the temperature dependence of the energy gap in In x Ga 1- x As 1- y N y/GaAs single quantum wells,” *Physical Review B*, vol. 63, no. 19, p. 195320, 2001.

[154] A. Polimeni, A. Patane, *et al.*, “Stokes shift in quantum wells: Trapping versus thermalization,” *Physical Review B*, vol. 54, no. 23, p. 16389, 1996.

[155] E. Grilli, M. Guzzi, *et al.*, “High-precision determination of the temperature dependence of the fundamental energy gap in gallium arsenide,” *Physical Review B*, vol. 45, no. 4, p. 1638, 1992.

[156] A. Baldereschi and M. Diaz, “Anisotropy of excitons in semiconductors,” *Il Nuovo Cimento B (1965-1970)*, vol. 68, no. 2, pp. 217–229, 1970.

[157] A. De and C. E. Pryor, “Optical dielectric functions of wurtzite III-V semiconductors,” *Physical Review B*, vol. 85, no. 12, p. 125201, 2012.

[158] A. Imada, S. Ozaki, *et al.*, “Photoreflectance spectroscopy of wurtzite CdS,” *Journal of applied physics*, vol. 92, no. 4, pp. 1793–1798, 2002.

[159] S. Logothetidis, M. Cardona, *et al.*, “Temperature dependence of the dielectric function and the interband critical points of CdSe,” *Physical Review B*, vol. 34, no. 4, p. 2458, 1986.

[160] W. Shan, T. Schmidt, *et al.*, “Temperature dependence of interband transitions in GaN grown by metalorganic chemical vapor deposition,” *Applied physics letters*, vol. 66, no. 8, pp. 985–987, 1995.

[161] L. Pavesi, F. Piazza, *et al.*, “Temperature dependence of the InP band gap from a photoluminescence study,” *Physical Review B*, vol. 44, no. 16, p. 9052, 1991.

[162] Z. Hang, H. Shen, *et al.*, “Temperature dependence of the E_0 and $E_0 + \Delta_0$ gaps of InP up to $600°C$,” *Solid state communications*, vol. 73, no. 1, pp. 15–18, 1990.

[163] S. Mukhopadhyay and D. A. Stewart, "First-principles study of the phonon dispersion and dielectric properties of wurtzite InP: Role of In 4 d electrons," *Physical Review B*, vol. 89, no. 5, p. 054302, 2014.

[164] F. Zhou, A. L. Moore, *et al.*, "Thermal conductivity of indium arsenide nanowires with wurtzite and zinc blende phases," *Physical Review B*, vol. 83, no. 20, p. 205416, 2011.

[165] R. T. Ross and A. J. Nozik, "Efficiency of hot-carrier solar energy converters," *Journal of Applied Physics*, vol. 53, no. 5, pp. 3813–3818, 1982.

[166] M. Khodr, "Effects of Temperature on Tunability of PbSe/PbSrSe Quantum Well Lasers in the Infrared Region," *Research Journal of Applied Sciences, Engineering and Technology*, vol. 10, no. 12, pp. 1384–1388, 2015.

[167] Y. Yang, X. Peng, *et al.*, "Hot Carrier Trapping Induced Negative Photoconductance in InAs Nanowires toward Novel Nonvolatile Memory," *Nano letters*, vol. 15, no. 9, pp. 5875–5882, 2015.

[168] C. K. Yong, J. Wong-Leung, *et al.*, "Direct Observation of Charge-Carrier Heating at WZ–ZB InP Nanowire Heterojunctions," *Nano letters*, vol. 13, no. 9, pp. 4280–4287, 2013.

[169] Y. Wang, H. E. Jackson, *et al.*, "Carrier thermalization dynamics in single Zincblende and Wurtzite InP nanowires," *Nano letters*, vol. 14, no. 12, pp. 7153–7160, 2014.

[170] F. Léonard, A. A. Talin, *et al.*, "Diameter-dependent electronic transport properties of Au-catalyst/Ge-nanowire Schottky diodes," *Physical review letters*, vol. 102, no. 10, p. 106805, 2009.

[171] J. Shah, *Ultrafast spectroscopy of semiconductors and semiconductor nanostructures.* Springer Science & Business Media, 2013, vol. 115.

[172] C. T. Bui, R. Xie, *et al.*, "Diameter-Dependent Thermal Transport in Individual ZnO Nanowires and its Correlation with Surface Coating and Defects," *Small*, vol. 8, no. 5, pp. 738–745, 2012.

[173] M. v. Swinkels, M. van Delft, *et al.*, "Diameter dependence of the thermal conductivity of InAs nanowires," *Nanotechnology*, vol. 26, no. 38, p. 385401, 2015.

[174] X. Lü, J. Chu, *et al.*, "Modification of the lattice thermal conductivity in semiconductor rectangular nanowires," *Journal of applied physics*, vol. 93, no. 2, pp. 1219–1229, 2003.

[175] A. I. Hochbaum and P. Yang, "Semiconductor nanowires for energy conversion," *Chemical reviews*, vol. 110, no. 1, pp. 527–546, 2009.

[176] P. Martin, Z. Aksamija, *et al.*, "Impact of phonon-surface roughness scattering on thermal conductivity of thin Si nanowires," *Physical review letters*, vol. 102, no. 12, p. 125503, 2009.

[177] D. J. Groenendijk, M. Buscema, *et al.*, "Photovoltaic and photothermoelectric effect in a double-gated WSe2 device," *Nano letters*, vol. 14, no. 10, pp. 5846–5852, 2014.

[178] T. J. Echtermeyer, P. Nene, *et al.*, "Photothermoelectric and photoelectric contributions to light detection in metal–graphene–metal photodetectors," *Nano letters*, vol. 14, no. 7, pp. 3733–3742, 2014.

[179] Y. Zhang, H. Li, *et al.*, "Photothermoelectric and photovoltaic effects both present in MoS2," *Scientific reports*, vol. 5, 2015.

[180] S. Limpert, A. M. Burke, *et al.*, "Bipolar Photothermoelectric Effect Across Energy Filters in Single Nanowires," *Nano Letters*, 2017.

[181] F. Leonard, E. Song, *et al.*, "Simultaneous thermoelectric and optoelectronic characterization of individual nanowires," *Nano letters*, vol. 15, no. 12, pp. 8129–8135, 2015.

[182] H. Venghaus, S. Suga, *et al.*, "Magnetoluminescence and Magnetoreflectance of the A Exciton of CdS and CdSe," *Physical Review B*, vol. 16, no. 10, p. 4419, 1977.

[183] J. Hopfdeld, "Fine structure in the optical absorption edge of anisotropic crystals," *Journal of Physics and Chemistry of Solids*, vol. 15, no. 1, pp. 97–107, 1960.

[184] A. Rodina, M. Dietrich, *et al.*, "Free excitons in wurtzite GaN," *Physical Review B*, vol. 64, no. 11, p. 115204, 2001.

[185] I. Broser and M. Rosenzweig, "Determination of excitonic parameters of the A polariton of CdS from magnetoreflectance spectroscopy," *Physical Review B*, vol. 22, no. 4, p. 2000, 1980.

[186] M. Furis, J. A. Hollingsworth, *et al.*, "Time-and polarization-resolved optical spectroscopy of colloidal CdSe nanocrystal quantum dots in high magnetic fields," *The Journal of Physical Chemistry B*, vol. 109, no. 32, pp. 15 332–15 338, 2005.

[187] R. G. Ulbrich and C. Weisbuch, "Resonant Brillouin scattering of excitonic polaritons in gallium arsenide," *Physical Review Letters*, vol. 38, no. 15, p. 865, 1977.

[188] J. Röseler and K. Henneberger, "Magnetopolaritons in Wurtzite-Type Crystals," *physica status solidi (b)*, vol. 93, no. 1, pp. 213–222, 1979.

[189] K. Hümmer, "Interband magnetoreflection of ZnO," *physica status solidi (b)*, vol. 56, no. 1, pp. 249–260, 1973.

[190] G. Pettinari, A. Polimeni, *et al.*, "Carrier mass measurements in degenerate indium nitride," *Physical Review B*, vol. 79, no. 16, p. 165207, 2009.

[191] D. Bimberg, "Anomaly of the linear and quadratic Zeeman effect of an effective-mass acceptor: C in GaAs," *Physical Review B*, vol. 18, no. 4, p. 1794, 1978.

[192] B. Skromme, R. Bhat, *et al.*, "Vertical transport in semiconductor superlattices probed by miniband-to-acceptor magnetoluminescence," *Physical review letters*, vol. 65, no. 16, p. 2050, 1990.

[193] R. Wheeler and J. Dimmock, "Exciton structure and Zeeman effects in cadmium selenide," *Physical Review*, vol. 125, no. 6, p. 1805, 1962.

[194] G. Stillman, C. Wolfe, *et al.*, "Magnetospectroscopy of shallow donors in GaAs," *Solid State Communications*, vol. 7, no. 13, pp. 921–925, 1969.

[195] D. Cabib, E. Fabri, *et al.*, "Ground and first excited states of excitons in a magnetic field," *Il Nuovo Cimento B (1971-1996)*, vol. 10, no. 1, pp. 185–199, 1972.

[196] F. Willmann, W. Dreybrodt, *et al.*, "GaAs Luminescence Transitions to Acceptors in Magnetic Fields," *physica status solidi (b)*, vol. 60, no. 2, pp. 751–759, 1973.

[197] P. Plochocka, A. Mitioglu, *et al.*, "High magnetic field reveals the nature of excitons in a single GaAs/AlAs core/shell nanowire," *Nano letters*, vol. 13, no. 6, pp. 2442–2447, 2013.

[198] J. Jadczak, P. Plochocka, *et al.*, "Unintentional high-density p-type modulation doping of a GaAs/AlAs core–multishell nanowire," *Nano letters*, vol. 14, no. 5, pp. 2807–2814, 2014.

[199] D. Sam-Giao, R. Mata, *et al.*, "Fine optical spectroscopy of the 3.45 eV emission line in GaN nanowires," *Journal of Applied Physics*, vol. 113, no. 4, p. 043102, 2013.

[200] P. Wojnar, E. Janik, *et al.*, "Giant spin splitting in optically active ZnMnTe/ZnMgTe core/shell nanowires," *Nano letters*, vol. 12, no. 7, pp. 3404–3409, 2012.

[201] E. Oh, J. H. Choi, *et al.*, "Magnetophotoluminescence and energy-dependent circular polarization from CdMnS nanowires," *Applied Physics Letters*, vol. 93, no. 4, p. 041911, 2008.

[202] M. Szymura, P. Wojnar, *et al.*, "Spin Splitting Anisotropy in Single Diluted Magnetic Nanowire Heterostructures," *Nano letters*, vol. 15, no. 3, pp. 1972–1978, 2015.

[203] P. Corfdir, B. Van Hattem, *et al.*, "Three-dimensional magneto-photoluminescence as a probe of the electronic properties of crystal-phase quantum disks in GaAs nanowires," *Nano letters*, vol. 13, no. 11, pp. 5303–5310, 2013.

[204] L. Zhang, J.-W. Luo, *et al.*, "Wide InP nanowires with wurtzite/zincblende superlattice segments are type-II whereas narrower nanowires become type-I: an atomistic pseudopotential calculation," *Nano letters*, vol. 10, no. 10, pp. 4055–4060, 2010.

[205] Y. Zhang, J. Wu, *et al.*, "III–V nanowires and nanowire optoelectronic devices," *Journal of Physics D: Applied Physics*, vol. 48, no. 46, p. 463001, 2015.

[206] M. Bouwes Bavinck, K. D. Jons, *et al.*, "Photon Cascade from a Single Crystal Phase Nanowire Quantum Dot," *Nano letters*, vol. 16, no. 2, pp. 1081–1085, 2016.

[207] J. Rossi, C. Wolfe, *et al.*, "Acceptor Luminescence in High-Purity n-Type GaAs," *Physical Review Letters*, vol. 25, no. 23, p. 1614, 1970.

[208] L. Meiners, "Temperature dependence of the dielectric constant of InP," *Journal of applied physics*, vol. 59, no. 5, pp. 1611–1613, 1986.

[209] D. Volm, B. Meyer, *et al.*, "Determination of the electron effective-mass tensor in 4H SiC," *Physical Review B*, vol. 53, no. 23, p. 15409, 1996.

[210] W. Dreybrodt, F. Willmann, *et al.*, "Energy of free and bound excitons in GaAs in a magnetic field," *Solid State Communications*, vol. 12, no. 11, pp. 1217–1220, 1973.

[211] G. Pettinari, A. Polimeni, *et al.*, "Compositional dependence of the exciton reduced mass in GaAs 1- x Bi x (x= 0–10%)," *Physical Review B*, vol. 81, no. 23, p. 235211, 2010.

[212] I. Vurgaftman, J. Meyer, *et al.*, "Band parameters for III–V compound semiconductors and their alloys," *Journal of applied physics*, vol. 89, no. 11, pp. 5815–5875, 2001.

[213] B. Santic, "On the hole effective mass and the free hole statistics in wurtzite GaN," *Semiconductor science and technology*, vol. 18, no. 4, p. 219, 2003.

[214] M. Feneberg, K. Lange, *et al.*, "Anisotropy of effective electron masses in highly doped nonpolar GaN," *Applied Physics Letters*, vol. 103, no. 23, p. 232104, 2013.

[215] T. Hofmann, T. Chavdarov, *et al.*, "Anisotropy of the Γ-point effective mass and mobility in hexagonal InN," *physica status solidi (c)*, vol. 3, no. 6, pp. 1854–1857, 2006.

[216] E. Venger, A. Melnichuk, *et al.*, "Anisotropy of the ZnO single crystal reflectivity in the region of residual rays," *physica status solidi (b)*, vol. 188, no. 2, pp. 823–831, 1995.

[217] K. J. Button, D. R. Cohn, *et al.*, "Zeeman splitting of anomalous shallow bound states in ZnO," *Physical Review Letters*, vol. 28, no. 25, p. 1637, 1972.

[218] P. Faria Junior, T. Campos, *et al.*, "Interband polarized absorption in InP polytypic superlattices," *Journal of Applied Physics*, vol. 116, no. 19, p. 193501, 2014.

[219] D. Thomas and J. Hopfield, "Bound exciton complexes," *Physical Review Letters*, vol. 7, no. 8, p. 316, 1961.

[220] V. I. Klimov, *Semiconductor and metal nanocrystals: synthesis and electronic and optical properties.* CRC Press, 2003.

[221] N. Traynor, R. Warburton, *et al.*, "Highly nonlinear Zeeman splitting of excitons in semiconductor quantum wells," *Physical Review B*, vol. 55, no. 23, p. 15701, 1997.

[222] L. K. Castelano, D. F. Cesar, *et al.*, "Zeeman splitting and spin dynamics tuning by exciton charging in two-dimensional systems," *Physical Review B*, vol. 84, no. 20, p. 205332, 2011.

[223] J. Jadczak, M. Kubisa, *et al.*, "High magnetic field spin splitting of excitons in asymmetric GaAs quantum wells," *Physical Review B*, vol. 86, no. 24, p. 245401, 2012.

[224] W. Bardyszewski and S. Łepkowski, "Nonlinear Zeeman splitting of magnetoexcitons in c-plane wurtzite GaN-based quantum wells," *Physical Review B*, vol. 90, no. 7, p. 075302, 2014.

[225] E. E. Salpeter and H. A. Bethe, "A relativistic equation for bound-state problems," *Physical Review*, vol. 84, no. 6, p. 1232, 1951.

[226] Z. Barticevic, M. Dobrowolska, *et al.*, "Theoretical and experimental investigation of the effective g factor of donor-bound electrons in InSb," *Physical Review B*, vol. 35, no. 14, p. 7464, 1987.

[227] K. S. Novoselov, A. K. Geim, *et al.*, "Electric field effect in atomically thin carbon films," *science*, vol. 306, no. 5696, pp. 666–669, 2004.

[228] A. K. Geim, "Graphene: status and prospects," *science*, vol. 324, no. 5934, pp. 1530–1534, 2009.

[229] F. Bonaccorso, L. Colombo, *et al.*, "Graphene, related two-dimensional crystals, and hybrid systems for energy conversion and storage," *Science*, vol. 347, no. 6217, p. 1246501, 2015.

[230] X. Li, X. Wang, *et al.*, "Chemically derived, ultrasmooth graphene nanoribbon semiconductors," *science*, vol. 319, no. 5867, pp. 1229–1232, 2008.

[231] A. Kuc, N. Zibouche, *et al.*, "Influence of quantum confinement on the electronic structure of the transition metal sulfide T S 2," *Physical Review B*, vol. 83, no. 24, p. 245213, 2011.

[232] L. Zhang and A. Zunger, "Evolution of electronic structure as a function of layer thickness in group-VIB transition metal dichalcogenides: emergence of localization prototypes," *Nano letters*, vol. 15, no. 2, pp. 949–957, 2015.

[233] M. Chhowalla, H. S. Shin, *et al.*, "The chemistry of two-dimensional layered transition metal dichalcogenide nanosheets," *Nature chemistry*, vol. 5, no. 4, pp. 263–275, 2013.

[234] I. Song, C. Park, *et al.*, "Synthesis and properties of molybdenum disulphide: from bulk to atomic layers," *RSC Advances*, vol. 5, no. 10, pp. 7495–7514, 2015.

[235] Q. H. Wang, K. Kalantar-Zadeh, *et al.*, "Electronics and optoelectronics of two-dimensional transition metal dichalcogenides," *Nature nanotechnology*, vol. 7, no. 11, pp. 699–712, 2012.

[236] G. Eda, T. Fujita, *et al.*, "Coherent atomic and electronic heterostructures of single-layer MoS2," *Acs Nano*, vol. 6, no. 8, pp. 7311–7317, 2012.

[237] J.-U. Lee, K. Kim, *et al.*, "Raman signatures of polytypism in molybdenum disulfide," *ACS nano*, vol. 10, no. 2, pp. 1948–1953, 2016.

[238] A. N. Enyashin, L. Yadgarov, *et al.*, "New route for stabilization of 1T-WS2 and MoS2 phases," *The Journal of Physical Chemistry C*, vol. 115, no. 50, pp. 24 586–24 591, 2011.

[239] J. Wilson and A. Yoffe, "The transition metal dichalcogenides discussion and interpretation of the observed optical, electrical and structural properties," *Advances in Physics*, vol. 18, no. 73, pp. 193–335, 1969.

[240] A. Goldmann, W. Gudat, *et al.*, *Electronic structure of solids: Photoemission spectra and related data.* Springer, 1994.

[241] A. Splendiani, L. Sun, *et al.*, "Emerging photoluminescence in monolayer MoS2," *Nano letters*, vol. 10, no. 4, pp. 1271–1275, 2010.

[242] K. F. Mak, C. Lee, *et al.*, "Atomically thin MoS 2: a new direct-gap semiconductor," *Physical review letters*, vol. 105, no. 13, p. 136805, 2010.

[243] A. Kumar and P. Ahluwalia, "Electronic structure of transition metal dichalcogenides monolayers 1H-MX2 (M= Mo, W; X= S, Se, Te) from ab-initio theory: new direct band gap semiconductors," *The European Physical Journal B*, vol. 85, no. 6, p. 186, 2012.

[244] T. Li and G. Galli, "Electronic properties of MoS2 nanoparticles," *The Journal of Physical Chemistry C*, vol. 111, no. 44, pp. 16 192–16 196, 2007.

[245] J. Kang, S. Tongay, *et al.*, "Band offsets and heterostructures of two-dimensional semiconductors," *Applied Physics Letters*, vol. 102, no. 1, p. 012111, 2013.

[246] D. Xiao, G.-B. Liu, *et al.*, "Coupled spin and valley physics in monolayers of MoS 2 and other group-VI dichalcogenides," *Physical Review Letters*, vol. 108, no. 19, p. 196802, 2012.

[247] Z. Zhu, Y. Cheng, *et al.*, "Giant spin-orbit-induced spin splitting in two-dimensional transition-metal dichalcogenide semiconductors," *Physical Review B*, vol. 84, no. 15, p. 153402, 2011.

[248] K. F. Mak, K. He, *et al.*, "Control of valley polarization in monolayer MoS2 by optical helicity," *Nature nanotechnology*, vol. 7, no. 8, pp. 494–498, 2012.

[249] H. Zeng, J. Dai, *et al.*, "Valley polarization in MoS2 monolayers by optical pumping," *Nature nanotechnology*, vol. 7, no. 8, pp. 490–493, 2012.

[250] A. Chernikov, T. C. Berkelbach, *et al.*, "Exciton binding energy and nonhydrogenic Rydberg series in monolayer WS 2," *Physical review letters*, vol. 113, no. 7, p. 076802, 2014.

[251] D. Y. Qiu, H. Felipe, *et al.*, "Optical spectrum of MoS 2: many-body effects and diversity of exciton states," *Physical review letters*, vol. 111, no. 21, p. 216805, 2013.

[252] K. F. Mak and J. Shan, "Photonics and optoelectronics of 2D semiconductor transition metal dichalcogenides," *Nature Photonics*, vol. 10, no. 4, pp. 216–226, 2016.

[253] T. C. Berkelbach, M. S. Hybertsen, *et al.*, "Theory of neutral and charged excitons in monolayer transition metal dichalcogenides," *Physical Review B*, vol. 88, no. 4, p. 045318, 2013.

[254] D. K. Zhang, D. W. Kidd, *et al.*, "Excited biexcitons in transition metal dichalcogenides," *Nano letters*, vol. 15, no. 10, pp. 7002–7005, 2015.

[255] X. Zhang, X.-F. Qiao, *et al.*, "Phonon and Raman scattering of two-dimensional transition metal dichalcogenides from monolayer, multilayer to bulk material," *Chemical Society Reviews*, vol. 44, no. 9, pp. 2757–2785, 2015.

[256] W. Zhao, Z. Ghorannevis, *et al.*, “Lattice dynamics in mono-and few-layer sheets of WS 2 and WSe 2,” *Nanoscale*, vol. 5, no. 20, pp. 9677–9683, 2013.

[257] C. Lee, H. Yan, *et al.*, “Anomalous lattice vibrations of single-and few-layer MoS2,” *ACS nano*, vol. 4, no. 5, pp. 2695–2700, 2010.

[258] X. Zhang, W. Han, *et al.*, “Raman spectroscopy of shear and layer breathing modes in multilayer MoS 2,” *Physical Review B*, vol. 87, no. 11, p. 115413, 2013.

[259] A. Molina-Sanchez and L. Wirtz, “Phonons in single-layer and few-layer MoS 2 and WS 2,” *Physical Review B*, vol. 84, no. 15, p. 155413, 2011.

[260] P. Tonndorf, R. Schmidt, *et al.*, “Photoluminescence emission and Raman response of monolayer MoS 2, MoSe 2, and WSe 2,” *Optics express*, vol. 21, no. 4, pp. 4908–4916, 2013.

[261] H. Terrones, E. Del Corro, *et al.*, “New first order Raman-active modes in few layered transition metal dichalcogenides,” *Scientific reports*, vol. 4, 2014.

[262] M. Benameur, B. Radisavljevic, *et al.*, “Visibility of dichalcogenide nanolayers,” *Nanotechnology*, vol. 22, no. 12, p. 125706, 2011.

[263] A. Huang, E. Ray, *et al.*, “Observation of interlayer excitons in monolayer mose2-wse2 heterostructure on bn substrate,” in *APS March Meeting Abstracts*, 2016.

[264] K.-C. Chiu, X.-Q. Zhang, *et al.*, “Synthesis and Application of Monolayer Semiconductors (June 2015),” *IEEE Journal of Quantum Electronics*, vol. 51, no. 10, pp. 1–10, 2015.

[265] S. Dhar, A. R. Barman, *et al.*, “A new route to graphene layers by selective laser ablation,” *Aip Advances*, vol. 1, no. 2, p. 022109, 2011.

[266] A. Castellanos-Gomez, M. Barkelid, *et al.*, “Laser-thinning of MoS2: on demand generation of a single-layer semiconductor,” *Nano letters*, vol. 12, no. 6, pp. 3187–3192, 2012.

[267] G. Eda, H. Yamaguchi, *et al.*, “Photoluminescence from chemically exfoliated MoS2,” *Nano letters*, vol. 11, no. 12, pp. 5111–5116, 2011.

[268] Z. Zeng, Z. Yin, *et al.*, “Single-Layer Semiconducting Nanosheets: High-yield preparation and device fabrication,” *Angewandte Chemie International Edition*, vol. 50, no. 47, pp. 11 093–11 097, 2011.

[269] Y.-H. Lee, X.-Q. Zhang, *et al.*, “Synthesis of large-area MoS2 atomic layers with chemical vapor deposition,” *Advanced Materials*, vol. 24, no. 17, pp. 2320–2325, 2012.

[270] Y. Zhan, Z. Liu, *et al.*, “Large-area vapor-phase growth and characterization of MoS2 atomic layers on a SiO2 substrate,” *Small*, vol. 8, no. 7, pp. 966–971, 2012.

[271] K.-K. Liu, W. Zhang, *et al.*, “Growth of large-area and highly crystalline MoS2 thin layers on insulating substrates,” *Nano Lett*, vol. 12, no. 3, pp. 1538–1544, 2012.

[272] Y. Gong, G. Ye, *et al.*, “Synthesis of Millimeter-Scale Transition Metal Dichalcogenides Single Crystals,” *Advanced Functional Materials*, vol. 26, no. 12, pp. 2009–2015, 2016.

[273] M. Amani, R. A. Burke, *et al.*, “High luminescence efficiency in MoS2 grown by chemical vapor deposition,” *ACS nano*, vol. 10, no. 7, pp. 6535–6541, 2016.

[274] C. Tan and H. Zhang, “Two-dimensional transition metal dichalcogenide nanosheet-based composites,” *Chemical Society Reviews*, vol. 44, no. 9, pp. 2713–2731, 2015.

[275] http://www.itrs.net/Links/2011ITRS/Home2011.html.

[276] B. Radisavljevic, A. Radenovic, *et al.*, "Single-layer MoS2 transistors," *Nature nanotechnology*, vol. 6, no. 3, pp. 147–150, 2011.

[277] S. Wu, S. Buckley, *et al.*, "Monolayer semiconductor nanocavity lasers with ultralow thresholds," *nature*, vol. 520, no. 7545, p. 69, 2015.

[278] Y.-M. He, G. Clark, *et al.*, "Single quantum emitters in monolayer semiconductors," *Nature nanotechnology*, vol. 10, no. 6, pp. 497–502, 2015.

[279] Z. Yin, H. Li, *et al.*, "Single-layer MoS2 phototransistors," *ACS nano*, vol. 6, no. 1, pp. 74–80, 2011.

[280] Z. Yin, B. Chen, *et al.*, "Au Nanoparticle-Modified MoS2 Nanosheet-Based Photoelectrochemical Cells for Water Splitting," *Small*, vol. 10, no. 17, pp. 3537–3543, 2014.

[281] F. Withers, O. Del Pozo-Zamudio, *et al.*, "Light-emitting diodes by band-structure engineering in van der Waals heterostructures," *Nature materials*, vol. 14, no. 3, pp. 301–306, 2015.

[282] Y. Zhang, T. Oka, *et al.*, "Electrically switchable chiral light-emitting transistor," *Science*, vol. 344, no. 6185, pp. 725–728, 2014.

[283] J. Xie, J. Zhang, *et al.*, "Controllable disorder engineering in oxygen-incorporated MoS2 ultrathin nanosheets for efficient hydrogen evolution," *Journal of the American Chemical Society*, vol. 135, no. 47, pp. 17 881–17 888, 2013.

[284] C. Xu, S. Peng, *et al.*, "Ultrathin S-doped MoSe 2 nanosheets for efficient hydrogen evolution," *Journal of Materials Chemistry A*, vol. 2, no. 16, pp. 5597–5601, 2014.

[285] D. Voiry, M. Salehi, *et al.*, "Conducting MoS2 nanosheets as catalysts for hydrogen evolution reaction," *Nano Lett*, vol. 13, no. 12, pp. 6222–6227, 2013.

[286] D. Kiriya, P. Lobaccaro, *et al.*, "General thermal texturization process of MoS2 for efficient electrocatalytic hydrogen evolution reaction," *Nano letters*, vol. 16, no. 7, pp. 4047–4053, 2016.

[287] H. Li, C. Tsai, *et al.*, "Activating and optimizing MoS2 basal planes for hydrogen evolution through the formation of strained sulphur vacancies," *Nature materials*, vol. 15, no. 1, p. 48, 2016.

[288] H. Li, Z. Yin, *et al.*, "Fabrication of single-and multilayer MoS2 film-based field-effect transistors for sensing NO at room temperature," *small*, vol. 8, no. 1, pp. 63–67, 2012.

[289] Q. He, Z. Zeng, *et al.*, "Fabrication of Flexible MoS2 Thin-Film Transistor Arrays for Practical Gas-Sensing Applications," *Small*, vol. 8, no. 19, pp. 2994–2999, 2012.

[290] K. Chang and W. Chen, "L-cysteine-assisted synthesis of layered MoS2/graphene composites with excellent electrochemical performances for lithium ion batteries," *ACS nano*, vol. 5, no. 6, pp. 4720–4728, 2011.

[291] C. Zhu, X. Mu, *et al.*, "Single-layered ultrasmall nanoplates of MoS2 embedded in carbon nanofibers with excellent electrochemical performance for lithium and sodium storage," *Angewandte Chemie International Edition*, vol. 53, no. 8, pp. 2152–2156, 2014.

[292] K. F. Mak, K. He, *et al.*, "Tightly bound trions in monolayer MoS2," *Nature materials*, vol. 12, no. 3, pp. 207–211, 2013.

[293] J. S. Ross, S. Wu, *et al.*, "Electrical control of neutral and charged excitons in a monolayer semiconductor," *Nature Communications*, vol. 4, p. 1474, 2013.

[294] S. Tongay, J. Zhou, *et al.*, “Thermally driven crossover from indirect toward direct bandgap in 2D semiconductors: MoSe2 versus MoS2,” *Nano letters*, vol. 12, no. 11, pp. 5576–5580, 2012.

[295] J. Shang, X. Shen, *et al.*, “Observation of excitonic fine structure in a 2D transition-metal dichalcogenide semiconductor,” *ACS nano*, vol. 9, no. 1, pp. 647–655, 2015.

[296] A. Hanbicki, M. Currie, *et al.*, “Measurement of high exciton binding energy in the monolayer transition-metal dichalcogenides WS 2 and WSe 2,” *Solid State Communications*, vol. 203, pp. 16–20, 2015.

[297] W. Zhao, Z. Ghorannevis, *et al.*, “Evolution of electronic structure in atomically thin sheets of WS2 and WSe2,” *ACS nano*, vol. 7, no. 1, pp. 791–797, 2012.

[298] A. M. Jones, H. Yu, *et al.*, “Optical generation of excitonic valley coherence in monolayer WSe2,” *Nature nanotechnology*, vol. 8, no. 9, pp. 634–638, 2013.

[299] H. R. Gutiérrez, N. Perea-López, *et al.*, “Extraordinary room-temperature photoluminescence in triangular WS2 monolayers,” *Nano letters*, vol. 13, no. 8, pp. 3447–3454, 2012.

[300] M. Dendzik, A. Bruix, *et al.*, “Contact-Induced Semiconductor-to-Metal Transition in Single-Layer WS _2,” *arXiv preprint arXiv:1708.02799*, 2017.

[301] A. Berkdemir, H. R. Gutiérrez, *et al.*, “Identification of individual and few layers of WS2 using Raman Spectroscopy,” *Scientific reports*, vol. 3, 2013.

[302] M. Amani, D.-H. Lien, *et al.*, “Near-unity photoluminescence quantum yield in MoS2,” *Science*, vol. 350, no. 6264, pp. 1065–1068, 2015.

[303] H. Wang, C. Zhang, *et al.*, “Ultrafast dynamics of defect-assisted electron–hole recombination in monolayer MoS2,” *Nano letters*, vol. 15, no. 1, pp. 339–345, 2014.

[304] S. Mouri, Y. Miyauchi, *et al.*, “Tunable photoluminescence of monolayer MoS2 via chemical doping,” *Nano letters*, vol. 13, no. 12, pp. 5944–5948, 2013.

[305] W. Su, H. Dou, *et al.*, “Tuning photoluminescence of single-layer MoS 2 using H 2 O 2,” *RSC Advances*, vol. 5, no. 101, pp. 82 924–82 929, 2015.

[306] H.-V. Han, A.-Y. Lu, *et al.*, “Photoluminescence Enhancement and Structure Repairing of Monolayer MoSe2 by Hydrohalic Acid Treatment,” *ACS Nano*, vol. 10, no. 1, pp. 1454–1461, 2016.

[307] S. J. Pearton, J. W. Corbett, *et al.*, *Hydrogen in crystalline semiconductors.* Springer Science & Business Media, 2013, vol. 16.

[308] S. Birindelli, M. Felici, *et al.*, “Single photons on demand from novel site-controlled GaAsN/GaAsN: H quantum dots,” *Nano letters*, vol. 14, no. 3, pp. 1275–1280, 2014.

[309] M. Yang, X. Cheng, *et al.*, “Anharmonicity of monolayer MoS2, MoSe2, and WSe2: A Raman study under high pressure and elevated temperature,” *Applied Physics Letters*, vol. 110, no. 9, p. 093108, 2017.

[310] D. Nam, J.-U. Lee, *et al.*, “Excitation energy dependent Raman spectrum of MoSe2,” *Scientific reports*, vol. 5, p. 17113, 2015.

[311] A. S. Pawbake, M. S. Pawar, *et al.*, “Large area chemical vapor deposition of monolayer transition metal dichalcogenides and their temperature dependent Raman spectroscopy studies,” *Nanoscale*, vol. 8, no. 5, pp. 3008–3018, 2016.

[312] P. Soubelet, A. Bruchhausen, *et al.*, “Resonance effects in the Raman scattering of monolayer and few-layer MoSe 2,” *Physical Review B*, vol. 93, no. 15, p. 155407, 2016.

[313] A. Arora, K. Nogajewski, *et al.*, "Exciton band structure in layered MoSe 2: from a monolayer to the bulk limit," *Nanoscale*, vol. 7, no. 48, pp. 20 769–20 775, 2015.

[314] A. Branny, G. Wang, *et al.*, "Discrete quantum dot like emitters in monolayer MoSe2: Spatial mapping, magneto-optics, and charge tuning," *Applied Physics Letters*, vol. 108, no. 14, p. 142101, 2016.

[315] S. Kumar, A. Kaczmarczyk, *et al.*, "Strain-induced spatial and spectral isolation of quantum emitters in mono-and bilayer WSe2," *Nano letters*, vol. 15, no. 11, pp. 7567–7573, 2015.

[316] K. O'Donnell and X. Chen, "Temperature dependence of semiconductor band gaps," *Applied physics letters*, vol. 58, no. 25, pp. 2924–2926, 1991.

[317] M. Koperski, K. Nogajewski, *et al.*, "Single photon emitters in exfoliated WSe2 structures," *Nature nanotechnology*, vol. 10, no. 6, pp. 503–506, 2015.

[318] A. Srivastava, M. Sidler, *et al.*, "Optically active quantum dots in monolayer WSe2," *Nature nanotechnology*, vol. 10, no. 6, pp. 491–496, 2015.

[319] J. Martín-Sánchez, A. Mariscal, *et al.*, "Effects of dielectric stoichiometry on the photoluminescence properties of encapsulated WSe2 monolayers," *Nano Research*, pp. 1–16, 2017.

[320] B. Wang, S. Yang, *et al.*, "Radiation-induced direct bandgap transition in few-layer MoS2," *Applied Physics Letters*, vol. 111, no. 13, p. 131101, 2017.

[321] A. Züttel, "Materials for hydrogen storage," *Materials today*, vol. 6, no. 9, pp. 24–33, 2003.

[322] S. J. Cartamil-Bueno, P. G. Steeneken, *et al.*, "Colorimetry technique for scalable characterization of suspended graphene," *Nano letters*, vol. 16, no. 11, pp. 6792–6796, 2016.

[323] T. F. Jaramillo, K. P. Jørgensen, *et al.*, "Identification of active edge sites for electrochemical H2 evolution from MoS2 nanocatalysts," *science*, vol. 317, no. 5834, pp. 100–102, 2007.

[324] M. Seel and R. Pandey, "Proton and hydrogen transport through two-dimensional monolayers," *2D Materials*, vol. 3, no. 2, p. 025004, 2016.

[325] S. Hu, M. Lozada-Hidalgo, *et al.*, "Proton transport through one-atom-thick crystals," *Nature*, vol. 516, no. 7530, pp. 227–227, 2014.

[326] D. Lloyd, X. Liu, *et al.*, "Band gap engineering with ultralarge biaxial strains in suspended monolayer MoS2," *Nano letters*, vol. 16, no. 9, pp. 5836–5841, 2016.

[327] R. Yang, J. Lee, *et al.*, "Tuning Optical Signatures of Single-and Few-Layer MoS2 by Blown-Bubble Bulge Straining up to Fracture," *Nano Letters*, vol. 17, no. 8, pp. 4568–4575, 2017.

[328] S. B. Desai, G. Seol, *et al.*, "Strain-induced indirect to direct bandgap transition in multilayer WSe2," *Nano letters*, vol. 14, no. 8, pp. 4592–4597, 2014.

[329] A. Kuznetsov, M. Gleeson, *et al.*, "Hydrogen-induced blistering mechanisms in thin film coatings," *Journal of physics: Condensed matter*, vol. 24, no. 5, p. 052203, 2011.

[330] W. Fichter, "Some solutions for the large deflections of uniformly loaded circular membranes," *NASA Tech. Pap.*, vol. 3658, pp. 1–24, 1997.

[331] D. Çakır, F. M. Peeters, *et al.*, "Mechanical and thermal properties of h-MX2 (M= Cr, Mo, W; X= O, S, Se, Te) monolayers: A comparative study," *Applied Physics Letters*, vol. 104, no. 20, p. 203110, 2014.

[332] S. P. Koenig, N. G. Boddeti, *et al.*, "Ultrastrong adhesion of graphene membranes," *Nature nanotechnology*, vol. 6, no. 9, pp. 543–546, 2011.

[333] R. Frisenda, M. Drüppel, *et al.*, "Biaxial strain tuning of the optical properties of single-layer transition metal dichalcogenides," *npj 2D Materials and Applications*, vol. 1, no. 1, p. 10, 2017.

[334] R. Roldán, A. Castellanos-Gomez, *et al.*, "Strain engineering in semiconducting two-dimensional crystals," *Journal of Physics: Condensed Matter*, vol. 27, no. 31, p. 313201, 2015.

[335] E. Khestanova, F. Guinea, *et al.*, "Universal shape and pressure inside bubbles appearing in van der Waals heterostructures," *Nature communications*, vol. 7, 2016.

[336] F. Wang, I. A. Kinloch, *et al.*, "Strain-induced phonon shifts in tungsten disulfide nanoplatelets and nanotubes," *2D Materials*, vol. 4, no. 1, p. 015007, 2016.

[337] Y. Yu, Y. Yu, *et al.*, "Engineering Substrate Interactions for High Luminescence Efficiency of Transition-Metal Dichalcogenide Monolayers," *Advanced Functional Materials*, vol. 26, no. 26, pp. 4733–4739, 2016.

[338] S. P. Koenig, L. Wang, *et al.*, "Selective molecular sieving through porous graphene," *Nature nanotechnology*, vol. 7, no. 11, pp. 728–732, 2012.

[339] D. Lloyd, X. Liu, *et al.*, "Adhesion, Stiffness, and Instability in Atomically Thin MoS2 Bubbles," *Nano Letters*, vol. 17, no. 9, pp. 5329–5334, 2017.

[340] F. Guinea, M. Katsnelson, *et al.*, "Energy gaps and a zero-field quantum Hall effect in graphene by strain engineering," *Nature Physics*, vol. 6, no. 1, p. 30, 2010.

[341] M. Cazalilla, H. Ochoa, *et al.*, "Quantum spin Hall effect in two-dimensional crystals of transition-metal dichalcogenides," *Physical review letters*, vol. 113, no. 7, p. 077201, 2014.

[342] H. Ochoa, R. Zarzuela, *et al.*, "Emergent Gauge Fields from Curvature in Single Layers of Transition-Metal Dichalcogenides," *Physical Review Letters*, vol. 118, no. 2, p. 026801, 2017.

[343] G. Pettinari, A. Polimeni, *et al.*, "Photoluminescence: A tool for investigating optical, electronic, and structural properties of semiconductors," in *Semiconductor Research*. Springer, 2012, pp. 125–170.

[344] G. Gobeli and H. Fan, "Semiconductor research, second quarterly rept," *Purdue University, Lafayette*, 1956.

[345] M. Cardona and Y. Y. Peter, *Fundamentals of semiconductors*. Springer, 2005.

[346] G. H. Wannier and A. Maradudin, "Elements of solid state theory," *Physics Today*, vol. 13, p. 60, 1960.

[347] H. Haug and S. W. Koch, *Quantum theory of the optical and electronic properties of semiconductors*. World Scientific Publishing Co Inc, 2009.

[348] R. Elliott, "Intensity of optical absorption by excitons," *Physical Review*, vol. 108, no. 6, p. 1384, 1957.

[349] C. Weisbuch and H. Benisty, "Microcavities in Ecole Polytechnique Fédérale de Lausanne, Ecole Polytechnique (France) and elsewhere: past, present and future," *physica status solidi (b)*, vol. 242, no. 11, pp. 2345–2356, 2005.

[350] F. Bassani and P. P. G. Electronicstates, *OPTICAL TRANSITIONS IN SOLIDS*. Pergamon press, 1975.

[351] K. Nash, M. Skolnick, *et al.*, “Diamagnetism as a probe of exciton localization in quantum wells,” *Physical Review B*, vol. 39, no. 15, p. 10943, 1989.

[352] S. Walck and T. Reinecke, “Exciton diamagnetic shift in semiconductor nanostructures,” *Physical Review B*, vol. 57, no. 15, p. 9088, 1998.

[353] Y. Zhang, A. Mascarenhas, *et al.*, “Magnetoexcitons in anisotropic semiconductors,” *Journal of applied physics*, vol. 83, no. 1, pp. 448–454, 1998.

[354] S. Shokhovets, O. Ambacher, *et al.*, “Conduction-band dispersion relation and electron effective mass in III-V and II-VI zinc-blende semiconductors,” *Physical Review B*, vol. 76, no. 12, p. 125203, 2007.

[355] D. A. Long, “The raman effect: a unified treatment of the theory of raman scattering by molecules,” *West Sussex*, 2002.

[356] W. E. Gifford and R. Longsworth, “Surface heat pumping,” in *Advances in cryogenic engineering.* Springer, 1966, pp. 171–179.

[357] L. Novotny and B. Hecht, *Principles of nano-optics.* Cambridge university press, 2012.

[358] J. Perenboom, S. Wiegers, *et al.*, “The new installation at the nijmegen high field magnet laboratory,” *Physica B: Condensed Matter*, vol. 346, pp. 659–662, 2004.

[359] http://www.ru.nl/hfml/research/levitation/diamagnetic/bitter-solenoid/.

[360] https://nationalmaglab.org/news-events/feature-stories/making-resistive-magnets.

[361] M. D. Bird, “Resistive magnet technology for hybrid inserts,” *Superconductor Science and Technology*, vol. 17, no. 8, p. R19, 2004.

[362] H. Kaufman, J. Harper, *et al.*, “Developments in broad-beam, ion-source technology and applications,” *Journal of Vacuum Science and Technology*, vol. 21, no. 3, pp. 764–767, 1982.

[363] C. Vieu, F. Carcenac, *et al.*, “Electron beam lithography: resolution limits and applications,” *Applied Surface Science*, vol. 164, no. 1, pp. 111–117, 2000.

[364] A. Tavakkoli KG, S. Piramanayagam, *et al.*, “Path to achieve sub-10-nm half-pitch using electron beam lithography,” *Journal of Vacuum Science & Technology B, Nanotechnology and Microelectronics: Materials, Processing, Measurement, and Phenomena*, vol. 29, no. 1, p. 011035, 2011.

[365] M. Z. Baykara, T. C. Schwendemann, *et al.*, “Three-Dimensional Atomic Force Microscopy–Taking Surface Imaging to the Next Level,” *Advanced materials*, vol. 22, no. 26-27, pp. 2838–2853, 2010.

[366] https://nationalmaglab.org/news-events/feature-stories/making-resistive-magnets.

[367] P. Eaton and P. West, *Atomic force microscopy.* Oxford University Press, 2010.